

Current Transport and Onset-Related Phenomena in an MPD Thruster Modified by Applied Magnetic Fields

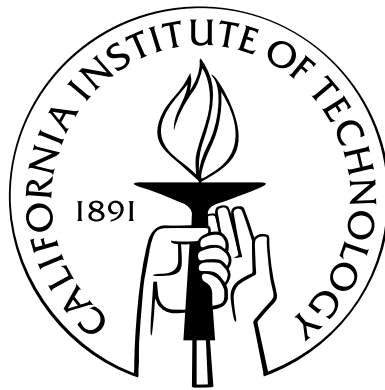
Thesis by

Robert Carlos Moeller

In Partial Fulfillment of the Requirements

for the Degree of

Doctor of Philosophy



California Institute of Technology

Pasadena, California

2013

(Defended November 7, 2012)

© 2013

Robert Carlos Moeller

All Rights Reserved

To my family, Claudia, Carmen, Rolf, Richard,
and the many great minds that continue to inspire

Acknowledgements

“By mutual confidence and mutual aid – great deeds are done, and great discoveries made”

– Homer, ancient Greek poet ca. 8th century BC and author of the *Iliad* and the *Odyssey*

Pondering over the many great people in my life who have made this journey of discovery and exploration possible leaves me humbled and awestruck — humbled by the gracious support and intelligence of these amazing individuals and awestruck by the sheer numbers who have played a part. No Ph.D. process is ever an individual effort, and mine has surely been one that bears the rewards of many inspiring family members, friends, and colleagues. I will never be able to fully acknowledge all those who have participated, but I can fondly reflect with immense gratitude on key players who have made the voyage one of my greatest pleasures and shepherded me through the many trials.

Though no words could ever properly convey my sentiments, I must first and foremost thank my wife, Claudia Rodriguez-Moeller. She has been my Muse through this entire journey, tirelessly and selflessly sharing her love, encouragement, and personal time to lift me up and soar over troubled waters. An amazing woman full of grace, she has made me beyond fortunate and truly blessed to have her in my life. She has been far more giving and patient than anyone ever should be, and for that, I now look forward to many future attempts in my small ways to repay the innumerable favors. I know with great confidence that we will be enjoying many new great adventures together.

Similarly beyond measure in patience and perseverance is Dr. Jay Polk. He has not only been my JPL advisor, but he has been an outstanding teacher, mentor, guide, and friend. All too often, he heeded my calls to set me again in the right direction. I have learned from him how to think like an experimentalist (even when I did not necessarily want to), how to let the data speak for itself to tell me something new, and how to not be afraid of trying something just to see if it works. I am also glad to have in him someone that can always make good travel recommendations and will be able to blacksmith my suit of armor and sword when the inevitable zombie apocalypse comes.

A heartfelt thank you goes to my Caltech advisor, Professor Joe Shepherd, and dissertation committee members Paul Bellan, Melany Hunt, and Dan Meiron for seeing me through the great sprint to the finish. The advice that I obtained on the experimental work and thesis have been incredibly helpful, and the encouragement and guidance was just what I needed to successfully see it through to the end.

My utmost respect and thanks go to many folks in the JPL Electric Propulsion Group, including Ray Swindlehurst, Al Owens, Dennis Fitzgerald, Lee Johnson, Dan Goebel, Rich Hofer, and others. I am convinced that Ray, Al, and Dennis were truly magicians, given the awe-inspiring things they would create or simply make the seemingly impossible work in the lab. I am forever grateful for the many little tricks on working with hardware that I picked up from them, however amateur I may have been with my handiwork, and their willingness to always lend a hand. I sincerely appreciate the many great lunches and conversations we had, whether it be about politics, the future of space exploration, or just how to take care of household plumbing problems. I will forever be grateful to Lee Johnson for letting me use the “Big Green” vacuum chamber so many times for my experiments and also for interesting conversations on the way things really work at NASA. I am happy to know that electric propulsion has a bright future with such an amazing group blazing the trail.

I am also immensely fortunate to have crossed paths with some amazing students in my research.

I can only hope that what I shared with them was half as useful as the lessons that I ultimately learned from working with them. Nick Robertson helped immensely on construction of the final triple Langmuir probe and measurements. Our many late-night conversations and activities in the lab kept me sane during the otherwise stressful final months of experiments. I am confident that he will be a major contributor to the future extension of humanity's endeavors in space. Vritika Singh was tremendously helpful in the testing and mounting of the applied-field magnets. Vritika is one of the kindest and most considerate people I have ever met, and her enthusiasm for space research and engineering truly reinvigorated my own passions for space. I know she will bring that same enthusiasm to all of her work. Rachel Trabert was also a great help during early testing with the thruster and single Langmuir probe, and I look forward to seeing her succeed in her future endeavors.

I will also forever be indebted and grateful to my immediate and extended family. My mother, Carmen, has been unwavering in her unconditional love and support. I have learned so much about patience and respect from such a kind and sweet woman. My father, Rolf, taught me from a young age a work ethic that I carry into everything I do, as he is a man who has lived a life of hard work and perseverance. I am proud to be able to share my doctoral victory with my parents and my brother, Richard. However far apart we may be, our bond is always strong. My deep thanks also go to Claudia's family — Ana, Gregorio, “the Olivias,” and Greg — and to Claudia's extended family for embracing me as one of their own, seeing me through many years of ups and downs in this process, and for always helping me to laugh, hit the gym for some kickboxing, or find other creative ways of unwinding and letting the stress out.

Thank you to my many friends Jason, Shane, Patrick, Chris, Wendy, Afna, Dheilan, Nicole, Jared, Teresa, Erik, Mike, and so many others. Figuring out how to let loose has never been a problem with a fun group like you, and I have found so much inspiration in unexpected ways from

each and every one of you. Very few know what I actually do, conveniently just referring to me as the “rocket scientist,” but to you I will always be the “ghetto scientist” (affectionately, of course).

I also have to thank Caltech. It is this enigma of a place, one that is at the same time inspiring yet slightly unstable (but ultimately in a good way). It is an environment where people dare to dream big and can actually accomplish the seemingly impossible through sheer audacity of engineering and scientific endeavor. It is also a place where some people are pushed to the brink of sanity by their own pursuits and end up walking around barefoot outside with orange-colored hair. It is a living, breathing entity of its own that ultimately, like my friend Mike Sekerak once put it, breaks you down to build you up again in the scientific equivalent of military elite training. You will never quite be the same after experiencing Caltech, but you will indeed be hardened and stronger intellectually because of it. So, thank you, Caltech.

A heartfelt thank you also goes to the various sponsors and fellowship programs that have helped by providing funding for my graduate school and research. Much gratitude goes to the Jet Propulsion Laboratory (JPL), including their Research and Technology Development (R&TD) program and both Cinzia Zuffada and Paula Grunthaner from the Center for Academic Partnerships (CAP) program. Also, thank you to NASA’s John Warren for aiding with Project Prometheus Program close-out funding for students. Finally, I extend many thanks to the NASA Graduate Student Researchers Program (GSRP) and National Defense Science and Engineering Graduate (NDSEG) fellowship programs for their support.

Of course, it is important to know where you have been and where you are going, and to that end, I thank the many friends and colleagues at JPL who have encouraged me and led me to where I am headed in my next journey. My deepest thanks go to Chet Borden, Kelley Case, Tom Spilker, Bill Smythe, Kim Reh, Brent Sherwood, and many others who have been my mentors and cheerleaders at JPL. I look forward to working with all of you in the future to help shape our ambitious new space

missions. *Ad astra per aspera!*

Abstract

This work focused on the effects of tailored, externally-applied magnetic fields on current transport and near-anode processes in the plasma discharge of a magnetoplasmadynamic thruster (MPDT). Electrical and plasma diagnostics were used to determine whether applied magnetic fields could mitigate the effects of the “onset” phenomena, including large-amplitude terminal voltage fluctuations and high anode fall voltages associated with unstable operation and anode erosion. A new MPDT was developed with a multi-channel hollow cathode and a concentric anode extending downstream of the cathode exit plane. This thruster was operated with quasi-steady pulses of 1 ms duration at power levels of 36 kW (20 V, 1800 A) to 3.3 MW (255 V, 13.1 kA) with argon propellant in three different magnetic configurations. These included purely self-generated magnetic fields (without external electromagnets) and two different externally-applied poloidal magnetic field topologies. One configuration used magnetic field lines tangential to the anode lip near the exit plane (and intersecting the anode further upstream), and the other configuration created a cusp with magnetic field lines intersecting the anode near the exit plane.

The influence of the applied fields on the discharge current streamlines, current densities, and key plasma properties (electron temperature, number density, and plasma potential) was studied. A primary finding was that the current pattern and current densities redistributed to follow the applied poloidal magnetic field lines, which created increased conduction paths to the anode. This shift was particularly pronounced for the tangential magnetic field, which moved the current attachment

upstream along the anode. Increased electron temperatures were also found in regions of high azimuthal current densities induced by the magnets.

Another major finding was that the anode fall voltage was substantially reduced with both applied magnetic field topologies over a large range of currents. For example, at 8 kA, the 20 V anode fall measured in the self-field configuration was completely eliminated in both applied-field configurations. At 10.7 kA, the cusp applied magnetic field decreased anode fall voltages from 45–83 V down to 15 V or lower along much of the anode. This reduction occurs because the applied magnetic field lines which intersect the anode provide a high conductivity path, reducing the local electric field required to sustain the radial current densities at the anode.

The amplitude and frequency of the voltage fluctuations were also reduced over a broad range of currents with the applied fields. The standard deviations of the fluctuations were lowered by 37–49% at 8–9 kA with both applied magnetic fields, and the cusp applied field still exhibited a 15% decrease at 10.7 kA. The current threshold at which the rapid increase in the magnitude and frequency of the voltage spikes occurred was typically increased by 1–2 kA with the applied fields. Nonetheless, the applied fields consistently reduced the magnitude of the voltage fluctuations at currents up to 10.7 kA, above which the fluctuations for all three configurations approached the same values. The applied B fields also reduced the magnitude of local transients in the ion saturation current. These results suggest a reduction in frequency and intensity of current-concentrating filaments and anode spots, along with an induced azimuthal rotational motion of the plasma in regions of high applied magnetic field. This result is significant because anode spots cause localized erosion of the anode and are the main life limiter at high currents.

In addition, decreases in the mean terminal voltages as large as 31% were measured with the applied magnetic fields. The cusp applied magnetic field reduced terminal voltages over the entire range of discharge currents, and the tangential magnetic field lowered terminal voltages below 10.7

kA. These effects were primarily attributable to the reduction in the anode fall voltage and result in substantial increases in the estimated thruster efficiency by up to 41% relative to self-field operation.

Overall, both applied magnetic field configurations enabled significant reductions in onset-related behaviors relative to self-field operation. These improvements should lead to reduced anode erosion, i.e., improved thruster lifetime, and increased thruster efficiency with the applied fields. The applied fields used in this study differ from both the topologies and relative field strengths typically used in the vast majority of conventional, so-called “applied-field MPD thrusters” (AF-MPDTs). These results suggest a distinctive and more effective approach to influencing the near-anode phenomena and mitigating the deleterious effects of onset with appropriately designed applied magnetic fields.

Contents

Acknowledgements	iv
Abstract	ix
List of Figures	xv
List of Tables	xx
1 Introduction	1
1.1 Background and Motivation	1
1.2 Review of Previous Work	7
1.2.1 A Brief Background on MPD Thruster Research	7
1.2.2 Onset Phenomena	8
1.2.3 Anode Fall Voltages and Applied Magnetic Fields	11
1.3 Thesis Outline	15
2 Experimental Setup and Diagnostics	18
2.1 MPD Thruster	18
2.2 External Magnets and Applied Magnetic Fields	22
2.3 Vacuum Facility	27
2.4 Discharge Circuit	28

2.5	Gas Pulse System	30
2.5.1	Hardware	30
2.5.2	Mass Flow Calibration	30
2.6	Diagnostics	32
2.6.1	Data Acquisition System	32
2.6.2	Terminal Voltage and Current Signals	33
2.6.3	Magnetic Probe Array	33
2.6.4	Triple Langmuir Probe	37
2.6.5	High-Speed Video Imaging	44
3	Influence of the Applied Magnetic Fields on Voltage-Current Characteristics and Voltage Fluctuations	45
3.1	Operating Conditions and Thruster Configurations	45
3.2	Collection of Data	46
3.3	Analysis of the Moments of the Voltage Signal Distribution	49
3.4	Analysis of the Transients and Power Spectrum of the Voltage Signal	57
3.5	Summary of Results	67
4	Magnetic Probing of Internal Magnetic Field Topology and Current Profiles	77
4.1	Operating Conditions and Thruster Configurations	77
4.2	Collection of Data	78
4.3	Analysis of Magnetic Fields and Current Patterns at High Discharge Current	80
4.4	Analysis of Current Densities at High Discharge Current	89
4.5	Analysis of Current Densities Along the Anode Over a Range of Discharge Currents	96
4.6	Summary of Results	99

5	Langmuir Probe Measurements of Plasma Properties and Potential	103
5.1	Operating Conditions and Thruster Configurations	103
5.2	Collection of Data	104
5.3	Analysis of Langmuir Probe Measurements Along the Anode at High Current . . .	106
5.4	Analysis of Langmuir Probe Measurements Along the Anode at Reduced Current .	113
5.5	Analysis of Langmuir Probe Measurements in the Thruster Interior	118
5.6	Assessment of Ion Saturation Current Fluctuations	124
5.7	Summary of Results	130
6	Interpretations and Conclusions	133
6.1	Effects on the Current Pattern, Conductivity, and Current Densities	133
6.2	Regions of Increased Heating and Induced Azimuthal Current Densities	144
6.3	Reduction of Anode Fall Voltages	150
6.4	Reduced Terminal Voltages, Fluctuations, Anode Heating, and Anode Spotting . .	159
6.5	Effect on Thrust and Efficiency	166
6.6	Summary and Conclusions	171
6.7	Recommendations for Future Work	176
A	Magnetic Force Densities	179
	Bibliography	185

List of Figures

1.1	Illustration of MPD thruster current, magnetic field, and acceleration forces.	6
2.1	Odysseus MPD thruster with magnets mounted on the vacuum chamber header. . . .	19
2.2	MPD thruster view into discharge chamber.	19
2.3	Schematic of the MPD thruster, applied-field magnets, and gas flow system.	20
2.4	MPD thruster firing.	22
2.5	MPD thruster close-up view highlighting external magnets and mounting rails. . . .	23
2.6	Applied magnetic field magnitude and flux lines for the tangential applied field. . . .	25
2.7	Applied magnetic field magnitude and flux lines for the cusp applied magnetic field.	26
2.8	Vacuum chamber facility at JPL used for the MPDT experiments.	27
2.9	Pulse forming network bank.	29
2.10	Schematic illustrating key elements of the MPDT ignition and PFN circuits.	29
2.11	Calibration of flow rate versus initial upstream plenum pressure.	32
2.12	Sample traces of voltage vs. time for the MPDT discharge.	34
2.13	Sample traces of current vs. time for the MPDT discharge.	34
2.14	Close-up view of magnetic probe array with B-dot coils.	36
2.15	Triple Langmuir probe schematic.	38
2.16	Triple Langmuir probe and tungsten wire tips alongside magnetic probe.	38
3.1	Example voltage traces during quasi-steady period for the self-field case.	47

3.2	Example voltage traces during quasi-steady period for the tangential applied-field case.	48
3.3	Example voltage traces during quasi-steady period for the cusp applied-field case. . .	48
3.4	Mean terminal voltage vs. current characteristics.	49
3.5	Standard deviation vs. current.	51
3.6	Skewness vs. current.	52
3.7	Kurtosis vs. current.	52
3.8	Population distribution histogram for voltage signal without magnets at 10.7 kA. . .	55
3.9	Population distribution histogram for voltage signal with tangential field at 10.7 kA.	56
3.10	Population distribution histogram for voltage signal with cusp field at 10.7 kA. . . .	56
3.11	Population distribution histogram for voltage signal without magnets at 8 kA.	57
3.12	Number of positive spikes >10% above mean voltage.	59
3.13	High-speed video showing evidence of anode spots in thruster at 9 kA.	60
3.14	Evidence of anode erosion in our MPD thruster.	61
3.15	Average peak amplitude of positive spikes >10% above mean voltage.	61
3.16	Average energy per spike for positive spikes >10% above mean voltage.	63
3.17	Total energy in the PSD spectrum, as integrated from 10 to 155 kHz.	64
3.18	Average duration of positive spikes >10% above mean voltage.	65
3.19	Effective average frequency of positive spikes >10% above mean voltage.	66
3.20	Power spectral density (PSD) examples for 3 shots without magnets at 10.7 kA. . . .	68
3.21	Power spectral density (PSD) examples for 3 shots with tangential B field at 10.7 kA.	68
3.22	Power spectral density (PSD) examples for 3 shots with cusp B field at 10.7 kA. . . .	69
3.23	Power spectral density (PSD) examples for 3 shots without magnets at 8.0 kA. . . .	69
3.24	Power spectral density (PSD) examples for 3 shots with tangential B field at 8.0 kA.	70
3.25	Power spectral density (PSD) examples for 3 shots with cusp B field at 8.0 kA. . . .	70

3.26	Power spectral density (PSD) examples for 2 shots without magnets at 5.5 kA. . . .	71
3.27	Power spectral density (PSD) examples for 2 shots with tangential B field at 5.5 kA.	71
3.28	Power spectral density (PSD) examples for 2 shots with cusp B field at 5.5 kA. . . .	72
3.29	Power spectral density (PSD) over full spectrum without magnets at 10.7 kA.	72
3.30	Power spectral density (PSD) over full spectrum with tangential B field at 10.7 kA. .	73
3.31	Power spectral density (PSD) over full spectrum with cusp B field at 10.7 kA.	73
4.1	Positions of magnetic probe array coils for B field mapping measurements.	79
4.2	Contour plot of azimuthal B field without magnets at 10.7 kA.	81
4.3	Contour plot of azimuthal B field for tangential applied-field configuration at 10.7 kA.	82
4.4	Contour plot of azimuthal B field for cusp applied-field configuration at 10.7 kA. . .	82
4.5	Contour plot of enclosed current fraction without magnets at 10.7 kA.	85
4.6	Contour plot of enclosed current fraction for tangential applied-field case at 10.7 kA.	85
4.7	Contour plot of enclosed current fraction with tangential applied field lines at 10.7 kA.	86
4.8	Contour plot of enclosed current fraction for cusp applied-field case at 10.7 kA. . . .	86
4.9	Contour plot of enclosed current fraction with cusp applied field lines at 10.7 kA. . .	87
4.10	Profiles of azimuthal B field near the anode vs. axial position at 10.7 kA.	88
4.11	Profiles of enclosed current fraction along the anode vs. axial position at 10.7 kA. . .	88
4.12	Profiles of current density along the anode vs. axial position at 10.7 kA.	90
4.13	Contour plot of radial current density at 10.7 kA without magnets.	92
4.14	Contour plot of axial current density at 10.7 kA without magnets.	92
4.15	Contour plot of poloidal current density at 10.7 kA without magnets.	93
4.16	Contour plot of radial current density at 10.7 kA with tangential B field.	93
4.17	Contour plot of axial current density at 10.7 kA with tangential B field.	94
4.18	Contour plot of poloidal current density at 10.7 kA with tangential B field.	94

4.19	Contour plot of radial current density at 10.7 kA with cusp B field.	95
4.20	Contour plot of axial current density at 10.7 kA with cusp B field.	95
4.21	Contour plot of poloidal current density at 10.7 kA with cusp B field.	96
4.22	Profiles of current density along anode over a range of currents without magnets. . .	97
4.23	Profiles of current density along anode over a range of currents with tangential B field.	98
4.24	Profiles of current density along anode over a range of currents with cusp B field. . .	98
5.1	Triple Langmuir probe positions for near-anode measurements.	105
5.2	Electron temperature along the anode at 10.7 kA without magnets.	107
5.3	Electron temperature along the anode at 10.7 kA with tangential B field.	107
5.4	Electron temperature along the anode at 10.7 kA with cusp B field.	108
5.5	Electron temperature along the anode at 10.7 kA comparing 3 configurations.	108
5.6	Plasma number density along the anode at 10.7 kA without magnets.	110
5.7	Plasma number density along the anode at 10.7 kA with tangential B field.	111
5.8	Plasma number density along the anode at 10.7 kA with cusp B field.	111
5.9	Plasma number density along the anode at 10.7 kA comparing 3 configurations.	112
5.10	Anode fall voltage along the anode at 10.7 kA without magnets.	114
5.11	Anode fall voltage along the anode at 10.7 kA with tangential B field.	114
5.12	Anode fall voltage along the anode at 10.7 kA with cusp B field.	115
5.13	Anode fall voltage along the anode at 10.7 kA comparing all 3 configurations.	115
5.14	Electron temperature along the anode at 8 kA comparing all 3 configurations.	116
5.15	Plasma number density along the anode at 8 kA comparing all 3 configurations.	117
5.16	Anode fall voltage along the anode at 8 kA comparing all 3 configurations.	117
5.17	Bubble plot of electron temperature without magnets at 10.7 kA and 9 kA.	121
5.18	Bubble plot of number density without magnets at 10.7 kA and 9 kA.	122

5.19	Bubble plot of number density with flow field overlay.	123
5.20	Ion saturation current signal fluctuations vs. time at 10.7 kA.	125
5.21	Ion saturation current signal fluctuations vs. time at 8 kA.	125
5.22	Ion saturation current power spectral density (PSD) at 10.7 kA.	126
5.23	Ion saturation current power spectral density (PSD) at 8 kA.	126
5.24	High-speed video frames of thruster discharge fluctuations at 9 kA.	129
6.1	Electrical conductivity calculated along the near-anode region at 10.7 kA.	136
6.2	Electron Hall parameter calculated along the near-anode region at 10.7 kA.	138
6.3	Electron temperature measurements along the near-anode region at 10.7 kA.	145
6.4	Azimuthal current density estimated along the near-anode region at 10.7 kA.	147
6.5	Total current density estimated along the near-anode region at 10.7 kA.	147
6.6	Ratio of drift velocity to ion thermal velocity along the near-anode region at 10.7 kA.	151
6.7	Ratio of measured radial current density to electron thermal current at 10.7 kA.	155
6.8	Ratio of measured radial current density to electron thermal current at 10.7 kA.	158
6.9	Calculated thrust efficiency for the three magnetic configurations.	168
6.10	Calculated thrust (N) for the three magnetic configurations.	169
6.11	Calculated Isp (s) for the three magnetic configurations.	169
A.1	Magnetic force density vector plot without magnets.	182
A.2	Magnetic force density vector plot with tangential applied field.	183
A.3	Magnetic force density vector plot with cusp applied field.	184

List of Tables

3.1	Comparison of terminal voltage signal means and relative reductions with applied magnetic fields.	50
3.2	Comparison of terminal voltage signal standard deviations and relative reductions with applied magnetic fields.	53

Chapter 1

Introduction

1.1 Background and Motivation

Future mission requirements will place challenging demands on candidate spacecraft propulsion technologies, from high delta-V maneuvers on robotic spacecraft to greater efficiency and faster trip times on human deep-space expeditions [1, 2, 3, 4, 5, 6, 7, 8, 9]. In particular, requirements for increasingly higher delta-V (large changes in velocity) over the course of such ambitious missions imply the need for higher specific impulse (I_{sp}) but with acceptable trip times (i.e., sufficient thrust to enable reasonable trip time constraints). The demand for higher specific impulse is made obvious when considering the “ideal rocket equation,” given by [10]

$$\frac{M_{initial}}{M_{final}} = \exp\left(\frac{\Delta v}{g_0 I_{sp}}\right) \quad (1.1)$$

where Δv is the velocity change of the maneuver (delta-V), $M_{initial}$ is the initial mass, M_{final} is the final mass after the delta-V maneuver, and g_0 is a constant given by the gravitational acceleration at Earth’s surface, 9.807 m/s². This equation shows the strong exponential dependence between mass, the delta-V, and the specific impulse of the propulsion system. A larger total launch mass for a spacecraft and its propellant ultimately translates into higher costs for the size of a launch vehicle,

material, engineering labor, etc. Thus, reducing total launch mass by reducing a spacecraft's total propellant load and decreasing the size and mass of the structure to support it has clear cost-saving benefits. For a given mission delta-V requirement, one can lower launch mass exponentially by increasing the I_{sp} of the propulsion system used.

Electric propulsion (EP) encompasses technologies with the potential to enable future advanced space missions, due in large part to high I_{sp} . EP is a class of technologies used for spacecraft propulsion in which an electrical power source is used to convert electrical input power into kinetic energy of the exhaust propellant for thrust. Specific impulses for EP thrusters are generally much higher (typically 800–10,000 s or higher I_{sp}) than those of conventional chemical propulsion thrusters (175–450 s I_{sp}). EP thruster technologies are generally classified into three sub-categories: electrothermal, electrostatic, and electromagnetic. Electrothermal thrusters (e.g., resistojets and arcjets) use electrical power to heat and add enthalpy to an expanding propellant gas, similar to chemical thrusters but with resistive heating instead of chemical reactions as the power source. Electrostatic thrusters (e.g., ion thrusters) primarily use electric fields to accelerate ions as thrust, and typically use a separate cathode discharge to neutralize the exhaust beam. Electromagnetic thrusters (e.g., magnetoplasmadynamic thrusters) generally use electromagnetic forces to accelerate a bulk plasma flow. Work in the field of EP also includes an array of more general applications, as well. The commercial space industry would benefit from higher-efficiency technologies for use in attitude control systems, station-keeping processes, and orbital transfer spacecraft [11]. Such advances imply lower propellant requirements, which directly translate into lower launch costs or increased payloads. Further, the discoveries made and technologies developed from the associated challenges in plasma physics, thermophysics, controls, and plasma-surface interactions could also have broad applications in manufacture and analysis of materials, thin-film deposition, energy conversion technologies, and other industrial applications [12]. Also, many physical processes in these thrusters

have analogies in other areas of plasma science ranging broadly from arc furnaces to astrophysical phenomena [13].

A magnetoplasmadynamic thruster (MPDT) is a high-power spacecraft electric propulsion device still in the research stage. The thruster is sub-classified as an electromagnetic (EM) accelerator because it incorporates electromagnetic forces to produce bulk acceleration in a plasma predominantly through Lorentz forces, $\mathbf{j} \times \mathbf{B}$, where \mathbf{j} is the current density and \mathbf{B} is the magnetic field. In these coaxial thrusters, current flows in the plasma between an inner cathode and a surrounding concentric anode in either pulsed (quasi-steady) or steady-state operation. The interaction of the high current discharge and either the self-induced (current-driven) or externally-applied magnetic field accelerates the plasma to produce thrust.

MPD thrusters can achieve one of the highest power-processing and thrust capabilities amongst EP systems, from 100s of kilowatts up to several megawatts and 10s to 100s of Newtons per thruster at high specific impulses (I_{sp}) of 1,000–10,000 s and higher [14]. Therefore, like state-of-the-art ion and Hall thrusters, MPDTs are capable of much higher specific impulses than those of conventional chemical thrusters, albeit with much higher thrust and power density for a given size of thruster. For a given total velocity change (ΔV) demanded by a high-power mission, MPDTs result in smaller and fewer thrusters and associated components than required by most other EP technologies. Ion thrusters and other well-established EP devices are not predicted to be scalable to the combined high specific impulse and relatively high thrust per engine of MPDTs due to fundamental limitations in their physical processes and achievable thrust densities. In many potential high-power applications, ion thrusters would not be practical due to the mass and volume of the large number of thrusters that would be required to process all of the necessary input power. Power levels of 100s of kW per thruster or higher may be required for enabling missions to the Moon, Lagrange points, asteroid, and Mars with megawatt-class spacecraft to support the large cargo infrastructure requirements of

human space exploration, and piloted missions could demand even higher power levels (multi-MW) to efficiently deliver sufficient mass or decrease trip times [3, 4, 5, 6, 7]. Also, high-power MPDTs could support rapid-response orbital transfer and repositioning for future defense and commercial applications. Thus, MPDTs can effectively fill a high-power niche in advanced propulsion for future space missions.

MPDTs surpass ion and Hall thrusters in terms of power processed per thruster, but the state-of-the-art lifetimes, specific impulses, and efficiencies are not nearly as high as currently achievable by ion and Hall thrusters. Presently, observed performance of MPDTs is typically between 30–50% electrical-to-jet power conversion efficiency, and thruster lifetimes much beyond 1000 hours are challenging [14]. Some limited testing with lithium MPDTs has demonstrated promising efficiencies above 60% [15, 16]. One could compare such performance metrics to state-of-the-art ion thruster development, where efficiencies as high as 81% and operation for tens of thousands of hours have been demonstrated for ion thrusters [17]. Consequently, there is a compelling case for pursuing research in MPDTs to achieve improved efficiencies and lifetimes in the higher power and thrust regime not achievable by ion thrusters. The long-term goals are to enable higher specific impulse operation at the increased power levels of interest, significantly increase efficiency, and enhance lifetime perhaps up to an order of magnitude or more.

The steady-state, self-field MPDT and applied-field MPDT (AF-MPDT) are high-power EP technologies with significant potential for increased performance to enable future mission applications. The self-field MPDT operates without magnets, using only its self-generated magnetic field for acceleration. AF-MPDTs use additional externally-applied magnetic fields typically to increase the thrust, particularly at relatively lower powers (10s of kW to order of 200 kW). In an MPD thruster, plasma acceleration is governed by the magnetohydrodynamic (MHD) momentum

equation, given by

$$\rho \frac{D\mathbf{u}}{Dt} = \mathbf{j} \times \mathbf{B} - \nabla P + \nu \rho \nabla^2 \mathbf{u} \approx \mathbf{j} \times \mathbf{B} - \nabla P \quad (1.2)$$

where ρ is the mass density, $\frac{D\mathbf{u}}{Dt}$ is the convective derivative of the center-of-mass velocity vector, \mathbf{j} is the current density vector, \mathbf{B} is the magnetic field vector, and P is the pressure. Initially, we include a viscous damping term (cf., Bellan [13]), where ν is the kinematic viscosity. The kinematic viscosity is primarily due to ion-ion collisions and neutral collisions and is typically very small for plasma conditions of interest. The Lorentz force term, $\mathbf{j} \times \mathbf{B}$, is the electromagnetic contribution to the force densities and becomes significant at high currents. Near the centerline, the pressure gradient term dominates. The electromagnetic accelerating forces are shown in Figure 1.1 for the geometry of poloidal current densities and their induced azimuthal magnetic field. The “blowing” component of the Lorentz force density, f_z , is given by

$$f_z = j_r B_\theta \quad (1.3)$$

and accelerates the plasma axially (resulting in thrust). The “pumping” component of the Lorentz force density, f_r , is given by

$$f_r = j_z B_\theta \quad (1.4)$$

and acts to radially constrain the plasma inward. In the radial direction, electromagnetic pumping forces are balanced by the radial kinetic pressure gradient. In the axial direction, electromagnetic blowing forces and the axial kinetic pressure gradient result in acceleration of the plasma.

At high currents, increased electromagnetic forces pinch the discharge toward the centerline, thus “starving” the near-anode region of charge carriers. In addition, the increased magnetic field near the centerline and cathode impede the mobility of electrons across the magnetic field lines [15].

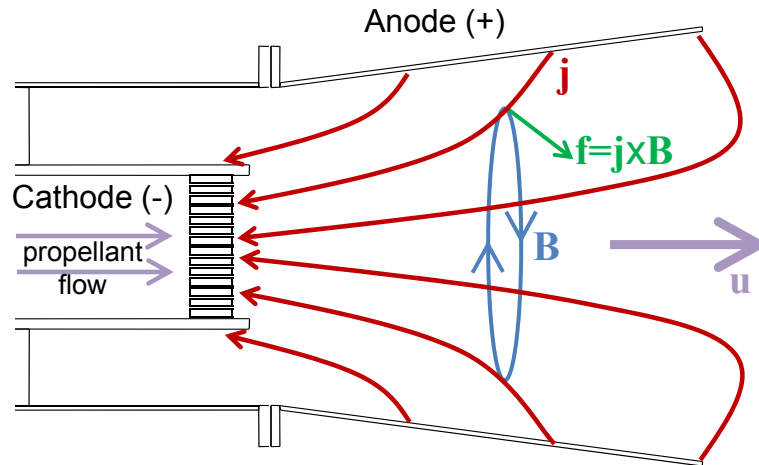


Figure 1.1: Illustration of MPD thruster current, magnetic field, and acceleration forces.

This reduction in electron transport to the anode at increasing discharge currents causes an increased magnitude in the anode fall voltage (potential difference between anode potential and local plasma potential) to accelerate the electrons to accommodate the necessary charge transport. However, the increase in anode fall voltage also results in increased energy flux to the anode. Significant power can be lost to the anode (reducing efficiency), and the high heat fluxes severely affect anode lifetime by inducing evaporation of anode material. In addition, in this “onset” condition (as it is commonly referred to in the literature) anode spots begin to form and vaporize material on the anode surface, resulting in significant anode erosion and large terminal voltage fluctuations [18], as will be discussed in more detail in Section 1.2. Operation at high currents well into these onset conditions is unstable, inefficient, and ultimately impractical due to severe erosion. Some means to control or mitigate the physical processes driving these deleterious behaviors must be identified to enable higher power, high efficiency, and long lifetime operation.

1.2 Review of Previous Work

1.2.1 A Brief Background on MPD Thruster Research

Although the basic concept and approach of coaxial MPD thrusters has existed for decades, research on the thrusters has been limited, largely due to lack of practical opportunities for sufficiently high power in past space missions as of yet. MPDTs presently remain in the fundamental research stage. In the U.S., MPDT research evolved out of arcjet studies as a natural extension of experimentation with lower flow rates and increasing currents in the 1960's [19, 20]. In Russia in the 1970's, a significant amount of experimental testing of various geometries, power levels, and propellants [21, 22] was conducted, partly as a push to investigate propulsion options to enable human missions to Mars during the U.S.-Soviet space race. However, much of this progress was limited to empirical investigations and qualitative insights. Small but intensive research efforts at Princeton University [20] and other academic institutions in Germany [23], Italy [24], and Japan [25] have also greatly advanced the knowledge of the MPDT field since this time, allowing for the framework of understanding the acceleration mechanisms and basic processes in these thrusters. Much of such works was focused on self-field MPDTs at higher power (many hundreds of kW to multi-MW) operated in "quasi-steady" pulsed mode. During the quasi-steady pulses, the pulse durations were long enough such that steady-state plasmadynamics were achieved, but thermodynamic equilibrium with electrodes and materials were not. Such operation enabled studies at very high power levels without the need for a steady-state high power source nor significant use of refractory components.

In addition, notable work was performed on applied-field MPDTs (AF-MPDTs) at relatively lower power levels (order of 10–100 kW) at steady state. Many of the performance characteristics of such AF-MPDTs were well summarized by Kodys [16]. Thrusters operating with lithium (Li) as the propellant were found to have the highest efficiencies. Li-fed thrusters are of particular

interest because the use of Li metal vapor as propellant allows for higher efficiency. This enhanced performance is due to the low first ionization potential of Li (only 5.4 eV) but relatively high second ionization potential (76.6 eV) and first excited state of the ion (71 eV), thus resulting in low “frozen flow” losses (unrecoverable energy lost to multiple ionization and excitation). Li-fed thrusters are also promising because seeding the lithium flow with a small amount of barium could dramatically reduce the cathode operating temperature and greatly extend lifetime [26]. Of particular relevance to Li-fed applied-field thrusters was the work by Fradkin at Princeton [27]. Fradkin investigated the acceleration mechanisms in applied-field Li thrusters through experiments at power levels from 10–35 kW and I_{sp} approaching 3000 sec. He proposed that the additional acceleration from the applied magnetic field could partially be explained in terms of the conversion of rotational energy induced by $j_r B_z$ and $j_z B_r$ forces into axial kinetic energy by magnetic nozzle expansion. This is particularly applicable to lower power MPD thrusters (e.g., 10s of kW) where the applied magnetic field strengths significantly exceed the self-generated magnetic field magnitudes.

Within the past 10–20 years, the increased interest in human deep-space missions (e.g., Mars, Moon, Lagrange points, and asteroids) greatly increased the relevance and interest in high-power electric propulsion. Consequently, significant progress was made in understanding some of the key issues in MPDTs during this time. Some key works have included the evaluation of performance envelopes [28], thrust scaling in MPDTs [14], and Russian experimental testing of various Li-fed MPDTs [15, 29, 30, 31, 32] during the 1990’s in collaboration with NASA.

1.2.2 Onset Phenomena

One of the critical topics that has pervaded much of the MPDT literature has been the issue of “onset” phenomena, as introduced by Malliaris et al. [33] at AVCO Corporation in 1972. It was also referred to as “critical current” or “critical mode” in the Russian literature [21, 34]. Onset represents

a collection of operating behaviors associated with a transition to large-amplitude terminal voltage fluctuations, transients in plasma properties, and growth in anode fall voltages in the plasma. Operation within onset conditions is associated with unstable operation and anode erosion. For a given thruster geometry and propellant choice, this transition occurs at some particular value of J^2/\dot{m} (where J is the total discharge current and \dot{m} is the mass flow rate) as either current is increased (at fixed mass flow rate) or flow rate is decreased (at fixed current). Once the transition to onset occurred, the thruster operation was characterized by high-amplitude terminal voltage fluctuations [35, 23]. Also, Hugel [36] and Diamant [37, 38] identified the formation of “anode spots” during onset. These anode spots are small, discrete points of current concentration on the anode surface and melting of the anode material. An important overall effect was that operation of the thruster in these onset conditions resulted in excessive erosion of the thruster materials, with particularly increased erosion of the anode surface [39].

Malliari et al. [33] identified that the critical value of J^2/\dot{m} where transition to onset occurs scales as $\sim M_{ion}^{-1/2}$, where M_{ion} is the ion mass of the propellant species. Therefore, lower atomic mass propellants (e.g., lithium, hydrogen) should allow stable operation (before onset) at higher currents before transition to onset-related behaviors at a fixed flow rate, which has been consistent with other experimental findings [15, 28]. Also, thruster geometries and flow conditions that enabled increased particle densities near the anode were found to increase the condition at which transition to onset occurs. For example, reducing the ratio of the anode to cathode radius (r_a/r_c) to increase particle density [33] or increased propellant injection at higher radii (closer to the anode) [40, 41] were found to increase the transitional value of J^2/\dot{m} .

Different models of what effectively causes onset have been proposed. Uribarri [42] classifies these models into two categories: anode starvation models and plasma instability models. In the anode starvation models, current conduction is considered to be a sheath-limited process. Elec-

romagnetic radial pumping forces increase with current and cause what is commonly referred to as “anode starvation” or “anode depletion,” in which a reduction in plasma density near the anode results in fewer charge carriers locally available to support the increasing current [21, 43, 44]. However, as discussed by Baksht and Shubin [21, 22], the current that can be drawn from the near-anode plasma is limited by the random thermal flux of electrons to the anode surface, which is directly proportional to local number density. This effect is only exacerbated by the presence of a transverse magnetic field (e.g., the azimuthal self-field of the MPDT) that impedes electron diffusion radially outward to replenish the electrons hitting the anode [45]. When the random thermal flux of electrons to the anode is insufficient to supply the requisite current density, electron-attracting anode fall voltages must form across the sheath and near-anode plasma to enable sufficient electron flux [43, 46]. Therefore, any mechanisms to either increase local electron number density near the anode or to more generally increase electron transport to the anode (without increasing the anode fall voltage) can potentially mitigate the sheath-limited aspects of onset.

Different plasma instability models have also been proposed as possible causes of onset. Authors have described the conditions for exciting drift instabilities due to the relative motion of the electrons and ions in the plasma currents, as described by Tilley et al. [47], and various plasma wave excitations have been measured in MPD thrusters in onset conditions (e.g., ion acoustic waves observed by Tikhonov et al.[44]). Onset in such models is typically associated with exceeding some critical value of the drift velocity ($v_d = \frac{j}{n|q_e|}$, where j is the current density, n is the plasma number density and q_e is the fundamental electron charge) for the inception of current-driven instabilities [22, 48].

Uribarri [42, 18] established a direct link between voltage fluctuations and anode spot formation and extinction, as well as a connection between the anode spots and melting or evaporation of anode material. He established that evaporated anode material effectively “seeds” the discharge with

additional plasma to sustain the discharge and overcome current starvation. Uribarri also presented a capacitively-coupled model of the how the spots could incite the terminal voltage fluctuations and postulated a current filamentation process as associated with spot formation. Recent work by Giannelli et al. [24, 49] identified conditions for the formation of azimuthal instabilities that would lead to such current filamentation in the MPD thruster discharge. Their model linked such filamentation with the current concentration associated with anode spots.

One interesting onset suppression methodology has been to increase the local number density near the anode. Kurtz et al. [23] diverted a fraction (2–10%) of the propellant flow to injection sites on their anode. They were able to increase the current at which onset transition occurred, but only by order of 5% at 10% flow fraction to the anode. The effectiveness of this approach is also further limited by the inefficiencies associated with anode mass injection, namely that the propellant introduced near the anode does not yield as much effective acceleration from the electromagnetic body forces that are higher closer to the thruster centerline (further from the anode). Therefore, introducing increasing fractions of the propellant at the anode would result in decreasing thrust efficiency. Kuriki et al. [50] also studied the effect of injecting propellant near the anode and identified improvements in thrust and efficiency. However, they identified similar increases in performance simply with the inclusion of their anode injection hood even without any additional anode gas flow. As an alternative, one might examine externally-applied magnetic fields as a potentially more effective means of onset mitigation, as will be discussed in the next section.

1.2.3 Anode Fall Voltages and Applied Magnetic Fields

Another issue in addition to the fluctuations and transients introduced with onset is the formation of large anode fall voltages at high thruster discharge currents. Gallimore [43, 46, 51] experimentally studied the anode power deposition problem in quasi-steady, self-field MPDTs operated between

150 kW to 7 MW with argon and helium propellants. He found approximately 20–40% of the power to the thruster being lost to the anode, a significant source of inefficiency for the thruster. He identified that the predominant cause of this power deposition was due to a significant anode fall voltage, i.e., the electron-attracting potential difference between the anode potential and the local plasma potential. He measured anode fall voltages of approximately 4–50 V in his tests. He explained the anode fall as due to the formation of large electric fields near the anode to provide sufficient current conduction across the strong azimuthal, self-generated B fields. Gallimore and Choueiri [52] proposed that this conduction was further limited by increased anomalous resistivity resulting from the onset of microturbulence in the plasma. Gallimore identified a connection between the electron Hall parameter (Ω_e , the ratio of electron cyclotron frequency to electron collision frequency) and increasing anomalous resistivity (i.e., reduced conductivity). The Hall parameter increased as the azimuthal magnetic field transverse to the anode increased with higher discharge currents. Work by Soulas and Myers [53] around this same time also confirmed the relationship between both increasing anode fall voltage and higher anode power deposition with increasing transverse magnetic field strength. Gallimore tested reducing the electron Hall parameter in the vicinity of the anode by embedding small permanent magnets around the anode to provide a canceling effect on much of the near-anode azimuthal magnetic field. His tests found that this local reduction of the Hall parameter decreased anode fall voltages by 37 to 50%. Gallimore suggested that perhaps using applied B fields intercepting the anode could reduce the anode fall voltage.

Foster [54, 55, 56] studied the mechanisms driving the formation of large anode sheath potentials in low pressure argon arc discharges in the presence of a transverse magnetic field of up to 120 Gauss. He used a simplified experimental setup with a DC plasma diode with a gas-fed hollow cathode discharging to a 2.5 cm stainless steel anode disk 6 cm away. An electromagnet provided a uniform transverse B field in the near-anode region. He identified that the anode fall voltage was

highly dependent on the local electron number density. Subsequently, he used an auxiliary electron discharge near the anode to increase local electron number density and found reductions in the anode fall voltage resulted in reduced anode power deposition of 15 to 25%. Also, Foster examined the application of an external magnetic field up to about 40 Gauss coaxial with the anode (intersecting B field), but he found this additional field to have surprisingly little effect on the anode fall voltage (only approximately 1–2 V decrease). However, he suggested that perhaps beneficial reductions in anode fall might only occur if the transverse magnetic field component were significantly decreased relative to the axial field. Also, the lack of a flowing plasma, simplified geometry (not coaxial electrodes), and different directions for the forces on the plasma in his experiments may be expected to yield different results than MPD thrusters.

Hoyt et al. [57, 58] examined the use of various applied magnetic fields in high-power coaxial accelerators operating in quasi-steady pulses from 2–12 MW. The constant-radius, narrow-channeled coaxial accelerator geometry used in his study is somewhat different than that used for typical MPDTs, but the Lorentz force-driven acceleration mechanisms are the same. He was able to reduce the anode fall by approximately 30 V with an applied B field relative to self-field operation (no magnets). He used a “magnetic Laval nozzle” shape in his applied B field design, in which the field lines converged and then diverged again as the plasma moved in the downstream direction. This B field shape had field lines intersecting the anode in the region upstream of the exit plane.

At Russia’s Moscow Aviation Institute (MAI), studies were conducted by Tikhonov et al. [30, 31] on applied-field lithium-fed thrusters. Their work involved primarily experimental testing and observations on AF-MPDTs at power levels up to 200 kW with specific impulse (I_{sp}) of 4500 s and about 48% efficiency. From the results of these (and earlier) tests and some related modeling efforts [44], Tikhonov suggested that the applied B field and thruster design should be such that the diverging anode surface be contoured to follow the local applied B field lines. This suggestion

would result in a transverse-only (non-intersecting) B field near the anode, which is counter to earlier recommendations by Gallimore, Hoyt, and others. Tikhonov suggested that contouring the B field along the anode in this manner avoids the concentration of anode current attachment to small areas near the anode exit, which results in undesirably high local anode heating and erosion. Localized current attachment downstream on the anode is an expected consequence of advection of the current streamlines downstream by the flowing plasma. He claimed that by contouring the anode with the B field, the current streamlines were shown to spread out over a larger area of attachment, thereby reducing anode current densities.

Also, testing in Russia of a 400–500 kW steady-state, Li-fed MPDT by Ageyev et al. [15] at 8–10 kA demonstrated stable operation and thrust efficiency of 60%. The operating conditions for this thruster should have put it in operation above onset. However, Ageyev used a relatively weak 100 Gauss solenoidal applied B field near the anode exit plane and was able to achieve stable, efficient operation. However, limited details were provided for this empirical demonstration.

In Japan, work was conducted by Tahara, Kagaya, et al. [25, 59, 60, 61] on quasi-steady MPD thrusters with externally-applied magnetic fields. Tahara identified that a strong, mostly axial applied magnetic field (mostly parallel to the anode) could suppress the magnitude of voltage fluctuations in their thruster operating conditions. These experiments by Tahara et al. [59], resulted in higher thrust and somewhat reduced cathode erosion with the applied B fields. However, they used very high applied magnetic fields of order 1000–2000 Gauss. Also, experiments by Kagaya, Tahara, et al. [61, 25] showed that their applied magnetic fields (1000–5700 Gauss) notably increased the terminal voltages and anode voltages for the discharge relative to self-field operation.

To date, there is still limited understanding of the processes that govern the overall current conduction in the near-anode region. Gallimore and Foster's primary motivations and investigations were to reduce anode fall voltage and not characterizing and understanding the current distribution.

Further, differences in geometry, plasma flow conditions (or lack thereof), magnetic topologies, and field strengths between Gallimore's Princeton Benchmark Thruster, Hoyt's coaxial accelerator, Foster's quiescent plasma experiment, and Tahara's thrusters can yield particularly different structure to the current streamlines and conduction in the near-anode region. Moreover, there is a conflict between competing suggestions from authors such as Gallimore and Hoyt (anode-intersecting B fields) and Tikhonov (anode-parallel B fields) for the prospects of using applied B fields to reduce anode falls but also avoid excessive current densities. Further, no details were made available about the current pattern or plasma properties of the promising Ageyev thruster design. Therefore, our research sought to understand the plasma discharge current pattern and conduction in the near-anode region of an MPDT. Our work specifically examines the effect of applied magnetic fields on the current distribution along the anode and current structure within the discharge as part of an investigation into the potential for reducing anode fall voltages and mitigating onset-related behaviors with the applied magnetic fields.

1.3 Thesis Outline

The goal of this work was to investigate the effects of externally-applied magnetic fields at modest field strengths on the plasma discharge and examine the prospect of their use to mitigate the behaviors associated with onset. The motivation is to determine how one can influence the current conduction to mitigate performance losses and anode erosion, thereby leading to potential increases in thruster efficiency, thrust, and lifetime.

For this investigation, we posed the following questions:

1. Can we mitigate behaviors such as the large-amplitude terminal voltage fluctuations and large anode fall voltages with applied magnetic fields primarily focused on the near-anode region?

2. What are the effects of the applied magnetic fields on the plasma properties and current transport in the thruster plasma discharge, particularly in the near-anode region?

There are several components to addressing this goal. The first investigation was to characterize the thruster terminal voltage-current characteristics to identify onset-related transitions and the growth of discharge voltage fluctuations (commonly referred to as “voltage hash”). This characterization was performed with the thruster operating in both self-field mode without magnets and with two distinct applied magnetic field topologies. The second study investigated the structure and behavior of the magnetic field, current pattern, and current densities inside the thruster discharge with a new magnetic probe array. To understand the influence on parameters that drive the changes in current conduction to the anode, a new triple Langmuir probe was used to study changes in the local plasma number density, electron temperature, and plasma potential with and without the applied magnetic fields. This progression of investigations allows us to examine the response of the thruster in transition to and above onset first at the system level (electrode voltages and related fluctuations), then in the plasma discharge bulk structure (internal magnetic field and current transport), and finally in the local plasma properties of the near-anode region (Langmuir probe measurements).

The subsequent chapters of this thesis are organized to convey the implementation approach and results of these investigations. Chapter 2 describes the experimental facilities, thruster, and diagnostics used for the experiments. Chapter 3 explores the influence of the applied magnetic fields on the voltage-current characteristics and voltage fluctuations as compared to self-field operation. Chapter 4 identifies the results of magnetic probing to explore the structure of the magnetic field, current pattern, and current densities with and without the applied magnetic fields. Chapter 5 details the findings of the Langmuir probe investigation of plasma properties and potential in the different operating conditions. Chapter 6 provides a synthesis of the results, extends the findings with additional calculations, suggests physical interpretations, and concludes with a summary of key findings

along with recommendations for future work.

Chapter 2

Experimental Setup and Diagnostics

2.1 MPD Thruster

To provide the fundamental testbed and framework for this research, a new high-power MPD thruster (MPDT) was designed and fabricated, along with supporting infrastructure and circuitry. Figures 2.1 and 2.2 show the MPDT, which was designated as the “Odysseus” thruster. Figure 2.3 shows a schematic highlighting the major components and dimensions of the MPDT.

The overall geometric proportions of the new Odysseus MPD thruster were modeled after the Russian Ageyev-type extended anode design with a multi-channel hollow cathode [15] and scaled up slightly in size to allow use of an existing tungsten cylinder as the cathode and maintain a similar anode to cathode radius (r_a/r_c) of 2.52 based on the anode exit radius and cathode outer radius. The tungsten cathode tube has an inner diameter of 8.9 cm and outer diameter of 10.2 cm. The inside of the multi-channel hollow cathode (MCHC) is tightly packed with thoriated tungsten 0.64 cm diameter welding rod segments cut to 2.5 cm lengths. Each of the interstitial spaces between adjacent cathode rods form open areas that effectively act as hollow cathodes, and the resulting increase in emission area allows the MCHC to provide the necessary high discharge currents with lower current densities than with a comparably sized solid rod cathode. Propellant is injected through the multi-channel hollow cathode as in the Ageyev thruster, not in the inter-electrode gap as is typically

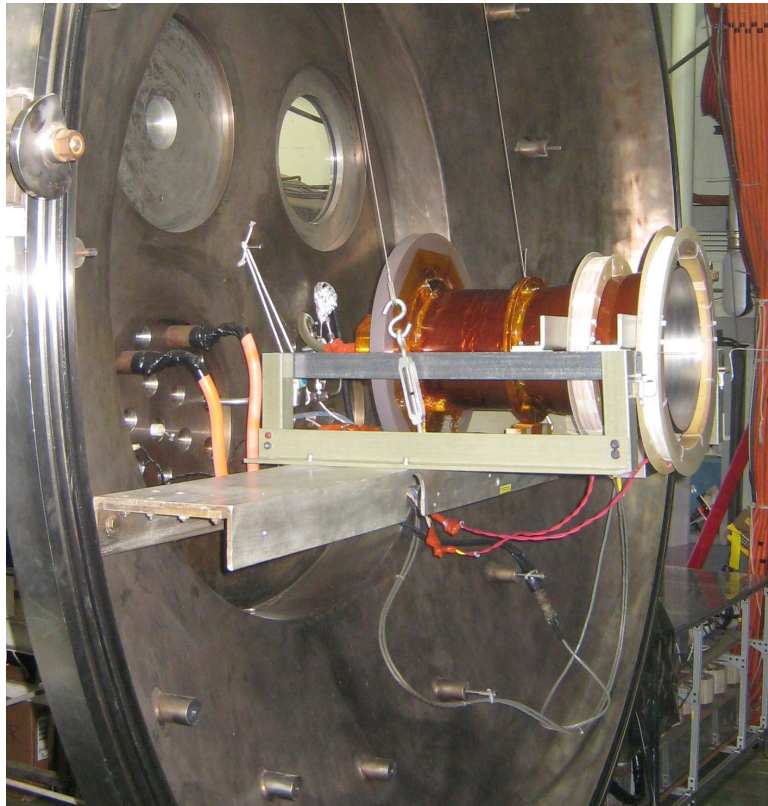


Figure 2.1: Odysseus MPD thruster with magnets mounted on the vacuum chamber header.

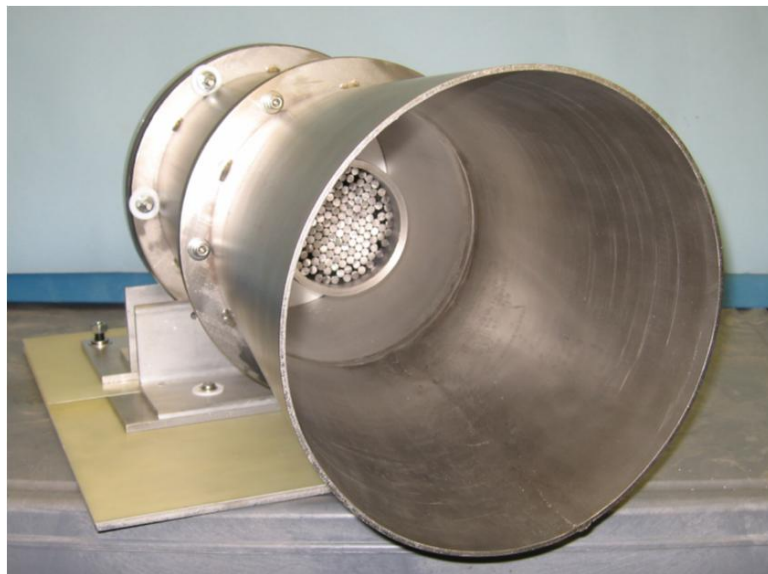


Figure 2.2: MPD thruster view into discharge chamber (shown without magnets and outer insulating surfaces).

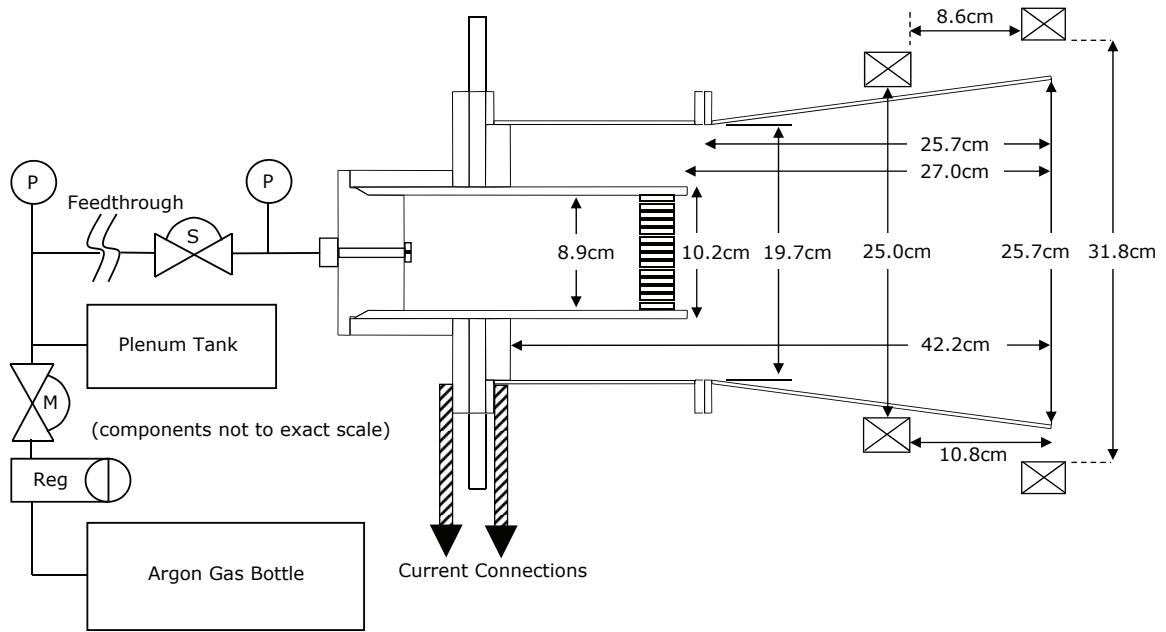


Figure 2.3: Schematic of the MPD thruster, applied-field magnets, and gas flow system. Note that the gas flow system components are not to scale.

done in gas-fed MPDTs. The anode is made of two segments made of 0.3 cm thick stainless steel mated together. The thruster anode body straight section has a 19.7 cm inner diameter, and the anode flared section extends downstream to an anode exit plane of 25.7 cm inner diameter. The anode and cathode flanges are mounted to a PVC plate which serves as an insulating interface. A boron nitride backplate is used to insulate between the anode and cathode in the upstream end of the discharge chamber. The axial distance from the boron nitride backplate to the anode exit plane is 42.2 cm. The anode flared section begins 1.3 cm axially downstream of the cathode exit plane and extends 25.7 cm axially upstream to the anode exit plane. Cathode-potential surfaces were also taped with Kapton tape to mitigate external arcing during testing. Aluminum was used for the rest of the mounting and support structure.

Due to cost and facility constraints that precluded high power steady-state operation, the thruster and discharge circuit were designed to operate in a quasi-steady pulsed mode. For quasi-steady operation, the thruster is pulsed for a long enough duration such that the plasma dynamics of interest

reach steady state, but total heating of the components of the thruster do not reach the same high-temperature thermal equilibrium of a steady-state thruster. Less costly materials can be used in lieu of refractory materials in some parts during quasi-steady operation. Non-refractory materials were used for all parts except the cathode. Avoiding the need for very high (order of 100s of kW to several MW) steady-state power also reduces operating costs and complexity. Such high-power, quasi-steady operation has been commonly used in many MPDT investigations to study dynamics and processes relevant to both pulsed and steady-state operation [33, 62, 25].

The MPDT was operated at quasi-steady power levels from 36 kW (20 V, 1800 A) to 3.3 MW (255 V, 13.1 kA) and initial mass flow rates at 0.6 g/s, 1.0 g/s, and 1.5 g/s. The data discussed in this study was obtained at 1.0 g/s, as this was found to be the lowest reliable and repeatable operating mass flow rate for the thruster, thus allowing the highest range of J^2/\dot{m} (ratio of current squared to mass flow rate) conditions for study. Figure 2.4 shows a photo of the MPDT during a test firing at approximately 750 kW. As a reference for comparison, the Ageyev thruster operated at a lower flow rate (0.2–0.3 g/s) and lower power (400–500 kW at 8–10 kA), largely due to operation with lithium as the propellant (decreased voltages and decreased ion mass) [15]. Our new thruster was operated with argon propellant at a broader range of currents. Somewhat higher flow rates were required to achieve reliably repeatable shots with this larger thruster geometry and operation in quasi-steady pulses. However, because the higher ion mass of argon results in onset initiating at lower values of J^2/\dot{m} than lithium [33], the range of currents in this investigation allowed study of conditions from below transition to onset to well above transition to onset.

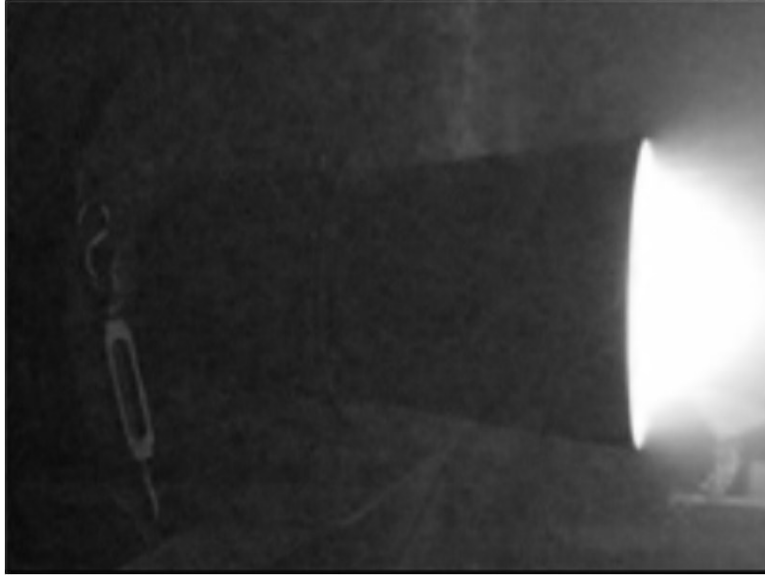


Figure 2.4: MPD thruster firing.

2.2 External Magnets and Applied Magnetic Fields

To investigate the influence of externally-applied magnetic fields on the thruster discharge, two solenoidal electromagnet coils were developed. These magnets were made of # 12 AWG copper insulated wire wound around a thin fiberglass insulating ring and side walls. These magnets were designed to mount as rings around the outer body of the anode flared section and were supported by adjustable fiberglass rails along the sides of the thruster mounting platform, as seen in Figure 2.5. The larger downstream magnet coil was 54 total turns, 33 mm wide, and 24 mm high, with an inner radius of 159 mm. This larger magnet was positioned with the front face extending 11 mm axially downstream of the anode exit plane. The smaller upstream magnet coil was 72 total turns, 35 mm wide, and 26 mm high, with an inner radius of 125 mm. This smaller magnet was positioned with its front face 108 mm axially upstream of the anode exit plane (i.e., its downstream face was separated axially by 86 mm from the upstream side of the larger magnet). The magnitudes and polarities of the currents in the two magnets could be driven independently to enable alteration of the shape and magnitude of applied poloidal magnetic field generated. Note that the term “poloidal” denotes

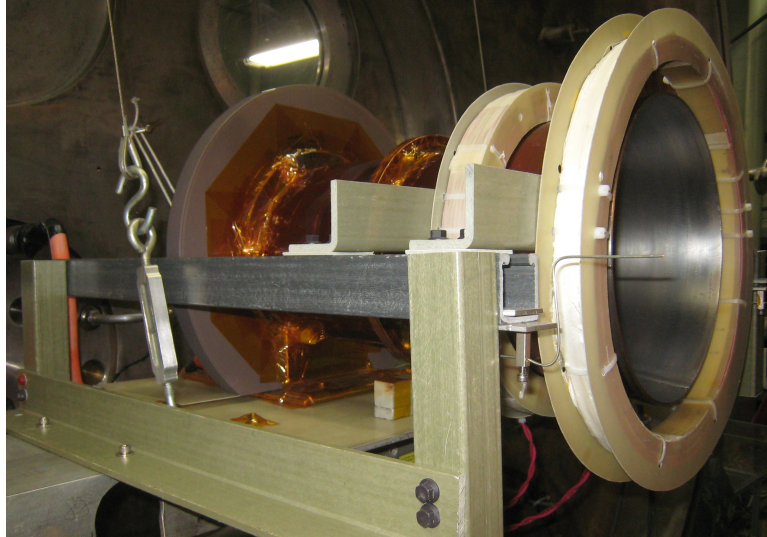


Figure 2.5: MPD thruster close-up view highlighting external magnets and mounting rails.

vectors with components only in the radial and axial directions (not azimuthal). Two Sorensen DCS-40-75 power supplies were triggered sufficiently before firing the PFN bank to ensure a DC current in the magnets to achieve a steady DC applied field before thruster firing.

Two particular applied B field configurations were used for most of the experimental testing. One configuration operated both magnets set at nominally 30 A each and in the same polarity, which generated magnetic field lines mostly tangential to the anode lip near the anode exit plane and anode-intersecting field lines upstream. This configuration is henceforth referred to as the “tangential” applied magnetic field in the text. The other configuration operated the smaller upstream magnet at 20 A and the larger downstream magnet at 30 A in the reversed polarity, which generated a cusp structure with magnetic field lines intersecting the anode in the region between the magnets. This configuration is henceforth referred to as the “cusp” applied magnetic field in the text that follows. Magnetic modeling results for these two configurations can be seen in Figures 2.6 and 2.7. At the specified operating currents, applied magnetic field strengths in the vicinity of the magnets (the downstream section of the anode) were mostly on the order of 50–200 Gauss, with somewhat higher peaks immediately next to the upstream magnet. Note that the cusp B field had lower peak B field

magnitudes near the anode. The applied magnetic fields were much lower near the cathode and centerline. At the location of the cathode tip (downstream front face) and cathode outer radius, the applied magnetic field was 40 Gauss for the tangential field and 11.5 Gauss for the cusp field. At the centerline of the cathode tip, the applied magnetic field was 42 Gauss for the tangential field and 12 Gauss for the cusp field. Also, the steady-state power applied to each magnet only ranged from 160–360 W, which was an insignificantly small fraction of the power to the thruster (36 kW to 3.3 MW).

In this investigation, the applied B fields used differ from those typically used in the vast majority of conventional, so-called “applied-field MPD thrusters” (AF-MPDTs) [16]. AF-MPDTs generally use much higher applied B field magnitudes relative to the thruster self-field, and their applied B field line structures (magnetic topologies) are generally predominantly axial, with very limited variation in curvature in the inter-electrode region. In our study, the applied B fields were designed to be smaller in relative magnitude to somewhat localize the effects of the applied magnetic fields to address near-anode phenomena. At the higher currents of interest for onset, our applied B fields yielded $B_{applied}/B_{selffield}$ much less than one near the outer radius at the cathode downstream face, and this ratio was only greater than one over the downstream section of the anode. The applied magnetic fields were also designed to allow significant anode-intersecting radial components to the topologies. These anode-intersecting regions were upstream along the anode (but still downstream of the cathode face) for the tangential B field and downstream closer to the anode exit for the cusp B field.

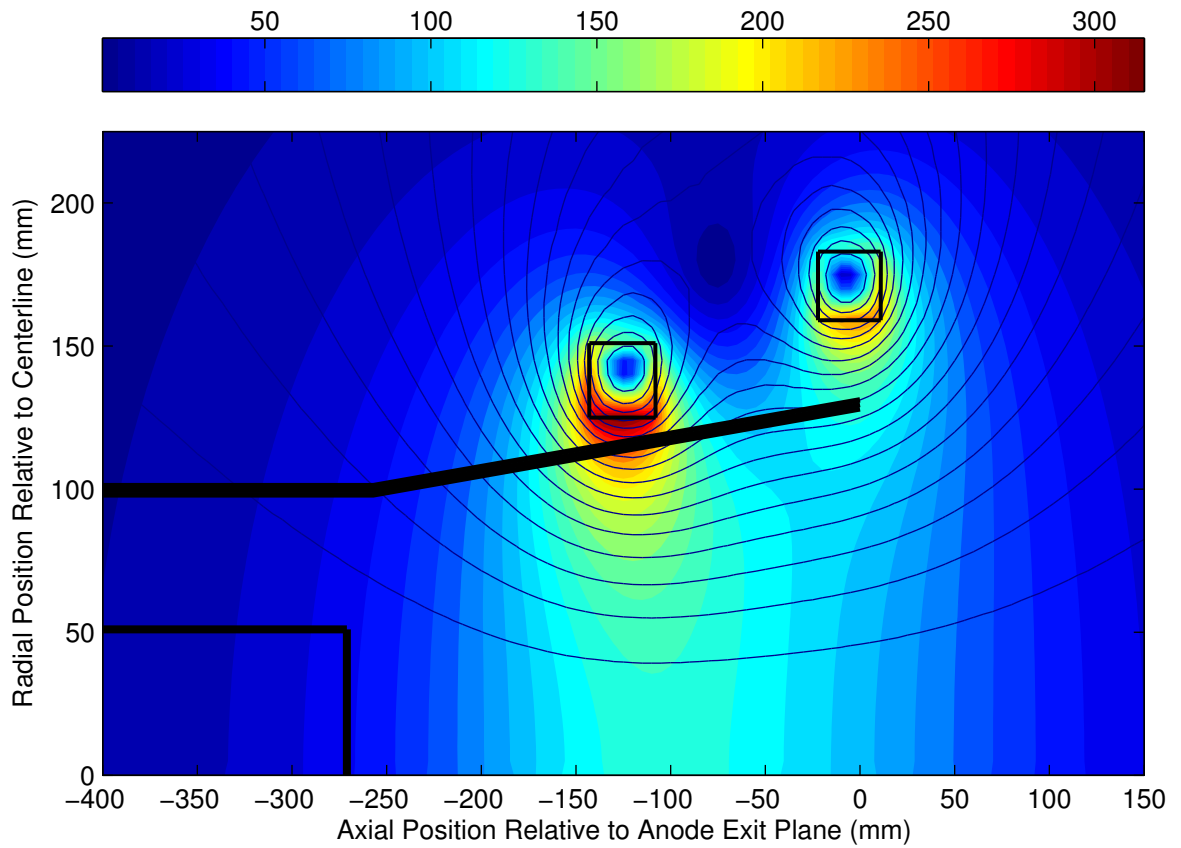


Figure 2.6: Applied magnetic field magnitude (shaded contours) and flux lines for the tangential applied magnetic field. Geometry for the magnets, thruster anode, and cathode are also shown. Color bar units for B field are in Gauss.

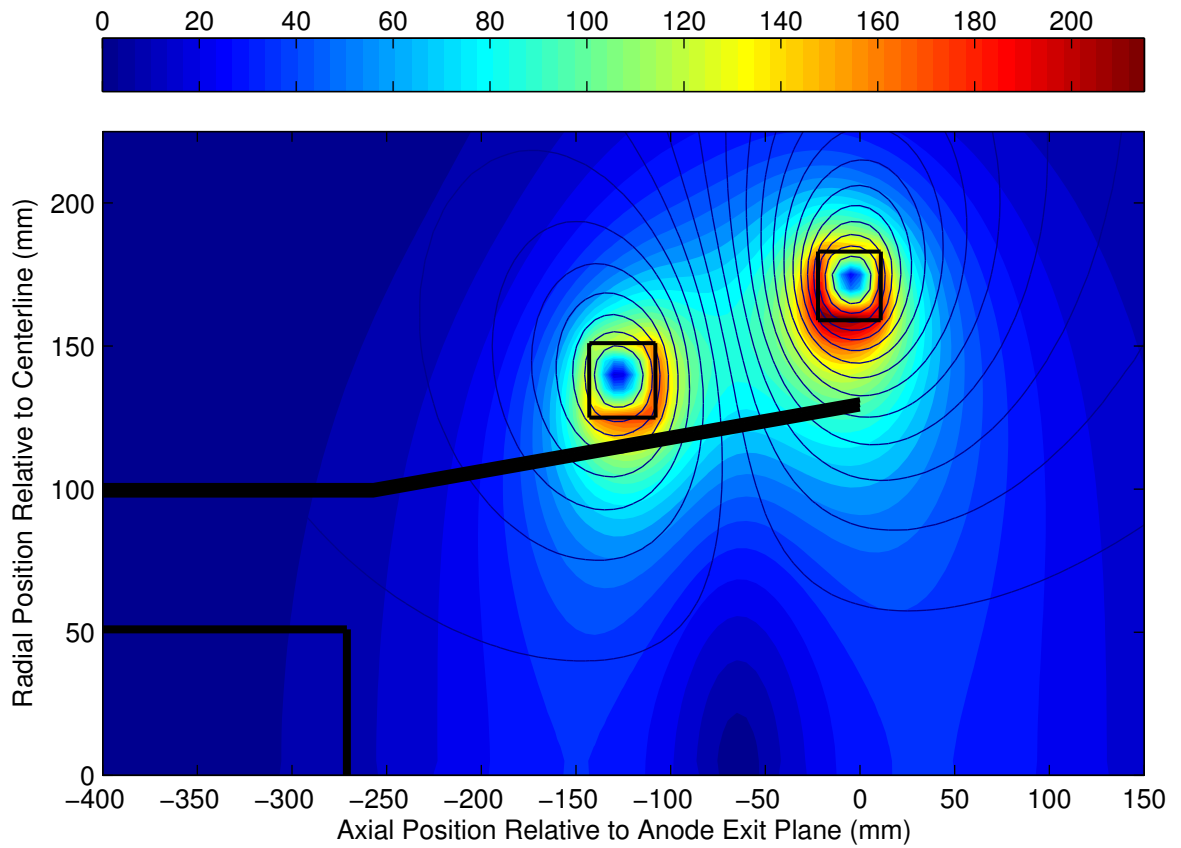


Figure 2.7: Applied magnetic field magnitude (shaded contours) and flux lines for the cusp applied field. Geometry for the magnets, thruster anode, and cathode are also shown. Color bar units for B field are in Gauss.



Figure 2.8: Vacuum chamber facility at JPL used for the MPDT experiments.

2.3 Vacuum Facility

The MPDT was operated in an existing vacuum chamber facility at the NASA Jet Propulsion Laboratory (JPL). The chamber is a large 2.3 m diameter by 4.5 m cylindrical length vessel, totaling approximately 18.7 m^3 volume. The MPDT was mounted to a removable header on the vacuum chamber and connected to gas and electrical feedthroughs on the chamber header. The chamber is nominally pumped using two Consolidated Vacuum Corporation (CVC) PMC-32C 32" oil diffusion pumps and one CVC PMC-48C 48" oil diffusion pump. The pumps were backed by two sets of Stokes 412H (10 hp, 300 cfm) roughing pumps with Roots RGS-SP-AVM 615 (7.5 hp, 1250 cfm) booster pumps. The background pressure was $1\text{--}3 \times 10^{-6}$ Torr prior to each thruster firing, as measured by a calibrated ion gauge at the opposite end of the chamber from the header with the mounted thruster. A photo of the vacuum chamber facility is shown in Figure 2.8.

2.4 Discharge Circuit

To operate the thruster in a quasi-steady mode with discharges on the order of a few milliseconds, two pulse forming network (PFN) banks previously used in the 1990s at JPL were refurbished, and a new charging, control, and timing circuit was designed. Each of the two PFN banks consists of a sequence of capacitors and inductors that are sized to provide a 1–2 ms quasi-steady current pulse under the range of load conditions. Each PFN is composed of eight matched capacitor-inductor stages, each containing one series 2.6 microhenry inductor and four parallel 2.4 millifarad electrolytic capacitors initially charged from 50 to 450 V (7.7 kJ). A high-voltage Quality Transformer and Electronics E202 power supply charged the banks. The two banks were connected in parallel, together providing up to 3.7 MW discharges in the thruster. Figure 2.9 shows a photo of one of the PFN banks. The PFN output during a discharge passed through an adjustable ballast resistor in series with the thruster high current feedthroughs to aid in load matching. The PFNs were tied to ground on the positive side, thus also connecting the thruster to ground on the anode side during discharges. Additional components aided in providing circuit protection and a load path for the PFNs in the event of the thruster failing to discharge.

To initiate the gas breakdown often required a higher initial voltage than the PFNs could supply. To provide the needed voltage and energy, an ignition circuit was connected in parallel to the thruster electrical feedthroughs and isolated via high-voltage, high-current diodes from the PFNs. This circuit used a 4 microfarad capacitor typically charged to 900 V by a Fluke 412B high-voltage power supply to initiate the discharge. The PFNs and the ignition circuit were triggered simultaneously by two International Rectifier 1000PK100 silicon controlled rectifiers (SCRs) activated by a Wavetek 801 pulse generator. The ignition circuit would dissipate its capacitor's energy in less than 100 microseconds, after which the PFNs would complete their discharge within a few ms. A schematic



Figure 2.9: Pulse forming network bank.

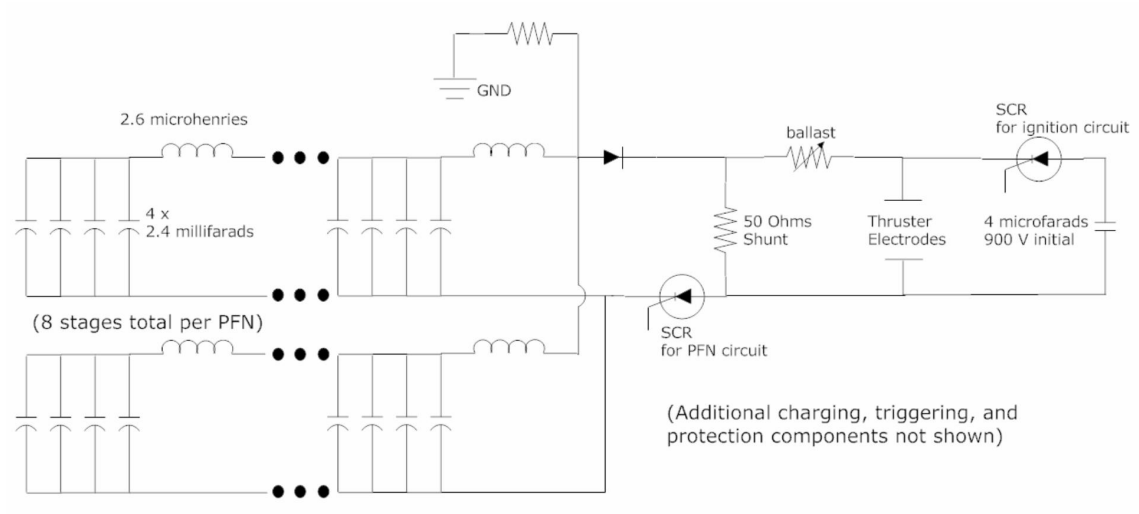


Figure 2.10: Schematic illustrating key elements of the MPD thruster ignition circuit and PFN discharge circuit.

highlighting key elements of the discharge circuit is shown in Figure 2.10.

2.5 Gas Pulse System

2.5.1 Hardware

A gas pulse system and drive circuitry were also developed and integrated into the timing circuit for the current discharge. The major components of the gas feed system are shown in Figure 3. The gas system utilizes a 3.5 L plenum tank pre-filled with argon to the desired pressure (8–50 psia) prior to each shot to match a specified flow rate. The plenum tank was connected through a gas feedthrough on the vacuum chamber to a Skinner direct-acting solenoid gas valve just upstream of the thruster gas feed connector. Upon opening the solenoid valve, the gas flow would be sonically limited by a choked orifice 1.51 mm (0.0595”) in diameter located at the upstream entrance to the multi-channel hollow cathode tube. Gas would flow through the cathode rods in the tube to supply gas to the thruster discharge, not supplied from the surrounding annular region of the discharge chamber as is common in most gas-fed MPDTs. Pressures in the plenum tank and just downstream of the solenoid valve were measured by pressure transducers (Statham PA208TC-50-350, 0-50 psia) during flow calibrations and thruster firings. The solenoid valve was actuated with a high-current insulated gate bipolar transistor (IGBT)-based pulse circuit tied to a 300 V power supply to overdrive the solenoid valve. A Hewlett Packard HP 214B pulse generator was used to trigger the gas pulse and then trigger the current discharge 50 ms later. By that time, the gas flow had reached steady state in the thruster, as measured by the downstream pressure transducer (downstream of the solenoid valve but upstream of the choked orifice).

2.5.2 Mass Flow Calibration

Mass flow calibration was performed with the gas pulse system connected to the thruster under vacuum conditions. Gas pulses were triggered over a range of argon plenum tank pressures between

8–50 psia for the 0.0595” choked orifice without firing the thruster. The approach to mass flow calibration was a modified form of the process outlined in the appendix of Gilland’s thesis to provide a calibration with lower uncertainty in instantaneous mass flow rate at the time of thruster discharge [63]. Measurements of the gas pulse were taken from the pressure transducer just downstream of the solenoid valve (but upstream of the choked orifice), and a total mass bit was calculated from the pulse based on the pressure drop in the plenum tank and application of the ideal gas law after the pulse (after a brief thermal equilibration time in the plenum tank). The downstream pressure response signals were integrated over the time durations for each full gas pulse to get a total pressure integral. Mass flow rate should be proportional to upstream plenum pressure for sonically choked flow. A linear least squares fit was calculated to identify the slope between the total mass bit (change in mass of the gas in the plenum) versus the pressure integral for each gas pulse over a range of initial plenum pressures. Since the mass bit is an integral over the same pulse time period as the pressure integral, this slope could then be used as the same constant of proportionality between mass flow rate and downstream pressure. For each gas pulse at a different initial plenum tank pressure, the downstream pressure at the time of the current discharge (45 ms after initiation of the gas pulse) was extracted from the measured response data and multiplied by the proportionality constant to obtain the instantaneous flow rate at that time. This approach provides a more accurate measure of flow rate at the time of thruster discharge since the gas pulse is not truly a square wave, but rather has an exponential pressure decay tail upon valve closing.

Plotting each of these calculated mass flow rates versus the initial plenum tank pressure yields the results in Figure 2.11. Standard deviation of the residuals for the curve fit of mass flow rate versus initial plenum pressure result in approximately $\pm 1\%$ uncertainty. The overall uncertainty in the mass flow estimate including uncertainties initial temperature and initial plenum pressure prior to each thruster firing is estimated at approximately $\pm 3\%$. The majority of the data for the thruster

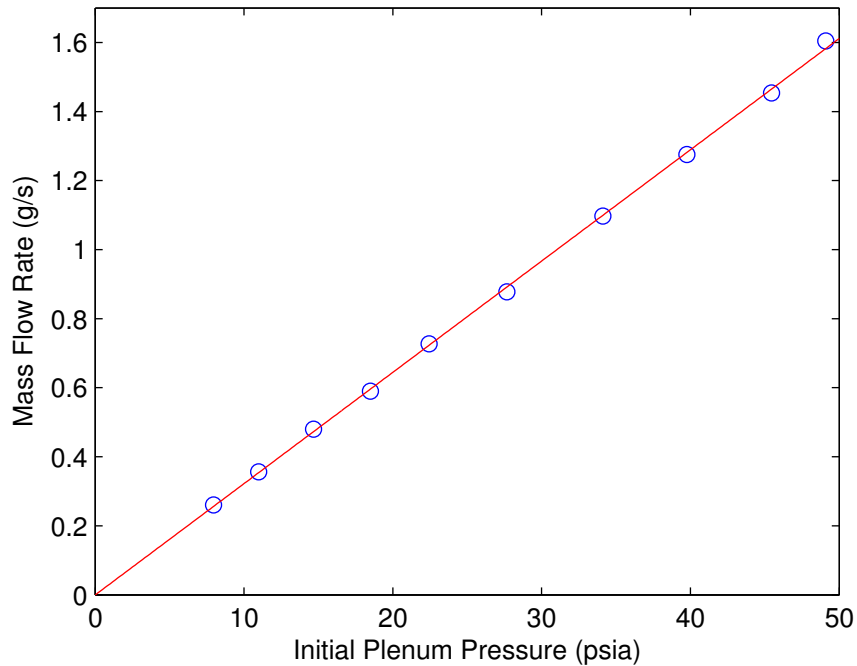


Figure 2.11: Calibration of flow rate versus initial upstream plenum pressure.

was obtained at a mass flow rate of 1 g/s.

2.6 Diagnostics

2.6.1 Data Acquisition System

All critical measurement signals to be analyzed were recorded via a digital data acquisition system (DAQ). Multiple National Instruments model PCI-6133 high-speed digital data acquisition cards were installed in a dedicated DAQ personal computer (PC). Each DAQ card provided eight simultaneously-sampled channels (each with their own analog-to-digital converter) at 14-bit resolution and 2.5 megasamples per second per channel. A custom LabVIEW software program was written to sample and record the buffered data from each thruster firing (“shot”) on the DAQ PC for later post-processing analyses. A Tektronix DPO2014 100 MHz digital oscilloscope was used for monitoring all non-critical signals (e.g., pressure transducers, PFN capacitor bank voltage, etc.) and

for recording higher sampling rate measurements of the thruster terminal voltage.

2.6.2 Terminal Voltage and Current Signals

Thruster discharge voltages and currents were measured during thruster firings to enable examination of terminal voltage versus current characteristic profiles and assessment of the growth of voltage fluctuations (“voltage hash”) at higher currents. Thruster terminal voltages were sampled with a 500:1 Tektronix P5205 high-voltage, active differential probe connected across the anode and cathode electrodes. The current was measured via a Pearson Electronics Inc. model 1330 pulse current monitor connected around the cathode-side high current cable connected to the PFN negative terminal. This current monitor transduced the current to a voltage during the thruster firing pulse with a calibration constant of 5 V per kA. The current monitor’s output voltage was attenuated through a 10:1 voltage divider and recorded on a National Instruments NI PCI-6133 DAQ card.

Example voltage and current traces are illustrated in Figure 2.12 and Figure 2.13, respectively. An increase in the magnitude of the voltage hash can be observed with increasing discharge current, as discussed in detail later in Chapter 3. To obtain the voltage-current (V-J) characteristic curves, the voltage and current traces were averaged over the quasi-steady time period of the thruster firing, typically 0.8 to 1.8 ms after triggering the PFN discharge.

2.6.3 Magnetic Probe Array

Sampling the magnetic field generated inside the thruster provided a fundamental data set for this research. Mapping of the magnetic field structure inside the thruster enables investigation of the influence of the external applied magnetic field on the internal magnetic topology in the discharge region, the current streamlines for the discharge, and current densities along the anode. Also, local magnetic field measurements enable determination of key parameters such as the electron Hall

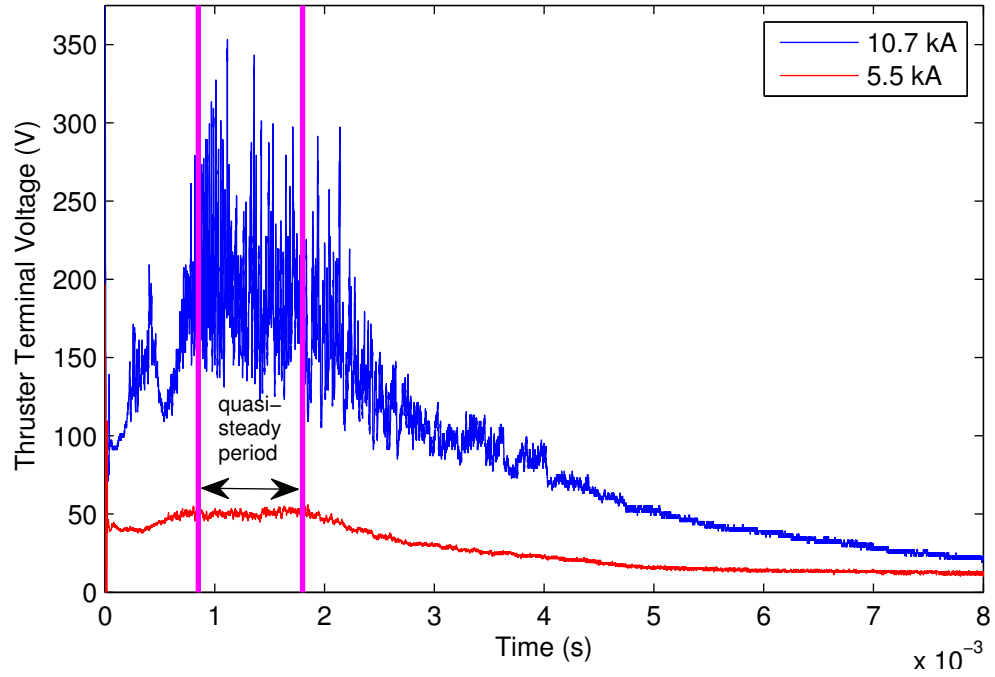


Figure 2.12: Sample traces of voltage vs. time for the MPDT discharge.

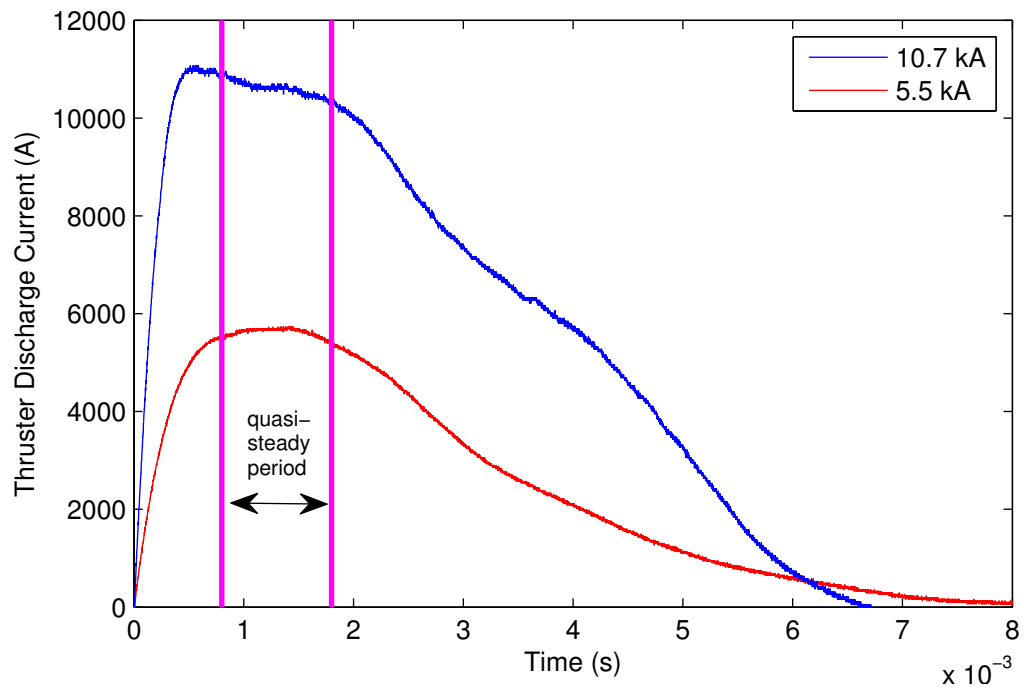


Figure 2.13: Sample traces of current vs. time for the MPDT discharge.

parameter and electron Larmor radius.

A new magnetic probe array (MPA) was constructed for simultaneous sampling of the magnetic field along 15 inductor coils positioned along the probe. Each small inductor performed as a so-called “B-dot” probe (measuring the change in B field with time), enabling measurement of an induced voltage V across the coil winding due to the time-varying magnetic flux inside the coil given by Faraday’s law:

$$V = -N \frac{d\Phi}{dt} = -NA \frac{dB}{dt} \quad (2.1)$$

where Φ is the magnetic flux bounded by the coil, N is the number of turns in the coil, A is the area of the coil, and $\frac{dB}{dt}$ is the instantaneous time rate of change of the magnetic field penetrating the coil.

Fourteen small commercial inductor chips (Coilcraft Inc., model 1008CS-472XGGB) were used (each chip was nominally 52 turns each, with 5 ± 0.1 microhenries inductance). The dimensions of the inductor chips were 2.8 mm by 2.9 mm by 2.0 mm. This approach was modeled after the work by Romero-Talamas, Bellan, and Hsu [64]. The chips were spaced axially every 20 mm for a total span of 260 mm, and these chips were inserted into a custom-fabricated Delrin plastic fixture made to fit these commercial chips’ dimensions. In addition, a hand-wound inductor coil was made by winding 105 turns of # 40 American Wire Gauge (AWG) magnet wire around a 3.5 mm diameter by 2 mm long core machined from Ultem rod. This hand-wound coil was glued to the tip of the Delrin probe stem with glyptal insulating enamel. While providing an additional 15th measurement, this hand-wound coil also acted as a calibration-correction coil for the smaller inductor chips due to the larger signal-to-noise ratio provided by the increased number of turns and larger coil diameter. All coils and the Delrin stem of the probe array were encased in an 8 mm diameter quartz tube to insulate them from the plasma. The tip of the probe and inductor coils can be seen in Figure 2.14.

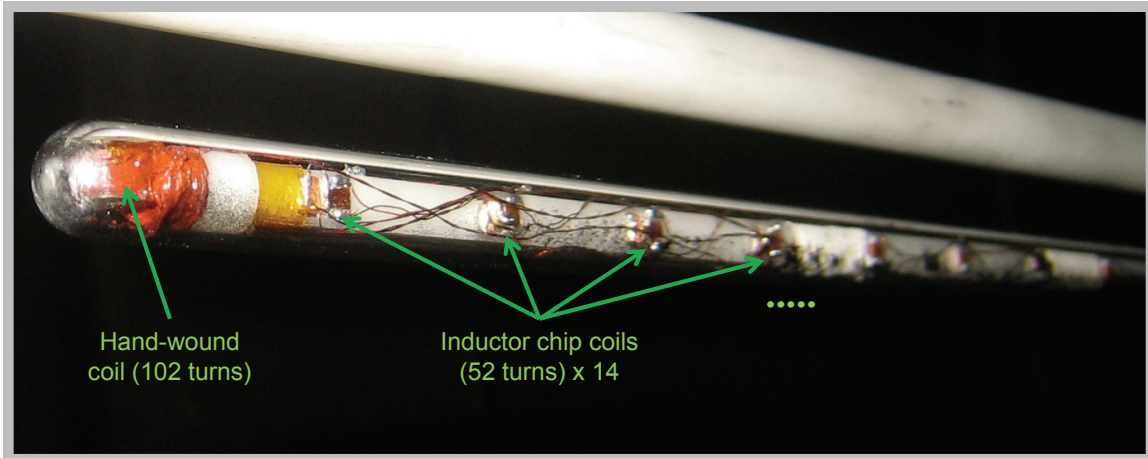


Figure 2.14: Close-up view of magnetic probe array with B-dot coils.

Each coil's leads were soldered to very fine # 38 AWG "Twistite" twisted pair wire by MWS Wire Industries. These wires ran the length of the Delrin stem and into a transitional stainless steel shielded tube, which provided electrostatic shielding and also additional axial stand-off distance between the probe and positioning stage mounting hardware to minimize the obstruction of the thruster exit plane. The metal tube was covered with Kapton tape and shrink wrap to insulate the metal from the plasma in the vicinity of the thruster. The metal tube opened to a shielded transition box at the top of the mounting structure affixed to a 3-axis (axial traverse, radial traverse, and horizontal rotation) positioning stage inside the vacuum chamber. Inside this aluminum box, the # 38 AWG wires transitioned to # 22 AWG twisted shielded pair wires bundled together and carried to the chamber feedthrough and outside the chamber to the aluminum shielded DAQ connection box. At the DAQ connection box, each coil's output was fed through a simple R-C low-pass filter circuit with cutoff frequency of approximately 90 kHz and terminated at 100 Ohms.

Time integration of the measured B-dot probe's induced voltage signal provided a measure proportional to the absolute magnetic field strength versus time. This time integration was performed numerically on a computer using the digitally recorded voltage trace for each coil. The integrated voltage was converted to magnetic field strength by using a pulsed Helmholtz coil for calibration.

The Helmholtz coil was constructed with a 2.54 cm (1”) radius and 2.54 cm (1”) axial separation between windings, each with 10 turns of insulated copper wire.

All coils used for the primary measurements were oriented such that they would measure the azimuthal component of the magnetic field inside the thruster. Enclosed current contours of the poloidal (radial and axial) current pattern were obtained by applying Ampere’s Law to the magnetic probe array measurements in the interior of the thruster discharge and exploiting azimuthal symmetry. This is discussed in more detail later in Chapter 4 on the magnetic probe measurements and analyses.

2.6.4 Triple Langmuir Probe

A triple Langmuir probe was constructed to enable high-speed measurements simultaneously of electron temperatures, plasma number densities, and plasma potentials. The triple probe method uses a steady applied voltage between two small conducting probes (wire tips in our case), and a third conducting probe acts as a floating potential probe [65]. The triple probe does not require any special high-frequency sweeping of the bias voltage as in a single or double probe apparatus. This makes the triple probe particularly well suited to the noisy, rapidly time-varying discharge environment of the pulsed thruster. Two probe wires effectively form a double probe with a potential difference $V_{d3} = V_3 - V_1$ held constant between them. One wire of the probe is allowed to “float” unbiased to the floating potential $V_2 = V_f$. For probe wires at V_1 and V_3 to balance as a floating double probe, the currents I_1 and I_3 must be equal and opposite such that the system draws no net current. A schematic of our triple Langmuir probe circuit and key elements is shown in Figure 2.15, and a photo of the sensing end of the triple Langmuir probe is shown in Figure 2.16.

To create the triple Langmuir probe, three tungsten wires each with 0.254 mm (0.010”) diameter and 3 mm long were individually fed through small alumina ceramic tubes with 0.8 mm (1/32”) diameter.

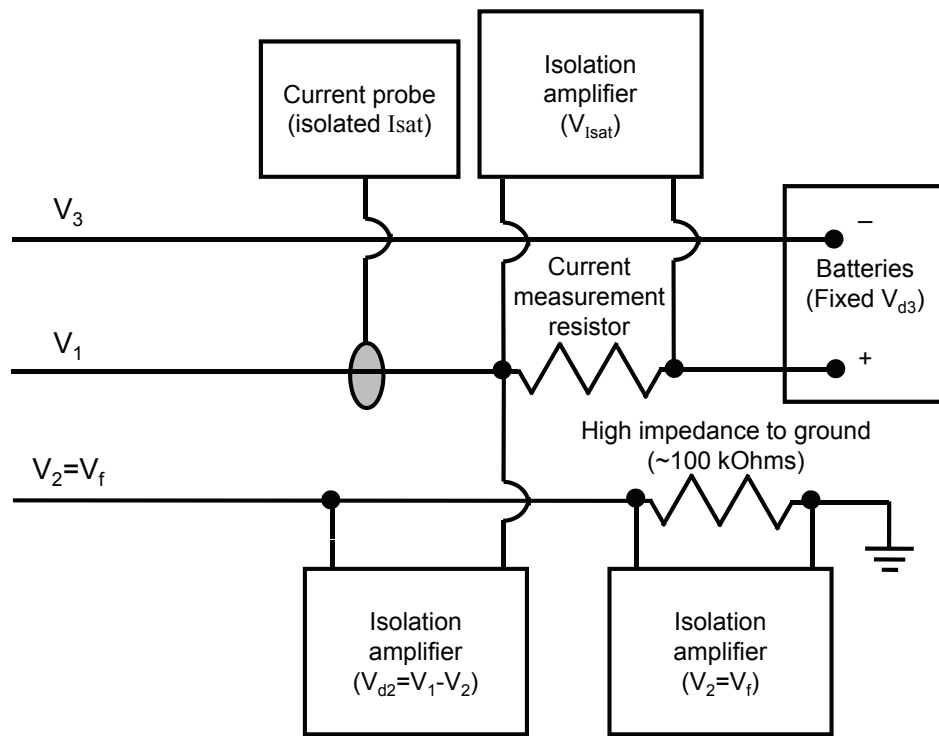


Figure 2.15: Triple Langmuir probe schematic.



Figure 2.16: Triple Langmuir probe and tungsten wire tips alongside magnetic probe.

outer diameter (OD) and sealed with ceramabond. Each of these ceramic tubes were glued into three inner holes spaced 1 to 1.5 mm apart within a 4-bore alumina ceramic tube with 4.8 mm (3/16") OD, and this was glued into the end of a stainless steel metal tube to act as an electrostatic shield. An outer alumina ceramic tube with 9.5 mm (3/8" OD) was placed over the metal tube to insulate the conductor from the plasma. This outer ceramic tube extended past the end of the 4-bore ceramic tube by approximately 1.5 cm to act as a "shadow shield" to mitigate against the layering of sputtering deposits that could coat the 3 small alumina tubes and form an electrically conducting layer between probe tips. The small, innermost ceramic tubes holding the tungsten wires extended an additional 1 cm past the outer ceramic tube to avoid any transverse or radial flow obstruction. For measurements near the anode, this geometry allowed measurements of plasma properties with the probe tips within approximately 3.5 to 4.5 mm away from the anode.

Inside the metal tube, the thin tungsten wires transitioned to # 22 AWG insulated copper wires. The metal tube extended along the same long axis of the magnetic probe back to the positioning stage mounting structure, where it connected to a metal transition box. Here, the wires were connected to BNC coaxial cables that ran from the positioning stage back to the chamber feedthrough, and the connections continued via BNC cables outside the chamber to an external circuit box wired to the DAQ inputs.

Primary circuit elements are shown in Figure 2.15. Potential differences that were not ground referenced were measured using Analog Devices AD215BY isolation amplifier circuits. The battery bias between two probe tips was made by two Eveready model number 732 lantern batteries connected in series for a fixed bias voltage, V_{d3} of 25.5 V. Batteries were used instead of an external power supply because of their inherently floating isolation, low noise, and fast time response. The inputs and outputs of isolation amplifiers were passively filtered with R-C low-pass filters with cut-off frequencies circa 120 kHz. Measurement signals were connected to the data acquisition system

(DAQ) for high-speed, simultaneous digital recording. Measurements from both an isolated current probe (Tektronix TCP312 current probe and TCPA300 amplifier) and voltages from a current-sensing shunt resistor were used to verify ion saturation current measurements independently. The current-sensing shunt resistor values used were 5.1 Ohms in regions of higher densities (and thus higher collected ion saturation current) and 15.3 Ohms in regions of lower densities. These values were selected to get sufficiently large signals of order 0.1 V for DAQ recording, but small enough so that they did not significantly perturb the 25.5 V voltage bias between probe tips.

It should be noted that early experiments were also conducted with a single Langmuir probe with rapid sweeps at 5 to 10 kHz of the bias voltage applied to the probe to generate the current-voltage characteristics. The analysis methods for the single Langmuir probe are discussed in Hutchinson's book [66]. The single probe used was also tungsten wire of the same dimensions, 0.254 mm (0.010") diameter and 3 mm long. This single probe technique was successful at low to moderate thruster discharge currents, up to approximately 9 kA at 1 g/s mass flow rate. However, above these currents, significant noise and ground fluctuations during the thruster firing coupled back to the power supply and driving ramp generator used for the applied bias voltage. This would result in unstable and unrepeatably voltage sweeps of the probe bias voltage and greatly limited the ability to obtain reliable data in the electron-collecting region. These effects at higher currents ultimately led to the construction and use of a triple Langmuir probe instead.

For the triple Langmuir probe, expressions for calculating electron temperature T_e , electron number density n_e , and plasma potential V_{plasma} are derived in Chen and Sekiguchi's original paper [65] and interrogated further for error analyses in Tilley's paper [67]. (Note, just for clarification, that in Tilley's paper, his schematic in Figure 1 shows the voltage bias V_{d3} drawn incorrectly with

the opposite polarity.) First, electron temperature T_e can be obtained from the implicit equation

$$\frac{1 - \exp(-\chi_{d2})}{1 - \exp(-\chi_{d3})} = \frac{1}{2} \quad (2.2)$$

where $\chi_{d2} = \frac{|q_e|V_{d2}}{kT_e}$ and $\chi_{d3} = \frac{|q_e|V_{d3}}{kT_e}$ are the non-dimensionalized potential differences, k is the Boltzmann constant, and q_e is the fundamental electron charge.

Electron number density, n_e , can be calculated from

$$n_e = \frac{\exp(1/2)I_{sat}}{|q_e|A_{probe}\left(\frac{kT_e}{M_i}\right)^{1/2}(\exp(\chi_{d2}) - 1)} \quad (2.3)$$

where $I_{sat} = I_3 = -I_1$ is the measured ion saturation current, A_{probe} is a single probe wire's exposed surface area (assuming equal sized probe tips), and M_i is the ion mass (argon in our case). Note that it can be shown that the expression $(\exp(\chi_{d2}) - 1)$ reduces to approximately 1 when the bias voltage V_{d3} is much greater than the electron temperature.

The plasma potential, V_{plasma} , is calculated from the electron temperature by

$$V_{plasma} = V_f + \frac{kT_e}{|q_e|} \ln\left(\sqrt{\frac{2M_i}{\pi m_e}}\right) \quad (2.4)$$

where V_f is the floating probe potential measured from V_2 , and m_e is the electron mass. Later, we will calculate our anode fall voltages, V_{fall} , defined as

$$V_{fall} \equiv V_{anode} - V_{plasma} \quad (2.5)$$

where V_{fall} is calculated as positive for electron-attracting fall potentials, and the anode potential V_{anode} is measured separately as a reference voltage and averaged during the quasi-steady thruster

firings.

Both T_e and n_e are calculated with the corrections for the ion current collected at the probe potential relative to the plasma potential as given in the numerical calculations by Laframboise [68]. Laframboise's calculations account for finite sheath thickness and ion temperature for a cylindrical probe in a collisionless and quiescent plasma, but are also applicable to a probe whose axis is aligned with the plasma flow. Ion temperatures in our analyses were assumed to be equal to the electron temperatures. This is deemed a reasonable assumption given that Bruckner and Kilfoyle found typical ion temperatures on the order of the electron temperature in their MPD thruster plumes [69, 70]. Also, we did not have a means to measure the fraction of multiply-charged ions, and thus, all calculations assumed only singly-ionized argon. By quasineutrality, this results in equal number density for electrons and ions, i.e., $n_e = n_i$. The effects of variations of these parameters on electron temperature and ion saturation current (thus, also on number density and plasma potential) were rigorously accounted for in our error analyses by using the methods described by Tilley [67]. Also, our large probe aspect ratio (length to radius) of 23.6 allows us to justifiably use Laframboise's infinite cylinder modeling results.

The triple Langmuir probe theory also requires additional assumptions for validity. The electron and ion population energy distributions must be Maxwellian, which is a well expected behavior in the quasi-steady conditions. The sheaths around the current-collecting probes must be collisionless, which is justified since the Debye length is typically on the order of $5 \mu\text{m}$ for our plasma properties. Also, we can neglect interactions between the sheaths of the three probe wires, as the separation distances between the probe wires (order of 1 mm) are much greater than the Debye length.

Magnetic field effects can also potentially cause significant variations. However, most magnetic field effects can be neglected since the probe wire radius of 0.127 mm is significantly smaller than the electron Larmor radius, which is order of 2 mm even in regions of high magnetic fields and

much larger in weaker magnetic field regions away from the applied-field magnet coils and thruster centerline. The one major effect that was taken into account in the error analyses was the effect on electron drift transverse to the probe axis. This effect was modeled as a transverse flow velocity error and accounted for in the error analysis methods described by Tilley, which yields approximately 5% additional uncertainty in T_e [67]. Also, Chen and Sekiguchi describe the effects of triple probe application to magnetoplasmas [65]. They note that additional magnetic field effects can be ignored if $(V_f - V_{plasma}) \gg (e/2m_e)(Bd)^2$, where B is the magnetic field intensity and d is the thickness of the ion sheath (order of a few times the Debye length). For our plasma properties and modest B field magnitudes, the right-hand side of this expression is only order of 5×10^{-4} V for our operating conditions, and our probe potential differences were always much larger than this extremely small value.

Care was taken to place the probe tips in front of the nearby magnetic probe (i.e., out of the magnetic probe's wake) and orient the triple probe tips in the axial flow direction to minimize the effect of flow disturbances and transverse plasma flow. The effects of the variations in probe angles were examined in our thruster by rotating the probe orientation angle with respect to the thruster centerline axis from -25 to +20 degrees. Values for ion saturation current and electron temperature are minimized when the probe axis is oriented with the flow direction, thus minimizing transverse current collection and providing more accurate measurements. With the probe axis oriented in the direction of the thruster axis, measurements were found to have less than 10% variation from minimum values. I.e., flow was indeed primarily in the thruster axis direction for the measurements inside the thruster.

Measured signals were averaged over the 1 ms quasi-steady time period and across multiple thruster shots to calculate mean values and associated statistics (e.g., standard deviations for use in estimating uncertainties) for each operating condition. However, for some of the shots in the near-

anode region, brief but significant transients would occasionally occur, which required analysis over piecewise segments of the quasi-steady period. Sometimes, the plasma density would drop out so dramatically (by much greater than two orders of magnitude) during some short-lived (typically less than 0.1 ms) transient as to cause unrealistically large or even negative T_e readings. In these cases, the triple Langmuir probe theory would break down (e.g., excessively large sheaths or overlapping sheaths between probes), and averaging over these events would not be physically accurate. For such selected brief transients events, we would break up the quasi-steady time period into one or more sufficiently long (greater than 0.4 ms) time periods where the plasma was sufficiently resident enough for the triple Langmuir probe theory to be physically valid.

2.6.5 High-Speed Video Imaging

A high-speed digital video camera was used to obtain images of the thruster discharge. These videos were taken during early testing with the thruster operating at 9 kA in self-field mode only (without magnets). These measurements used two Vision Research cameras, including model Phantom V710 and model Phantom V7.3.

In addition to being an effective troubleshooting diagnostic during early tests with the thruster, the high-speed imaging was particularly useful for providing qualitative insights into transient phenomena in the plasma discharge during quasi-steady operation. High-speed imaging frames were taken looking at the thruster through view ports in the vacuum chamber. Videos were taken from an end view looking directly upstream into the anode and cathode, as well as a side view looking at the thruster plume and a few cm upstream of the anode exit plane. A series of neutral density filters were used as needed to reduce luminosity to avoid saturation of the camera charge-coupled device (CCD) detector. The high-speed images presented later used exposure times was around 1-5 μs and imaging rates of 10,000 frames/s (100 μs intervals between frames).

Chapter 3

Influence of the Applied Magnetic Fields on Voltage-Current Characteristics and Voltage Fluctuations

3.1 Operating Conditions and Thruster Configurations

Thruster discharge voltages and currents were measured during thruster firings to construct voltage versus current characteristics and determine the influence of the applied magnetic fields on the voltage fluctuations (“voltage hash”) at higher currents. Section 2.6.2 described how the voltage and current measurements were obtained.

These data were obtained over a range of PFN voltages to span thruster current levels from 1.8 kA to 13.1 kA. This broad range was selected to cover a wide set of operating conditions and examine transitions and trends from well below onset to well above onset. To obtain the various voltage and current statistics presented in this section, the voltage and current traces were averaged over the time span during which the thruster was quasi-steady, generally 0.8 to 1.8 ms after triggering the PFN discharge as seen in Figure 2.12. The flow rate was held constant at 1.0 g/s. This flow rate was chosen because it was sufficiently low to allow a range of J^2/\dot{m} values (approximately 4 to 172 kA²s/g) well above typical onset values for other thrusters (e.g., beyond 80 to 110 kA²s/g in the Princeton Benchmark Thruster), yet still provided sufficient flow in our large thruster geome-

try for stable, repeatable operation [42]. Configurations examined included no magnets (self-field operation), the applied tangential B field, and the applied cusp B field.

3.2 Collection of Data

Some example terminal voltage and current traces over the entire PFN firing duration were shown earlier in Figure 2.12 and Figure 2.13, respectively. As expected, an increase in the magnitude of the voltage fluctuations is observed with increasing discharge current. To see a clearer picture of the structure of the hash, we examine the data during the quasi-steady portion of the time series traces for the three applied B field configurations at three different operating current levels. The voltage traces in Figure 3.1 show example traces for the case without magnets (self-field operation). A fairly quiescent mode of operation is observed in the voltage response at the lower 5.5 kA. However, we observe an intermediate mode of operation in the 8.0 kA trace wherein the voltage fluctuations become more pronounced, albeit still primarily oscillating equally positive and negative relative to the mean. At the higher 10.7 kA, we see a substantial growth in the magnitude of the voltage hash along with predominantly positively biased spikes in the voltage fluctuations relative to the mean. We will explore the nature of these spikes via statistics in the following section. These results are consistent with the behaviors and three different regimes of voltage hash observed by Uribarri in his own data for the Princeton Benchmark Thruster [18].

We next examine the influence of the applied magnetic fields. Figure 3.2 shows example voltage traces with the thruster under the influence of the tangential applied B field at the same operating currents. In this case, it can be seen even by inspection that there is a reduction in the mean voltage relative to the no-magnets case, at least for the 5.5 kA and 8.0 kA cases. Overall, a reduction in the magnitude of the voltage fluctuations is also evident. The reduction in the mean voltages and the reduction in the magnitude of the spikes will be analyzed statistically and discussed further

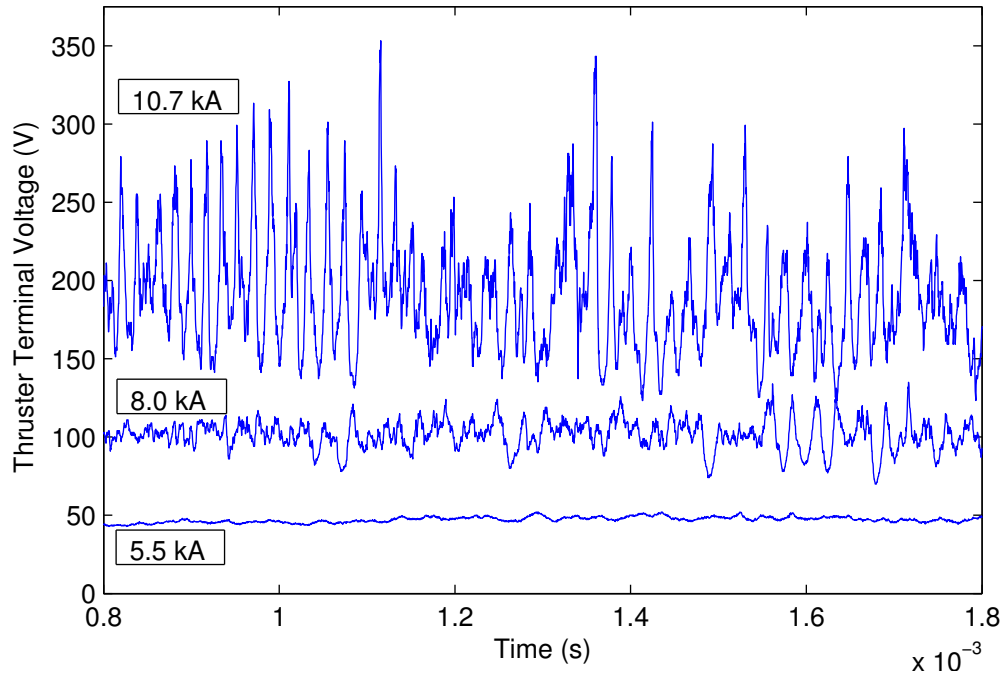


Figure 3.1: Example voltage traces during quasisteady period (1 ms duration) for the no-magnets case (self-field operation). Traces shown compare 10.7 kA, 8.0 kA, and 5.5 kA.

later. The three types of regimes of structure to the voltage hash found in the self-field case are also observed with the tangential applied B field. These include a quiescent mode in the 5.5 kA case, an intermediate mode in the 8.0 kA case, and a positively biased spiky hash in the 10.7 kA case.

In Figure 3.3, we see examples of the voltage traces with the applied cusp B field. This case responds similarly to the tangential B field configuration, with reduced mean voltage and a reduction in the amplitude of the voltage fluctuations. Moreover, a somewhat steadier response is observed in the cusp B field voltage time series, exhibiting fewer and smaller-amplitude transitory excursions (drops or rises relative to the moving average) than we saw in the other two configurations. This response is perhaps indicative of a slightly steadier and stable behavior due to the cusp B field.

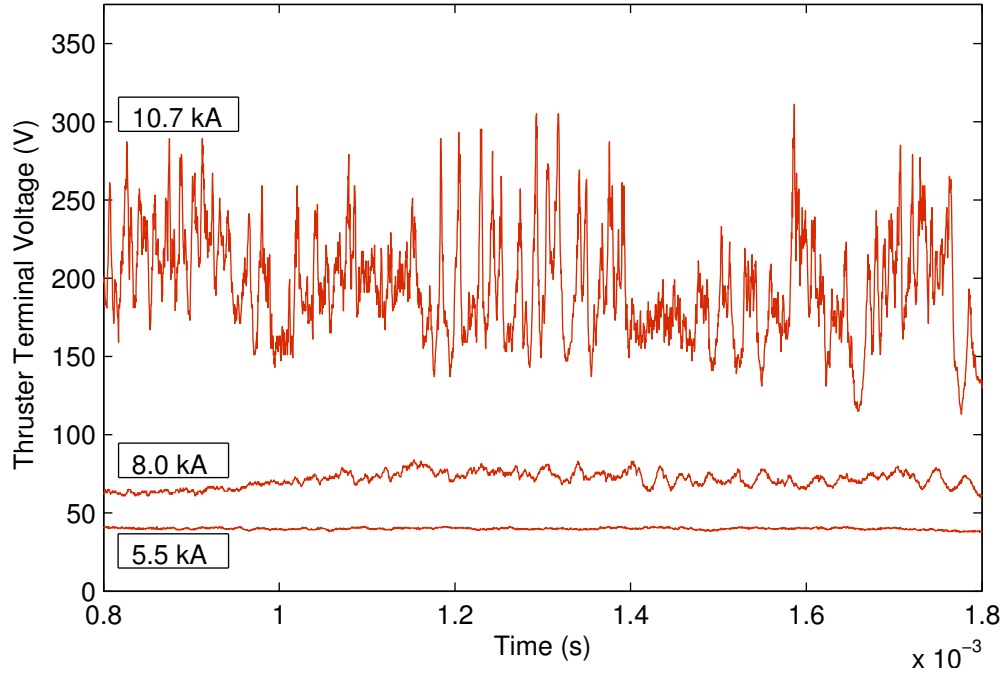


Figure 3.2: Example voltage traces during quasisteady period (1 ms duration) for the tangential applied B field case. Traces shown compare 10.7 kA, 8.0 kA, and 5.5 kA.

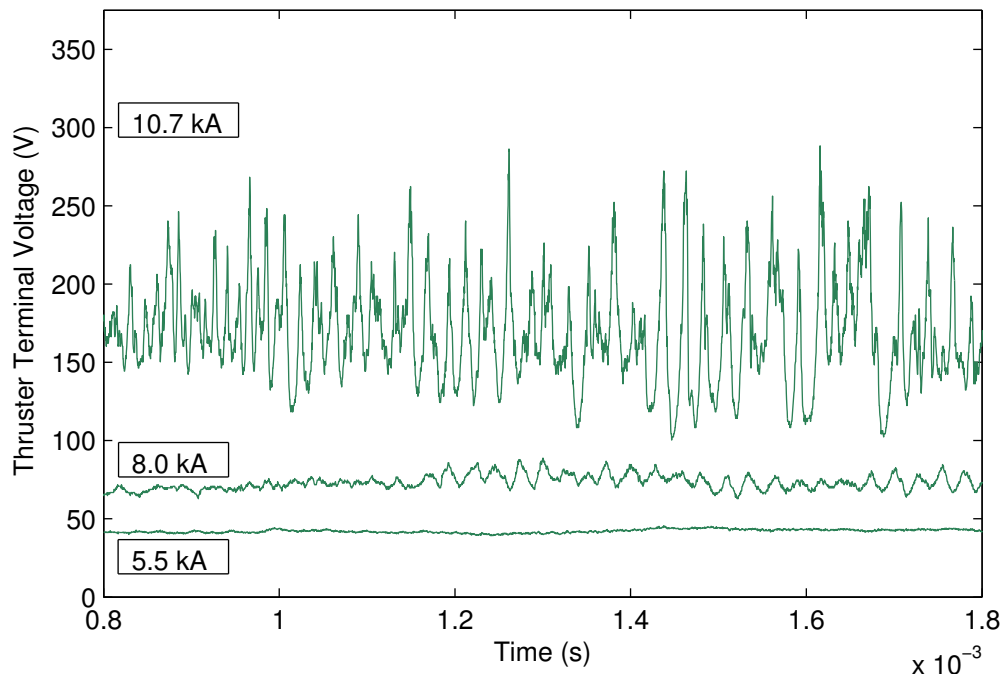


Figure 3.3: Example voltage traces during quasisteady period (1 ms duration) for the cusp applied B field case. Traces shown compare 10.7 kA, 8.0 kA, and 5.5 kA.

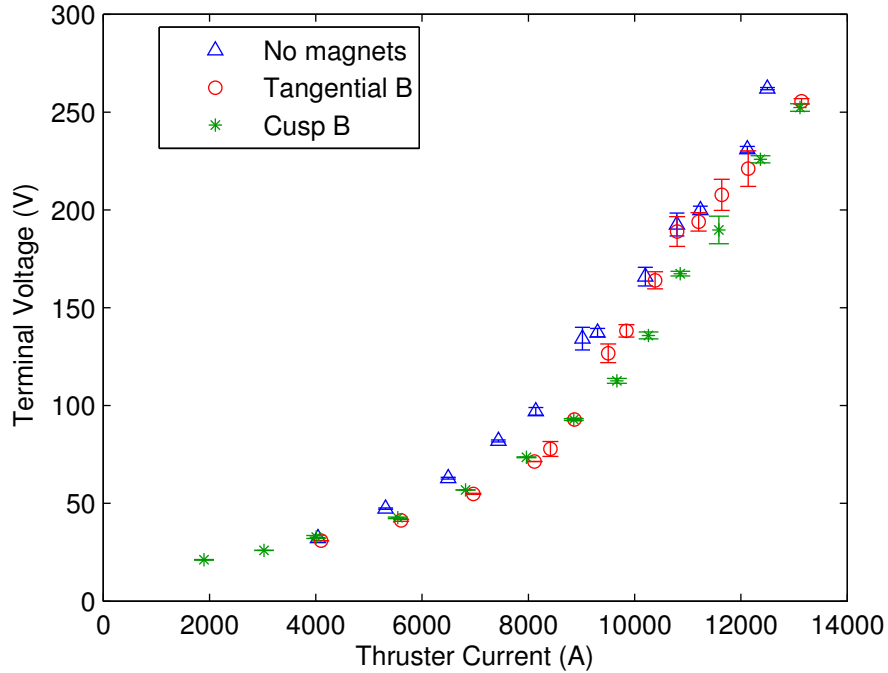


Figure 3.4: Mean terminal voltage vs. current characteristics comparing cases with no magnets, tangential B field, and cusp B field.

3.3 Analysis of the Moments of the Voltage Signal Distribution

We begin our examination of the thruster terminal voltage response by analyzing the voltage-current characteristics (also commonly referred to as the “V-J curves” in the literature). Each individual voltage time series is analyzed over the 1 ms quasi-steady period from 0.8 ms to 1.8 ms. Additionally, multiple shots of the thruster were taken at each discharge current condition shown and then repeated for each applied B field configuration. These multiple shots were averaged to obtain the data shown in Figure 3.4. Note that the error bars shown in the plots represent the standard errors of the means, and are dominated by the shot-to-shot variability. As expected, we see the monotonically increasing growth in mean terminal voltage as the current is increased. An initially linear trend for lower currents is observed below approximately 8.5 kA. Above this value, the voltage increases more rapidly with increasing current. This trend is typically associated with a higher growth rate in voltage with increasing current above full ionization conditions [62].

<i>J</i> (kA)	Mean voltage (V)	Reduction in mean (V)	+/- 95% confidence intervals (V)	Relative reduction in mean	+/- 95% confidence intervals
	No magnets (self-field):				
8.0 kA	97.0				
9.0 kA	134.2				
10.7 kA	192.5				
	Tangential B field:				
8.0 kA	71.4	-25.7	3.8	-26.5%	3.9%
9.0 kA	92.9	-41.3	11.4	-30.8%	8.5%
10.7 kA	188.9	-3.6	18.8	-1.9%	9.7%
	Cusp B field:				
8.0 kA	73.5	-23.5	3.8	-24.2%	4.0%
9.0 kA	92.8	-41.4	11.3	-30.9%	8.4%
10.7 kA	167.4	-25.1	11.6	-13.0%	6.0%

Table 3.1: Comparison of terminal voltage signal means and relative reductions with applied magnetic fields.

The V-J curves exhibit one of the most significant effects of the applied magnetic fields. With the applied magnetic fields, we observe a significant decrease in the mean thruster voltage for a given current level over a broad range of currents. For example, with the tangential applied magnetic field, we obtain a reduction in the mean voltage of $25.7\% \pm 3.9\%$ (95% confidence interval) relative to the self-field at 8.0 kA. A similar reduction of $24.2\% \pm 4.0\%$ is seen with the cusp applied magnetic field at 8.0 kA. At 9.0 kA, a $30.8\% \pm 8.5\%$ reduction and a $30.9\% \pm 8.4\%$ reduction are measured for both the tangential and cusp fields, respectively. As current is increased further, the tangential field case begins to approach the response without magnets. However, the cusp magnetic field configuration still exhibits a relative reduction of $13.0\% \pm 6.0\%$ at 10.7 kA and a slightly decreased but still notable voltage reduction through the full range of measured currents (13.1 kA). All uncertainties cited above are based on 95% confidence intervals. These mean voltages and associated reductions with the applied magnetic fields are summarized in Table 3.1.

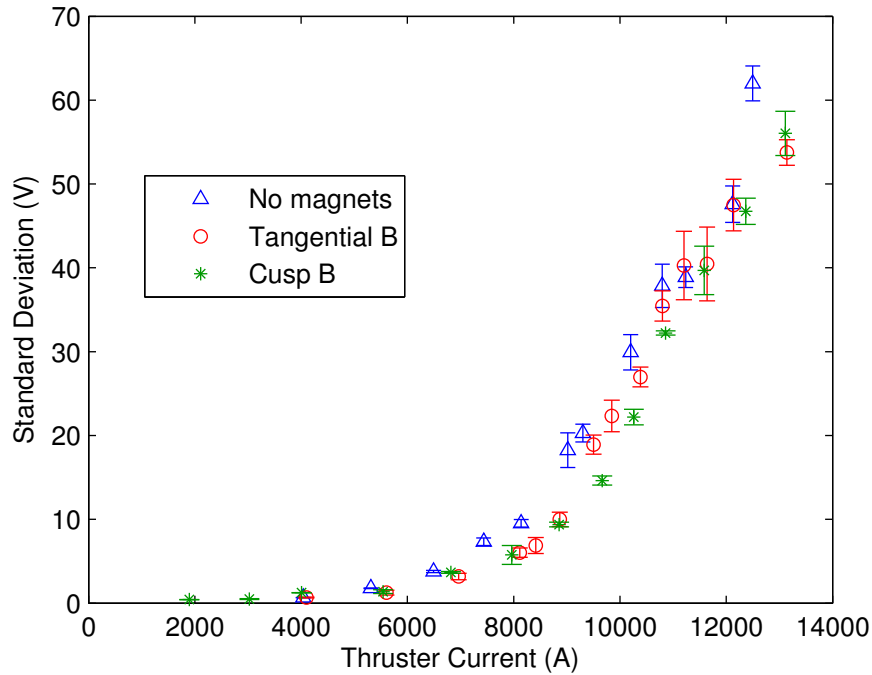


Figure 3.5: Standard deviation vs. current comparing cases with no magnets, tangential B field, and cusp B field.

This mean voltage reduction is counter to the results of Tahara, Kagaya, et al. [61, 25], who measured increased terminal voltages with their applied B fields relative to self-field operation. However, their applied B fields were much higher magnitude (1000-5700 Gauss), and they were much more axial in shape (primarily parallel to the anode).

We continue our assessment of the voltage signals by analyzing the higher-order moments of the distribution for the voltage time series during the quasi-steady time interval. As with the V-J curves, the same averaging process over multiple shots was performed on the higher-order moments of the distribution. These moments include the standard deviation, skewness, and kurtosis shown in Figures 3.5, 3.6, and 3.7, respectively. Note that the convention chosen for the equation used to calculate the kurtosis includes the “-3” correction term such that the kurtosis of a Gaussian distribution is zero. This is sometimes referred to as the “excess kurtosis.” Again, the error bars shown in the plots represent the standard errors of the means, and are dominated by the shot-to-shot variability.

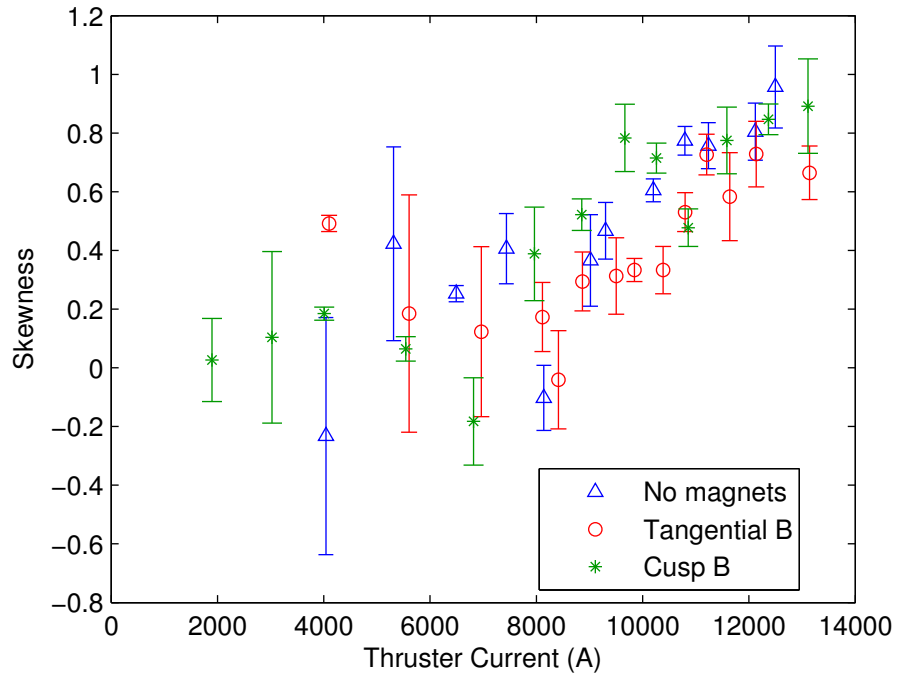


Figure 3.6: Skewness vs. current comparing cases with no magnets, tangential B field, and cusp B field.

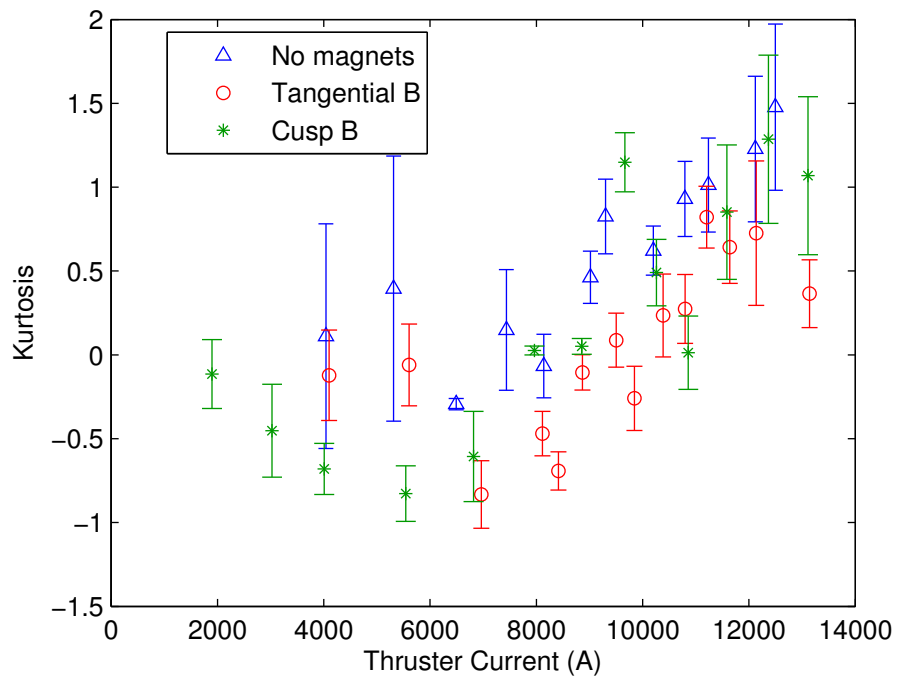


Figure 3.7: Kurtosis vs. current comparing cases with no magnets, tangential B field, and cusp B field.

<i>J</i> (kA)	<i>Standard deviations average</i> (V)	<i>Reduction in standard deviation</i> (V)	<i>Relative reduction in standard deviation</i>
	No magnets/self-field:		
8.0 kA	9.5		
9.0 kA	18.3		
10.7 kA	37.9		
	Tangential B field:		
8.0 kA	6.0	-3.5	-36.6%
9.0 kA	10.0	-8.3	-45.3%
10.7 kA	35.5	-2.4	-6.3%
	Cusp B field:		
8.0 kA	5.8	-3.8	-39.5%
9.0 kA	9.4	-8.9	-48.7%
10.7 kA	32.2	-5.6	-14.8%

Table 3.2: Comparison of terminal voltage signal standard deviations and relative reductions with applied magnetic fields.

The standard deviations of the voltage traces also exhibit a significant reduction in magnitude over a range of currents for the applied B field configurations. This is indicative of a reduction in the magnitude of the voltage hash, i.e., lower-amplitude RMS fluctuations about the mean voltage. Relative to the case without magnets, the tangential applied B field case yields a 36.6% reduction at 8 kA and 45.3% reduction at 9 kA. At 10.7 kA, the tangential B field case exhibits a small 6.3% reduction, but the differences are beginning to return to a similar range of response as the self-field case. For the cusp applied B field, a reduction of 39.5% is observed relative to the self-field case at 8 kA, 48.7% reduction at 9 kA, and still 14.8% reduction at 10.7 kA. Beyond this current level, the cusp B field response also trends towards the same behavior as without the magnets. Table 3.2 provides a comparison of the voltage signal standard deviations and relative reductions due to the applied magnetic fields.

There is a transition to significantly increased growth in the standard deviations with increasing current that occurs between 7.5 kA to 9 kA. This transition is near the same current range where the

thruster voltage transitioned to a stronger increasing dependence on current.

The skewness (third moment of the signal distribution) is a general measure of how the voltage hash fluctuations deviate from a Gaussian distribution toward a population that has a “broader, longer tail” biased to one side of the mean. Given our previous observation of the positively biased nature of the voltage spikes at higher currents as seen in the time series traces, we expect to see a growth in the positive skewness of the voltage signals. This trend is indeed observed. With increasing current, the skewness increases from values near zero at lower currents to increasingly positive values for currents beyond approximately 8 kA. However, we do not see a systematically different response in the skewness with the magnets on than without the magnets.

The kurtosis (fourth moment of the signal distribution) is a measure of how peaked or flattened the data are relative to a Gaussian distribution. In this case, increasing kurtosis gives a sense of whether the voltage hash distribution shifts from Gaussian toward a population biased with a “heavy tail” well to the positive side of the mean (i.e., a positive “bump” in population distribution counts at a high amplitude). Such a population would occur if there are relatively infrequent but large-amplitude spikes in the voltage signal, as opposed to frequent, modestly sized fluctuations. We observe such behavior in the time traces and see a general trend of increasing kurtosis above approximately 8 kA. There is a trend of lower kurtosis with the magnets on, particularly for the tangential B field case up to approximately 10.7 kA. However, the differences for the cusp B field case relative to without the magnets are not consistently lower over the range of currents, oscillating between lower values and statistically similar values relative to without the magnets.

To elucidate the basis of these statistical results, we can examine the population distributions of the voltage time series. Examples of these distributions are shown in Figures 3.8, 3.9, and 3.10 for the signals at the higher current near 10.7 kA. A longer tail to the distribution on the positive side of the mean (a contributor to positive skewness) is observed, and in the example without magnets,

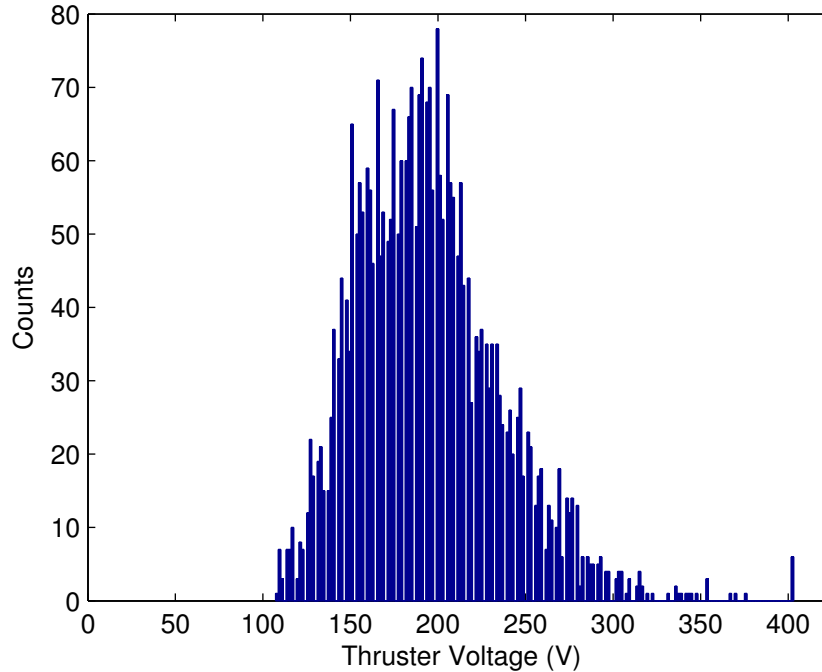


Figure 3.8: Population distribution histogram example for the voltage signal without magnets at 10.7 kA.

we can see a small peak of some high-amplitude positive spikes extending to just over 400 V in the distribution (a likely contributor to positive kurtosis). At lower currents, we observed population distributions that are more symmetric, Gaussian-like distributions are observed in the self-field case at a lower current circa 8 kA in Figure 3.11.

To examine similarities in thruster behavior, it is useful to compare our results to the data observed by Uribarri for their Princeton Benchmark Thruster in his examination of the voltage signal means, standard deviations, skewness, and kurtosis [42]. We observed similar trends in the growth of the means and standard deviations, including a departure to significantly growing standard deviations (or magnitudes of the fluctuations) around 90 to 100 $\text{kA}^2/\text{s/g}$. We also observed a positive growth in the skewness and kurtosis with increasing current, albeit the magnitude for both was much greater in the Princeton Benchmark Thruster. Uribarri observed in their Princeton Benchmark Thruster that the skewness and kurtosis both peaked circa 110 $\text{kA}^2/\text{s/g}$ with increasing current,

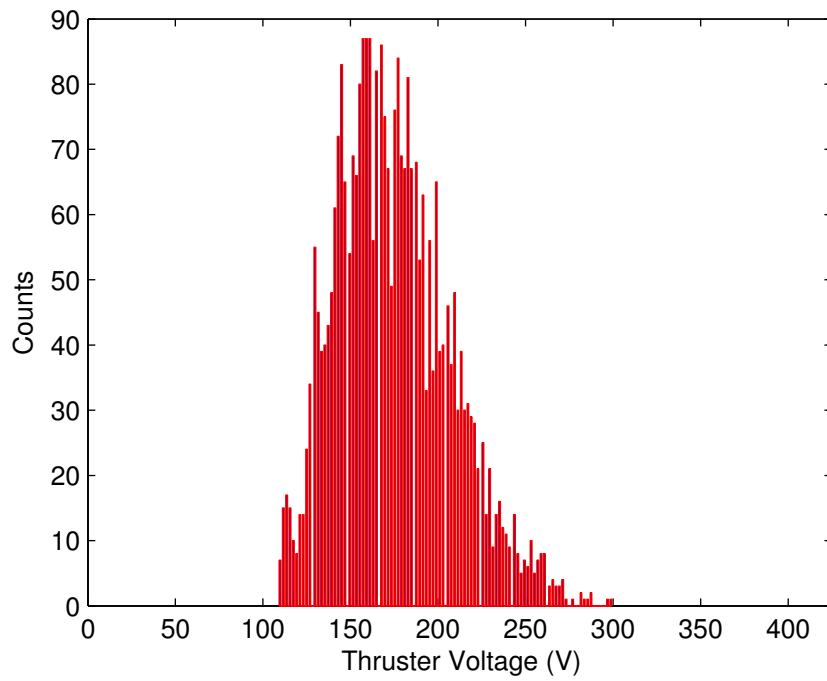


Figure 3.9: Population distribution histogram example for the voltage signal with tangential B field at 10.7 kA.

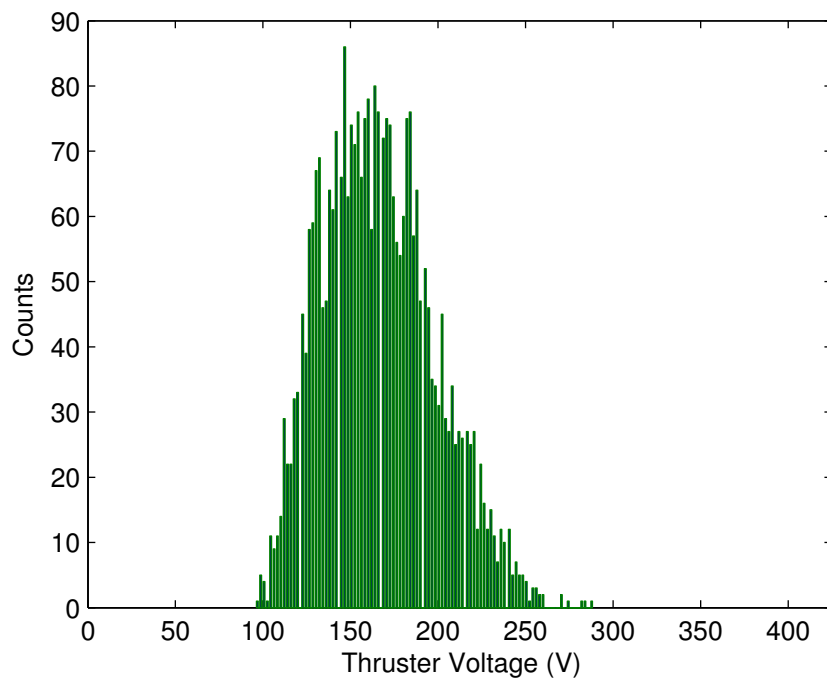


Figure 3.10: Population distribution histogram example for the voltage signal with cusp B field at 10.7 kA.

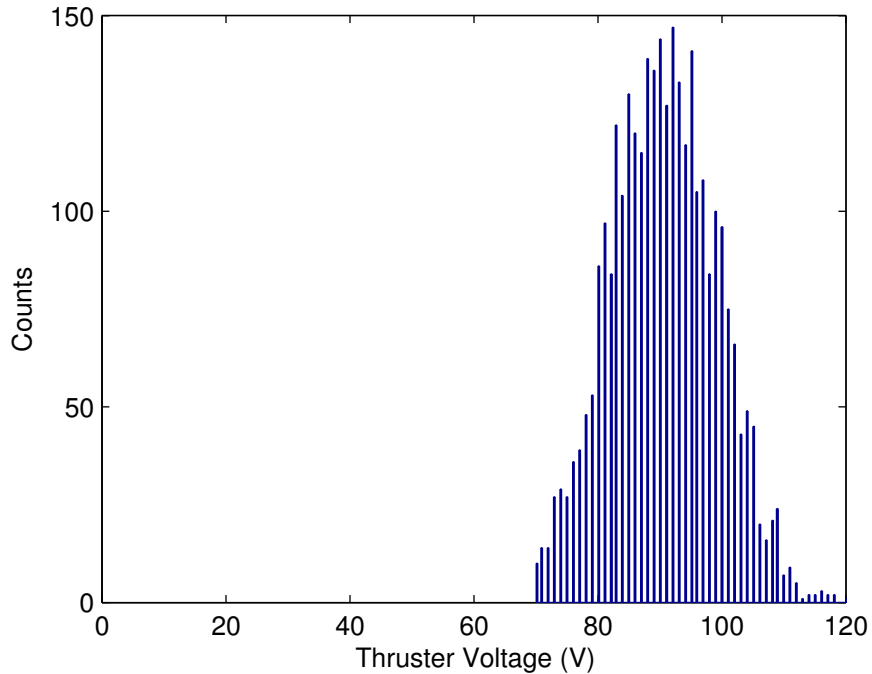


Figure 3.11: Population distribution histogram example for the voltage signal without magnets at lower 8 kA current.

then began to decrease back toward zero. We did not clearly observe this feature in our thruster's data. It is possible, for example, that such a decreasing response would have been observed at much higher currents and that the kurtosis was beginning to exhibit a downward trend near the highest-current data point of 13.1 kA. However, without data beyond this current, it is impossible to make such a claim with certainty. These results will be discussed further in Section 3.5.

3.4 Analysis of the Transients and Power Spectrum of the Voltage Signal

To explore further into the temporal and frequency-dependent response of the voltage signal, we analyze various aspects of the transient spikes and power spectra of the voltage signals. To begin this analysis, we pick a threshold of 10% above the mean thruster voltage for each signal. Then, we analyze the positive spikes that exceed this threshold and perform the same averaging over multiple

shots and uncertainty analysis for the standard error to characterize shot-to-shot variation.

First, we count the number of positive spikes exceeding this threshold of 10% above the mean voltage over the 1 ms quasi-steady period, as seen in Figure 3.12. Clearly, a transition to sufficiently high-amplitude spikes occurs beginning at 5.5–6.5 kA for the self-field case, and the number of spikes grows steadily until approximately 9 kA, where the number of spikes approaches a constant value. The initial transition begins at somewhat higher currents, circa 7–8 kA for both cases with magnets on, and the values increase until approximately 10.7 kA. Overall, the applied magnetic fields increase the current threshold for the rapid growth of large-amplitude spikes by approximately 1–2 kA. The spike-reducing effects of the applied fields can be seen more clearly if we examine the response at fixed current values. For a fixed, specified current in the transition region between approximately 6 to 10.7 kA, the applied magnetic fields result in a significant drop in the number of positive spikes. For example, the applied magnetic fields result in 73–77% reduction in the number of spikes at 8 kA and 47–50% at 9 kA. Because anode spots have been shown to correlate with voltage hash, one can argue that the number of spikes is related to the number of anode spots being formed on the surface of the anode, as indicated in the work by Uribarri [42].

The introduction of anode spotting as a possible mechanism is relevant because evidence of anode spots occurring in our thruster was obtained via high-speed video imaging. Figure 3.13 shows 9 frames taken with 1 μs exposure times and separated by 100 μs intervals looking upstream into our thruster during the quasi-steady period. The thruster was firing at 9 kA in self-field mode (no magnets). These images show the higher-luminosity regions around the inner perimeter of the anode lip migrating around the anode over time. Similar to observations by Uribarri [42] and Diamant [37], these luminous regions are associated with localized, higher-current concentrations along the anode, which have been shown to be associated with anode spotting and current filamentation. Figure 3.14 also shows photographic evidence of anode damage in our thruster by melting due to localized

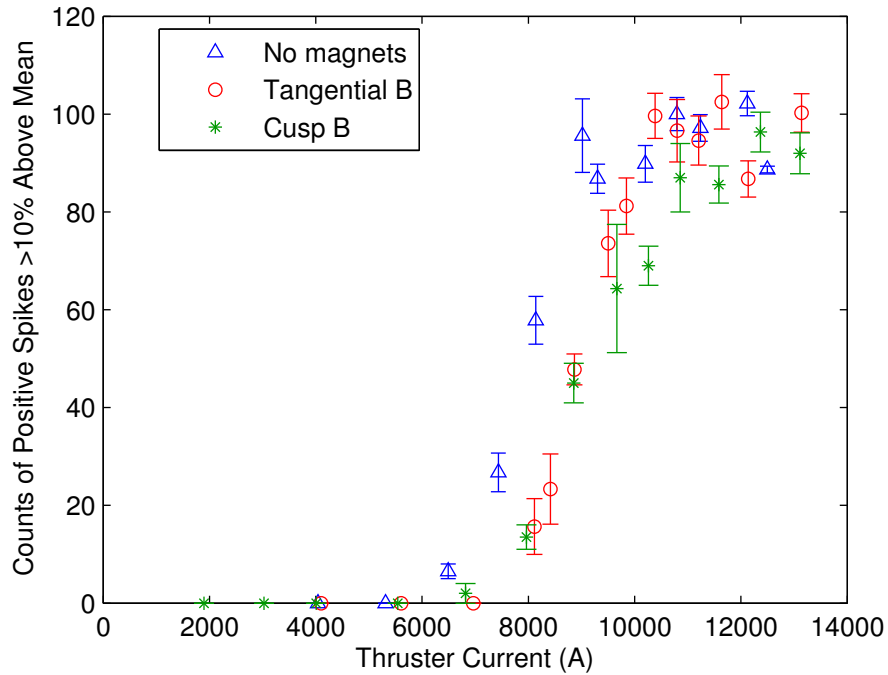


Figure 3.12: Number of positive spikes >10% above mean voltage.

heating and surface pitting due to anode spots. This relationship between the terminal voltage fluctuations and anode spots will be discussed further in Chapter 6. Reductions in the number of voltage spikes and potentially in the number of anode spots (and associated erosion) appear to be beneficial effects of the applied magnetic fields.

Next, we examine the peak amplitude of the positive spikes, as averaged over all spikes in the voltage trace and subsequently averaged over multiple shots. In Figure 3.15, we again observe an increase in the current threshold and a small reduction in the average amplitude due to the applied magnetic fields. Relative to the self-field case, this reduction is approximately 22% for the cusp B field and 34% for the tangential B field at 8 kA, and the reduction extends to approximately 40% at 9 kA for both applied fields.

Perhaps a better measure of intensity for the spikes is the signal energy contained in each individual spike, as shown in Figure 3.16. Here, we subtracted the mean and computed the integral $\int V^2 dt$ for each positive spike exceeding the threshold (greater than 10% of the mean voltage) in a

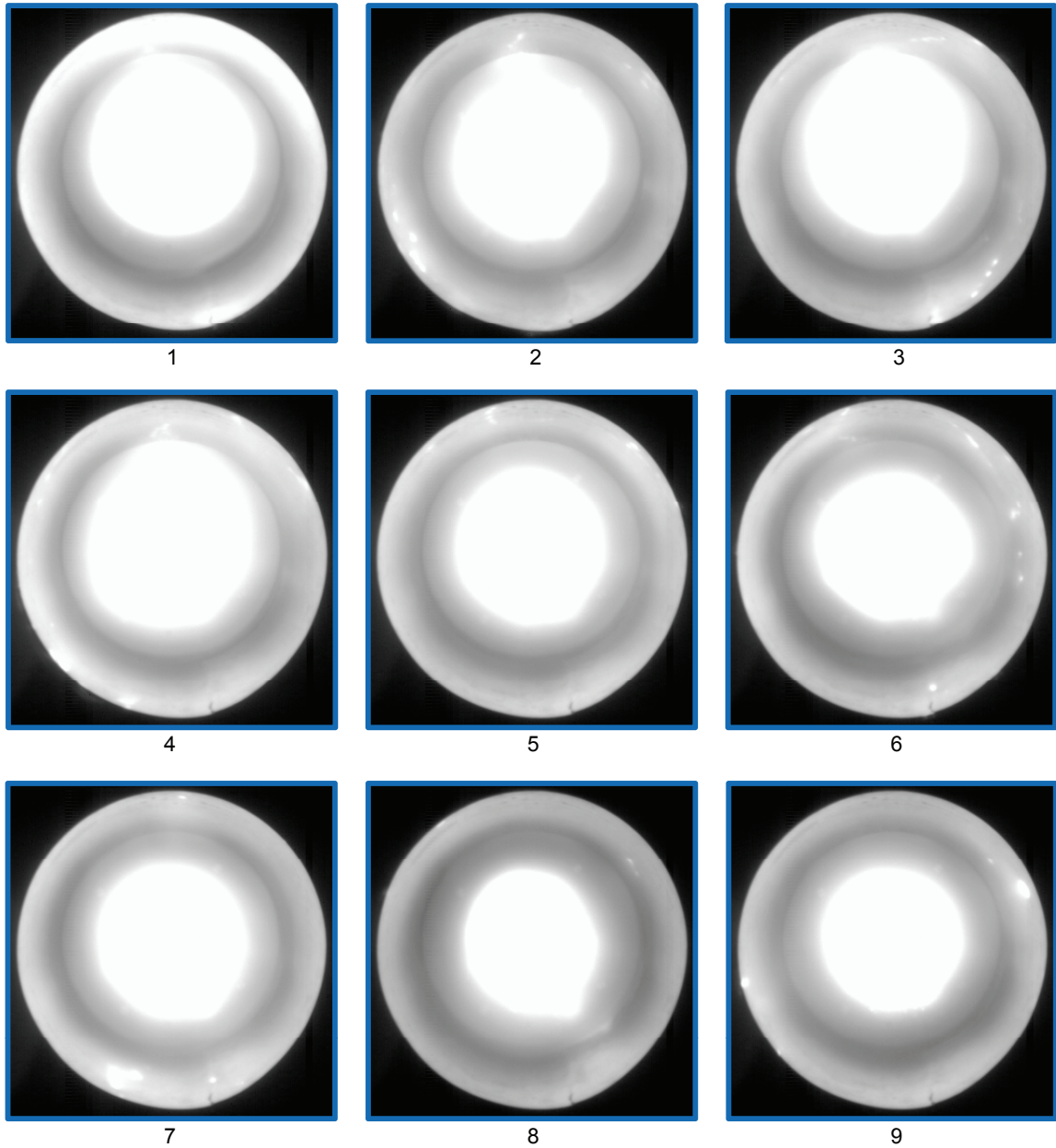


Figure 3.13: High-speed video imaging frames showing evidence of anode spots in thruster at 9 kA. Frames represent $1 \mu\text{s}$ exposure times separated by $100 \mu\text{s}$ intervals.

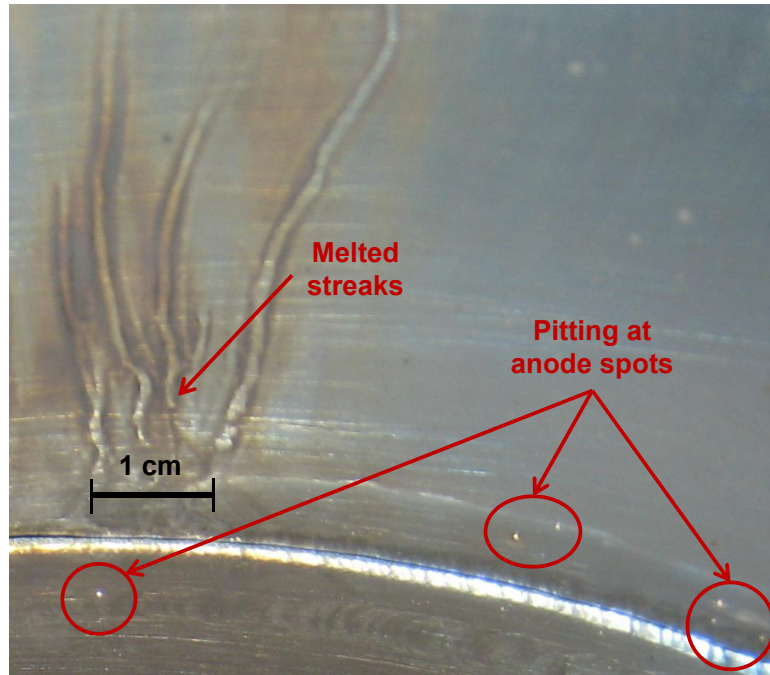


Figure 3.14: Evidence of anode erosion in our MPD thruster.

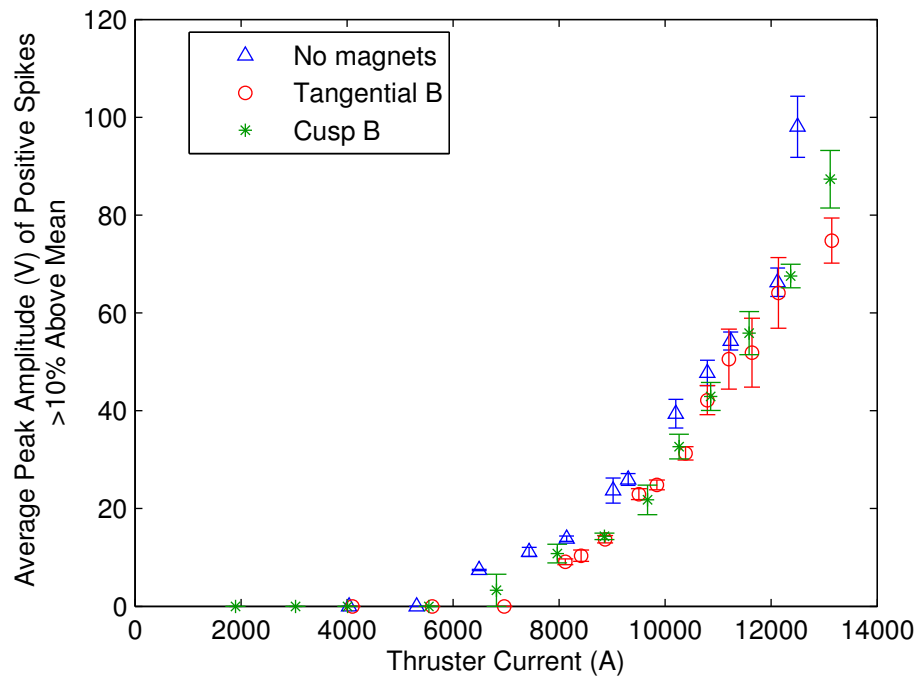


Figure 3.15: Average peak amplitude of positive spikes >10% above mean voltage.

given voltage trace, averaged over all spikes in that trace, and repeated and averaged over multiple shots. Since the power in a signal is proportional to the square of its amplitude (or its magnitude), this calculation yields a measure of the average energy of the positive spikes. In these data, we observe a clear transition to much faster growth in the average energy of the spikes at approximately 9 kA for the self-field case and approximately 9.5–9.7 kA with the applied B fields. At 9 kA, the applied B fields yield approximately 57% lower energy, but the average energy rapidly rises at higher current and approaches values similar to the self-field case.

Again, we can attempt to relate this amplitude to the anode spots. Uribarri [42] and Giannelli et al. [24] proposed capacitively-coupled anode sheath models that associated anode spots and current filamentation with fluctuations in the voltage signal. Based upon these models, we expect the energy in the voltage hash spikes to be related to the magnitude of the current carried in the filaments at the anode spots. A reduction in spike energy is observed with the applied-field magnets at currents below approximately 10 kA. Combined with a potential reduction in the number of spots (related previously to the observed decrease in number of spikes), we observe what is thought to be an overall decrease in both the intensity and frequency of the anode spots with the applied magnetic fields. This will be discussed further in Chapter 6.

Another way to examine the energy content in the voltage signal is to take the power spectral density (PSD) of the signal in frequency space and integrate over a range of frequencies. The mean of the voltage signal is subtracted before performing the PSD analysis. The results of this analysis are shown in Figure 3.17. We chose to integrate over the frequency range from 10 kHz to 155 kHz. As will be shown later in some example plots of the PSDs, the bulk of the energy content is in the 10s of kHz, so we chose a cutoff of 155 kHz to exclude all of the low-amplitude random noise in the higher frequencies. Further, by ignoring the frequency content below 10 kHz, we avoid energy content associated with very low-frequency shifts in the mean signal over the 1 ms quasi-steady

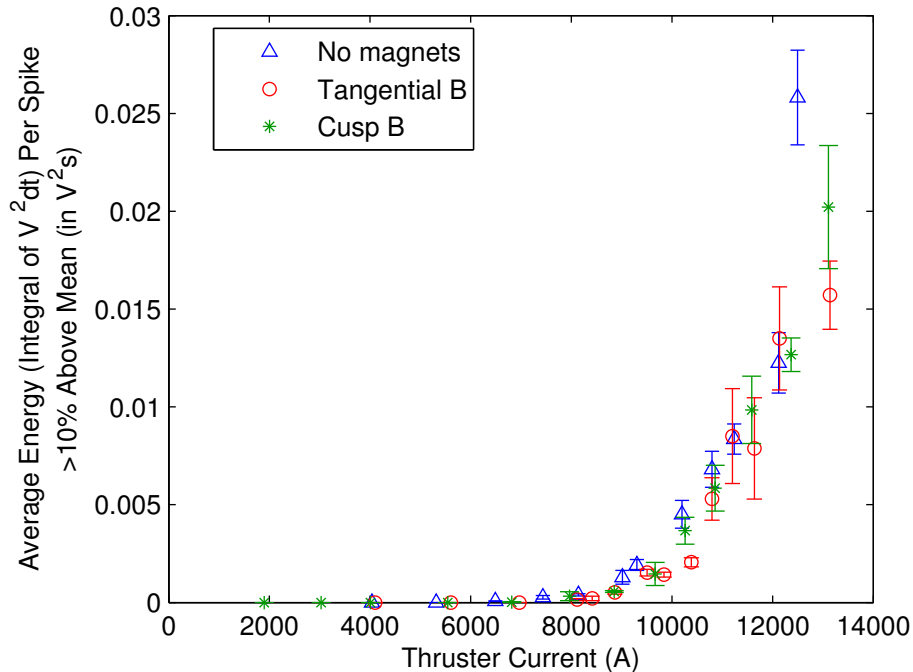


Figure 3.16: Average energy per spike for positive spikes $>10\%$ above mean voltage. Here, energy is calculated as the integral of $V^2 dt$ over each spike relative to the mean and averaged over all spikes.

period that irrelevant to the examination of the voltage hash fluctuations. In this plot, we see a similar relationship as we saw in the previous plot of the signal energy in each of the positive spikes obtained via integration and averaging in the time domain. This is as expected, as we are examining similar energy content in slightly different ways (i.e., temporal analysis versus frequency analysis). We observe a similar transition as before to much larger growth in the energy at approximately 9 kA without magnets and approximately 9.5 to 9.7 kA with both applied B fields. The applied B fields result in approximately a 73% reduction in the energy at 9 kA and approximately 40% at 10.3 kA. The values begin to statistically overlap at higher currents.

Subsequently, we consider the timing of the events associated with the positive spikes more than 10% above the mean voltage. The average duration of these spikes is plotted in Figure 3.18. Spikes that are below this threshold are ignored, and so the values are zero for sufficiently low currents. Beginning at approximately 8 kA and higher, all three magnetic configurations begin to statistically

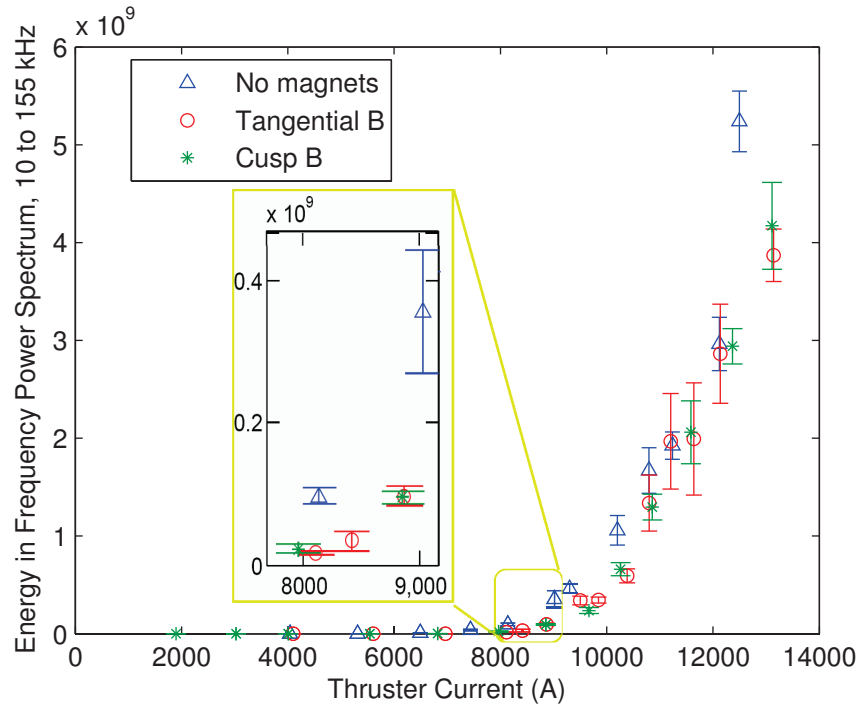


Figure 3.17: Total energy in the PSD spectrum, as integrated from 10 to 155 kHz. The inset yellow box shows a zoomed in view of the region from 8–9 kA.

overlap. Although there is a steady growth in the duration of the spikes (on the order of a few microseconds) with increasing current, the data mostly overlap for all three magnetic configurations. This suggests that the aspects of the anode spotting events associated with the voltage hash spike durations may not differ due to the applied magnetic fields. Instead, the duration of these events may be associated primarily with the other invariant aspects of our thruster, e.g., anode material, which of course is fixed for all magnetic field configurations.

Further, we can calculate an average time span between positive spike events. By taking the inverse of this time span, we obtain an effective average frequency of the spikes greater than 10% above the mean, as plotted in Figure 3.19. As expected, we find a functional form that is nearly identical to the earlier plot showing the counts of number of positive spikes in Figure 3.12. The transitions occur at similar current ranges and the magnitude of the reductions due to the applied B fields is the same. The frequency grows with current until it asymptotes in a range spanning an

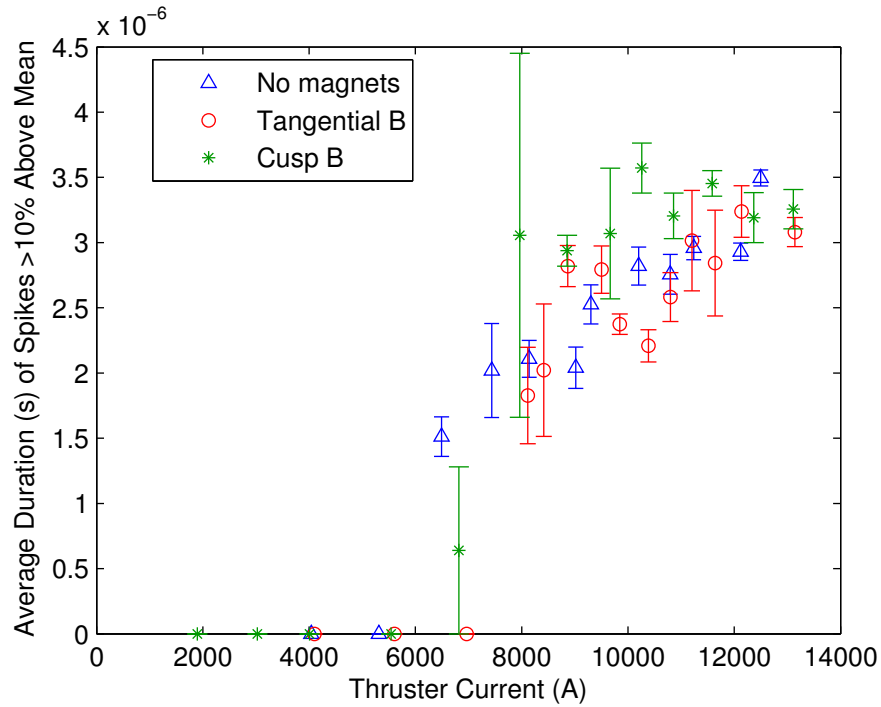


Figure 3.18: Average duration of positive spikes $>10\%$ above mean voltage.

effective average frequency between 82 to 103 kHz. Note that this frequency range is higher than the specific peaks we discuss later in the power spectral frequency analysis of the signals, as this represents an effective averaging over all of the sufficiently large spikes (including higher frequency spikes) crossing the threshold above 10% of the signal mean.

We next examine the frequency domain content contained in the voltage signals, for which example power spectral density plots (PSDs) are shown in Figures 3.20 to 3.31. The PSDs were calculated using Welch's method to reduce noise in the power spectra. The mean was subtracted from the 1 ms quasi-steady interval voltage signal time series, then the signal was segmented into 5 time-interval windows with 50% overlap between consecutive windows. A Hamming windowing function was applied and a periodogram was generated for each window interval, and then the resulting periodograms were time-averaged. Figures 3.20 to 3.28 show the PSDs of multiple example shots in the frequency range below 200 kHz, which highlight that the highest energy content is

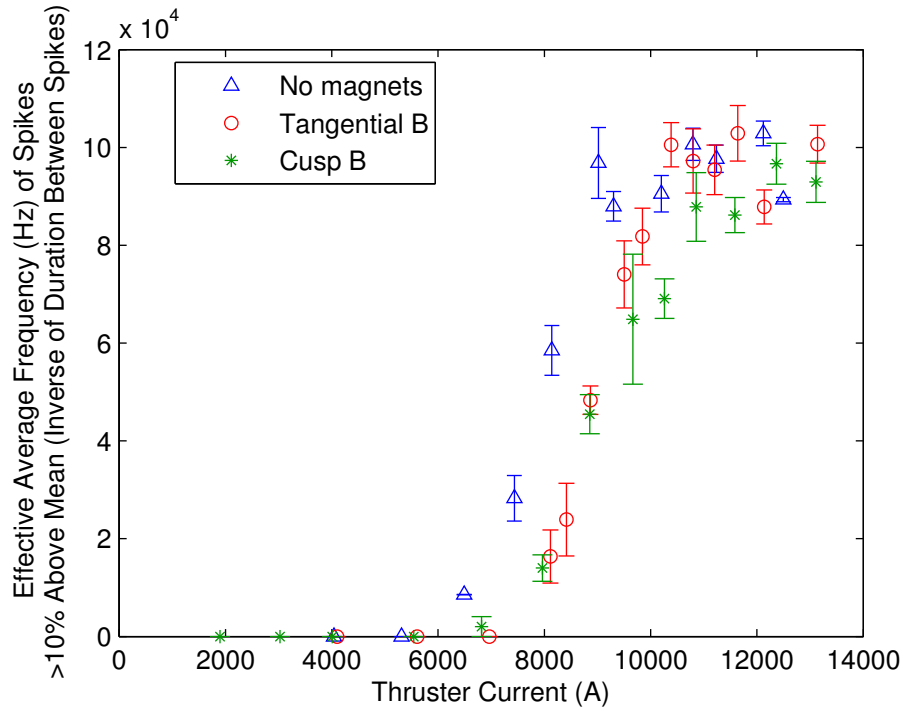


Figure 3.19: Effective average frequency of positive spikes $>10\%$ above mean voltage. This is calculated as the inverse of the average duration between positive spikes above the threshold.

observed in the 10s of kHz. Figures 3.20 to 3.22 show the PSDs at 10.7 kA. Peaks can be clearly seen primarily in the range between approximately 40 to 60 kHz. At the same current, a shift to smaller-amplitude peaks at slightly lower frequencies can be seen in the PSDs with the applied B fields relative to the self-field case. Figures 3.23 to 3.25 give example PSDs at 8 kA, where we observe characteristic peaks near 40 kHz without magnets and significantly attenuated peaks at just below 40 kHz. Figures 3.26 to 3.28 show example PSDs at 5.5 kA. At this lower current, the peaks are much smaller in magnitude (consistent with the very small voltage signal fluctuations). The self-field case still yields some peaks above 20 kHz, and the applied B field cases again exhibit a shift to slightly lower frequencies near 20 kHz and significantly lower amplitudes. These shifts to lower frequencies and lower amplitudes are consistent with the previous temporal domain analyses of the effective average frequency and energy of the spikes.

Figures 3.29 to 3.31 show example PSDs over the full frequency spectrum at the 10.7 kA higher

current operating point. In these figures, displayed as log-log plots, we can still see the distinct peaks in the 10s of kHz. However, we can now also see the broader $1/f^\beta$ form of the decreasing PSD dependence with increasing frequency at higher frequencies. A curve fit of the form $1/f^\beta$ over the range of frequencies from 155 kHz to 1 MHz results in a range of values near $\beta = 2$, as shown in the figures. Note that the turnover to flatter frequency response at even higher frequencies in the plots is due to the very small amplitude fluctuations at these higher frequencies showing up in the finite resolution bit noise of the least significant bit of the digitization. This $1/f^\beta$ form to the signal implies that the frequency content at these relatively higher frequencies (above approximately 100 kHz) is primarily due to random processes. This is an interesting finding that agrees with the results of Uribarri's work in their Princeton Benchmark Thruster. In particular, this $1/f^2$ relationship is characteristic of Brownian fluctuations for this higher frequency content. The Brownian fluctuations are characteristically related to the random walk of the time interval between individual voltage spike-inducing events, and it is generally a property of randomly perturbed, self-organizing systems.

However, this relationship at higher frequencies does not mask the clear appearance of distinct peaks in the PSDs at the lower frequencies. Further, the lower-frequency content clearly dominates the overall power in the voltage signals. Figures 3.29 to 3.31 also show overlay plots of the fraction of cumulative total power vs. frequency. It is clear from these plots that more than 90% of the power content in the PSD is below 100 kHz.

3.5 Summary of Results

In this chapter, we examined in detail the voltage-current characteristics and voltage fluctuations (“voltage hash”) related to onset with rising current. We examined the nature of these fluctuations in the temporal and frequency domains at a range of currents with the three major magnetic configurations: no magnets, the applied tangential B field, and the applied cusp B field. Several key

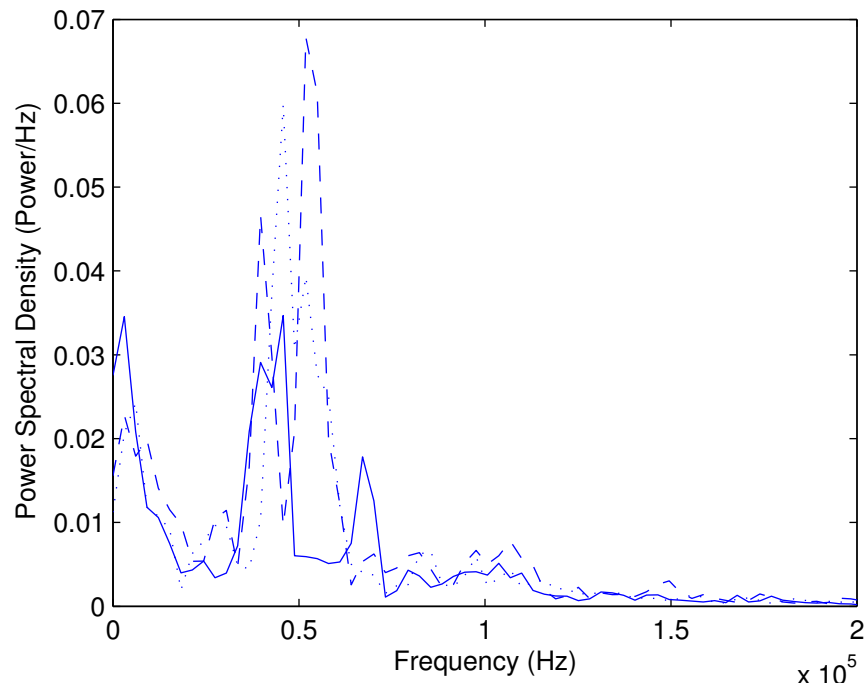


Figure 3.20: Power spectral density (PSD) examples for 3 shots without magnets at 10.7 kA.

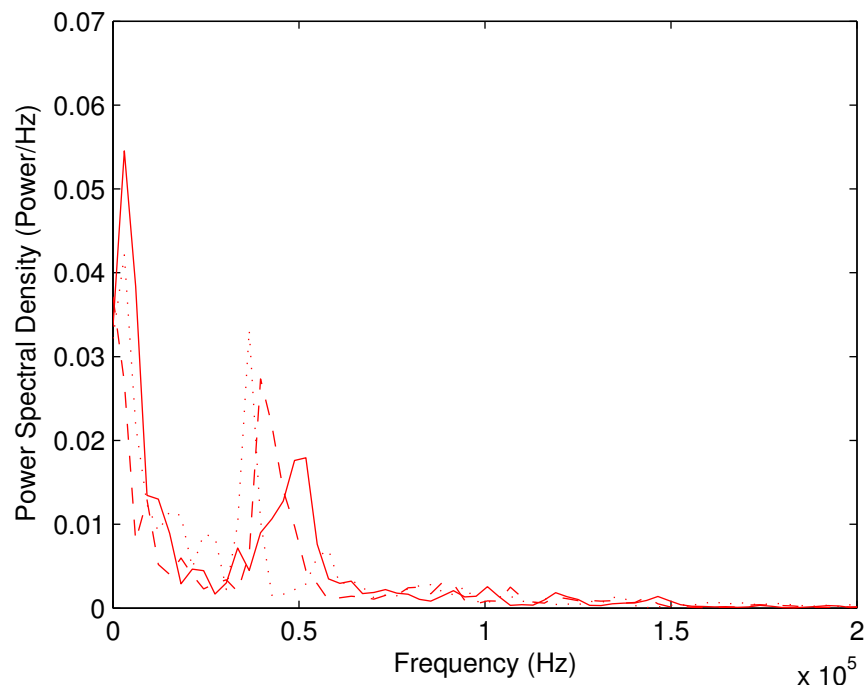


Figure 3.21: Power spectral density (PSD) examples for 3 shots with tangential B field at 10.7 kA.

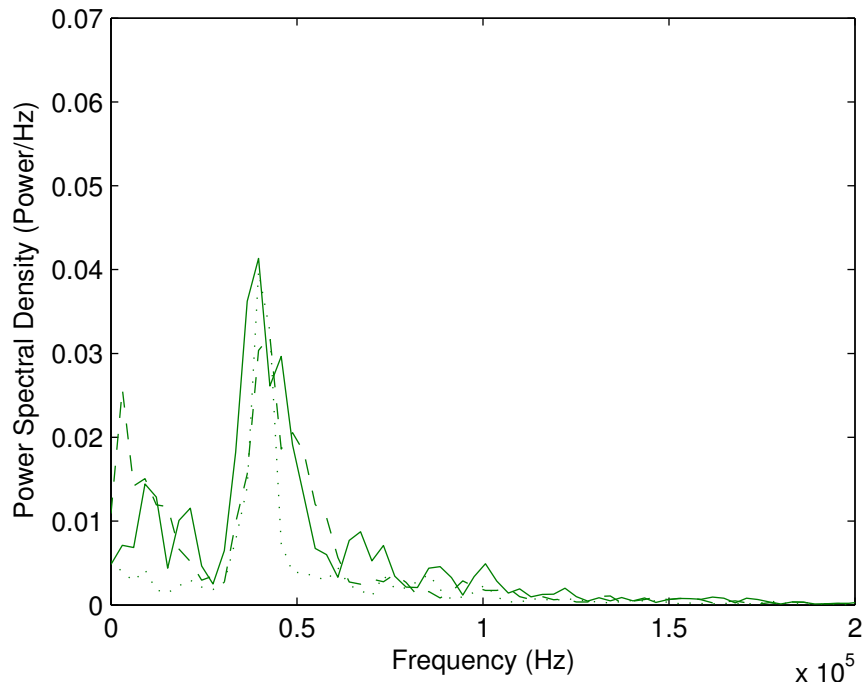


Figure 3.22: Power spectral density (PSD) examples for 3 shots with cusp B field at 10.7 kA.

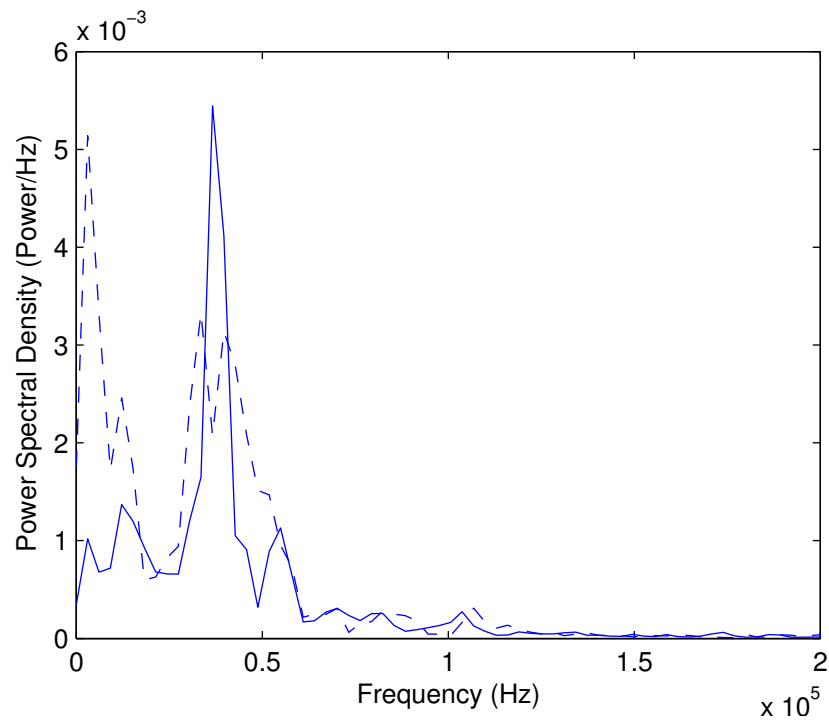


Figure 3.23: Power spectral density (PSD) examples for 3 shots without magnets at 8.0 kA.

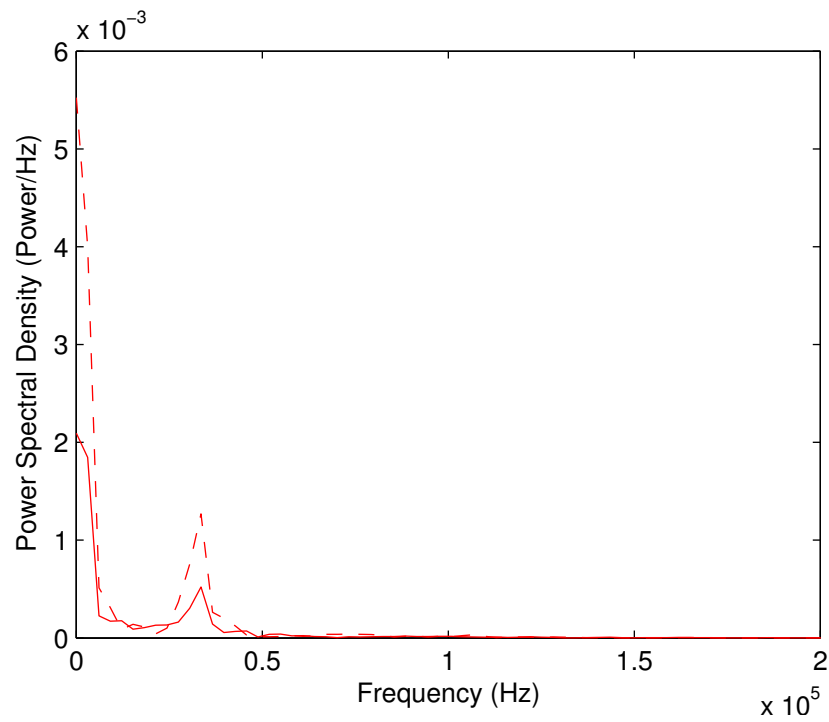


Figure 3.24: Power spectral density (PSD) examples for 3 shots with tangential B field at 8.0 kA.

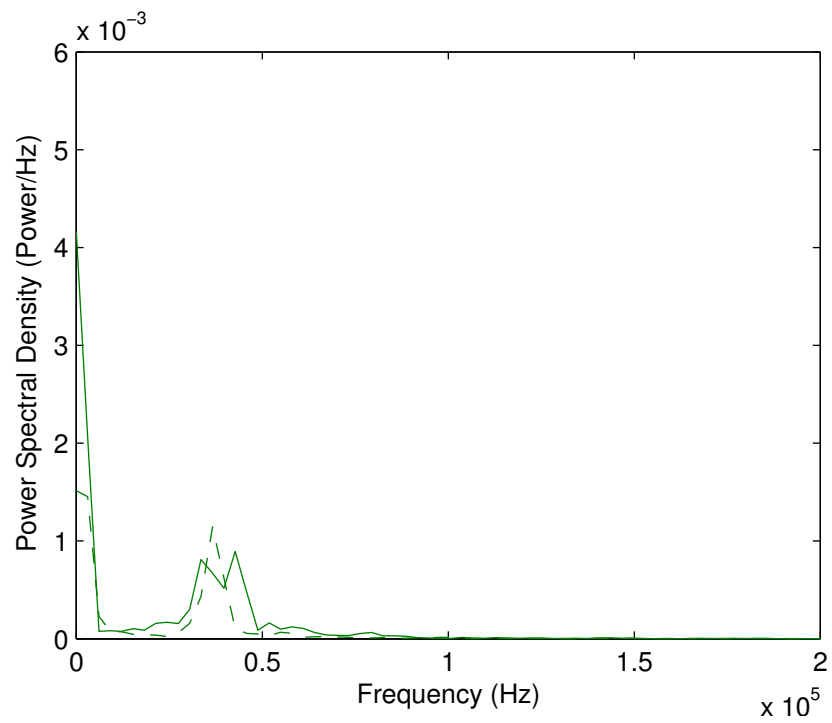


Figure 3.25: Power spectral density (PSD) examples for 3 shots with cusp B field at 8.0 kA.

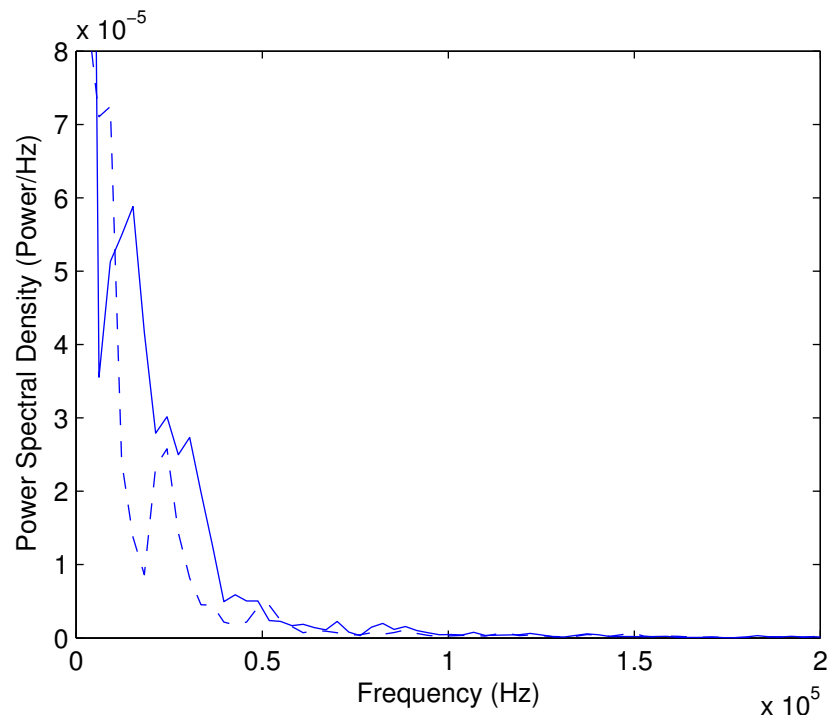


Figure 3.26: Power spectral density (PSD) examples for 2 shots without magnets at 5.5 kA.

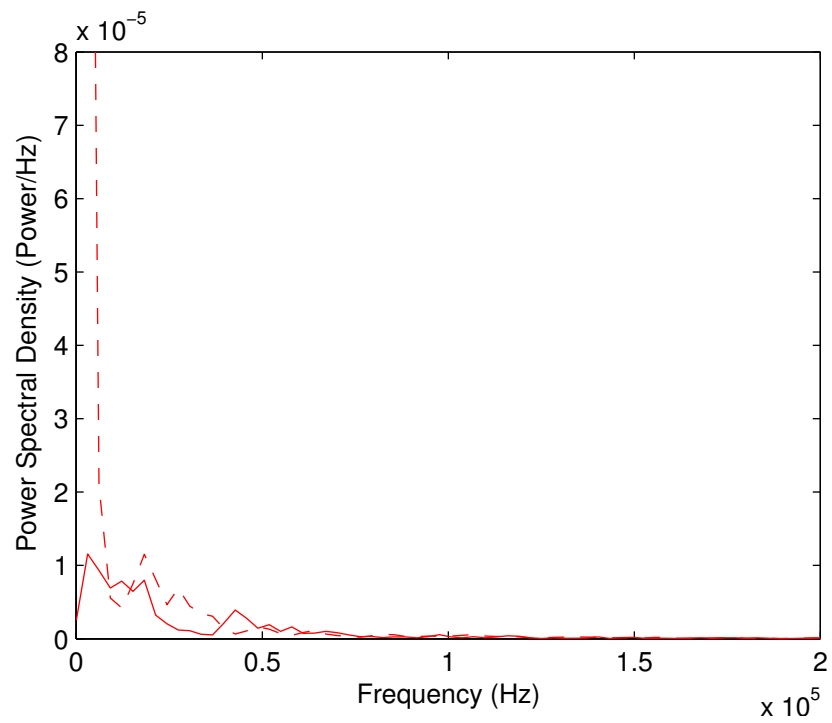


Figure 3.27: Power spectral density (PSD) examples for 2 shots with tangential B field at 5.5 kA.

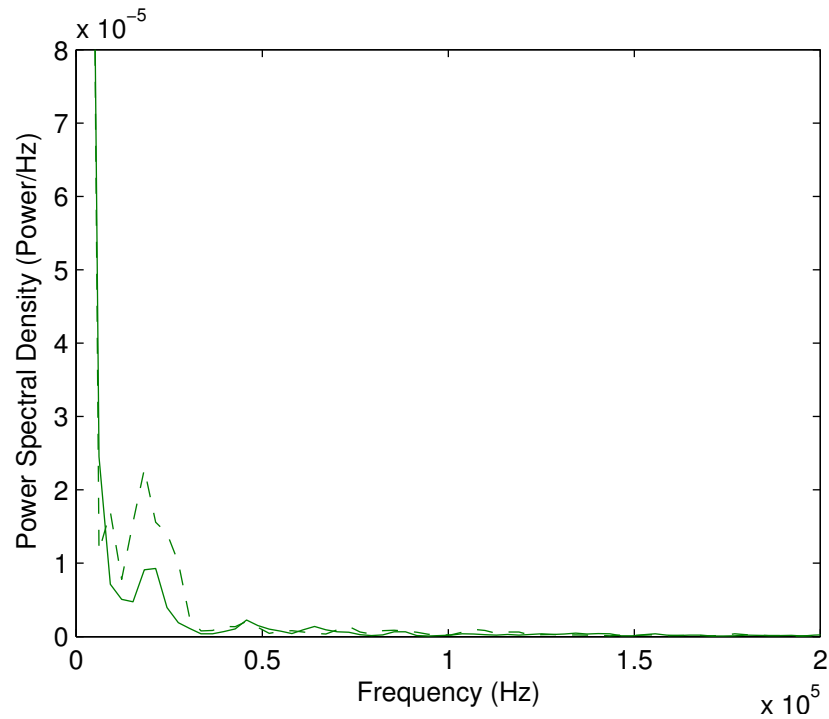


Figure 3.28: Power spectral density (PSD) examples for 2 shots with cusp B field at 5.5 kA.

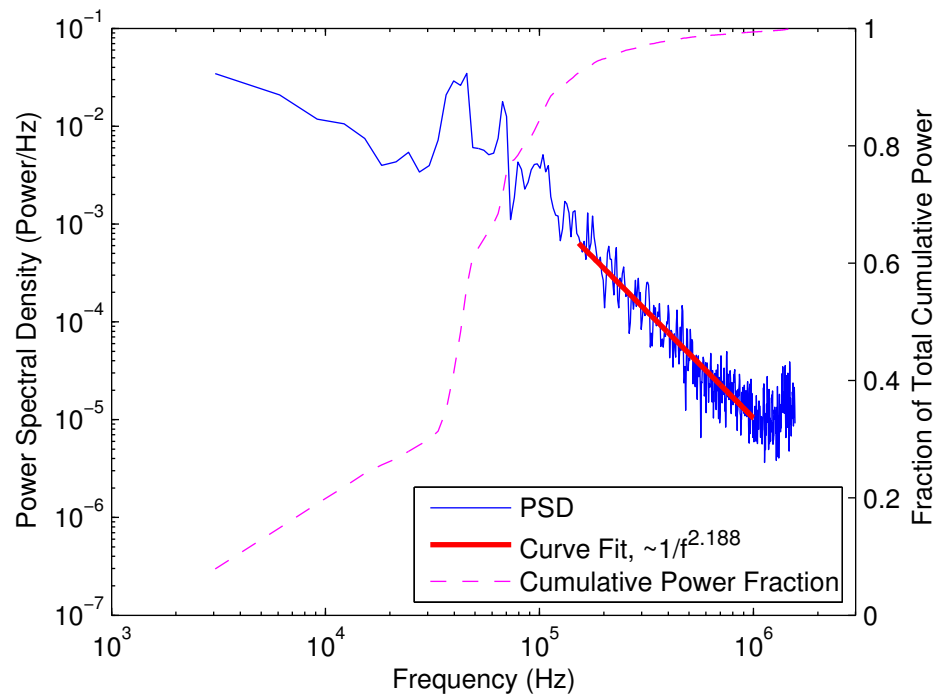


Figure 3.29: Log-Log plot of power spectral density (PSD) example over the full spectrum without magnets at 10.7 kA. Also shown are the $1/f^\beta$ curve fit (over range from 155 kHz to 1 MHz) and the fraction of cumulative integrated power versus frequency.

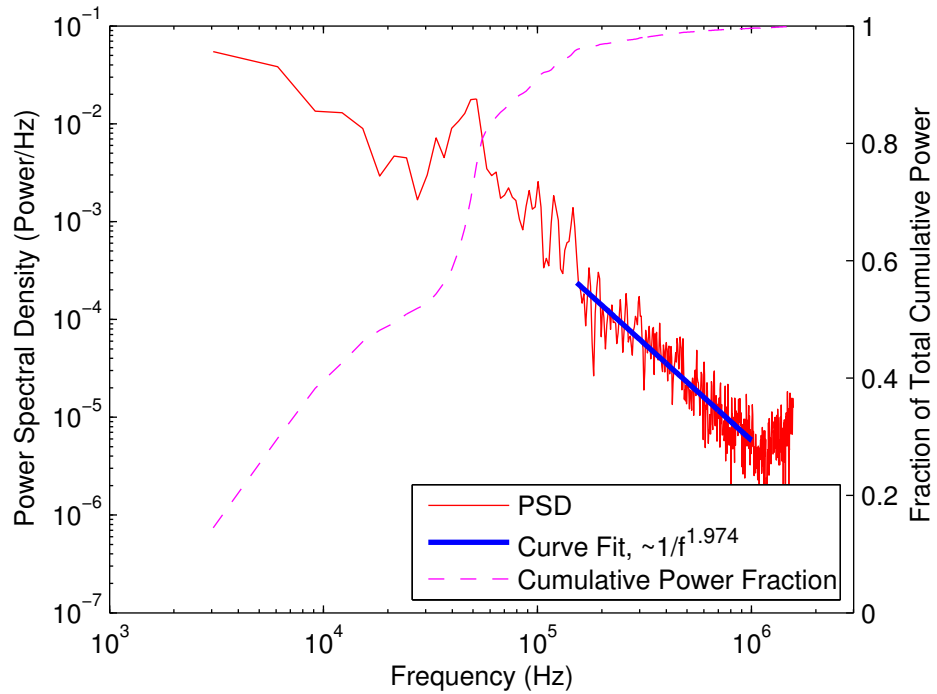


Figure 3.30: Log-Log plot of power spectral density (PSD) example over the full spectrum with tangential B field at 10.7 kA. Also shown are the $1/f^\beta$ curve fit (over range from 155 kHz to 1 MHz) and the fraction of cumulative integrated power versus frequency.

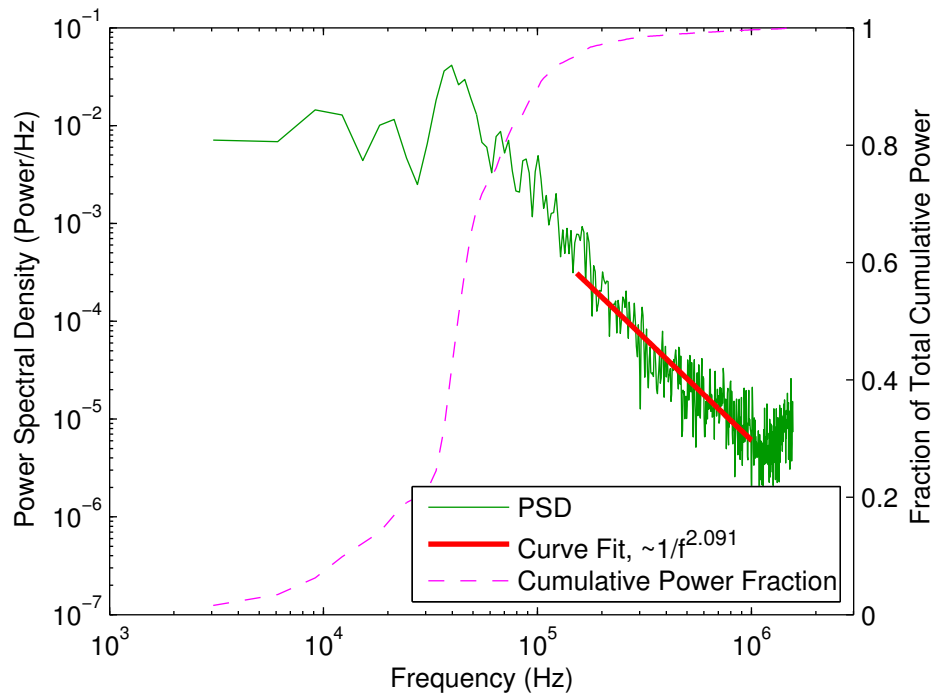


Figure 3.31: Log-Log plot of power spectral density (PSD) example over the full spectrum with cusp B field at 10.7 kA. Also shown are the $1/f^\beta$ curve fit (over range from 155 kHz to 1 MHz) and the fraction of cumulative integrated power versus frequency.

findings arose.

Substantial reductions in the mean voltages over a broad range of operating currents are achieved with the applied magnetic fields. Relative to the self-field case, both applied B field configurations yielded reductions of approximately 25% at 8 kA and approximately 31% at 9 kA. As current increased, the tangential B field case approached response similar to without the magnets. However, the cusp B field case continued with modest reductions in the mean voltage throughout the entire range of currents. This mean voltage reduction is counter to the results of Tahara, Kagaya, et al. [61, 25], who measured increased terminal voltages with their predominantly axial and higher-magnitude applied B fields. Overall, this implies a significant potential improvement in the total thruster efficiency by achieving the same current at reduced input power (lower $P_{in} = VJ$). This effect on efficiency will be analyzed later in Section 6.5.

The applied magnetic fields yield significant reductions in the magnitude and frequency of the voltage fluctuations. The standard deviations essentially track the magnitude of the RMS fluctuations about the mean voltage, which clearly grow with increasing current, and grow more rapidly above 8 or 9 kA. The applied B fields result in a 37–49% reduction in the standard deviations at 8–9 kA. The cusp applied B field still exhibits a 15% reduction at 10.7 kA. Both cases trend toward similar magnitudes as without magnets for higher currents. A detailed examination of the transients in the voltage signals was conducted. Again, the applied magnetic fields resulted in substantial reductions in these transients, e.g., the number and average frequency of positive spikes. These reductions were most substantial particularly around the range of 8–9 kA, which seemed to manifest as a recurring transitional region in the response behavior of the voltage transients. In general, relative to without the magnets, the applied B fields resulted in an approximately 1–2 kA higher current threshold at which these transients transition to significantly larger growth with increasing current. High-speed video imaging evidence of anode spots was shown in Figure 3.13, supporting

a link between these fluctuations and anode spots. In reducing the frequency and magnitude of the terminal voltage fluctuations, the applied magnetic fields may also yield a decrease in anode spots and associated erosion, which will be discussed further in Chapter 6.

Distinct peaks are observed in the PSDs at low frequencies (10s of kHz), and a $1/f^\beta$ dependence is observed at higher frequencies. In the frequency-domain analyses, peaks in the power spectral density (PSD) plots in the range of approximately 40–60 kHz were observed at higher currents around 10.7 kA and down to approximately 20–30 kHz for lower currents. These peaks repeatedly occurred in this range across multiple shots. The applied B fields consistently resulted in significantly lower amplitudes and a shift to slightly lower frequencies for the peaks relative to without the magnets. While these lower-frequency peaks clearly dominated the power content in the PSDs, at higher frequencies (above approximately 100 kHz), a $1/f^\beta$ relationship was observed. This finding, consistent with the work by Uribarri on the Princeton Benchmark Thruster, implies that the content at these higher frequencies is dominated by random processes.

Also, in Uribarri's examination of skewness and kurtosis statistics for his Princeton Benchmark Thruster voltage signals, he observed a trend of initially near-zero values, followed by an increasing value as current increased, and then subsequently values decreasing again toward zero (Gaussian) for J^2/\dot{m} above approximately 110 kA²/g [42]. We observed the similar trend of near-zero skewness and kurtosis values followed by an increase with increasing current, but we did not see a clear indication of reduced values at much higher currents. Uribarri argued that such a return toward Gaussian statistics in his data could be associated with an increase in the number (or frequency) of anode spotting events, which generate the voltage hash. Thus, eventually an overlapping of voltage spikes in time would result in a smoothing of the spikes in the voltage signal and a return toward a Gaussian distribution. However, key differences between our two thrusters could possibly be the cause of the observed difference. First, the anode material is stainless steel in our thruster. However,

the behavior seemed to be observed in Uribarri's data for copper, graphite, and lead anodes, suggesting some relative independence with anode material. In addition, our thruster and anode are much larger geometrically and operated at much lower flow rate and thus lower local plasma densities (as will be shown in Chapter 5) than the Princeton Benchmark Thruster. These factors, along with the extended axial length of the conductive anode surface bounding the regions of high magnetic field (unlike the ring-shaped anode of the Princeton Benchmark Thruster) could all factor into why we may observe a different set of statistics for the response of the voltage hash at higher currents due to anode spot formation.

The next step is to examine the thruster discharge properties in more detail with *in situ* probes. The behaviors reported in this chapter will be re-examined later in combination with what we learn from the magnetic and Langmuir probing experiments. Further interpretations will be discussed later in Chapter 6, including a connection between the reduced intensity and frequency of voltage fluctuations with the applied B fields and decreased anode spot damage.

Chapter 4

Magnetic Probing of Internal Magnetic Field Topology and Current Profiles

4.1 Operating Conditions and Thruster Configurations

A multiple-station magnetic probe array (MPA) with a series of B-dot coils was positioned to measure the azimuthal magnetic fields inside the thruster discharge chamber and the near-field plume regions. Each B-dot coil is an inductor that measures voltages induced by the time rate of change of the magnetic field penetrating the coil. This signal can be integrated in time to measure a signal proportional to the local magnetic field. The MPA was used during thruster firings to acquire data to reconstruct the topology of the magnetic fields and discharge currents in the thruster plasma. Section 2.6.3 describes the magnetic probe array and how it is used to measure magnetic fields *in situ*.

Data from the MPA along the near-anode region were obtained over a range of PFN voltages to span thruster current levels from 1.8 kA to 13.1 kA. As with the thruster voltage and current measurements, this broad range was selected to cover a wide set of operating conditions from well below onset to well above onset and examine whether there are any transitions or trends. Again, the flow rate was held constant at 1.0 g/s. This flow rate was chosen because it was sufficiently low to allow a range of J^2/\dot{m} values (approximately 4 to 172 kA²s/g) well above typical onset

values for other thrusters (e.g., beyond 80 to 110 kA²/g in the Princeton Benchmark Thruster [42]), yet still provided sufficient flow in our large thruster geometry for stable, repeatable operation. Configurations examined included no magnets (self-field operation), the applied tangential B field, and the applied cusp B field.

However, most of the measurements with the MPA were taken at a relatively high current of 10.7 kA, including all of the data at smaller radii in the interior (away from the anode). It is this larger set of data at this higher current that allows for the contour plots of magnetic fields and current streamlines in the thruster interior that are discussed later in Section 4.3. This high current is well in the onset regime, as evidenced by the large-magnitude terminal voltage fluctuations shown in Chapter 3. This discharge current value was chosen as a representative and repeatable condition for evaluation of the thruster properties nominally within onset, and, in particular, to observe key spatial variations in the thruster discharge between the self-field operation (no magnets) and the configurations with the tangential and cusp applied magnetic fields.

The time-varying signals from the probe's B-dot coils were integrated and then averaged over the thruster's quasi-steady time period, generally 0.8 to 1.8 ms after triggering the PFN discharge. These results were averaged over both time and across multiple shots at each operating condition to generate the means and estimate random uncertainties that are presented in the following sections. MPA measurements were obtained concurrently with the voltage and current measurements discussed in Chapter 3.

4.2 Collection of Data

During each thruster firing, all 15 stations of B-dot coils on the MPA were sampled simultaneously on a high-speed 14-bit DAQ at 2.5 megasamples per second per channel and saved via LabVIEW for post-processing analysis on a PC. Integration of the time-varying signals and calibration with

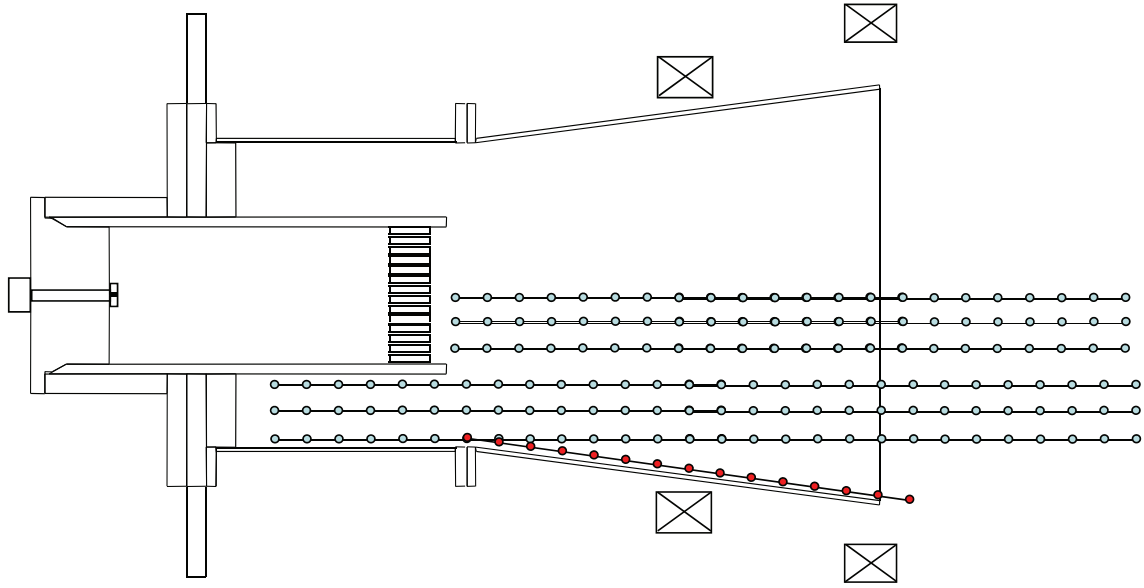


Figure 4.1: Positions of magnetic probe array coils for B field mapping measurements. The probe array position line for measurements along the anode flared section is highlighted in red.

a Helmholtz coil enabled calculation of the measured azimuthal B field at each coil position. The equations for the MPA B-dot coil signals are given in Section 2.6.3.

The MPA was positioned at different locations to obtain measurements throughout the plasma discharge region. All data while varying total thruster currents were obtained with the probe's long axis positioned along the anode flared section, 4-5 mm from the anode inner radius. This offset was dominated by the 4 mm radius of the probe's outer quartz tube. For the data taken at the constant higher current, the probe was moved and angled around the interior and near-field plume of the thruster using a three-axis positioning stage. Multiple shots were taken at each new probe position while conducting the interior spatial mapping. At each new probe position, all 15 stations of the probe array were measured during each shot. The position grid in Figure 4.1 shows the positions of the individual B-dot coils in the half-plane of the thruster used to construct the interior contour maps and near-anode profiles.

4.3 Analysis of Magnetic Fields and Current Patterns at High Discharge Current

We begin our examination of the MPA probe data with measurements taken at the high current conditions at approximately 10.7 kA. As shown in the previous chapter, the thruster is operating well within conditions associated with onset (large-amplitude voltage fluctuations at high frequency) at this relatively high thruster discharge current. Figures 4.2, 4.3, and 4.4 show shaded contour plots of the azimuthal B field generated during the thruster firing for the configurations with no magnets (self-field), tangential applied B field, and cusp applied B field, respectively. These contour plots show azimuthal B field in units of Gauss, as specified in the color bar legend. The contour plots are drawn such that the vertical axis shows radial position with the bottom of the vertical axis at the thruster centerline ($r = 0$), and the horizontal axis is the axial position measured relative to the anode exit plane ($x = 0$). The cathode body is in the lower left side of the plots, with the cathode exit plane at $x = -270$ mm. The anode inner radius is shown on the top side of the figures.

As expected, the magnetic field generally increases as we traverse further upstream in the thruster. We also see a dip in the contours radially inward just downstream of the cathode face. As will be shown later, these effects are due to the increasing enclosed current in the upstream axial direction deeper inside the thruster discharge and the electromagnetic radial pinch on the plasma in front of the cathode. Relative to the self-field case, the tangential and cusp applied B fields result in azimuthal B field contours that extend further downstream. Also, the tangential applied B field case shows a clear compression and shift of the B field contours in the near-anode region to a more central location along the anode wall. This results in a steeper gradient in azimuthal B field in the central near-anode region for the tangential applied B field case. These azimuthal magnetic field results can be compared to the poloidal magnetic fields produced by the magnets, as were shown

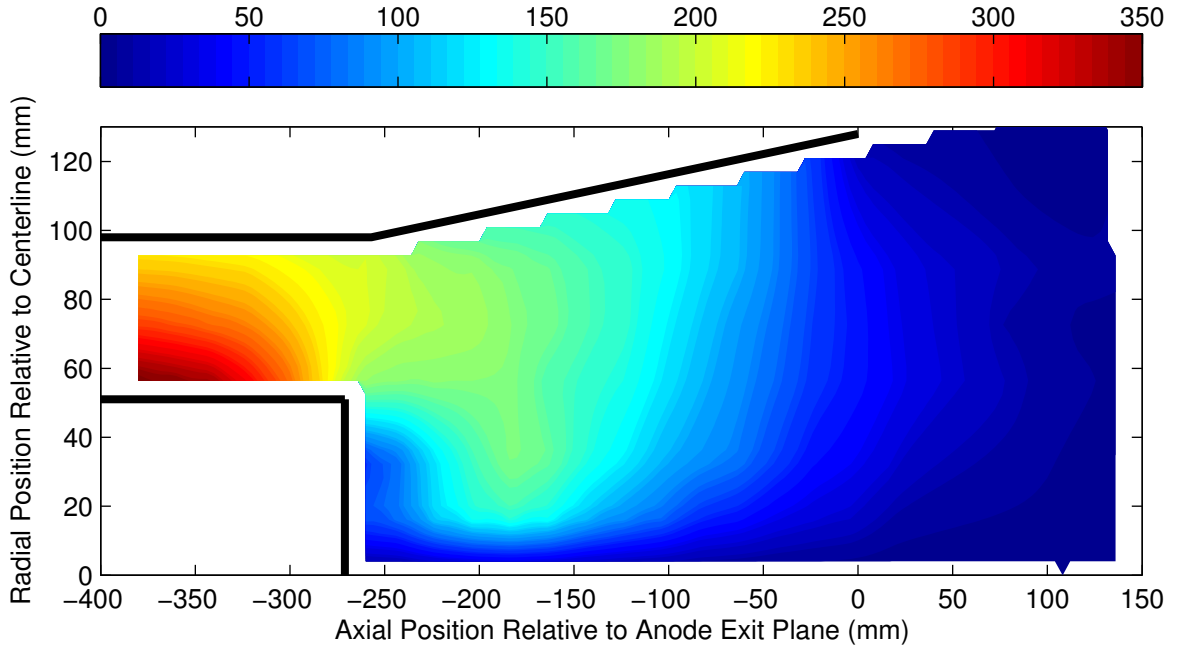


Figure 4.2: Contour plot of azimuthal B field without magnets at 10.7 kA. Contour values are in Gauss.

earlier in Figures 2.6 and 2.7.

To provide further insights into the structure of the MPD current discharge, the azimuthal B field measurements can be used to calculate the enclosed current and current streamlines. To obtain the enclosed current, J_{enc} , from our azimuthal B field measurements, we use the pre-Maxwell equation for Ampere's Law (where we can ignore the time-varying term for slow, low-frequency phenomena in our thruster):

$$\nabla \times \mathbf{B} = \mu_0 \mathbf{j} \quad (4.1)$$

where \mathbf{B} is the magnetic field vector, μ_0 is the permeability of vacuum, and \mathbf{j} is the current density vector. By integrating both sides over a bounded surface of constant radius about the centerline and invoking Stokes' theorem, the right-hand side of the equation becomes proportional to the total enclosed current crossing the surface. The left-hand side of the equation becomes a line integral over the surface boundary's constant radius. By invoking the assumption of azimuthal symmetry,

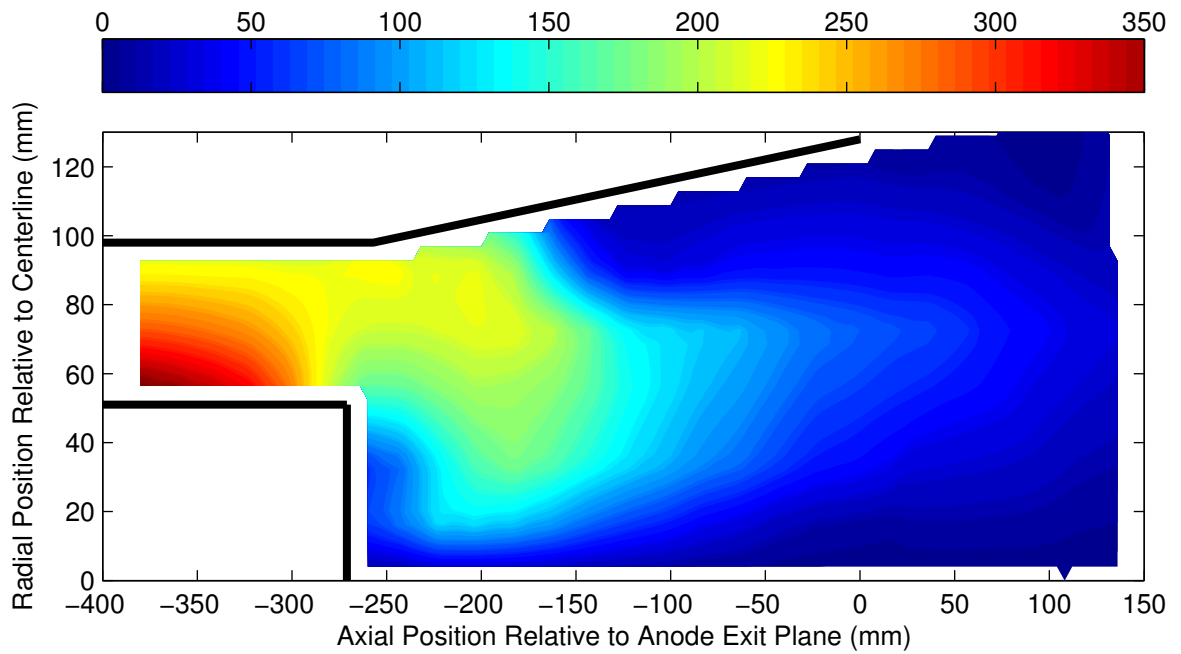


Figure 4.3: Contour plot of azimuthal B field for tangential applied B field configuration at 10.7 kA. Contour values are in Gauss.

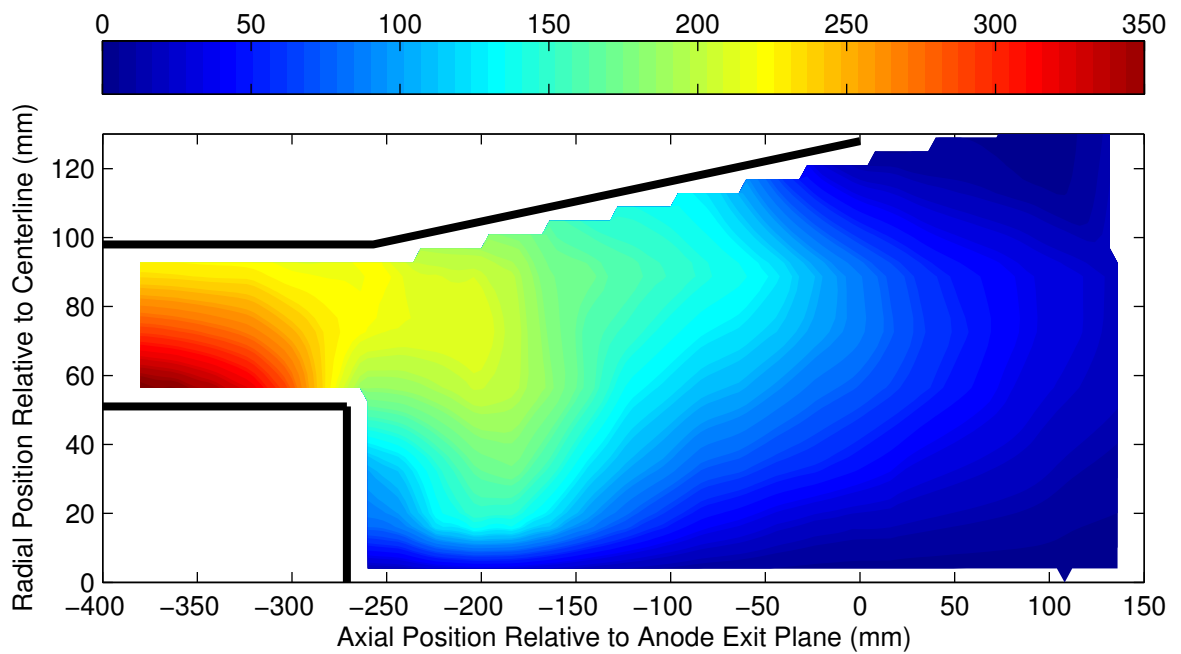


Figure 4.4: Contour plot of azimuthal B field for cusp applied B field configuration at 10.7 kA. Contour values are in Gauss.

we obtain a line integral over constant azimuthal B field over a path length of $2\pi r$, which yields:

$$J_{enc} = \frac{2\pi r B_{\theta}}{\mu_0} \quad (4.2)$$

where J_{enc} is the poloidal current enclosed by the contour, r is the radius, and B_{θ} is the azimuthal magnetic field component.

Figures 4.5, 4.6, and 4.8 show contour plots of the enclosed current fraction for the configurations with no magnets, tangential applied B field, and cusp applied B field, respectively. The contour lines are shown for constant specified values (0.1, 0.2, ..., 0.9) of the fraction of the total discharge current for the thruster firing at approximately 10.7 kA. Thus, these lines represent the current streamlines in the thruster. In all three configurations, we observe a shift toward the centerline of the current streamlines just in front of the cathode due to the electromagnetic forces causing a radial pinch inward. The radial pumping forces are a consequence of the magnetic force densities having a significant radial component. The magnetic force densities associated with the poloidal current pattern are calculated and shown in Appendix A for all three magnetic configurations. Also, note that the fact that the enclosed current values are still slightly positive at the anode exit plane ($x=0$) and go to zero just slightly downstream of the anode exit implies that the current attachment pattern likely has a small amount of current that loops outside of the anode exit plane to attach along the anode front face and the 10–15 mm wide exposed strip on the anode exterior not covered by the insulating Kapton.

In Figure 4.5 for the self-field case, we observe the current streamlines attach broadly across most of the anode surface. There is small compression in the current streamlines along the anode lip near the anode exit plane, which is an expected consequence of the convection of the current streamlines downstream due to the flowing plasma.

In Figure 4.6, the current streamlines exhibit a marked shift due to the tangential applied B field. Figure 4.7 shows the same contour plot with an overlay of the tangential applied B field lines. The current streamlines are convected further downstream in the interior of the thruster. Most strikingly, the current conduction and attachment are clearly shifted upstream to strong concentration at a more central location along the anode. The current streamlines are convected downstream and then curve back significantly upstream to the central anode region near axial positions $z = -140$ mm to $z = -200$ mm. These streamlines follow along the curvature of the applied B field lines at higher radial positions, where the B field lines turn radially toward the anode. The B field lines intersect the anode in this region further upstream from the anode exit. Downstream near the anode lip, the tangential applied B field lines were designed to be near-parallel to the anode. In this downstream region, the current pattern follows the mostly axial applied B field lines, preventing any significant attachment in this region.

The cusp applied B field case shown in Figure 4.8 exhibits a behavior more similar to the self-field case. Figure 4.9 shows the same contour plot with an overlay of the cusp applied B field lines. Again, there is a convection of the current streamlines further downstream than without the magnets, and the current streamlines turn more sharply back upstream to attach along the anode. The current streamlines near the anode follow along the cusp applied B field lines and attach downstream along where the cusp radial B field lines intersect the anode.

Next, we examine in more detail the data as profiles along the near-anode region to reveal insights on the current conduction to the anode. Figure 4.10 shows profiles of the azimuthal B field near the anode versus axial position for the thruster firing at approximately 10.7 kA in all three magnetic configurations. Figure 4.11 shows the same profiles for the enclosed current fraction calculated from the azimuthal B field profile, accounting for the varying radius along the anode surface in the flared section. The error bars represent the uncertainties in the mean measurements,

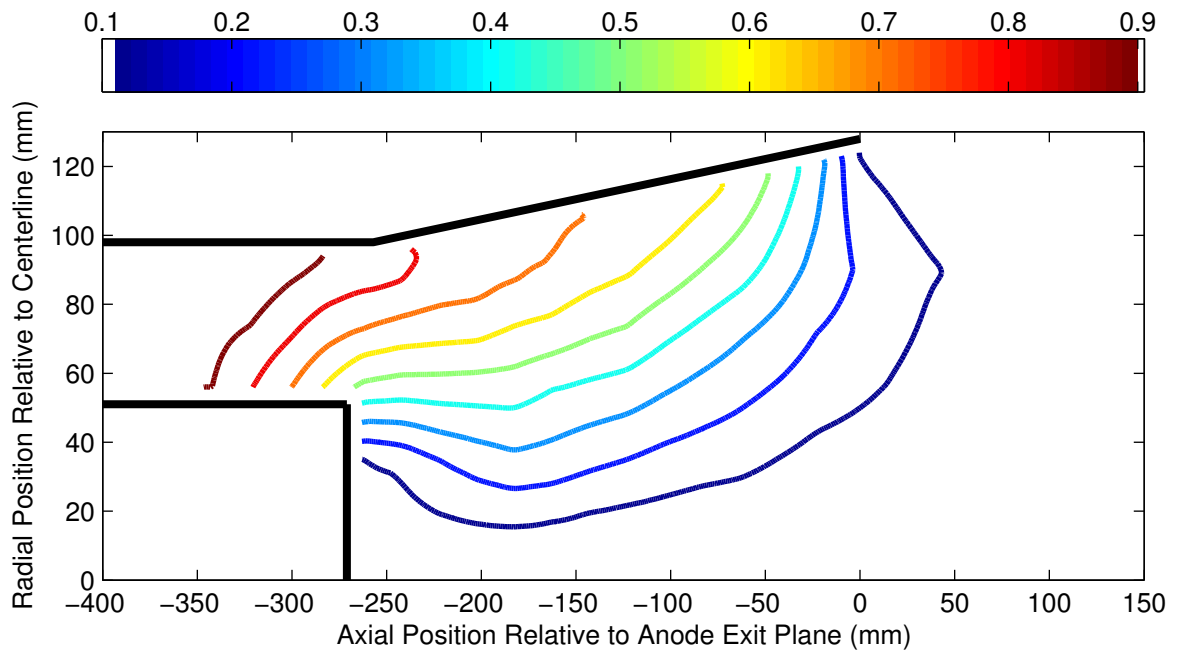


Figure 4.5: Contour plot of enclosed current fraction without magnets at 10.7 kA. Contours are shown at (0.1, 0.2, ..., 0.9) of total enclosed current.

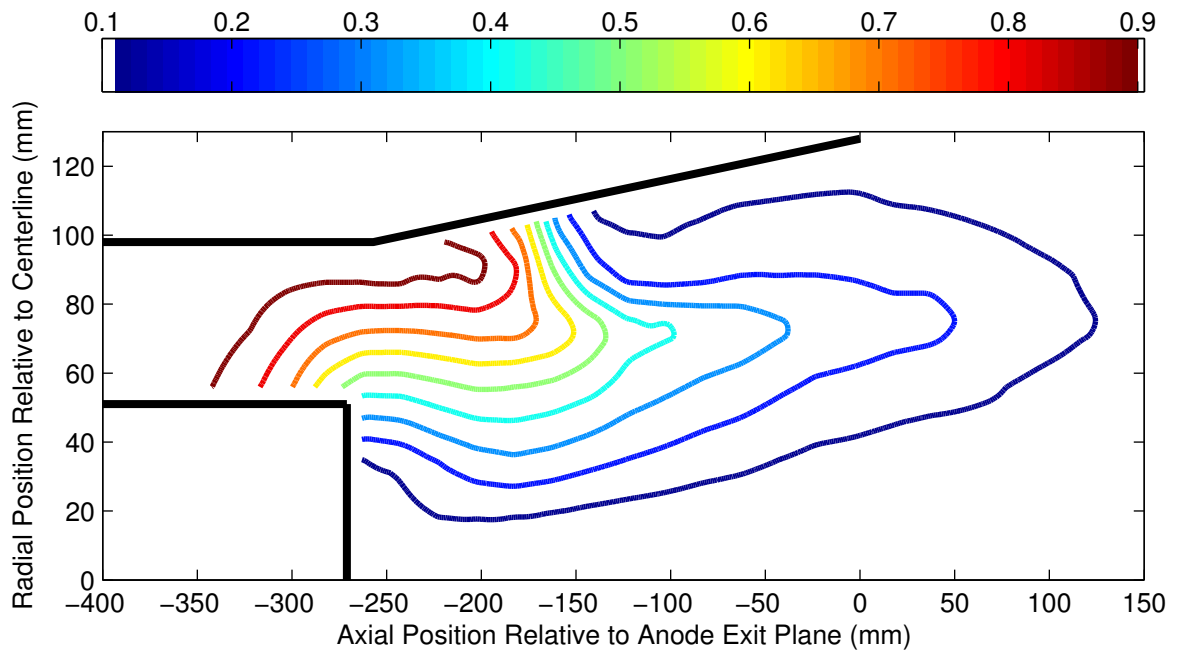


Figure 4.6: Contour plot of enclosed current fraction for tangential applied B field configuration at 10.7 kA. Contours are shown at (0.1, 0.2, ..., 0.9) of total enclosed current.

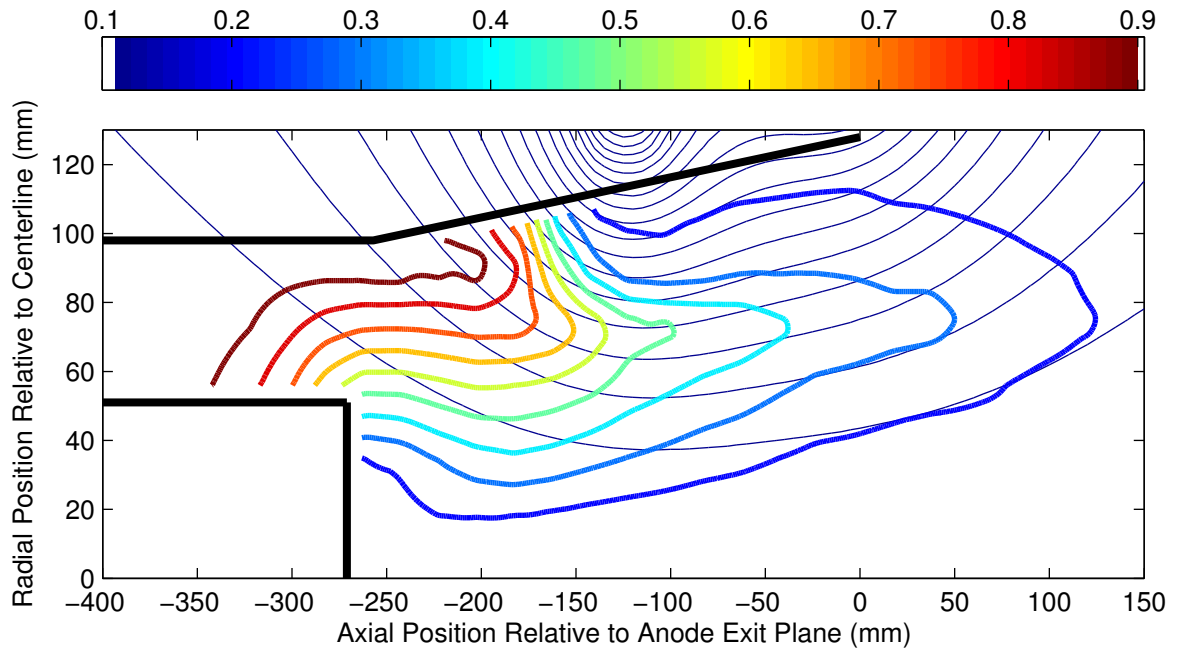


Figure 4.7: Contour plot of enclosed current fraction for tangential applied B field configuration at 10.7 kA. Applied B field lines are also shown. Contours are shown at (0.1, 0.2, ..., 0.9) of total enclosed current.

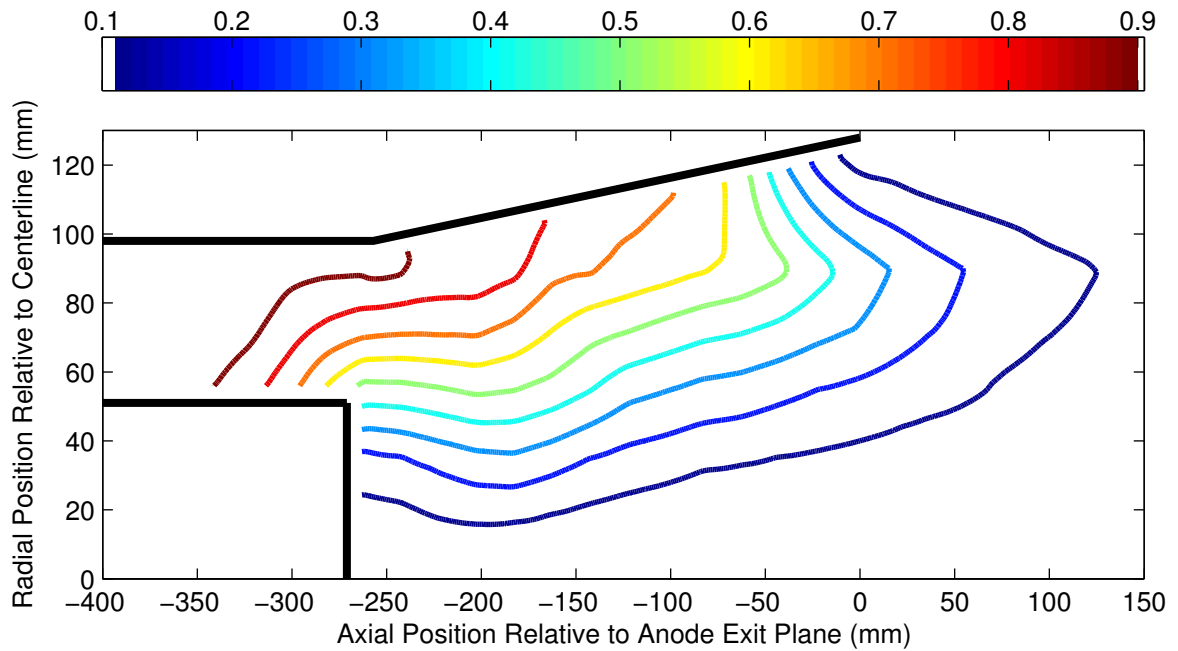


Figure 4.8: Contour plot of enclosed current fraction for cusp applied B field configuration at 10.7 kA. Contours are shown at (0.1, 0.2, ..., 0.9) of total enclosed current.

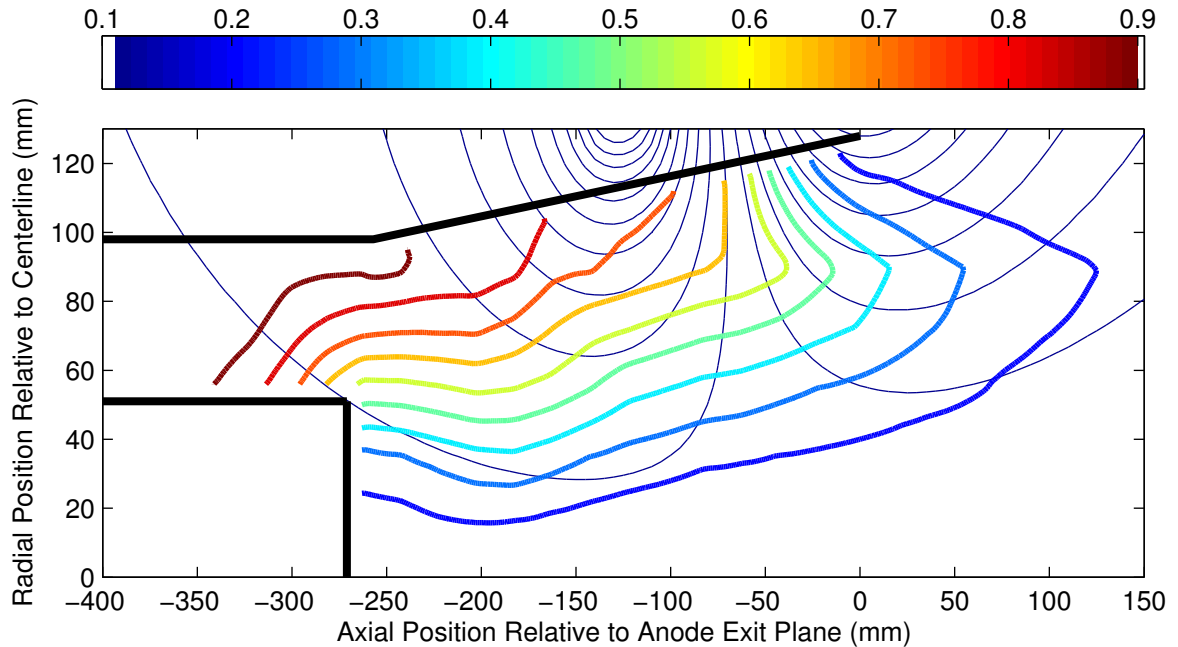


Figure 4.9: Contour plot of enclosed current fraction for cusp applied B field configuration at 10.7 kA. Applied B field lines are also shown. Contours are shown at (0.1, 0.2, ..., 0.9) of total enclosed current.

which are dominated primarily by the shot-to-shot variation over multiple thruster firings. The curve fit for each configuration was generated as a least-squares piecewise cubic spline fit. To match the appropriate physical constraint that the enclosed current along the anode must be a monotonically decreasing function with increasing distance downstream, a constraint was included to enforce a monotonically decreasing functional form to the entire curve fit.

Figure 4.11 shows that the regions of steepest gradients in enclosed current are shifted between the three applied B field configurations. There are significant differences between the three cases, and these gradients in enclosed current will be used next to calculate the current densities along the anode.

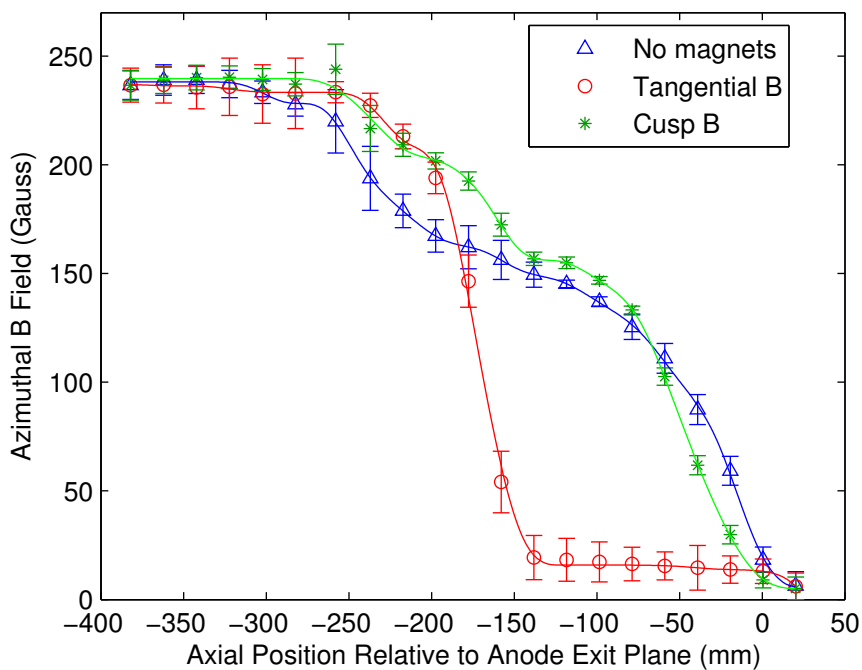


Figure 4.10: Profiles of azimuthal B field near the anode vs. axial position at 10.7 kA. All 3 magnetic configurations are shown for comparison.

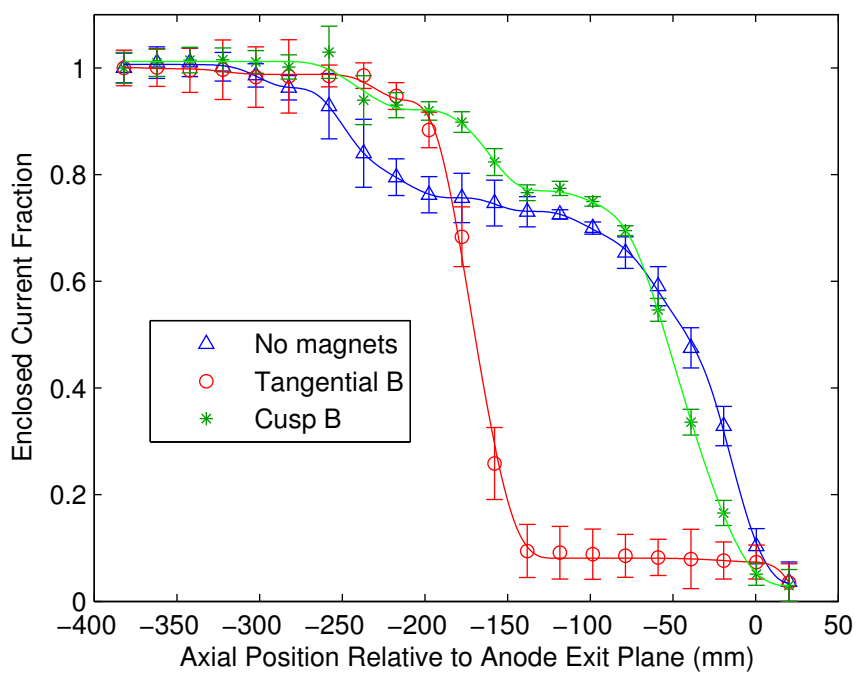


Figure 4.11: Profiles of enclosed current fraction along the anode vs. axial position at 10.7 kA. All 3 magnetic configurations are shown for comparison.

4.4 Analysis of Current Densities at High Discharge Current

To examine the implications of these large gradients in enclosed current and identify regions of highest current attachment, we next calculate the current densities along the same anode profile. To obtain the current density along the anode, we note that all changes in enclosed current axially along the anode must be the result of current conduction to the anode wall. Thus, we easily obtain an expression for the radial current density along the anode by considering the change in enclosed current, dJ_{enc} , across an infinitesimally small ring of the anode surface of azimuthal span $2\pi r$ and axial extent dz as

$$j_r = -\frac{1}{2\pi r} \frac{\partial J_{enc}}{\partial z} \quad (4.3)$$

where j_r is the radial current density and r is the radius along the anode.

Figure 4.12 shows the profiles of current densities along the anode versus axial position, as calculated from the enclosed current data for the multiple magnetic configurations again at approximately 10.7 kA. Here, the error bars represent the uncertainties calculated from multiple curve fits of enclosed current obtained for multiple repeat shots. The error bars for the current densities again represent uncertainties dominated by the shot-to-shot variability of the enclosed current gradients. These profiles of current densities provide the clearest indication of where the current attachment is concentrating along the anode.

The current density for the self-field case peaks primarily downstream along the anode lip, close to the anode exit plane. There is some modest additional rise in current density further upstream, peaking again near $x = -260$ mm. The cusp applied B field case exhibits a modest shift upstream of the peak current density by approximately 15-20 mm, shifting to the region of the anode-intersecting cusp B field. As seen in the previous data, the tangential applied B field case results in a marked shift upstream, where the current density peaks strongly in the central anode region where the magnetic

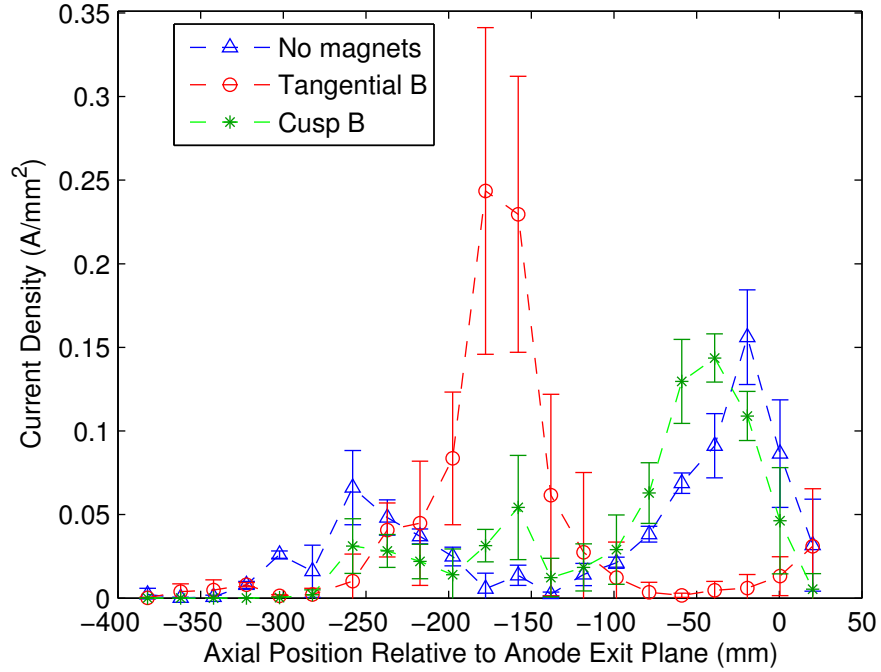


Figure 4.12: Profiles of current density along the anode vs. axial position at 10.7 kA. All 3 magnetic configurations are shown for comparison.

field lines begin to turn radially outward and intersect the anode.

We can also look generally at the poloidal current densities throughout the thruster plasma discharge by simply examining the radial component j_r and axial component j_z of equation 4.1. We use the gradients of our azimuthal magnetic field measurements in cylindrical coordinates to calculate

$$j_r = -\frac{1}{\mu_0} \frac{\partial B_\theta}{\partial z} \quad (4.4)$$

$$j_z = \frac{1}{\mu_0} \frac{1}{r} \frac{\partial}{\partial r} (r B_\theta) = \frac{1}{\mu_0} \left(\frac{B_\theta}{r} + \frac{\partial B_\theta}{\partial r} \right) \quad (4.5)$$

Figures 4.13 through 4.21 show shaded contour plots of the radial, axial, and total magnitude of poloidal current densities generated during the thruster firing for the various applied B field configurations. These contour plots show current densities in units of A/mm^2 , as specified in the color bar legend, and are drawn with the same position axes as the previous contour plots. Note that

the color bar scales differ on all plots (based upon the range of values in each case), and the values change polarity over the range of negative to positive values for the plots of radial and axial current densities.

Without the magnets, we can clearly see the regions of high outward radial current densities near the cathode outer radius and downstream near the anode lip, where Figure 4.12 previously showed a clear a peak in the current density along the anode. We also observe high inward radial current densities and high axial current densities directly in front of the cathode, where the plasma pinches toward the centerline under the radial electromagnetic pinching forces.

The contour plots for the tangential applied B field case exhibit similarly high current densities near the cathode and centerline. In addition, as expected from the regions of high current density along the anode in Figure 4.12, we observe a region of high outward radial current density upstream in the mid-anode region. This configuration also exhibits a strong axial current density in the upstream direction circa radial position $r = 80$ mm, where the current streamlines are pulled back toward the upstream anode attachment region.

With the cusp applied B field, we again observe the high current densities near the cathode and centerline. Further, high outward radial current densities are seen downstream on the anode in the region where the cusp applied B field lines intersect the anode. Also, we can see a region in the interior of the thruster centered around axial position $z = -150$ mm with relatively high outward radial current densities that extends from the centerline region outward toward the anode near $z = -170$ mm. In addition, we observe a region near the anode lip with relatively high axial current densities in the upstream direction, where the current streamlines are returning toward the anode.

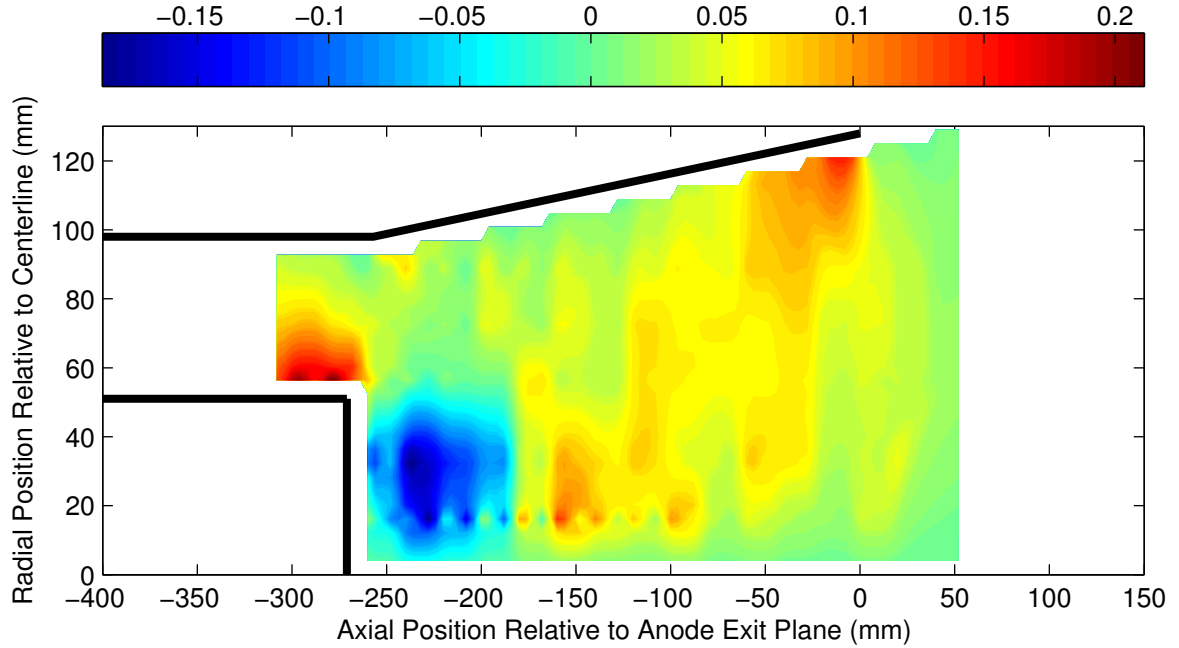


Figure 4.13: Contour plot of radial current density at 10.7 kA for the configuration without magnets.

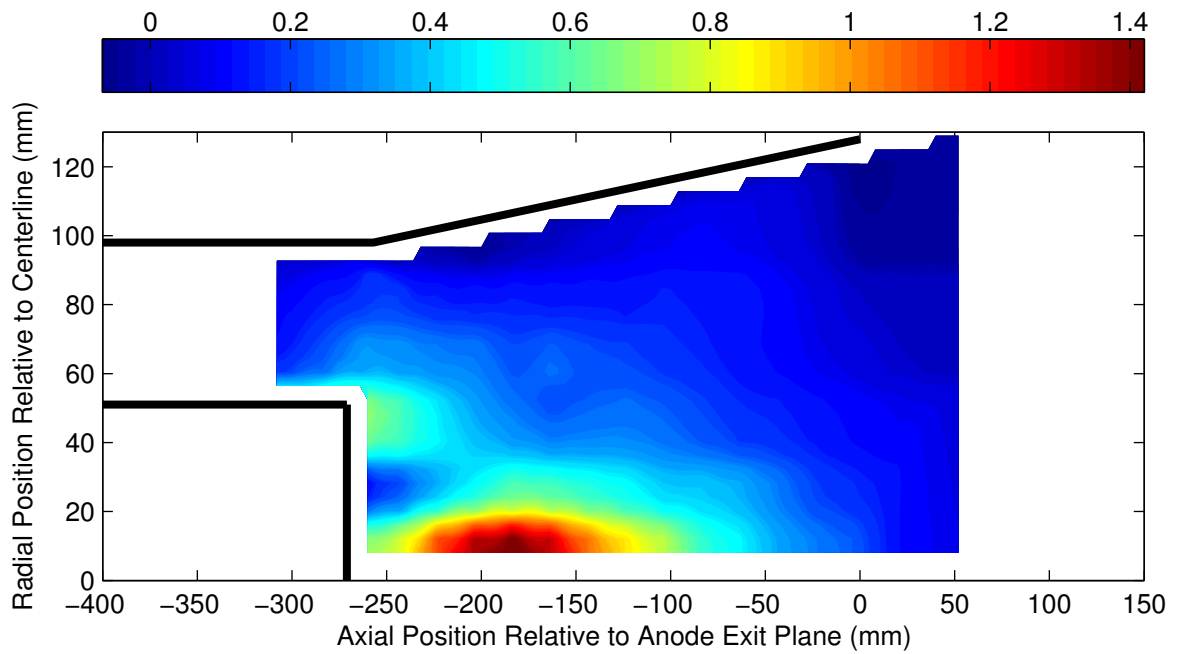


Figure 4.14: Contour plot of axial current density at 10.7 kA for the configuration without magnets.

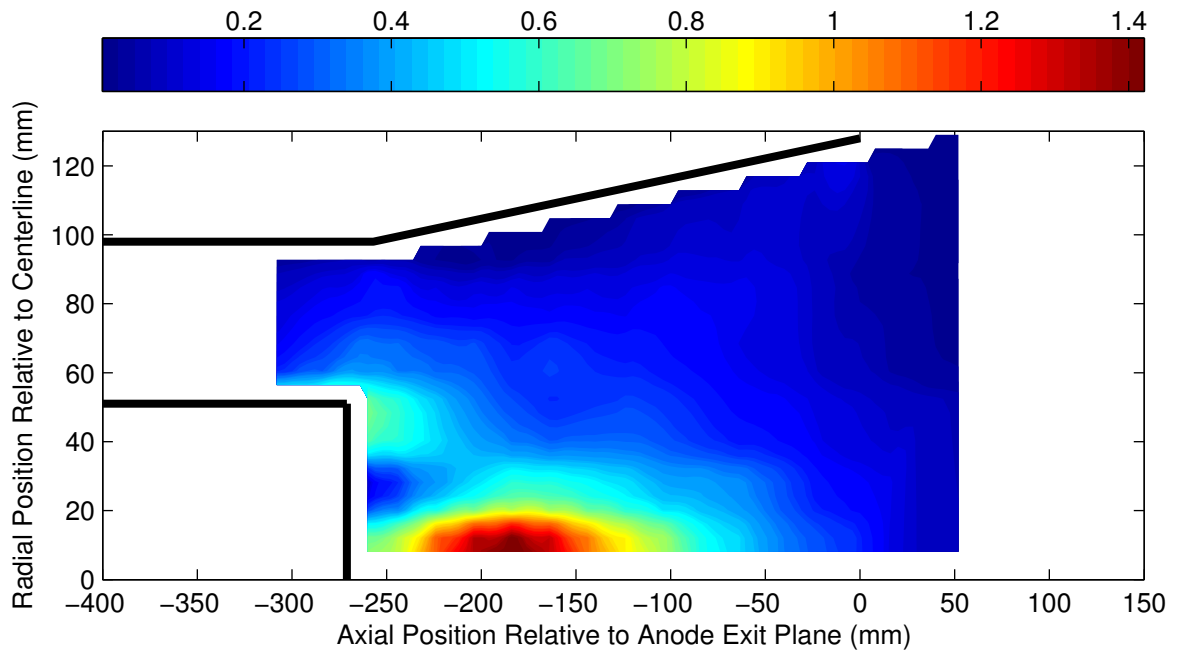


Figure 4.15: Contour plot of total magnitude of poloidal current current density at 10.7 kA for the configuration without magnets.

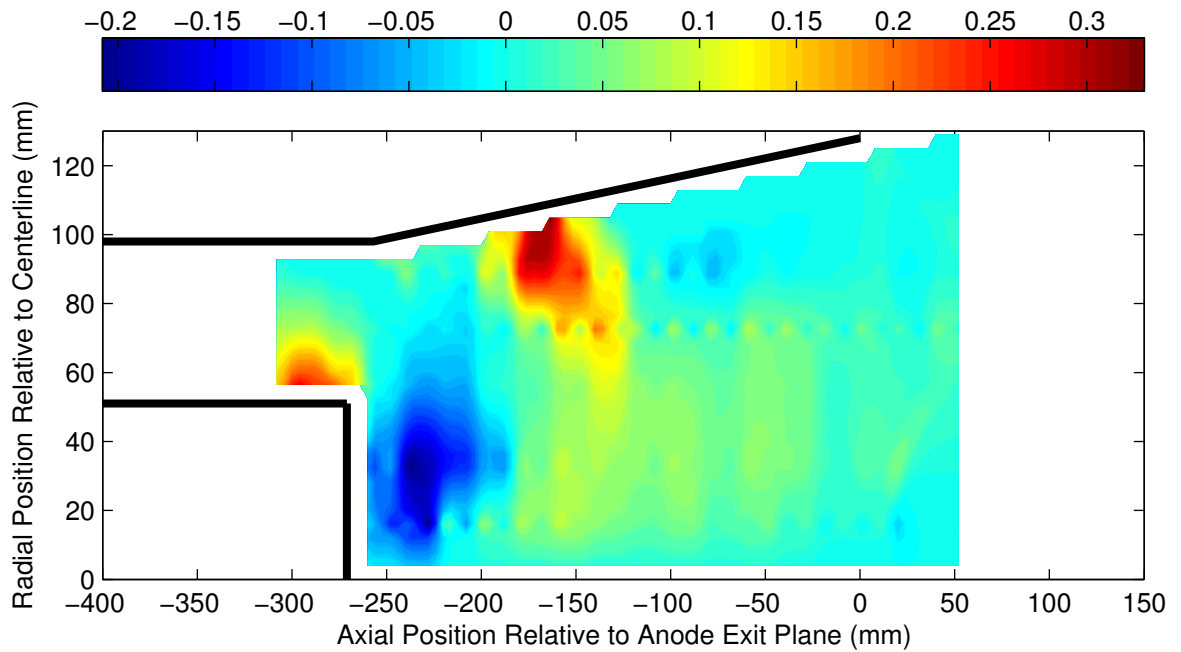


Figure 4.16: Contour plot of radial current density at 10.7 kA for the configuration with tangential applied B field.

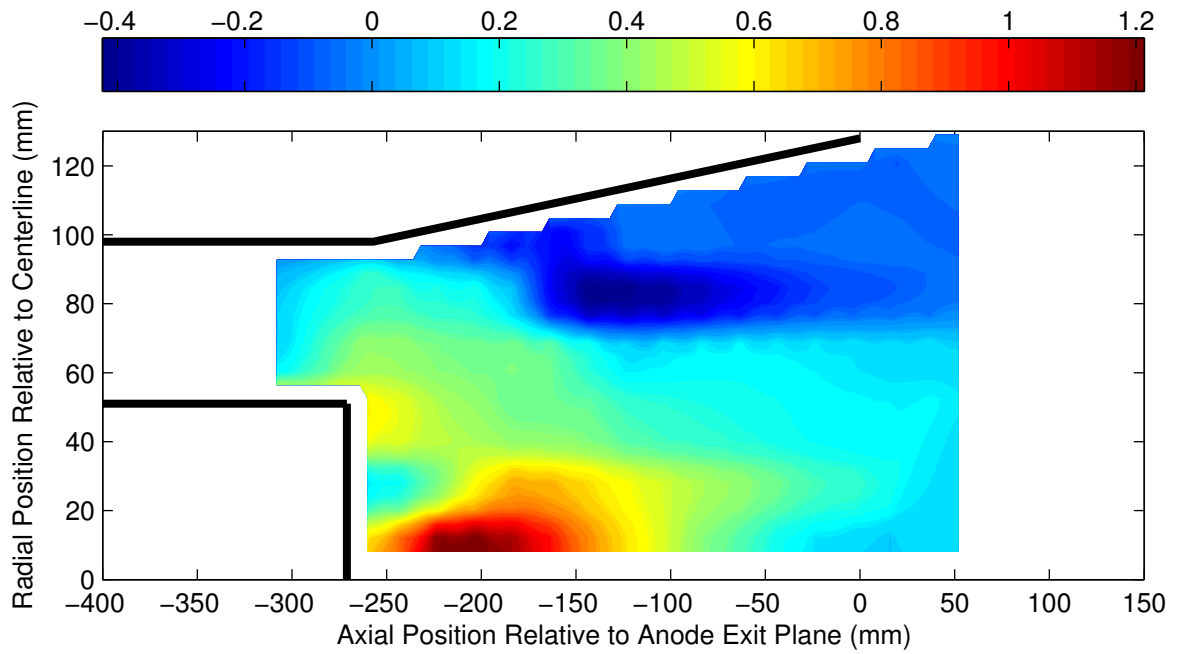


Figure 4.17: Contour plot of axial current density at 10.7 kA for the configuration with tangential applied B field.

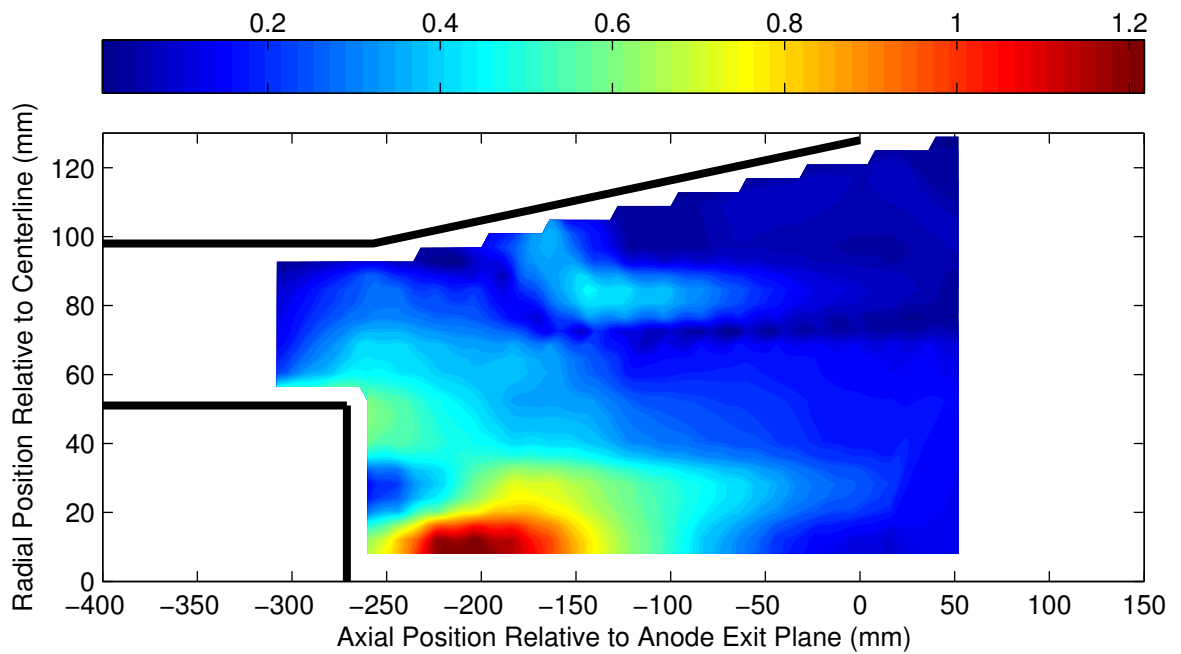


Figure 4.18: Contour plot of total magnitude of poloidal current density at 10.7 kA for the configuration with tangential applied B field.

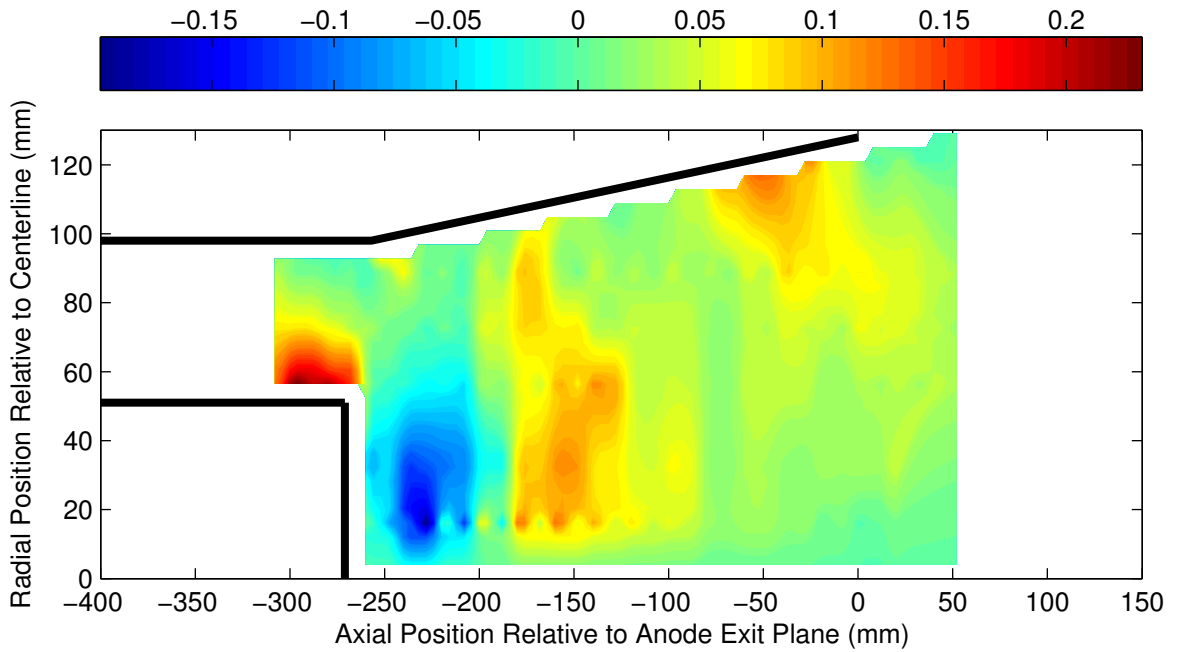


Figure 4.19: Contour plot of radial current density at 10.7 kA for the configuration with cusp applied B field.

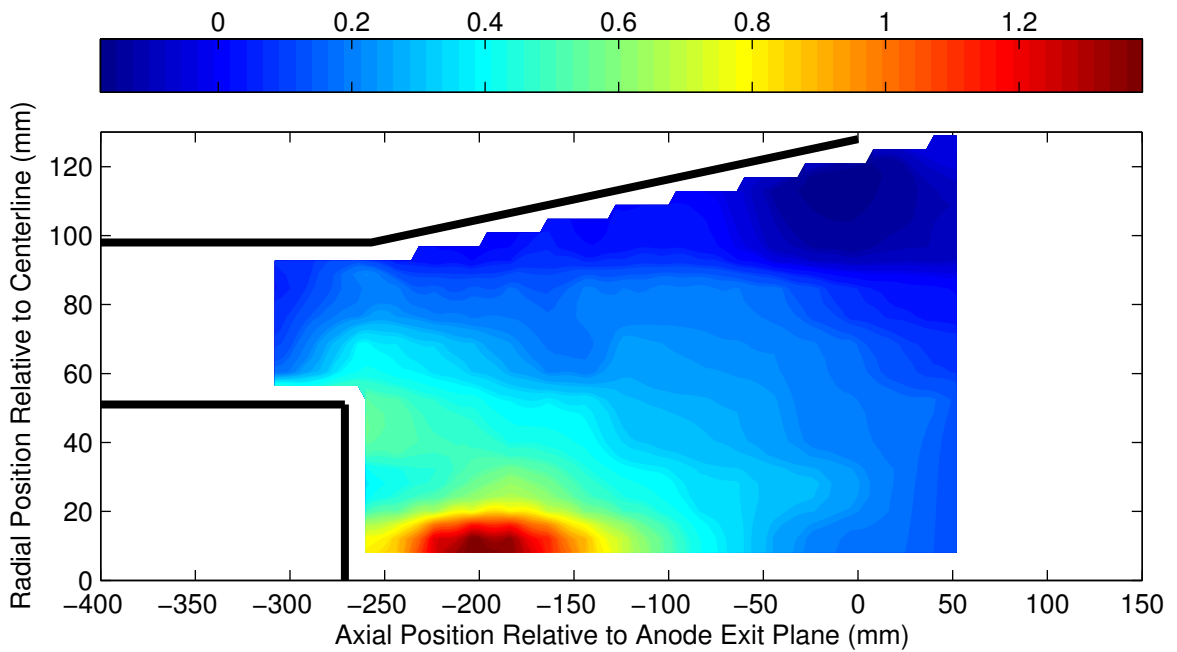


Figure 4.20: Contour plot of axial current density at 10.7 kA for the configuration with cusp applied B field.

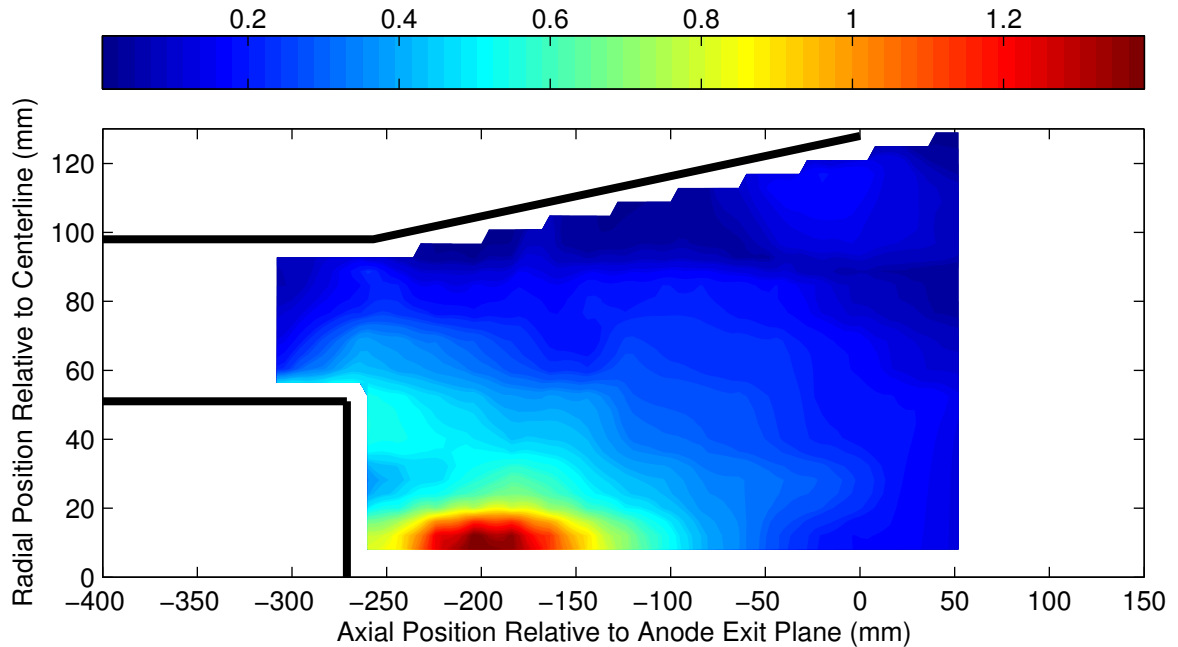


Figure 4.21: Contour plot of total magnitude of poloidal current density at 10.7 kA for the configuration with cusp applied B field.

4.5 Analysis of Current Densities Along the Anode Over a Range of Discharge Currents

Next, we examine the effect of increasing thruster discharge current on the current densities along the anode. Figures 4.22, 4.23, and 4.24 show the current density profiles over a range of thruster operating currents for the self-field, tangential B field, and cusp B field configurations, respectively. Note that these profiles only span the axial range along the flared section of the anode and do not extend as far upstream in the thruster as the previous profiles shown only at 10.7 kA. However, this region contains most of the enclosed current and highlights the areas of highest current densities.

In each configuration, we observe that the general functional form of the current density profile is preserved over the range of currents. Overall, increasing thruster current results in increasing the magnitudes of the local current densities. Without the magnets, the peak current densities are again observed well downstream near the anode exit plane, with some additional significant conduction

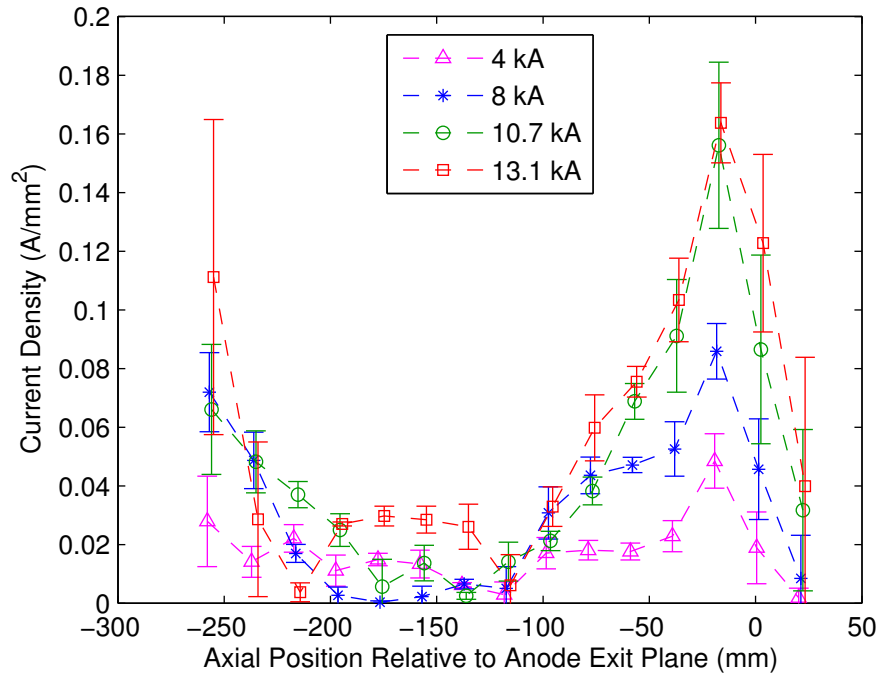


Figure 4.22: Profiles of current density along the anode vs. axial position over a range of thruster currents for the configuration without magnets.

upstream near the transition from the flared section to the straight anode section ($x = -257$ mm) just slightly downstream of the cathode exit plane. The tangential applied B field yields a significant peak in the current density further upstream along the anode. The axial location of this peak moves downstream as current is increased. The cusp applied B field case shows highest current densities in the downstream region where the cusp field lines intersect the anode surface downstream. Again, we observe a modest shift downstream of the axial location of the current density peak as thruster current increases. Also, both applied B field cases exhibit a modest axial broadening of the region of highest current density with increasing thruster current. The effect of the current density peaks shifting axially downstream and broadening with increasing discharge current is likely due to the increased convection of the current streamlines further downstream in the thruster exhaust plume.

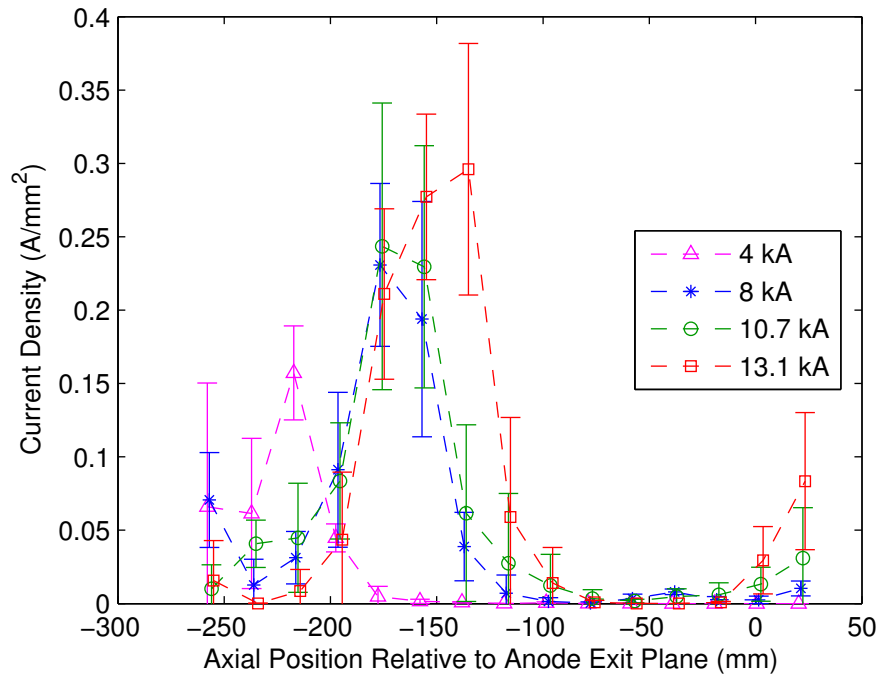


Figure 4.23: Profiles of current density along the anode vs. axial position over a range of thruster currents for the configuration with tangential applied B field.

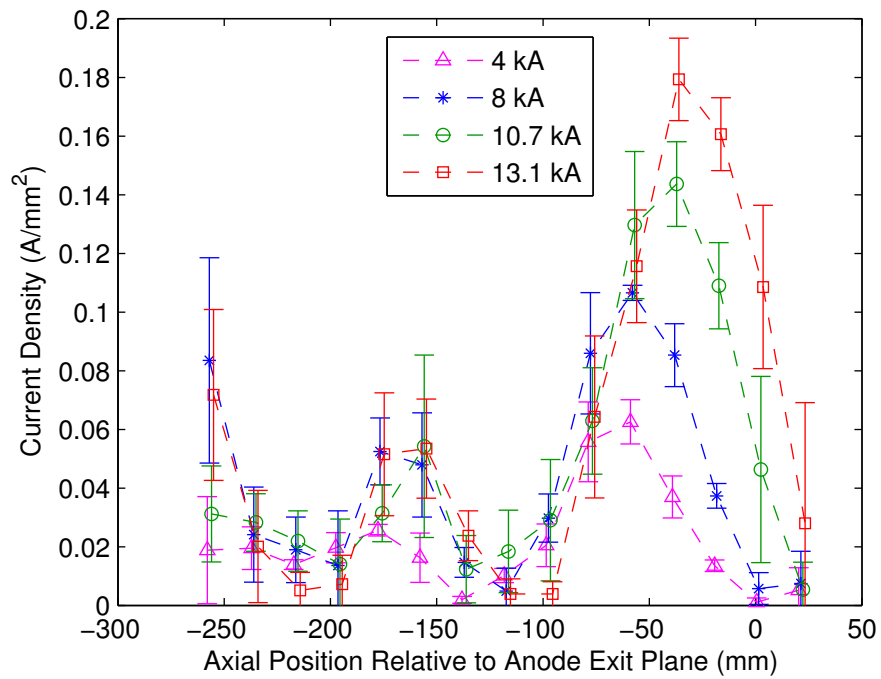


Figure 4.24: Profiles of current density along the anode vs. axial position over a range of thruster currents for the configuration with cusp applied B field.

4.6 Summary of Results

In this chapter, we reviewed the results of the magnetic probing inside the thruster's inter-electrode discharge region and near-field plume. These data were used to create maps of the azimuthal magnetic field generated by the thruster discharge and poloidal current streamlines with the thruster operating near 10.7 kA without magnets, with applied tangential B field, and with applied cusp B field. Current densities were calculated in the thruster interior and along the anode for this high current condition. Current densities along the anode were also examined over a range of currents from 4 kA to 13.1 kA. The following interesting results were identified:

The applied-field magnets caused a clear shift in the current pattern and modified the anode attachment region. All configurations, including self-field, exhibited the expected convection of the current streamlines downstream in the thruster. Current streamlines are blown downstream and extend past the anode exit plane before they turn back upstream at increasing radii to attach to the anode surface. We also observe the expected radial pinching forces resulting in a radial compression of the plasma and current streamlines in front of the cathode, where radial $\mathbf{j} \times \mathbf{B}$ forces are high. However, use of the externally applied magnetic fields results in marked differences in the current pattern. The current streamlines follow the applied B field lines in the near-anode attachment region. The tangential B field causes the current streamlines to shift significantly upstream to follow along where the applied magnetic field lines begin to turn radially outward toward the anode. The applied B field prevents any significant attachment in the downstream region where the applied B field lines are contoured parallel to the anode. The cusp applied B field case exhibits a more subtle but still evident shift in the current streamlines to follow along the cusp field lines near the anode. In addition, both applied B field cases exhibit an extension of their current streamlines somewhat further downstream in the near-field plume of the thruster. This increased downstream

convection is likely due to an increased magnetic Reynolds number for these configurations. The magnetic Reynolds number, Re_m , is given by [71]

$$Re_m = \frac{uL}{\eta_m} \quad (4.6)$$

where u is the flow velocity, L is the characteristic length scale, and η_m is the magnetic diffusivity given by

$$\eta_m = \frac{1}{\mu_0\sigma_0} \quad (4.7)$$

where μ_0 is the permeability of free space and σ_0 is the electrical conductivity. For higher Re_m , magnetic field flux lines are more strongly convected with the plasma flow. The applied magnetic fields are expected to increase acceleration, thus increasing u , and the electrical conductivity is increased in the directions parallel to the applied magnetic field. Both of these effects increase the magnetic Reynolds number and thus extend the convection of azimuthal magnetic field and enclosed current downstream.

The modified current patterns due to the applied magnetic fields result in related shifts in the regions of high current densities along the anode, and the current attachment pattern clearly follows the applied B field lines near the anode. The self-field configuration exhibits highest radial current densities along the anode lip near the anode exit plane, with some additional significant current attachment upstream at the base of the anode flared section. The tangential applied B field causes a shift in the concentration of current density well upstream along the anode flared section to where the radial curvature of the applied B field lines begins to intersect the anode surface. This concentration results in higher peak current densities than without magnets, but reduces the current attachment in the downstream anode lip region to negligibly small levels. The cusp applied B field results in a shift of the current density peak region to slightly upstream of

the self-field case. Cusp configuration anode current density is slightly broadened and relocated to where the cusp applied B field lines are strongly intersecting the anode. These shifts in the regions of highest current densities are influenced by the shape of the poloidal applied B field lines, effectively resulting from the higher conduction along the direction parallel to the applied B field than conduction perpendicular to the B field. This effect will be discussed further in Section 6.1 and is particularly important in the near-anode region, where the applied B field magnitudes are higher and the ratio of the applied B field to the self-generated azimuthal B field is also increased.

Regions of high current densities can be clearly identified in the interior of the thruster discharge. We observe regions of high current densities in the inter-electrode discharge volume. All operating configurations exhibited high current densities around the downstream perimeter and in front of the cathode. High axial current densities were also observed along the thruster centerline, where electromagnetic pinching forces compress the plasma and current streamlines. Additionally, near the regions of high radial current density identified along the anode, we can see regions of high current densities that extend into the interior of the discharge, following along the enclosed current streamlines. For each configuration, this results in relatively high axial current densities pointed in the upstream direction near regions just downstream of where the peak current densities occur along the anode. In the cusp applied B field configuration, we also see a region near axial position $z = -150$ mm of relatively high outward radial current density that extends from the centerline region outward toward the anode near $z = -170$ mm.

Over a broad range of thruster currents, the current densities along the anode for each fixed applied-field configuration follow a similar functional form, with modest shifts downstream of the peak current densities with increasing thruster current. Measurements of current densities along the anode were made over the range of 4 kA to 13.1 kA average thruster discharge currents. These results identified that, for a given magnetic configuration, a similar form to the

current density profile along the anode was observed over the range of thruster currents, albeit with increasing magnitudes as thruster current increased. As thruster current increased, the applied B field configurations also exhibited a small shift axially downstream and a modest axial broadening for the region of highest current density along the anode. These effects with the applied magnetic fields are likely caused by increased downstream convection of the current streamlines as thruster discharge current is increased. Again, the magnetic Reynolds number would increase as flow velocity u is increased with higher discharge current.

In Chapter 6, we will examine these effects in more detail to consider the underlying causes.

Chapter 5

Langmuir Probe Measurements of Plasma Properties and Potential

5.1 Operating Conditions and Thruster Configurations

A new triple Langmuir probe was developed for local measurements at selected locations in the thruster of key plasma properties, namely the electron temperature (T_e), electron number density (n_e), and the anode fall voltage measured from the plasma potential ($V_{fall} = V_{anode} - V_{plasma}$). The focus of most measurements was the near-anode region, particularly in the regions of highest current densities calculated from the previous magnetic probe measurements. Section 2.6.4 described the Langmuir probe apparatus and the equations for calculating the plasma properties.

Measurements with the triple Langmuir probe were obtained at specific thruster discharge current levels at 8 kA and 10.7 kA, with most data at the higher 10.7 kA current. Operation at 10.7 kA was selected to examine properties well into onset conditions (as evidenced earlier in Chapter 3 on terminal voltage signal analyses) and allow comparison with the bulk of the magnetic probe data and current profiles obtained at this same current. Additionally, operation at 8 kA was conducted at two locations near the anode where the current densities were found to be highest to examine any relative differences at this more moderate, intermediate current where the thruster was shown to just begin transition to the early effects of onset. Mass flow rate was again held constant at 1.0 g/s

for consistency with previous measurements. To again examine the effects of the applied magnetic fields, triple probe measurements were obtained with all three magnetic configurations: no magnets (self-field operation), applied tangential B field, and applied cusp B field.

For each thruster firing, the Langmuir probe's time-varying signals were averaged over the thruster's quasi-steady time period, generally 0.8–1.8 ms after triggering the PFN discharge. These results were averaged over both time and across multiple shots at each operating condition to generate the means and propagate appropriate statistical uncertainties.

A single Langmuir probe was also used briefly in earlier testing at discharge currents up to 9 kA. The single probe measurements were limited to self-field operation and will only be used selectively later in the analysis section of this chapter for relative comparison of the number density and electron temperature spatial variations in the interior of the thruster.

5.2 Collection of Data

Langmuir probe voltage signals (via associated isolation amplifiers), anode voltage, and current probe measurements were recorded on a high-speed 14-bit DAQ at 2.5 megasamples per second per channel and saved via LabVIEW for post-processing analysis on a PC. These measurements were low-pass filtered at approximately 100 kHz cutoff frequency. The voltage on the batteries was also periodically monitored to ensure no significant reductions or excursions from nominal bias voltage during operation.

The Langmuir probe was repositioned over multiple sets of thruster shots to obtain measurements at various locations in the plasma discharge. For the measurements in the near-anode region, the Langmuir probe's long axis was aligned along the anode flared section. The probe tips were radially separated from the anode surface by 3.5–4.5 mm, limited primarily by the outer ceramic tube. The positions of the probe tips near the anode are shown in Figure 5.1. Note that the Langmuir

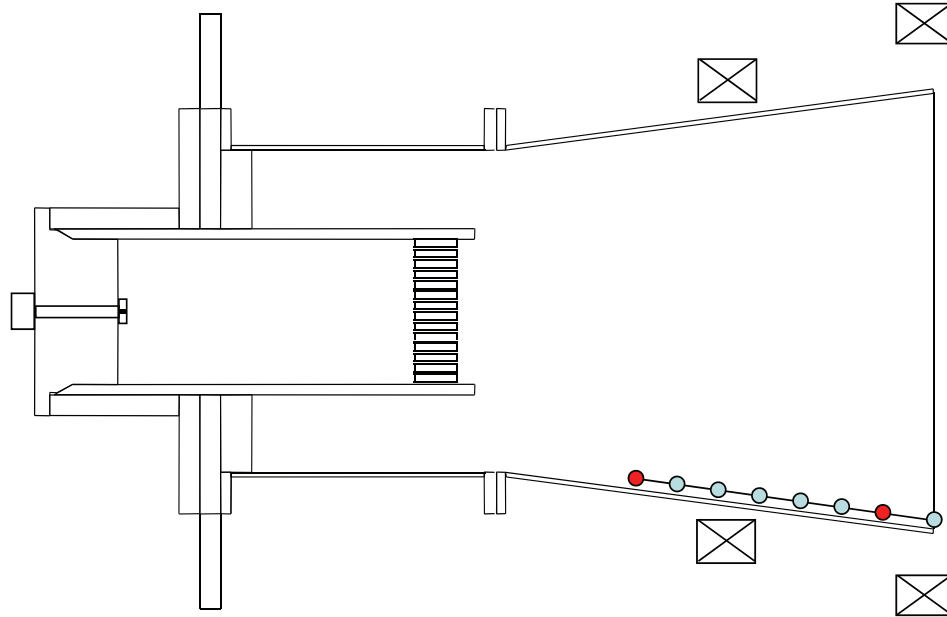


Figure 5.1: Triple Langmuir probe positions for near-anode measurements with all three magnetic configurations. Note: All eight positions along anode were included in testing at 10.7 kA. Two points in red denote the positions also measured at 8 kA.

probe measurement positions along the anode did not extend as far upstream as the magnetic probe. Measurements were limited to focusing on the regions of highest current density, which extended from the anode exit plane to the axial position at approximately $z = -179$ mm upstream of the anode exit plane (the region of highest current density for the tangential applied B field configuration). The probe was repositioned using a three-axis positioning stage.

Signals were averaged over the 1 ms quasi-steady time period (or appropriately well-behaved and reliable piecewise segments of at least 0.4 ms within this period). Measurements were also averaged across multiple thruster shots for each operating condition. The mean values and associated statistics (e.g., standard deviations for use in estimating uncertainties) were included in the uncertainty analyses. The equations for calculating n_e , T_e , and V_{fall} and approach for uncertainty analyses are described earlier in Section 2.6.4.

5.3 Analysis of Langmuir Probe Measurements Along the Anode at High Current

The previous analyses with the magnetic probe data indicated clear regions of high current density along the anode and a shift in the current patterns with the applied magnetic fields. Thus, our investigation of the local plasma properties begins with measurements circa 10.7 kA along the near-anode region in a strip of points from the anode lip at the exit plane and traversing upstream to the axial position $z = -179$ mm. Note that the tangential applied B field case exhibited peak current densities circa $z = -179$ mm, and the cases without magnets and with cusp applied B field showed highest current densities in the region around $z = -29$ mm.

First, we examine the profiles of electron temperature for each magnetic configuration. Figures 5.2, 5.3, and 5.4 show the measured electron temperatures (in eV) for the self-field, tangential applied B field, and cusp applied B field cases, respectively. Figure 5.5 shows all three configurations plotted together. Self-field operation suggest a general trend of increasing electron temperature along the anode as we traverse downstream. This generally follows the trend also seen in the increasing current density along the downstream section of the anode, as shown previously in Figure 4.12. The tangential applied B field case exhibits an increase in T_e at $z = -150$ mm, near where the highest current densities were measured. In addition, we observe higher T_e in the mid-region of the profile at $z = -79$ mm, -104 mm, and -129 mm. These values are near the regions of high applied B field intensity, and may be associated with regions of high induced azimuthal current density. The cusp applied B field exhibits a similar increase in T_e upstream and in the mid-region of the profile, albeit shifted approximately 25 mm downstream. This may be due to the downstream shift in the current pattern relative to the tangential applied B field, and thus a related shift downstream in the regions of higher induced azimuthal current density. This will be shown later in Section 6.2.

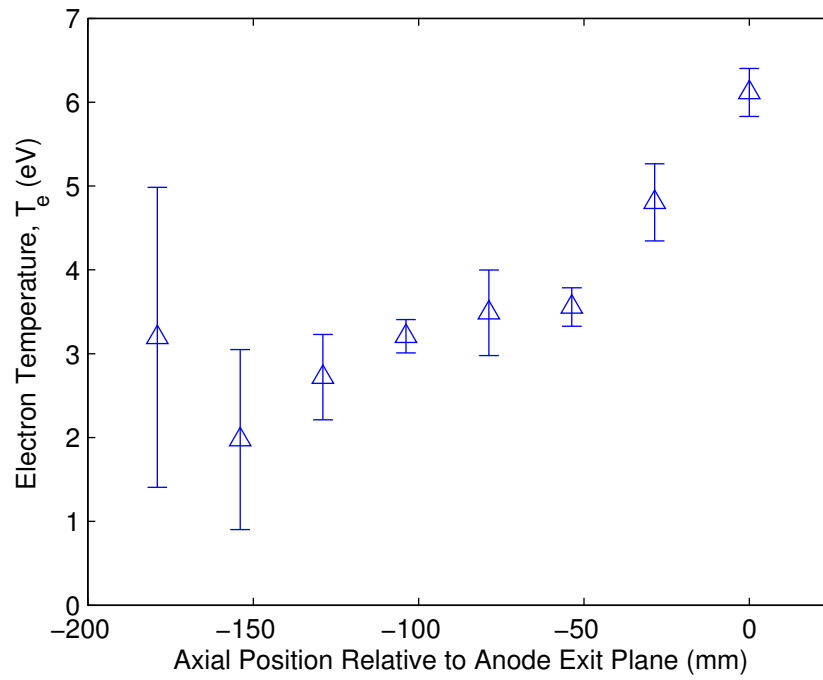


Figure 5.2: Electron temperature along the anode vs. axial position at 10.7 kA for the configuration without magnets.

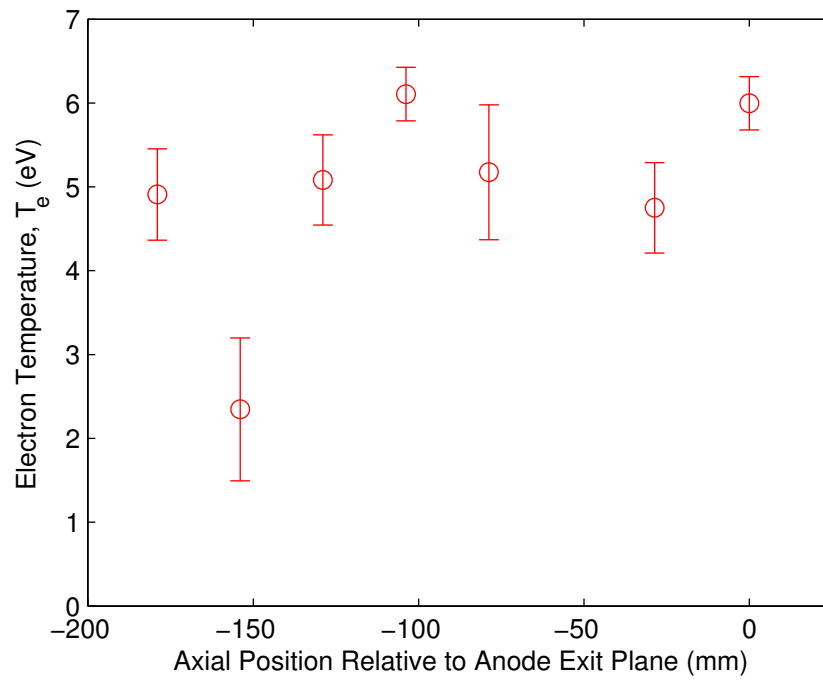


Figure 5.3: Electron temperature along the anode vs. axial position at 10.7 kA for the configuration with tangential applied B field.

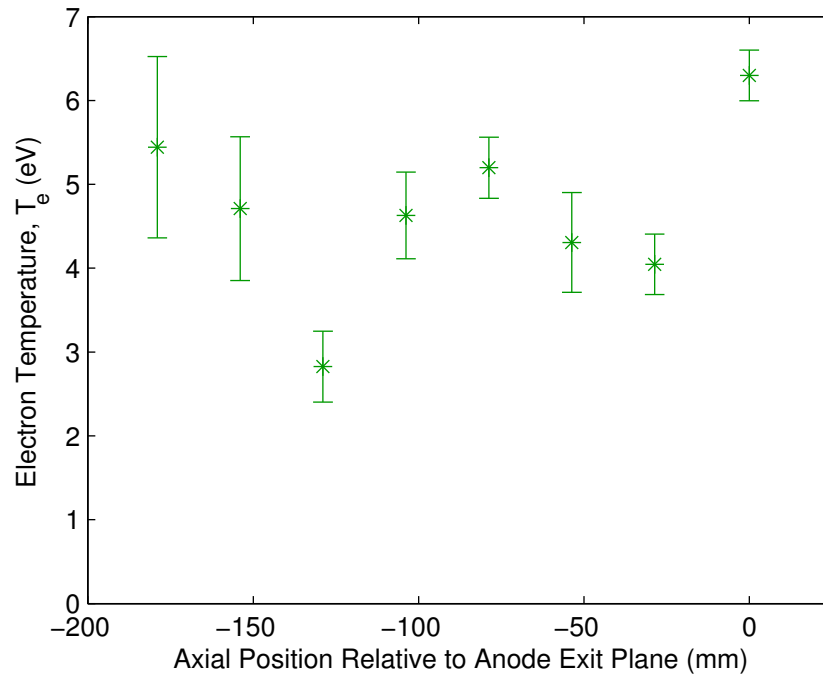


Figure 5.4: Electron temperature along the anode vs. axial position at 10.7 kA for the configuration with cusp applied B field.

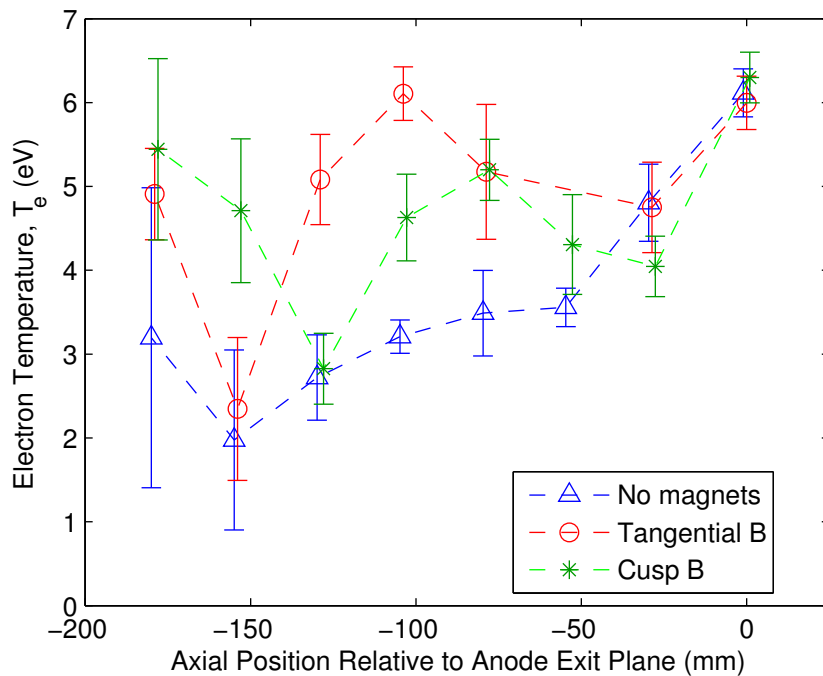


Figure 5.5: Electron temperature along the anode vs. axial position at 10.7 kA comparing all magnetic configurations. The dashed connecting lines are only as guides for the eye, not an implied functional relationship.

Subsequently, we consider the electron number density (i.e., the plasma density, assuming $n_e = n_i$ for quasineutrality), as calculated from the measured T_e and ion saturation current. The profiles for n_e along the anode are shown in Figures 5.6, 5.7, and 5.8 for the self-field, tangential applied B field, and cusp applied B field configurations, respectively. Figure 5.9 plots all three cases together for direct comparison. Without the magnets, we observe a general trend of increasing number density as we move downstream along the anode, increasing by a factor of 4.2 over the extent of the profile. This trend is likely due to the expansion of the plasma from the cathode emission zone outward towards the anode and accelerating downstream, resulting in higher number densities downstream, as will be discussed later. With the tangential applied B field, we see a significant increase of a factor of 5 in the number density upstream at $z = -179$ mm, near the region of highest current density. In addition to a possible change in the flow field for the tangential applied B field, this region may be experiencing a zone of increased ionization due to the higher current densities. Just downstream of this location, we observe a significant drop off to lower densities along the anode, likely due to the contouring of the strong magnetic field lines in this region, followed by an increase in the number densities again downstream from $z = -79$ mm to the anode exit plane as the plasma expands toward the anode. Except for the region of highest current attachment at $z = -179$ mm, the number density decreases relative to the self-field case. In the case of the cusp applied B field, the data show a generally steadier trend to the number density along the anode. Uncertainties in the absolute values of the measurements suggest that the measurements are not statistically significant in their difference relative to self-field operation, except for the increased number density of the tangential B field case upstream at $z = -179$ mm. However, relative differences do suggest the possibility of small increases in number densities around $z = -29$ mm and $z = -154$ mm for the cusp applied B field case relative to without magnets. These are the locations associated with the higher current densities in the cusp configuration, and this may suggest a modestly increased

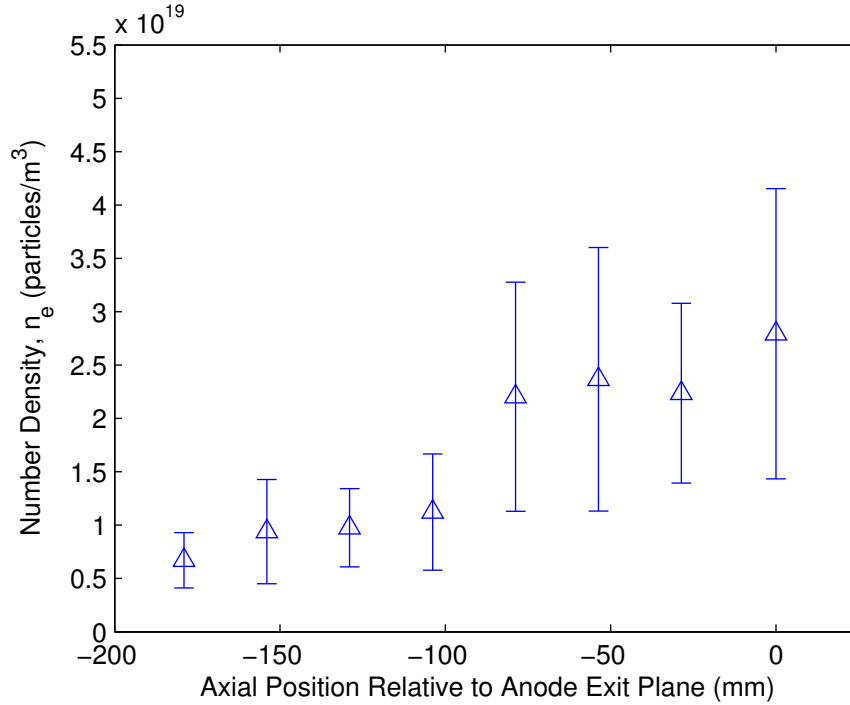


Figure 5.6: Plasma number density along the anode vs. axial position at 10.7 kA for the configuration without magnets.

number density to support increased electron random thermal flux to the anode. These are also the regions where the cusp B field lines turn radially toward the anode. It is possible that there is an increased diffusion of the plasma from the interior plasma radially toward the anode in this region of increased radial B field. Such diffusion will be discussed later in Section 6.1.

As a comparison, Gallimore [43] measured electron temperatures in the range of 2-3.7 eV in interelectrode gap at the anode exit plane of the self-field Princeton Benchmark Thruster. These temperatures are lower than some of our measurements at 10.7 kA for the self-field case downstream and are lower than most measurements with the applied magnetic fields. However, his smaller thruster geometry and higher flow rates (4 g/s and 16 g/s) resulted in plasma number densities of order 10^{20} - 10^{21} m $^{-3}$, which are 1-2 orders of magnitude higher than our measured number densities. Our lower number densities result in the resistive heating energy being distributed amongst fewer particles, generally resulting in higher average temperatures. Also, increased heating from the az-

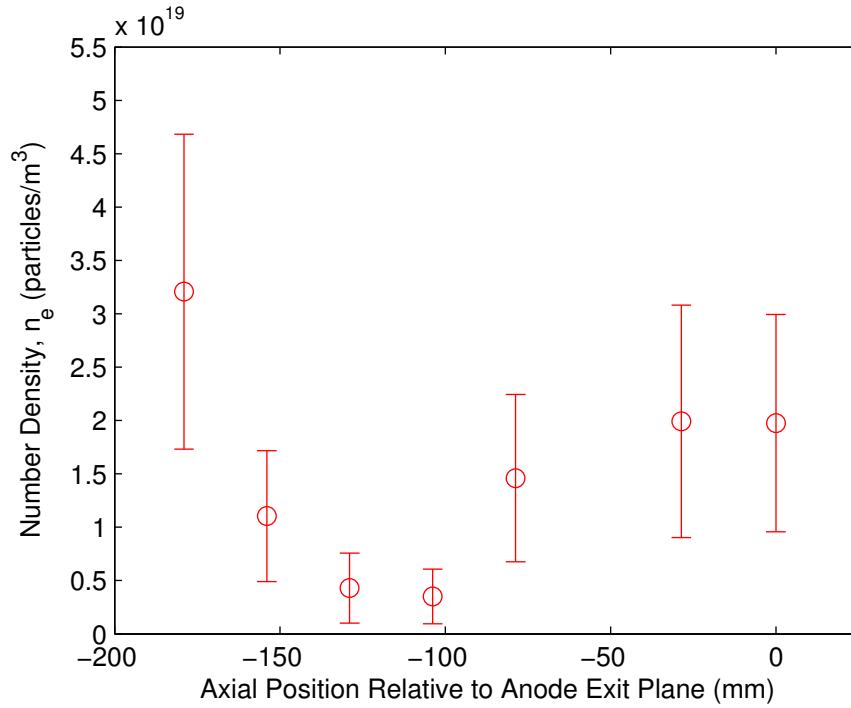


Figure 5.7: Plasma number density along the anode vs. axial position at 10.7 kA for the configuration with tangential applied B field.

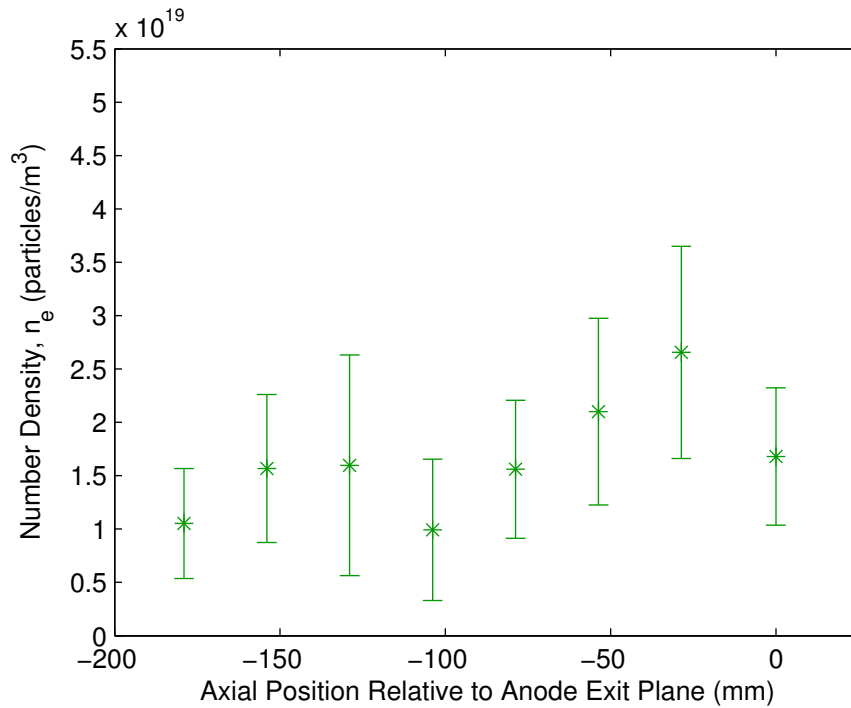


Figure 5.8: Plasma number density along the anode vs. axial position at 10.7 kA for the configuration with cusp applied B field.

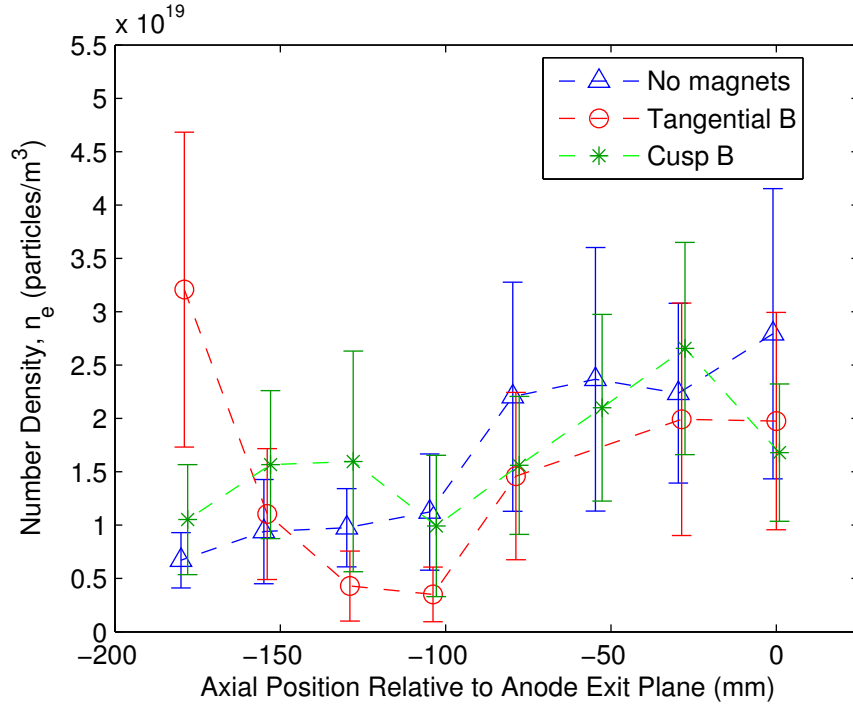


Figure 5.9: Plasma number density along the anode vs. axial position at 10.7 kA comparing all magnetic configurations. The dashed connecting lines are only as guides for the eye, not an implied functional relationship.

imutal current density likely explains the higher temperatures in the applied B field cases. Burton et al. [72] measured electron temperatures of 6-8 eV within several cm in front the exit plane of their argon MPDT, where they also measured number densities of order $5 \times 10^{19} \text{ m}^{-3}$. Their electron temperatures decreased to 1.5 eV much farther downstream in the plume. As will be shown later, our measured electron temperatures at the lower 8 kA operating point (and lower resistive heating) are in this lower range observed by Gallimore.

With the measurements of electron temperatures and floating potentials from the triple probe, we can calculate the plasma potential and cast it as the anode fall voltage, $V_{fall} = V_{anode} - V_{plasma}$. Note that the form of this expression implies electron-attracting positive fall potentials and electron-repelling negative fall potentials. Figures 5.10, 5.11, and 5.12 show the measured anode fall voltage for the self-field, tangential applied B field, and cusp applied B field cases, respectively. Figure

5.13 overlays all three configurations together. Without the magnets, we observe a generally very high anode fall voltage from approximately 45 to 84 V. Such significant potential drops that will be seen by the electrons in the near-anode plasma will result in high-energy acceleration through this potential well. The associated high-energy electrons will impact the anode surface, causing anode erosion. With the tangential applied B field, a significant drop in the anode fall voltage is seen from $z = -129$ mm to $z = -79$ mm. The drop in this region is likely associated with the significant decrease in current density demands in this region under this applied-field configuration. In the case of the cusp applied B field, we measure an impressive reduction in the anode fall voltage most of the profile from $z = -129$ mm to the anode exit plane. Here, we observe the average anode fall voltages drop by 42 to 70 V and ultimately reduced to only 3 to 14 V. In this case, we suspect that the radially intersecting magnetic field lines result in a significant increase in electron mobility to the anode surface in these regions of measured high current density (e.g., circa $z = -29$ mm), thus mitigating the need for large anode fall voltages to sustain the required current density. This effect of increased current conduction along the applied B field lines intersecting the anode will be assessed in Section 6.1.

5.4 Analysis of Langmuir Probe Measurements Along the Anode at Reduced Current

The plasma properties were also measured at 8 kA thruster discharge current to determine whether the applied magnetic fields at this intermediate current condition caused similar effects on the plasma properties as at higher current. At 8 kA, where the beginning effects of transition to onset resulted in much lower magnitude and frequency of voltage fluctuations and transients, as shown in Chapter 3. The terminal voltage reduction was also larger at 8 kA than at 10.7 kA. Figures 5.14,

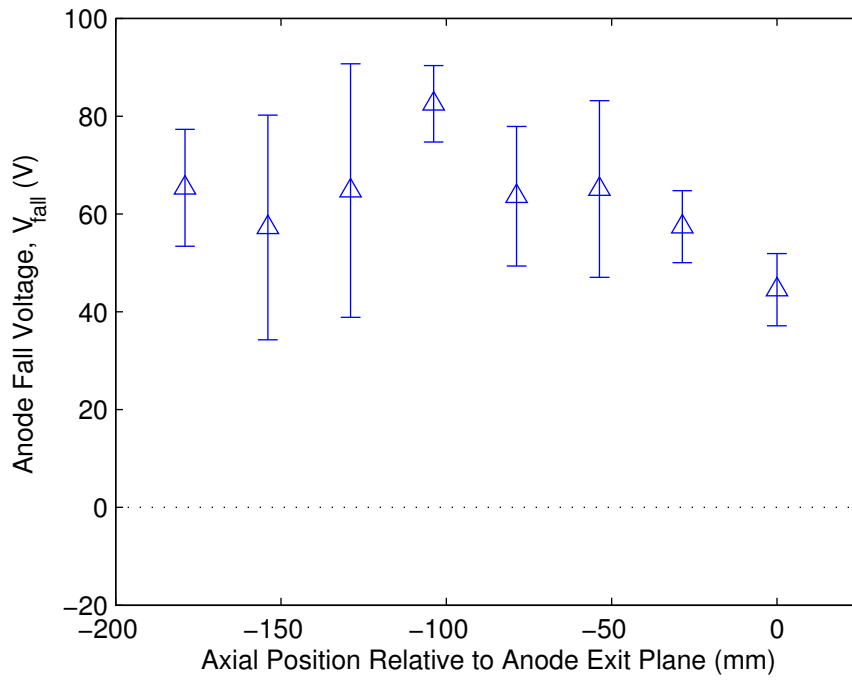


Figure 5.10: Anode fall voltage along the anode vs. axial position at 10.7 kA for the configuration without magnets.

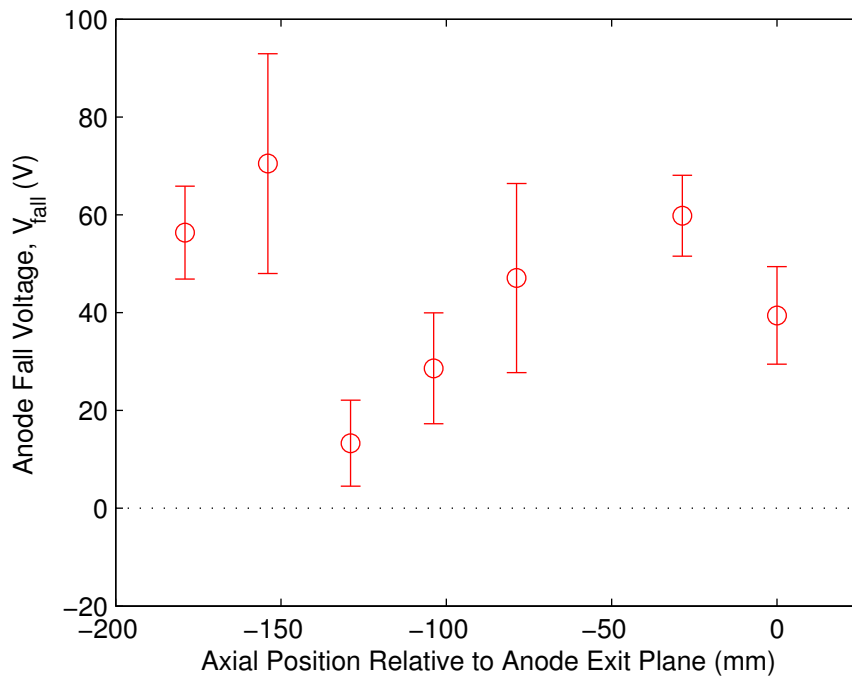


Figure 5.11: Anode fall voltage along the anode vs. axial position at 10.7 kA for the configuration with tangential applied B field.

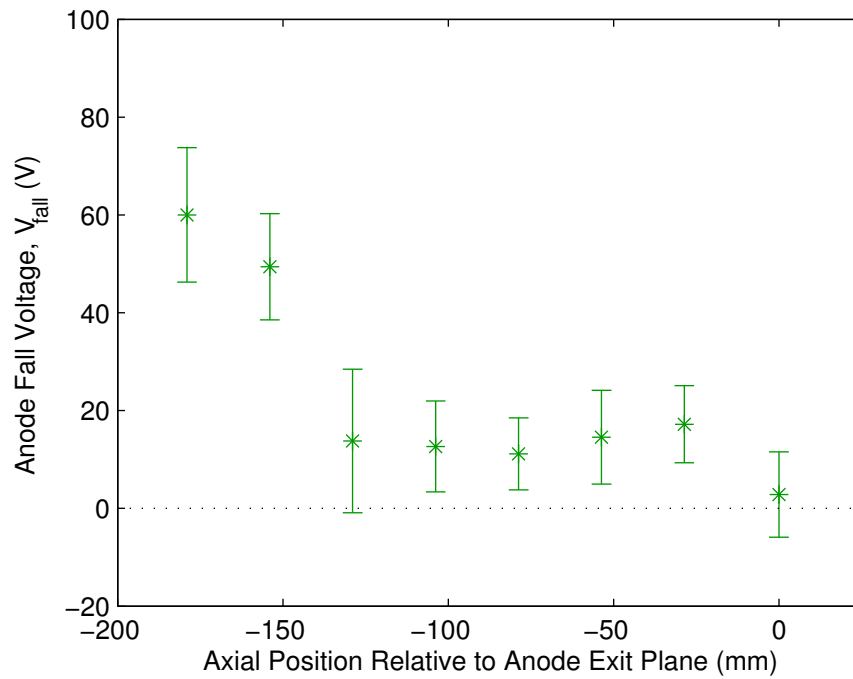


Figure 5.12: Anode fall voltage along the anode vs. axial position at 10.7 kA for the configuration with cusp applied B field.

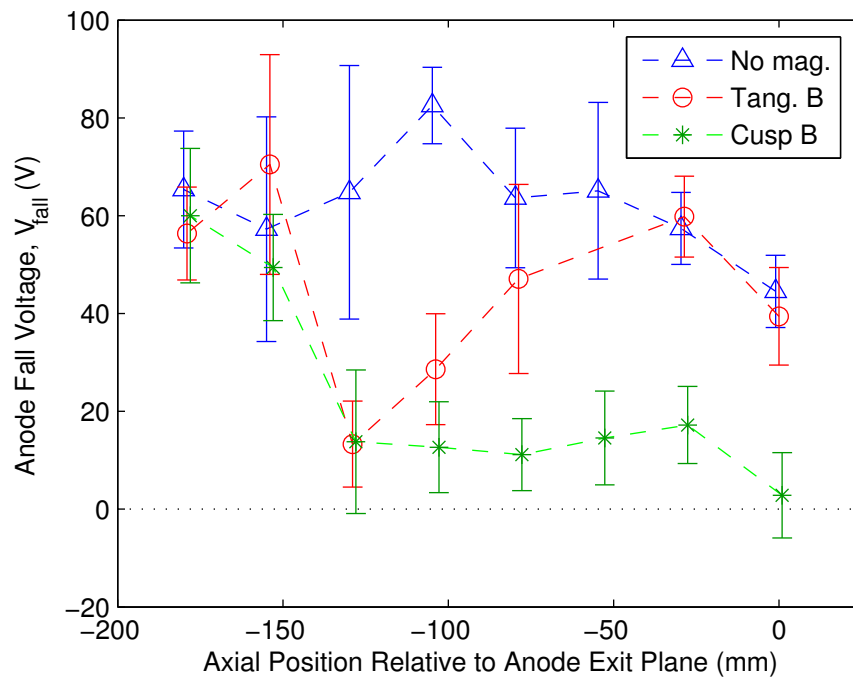


Figure 5.13: Anode fall voltage along the anode vs. axial position at 10.7 kA comparing all magnetic configurations. The dashed connecting lines are only as guides for the eye, not an implied functional relationship.

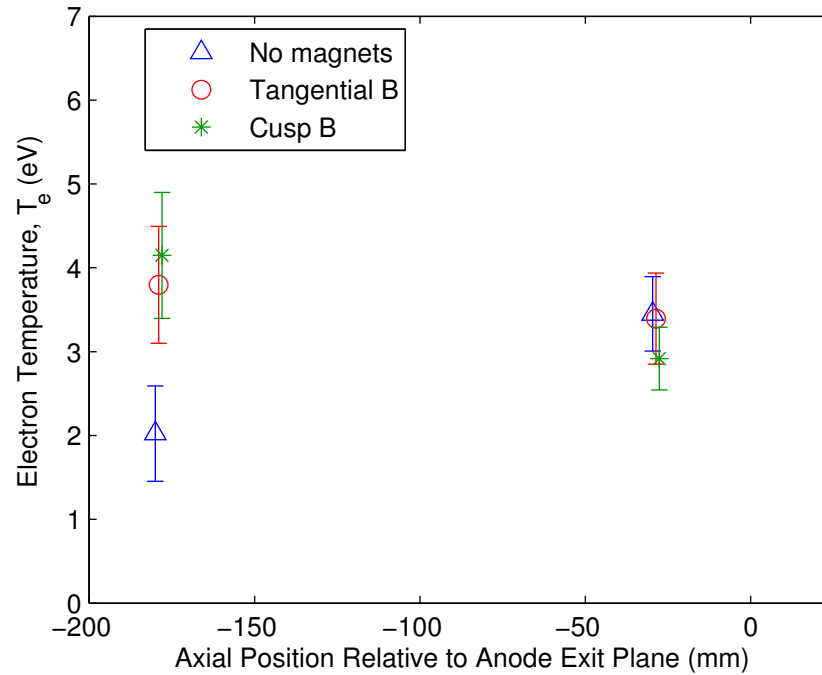


Figure 5.14: Electron temperature for two axial positions along the anode at 8 kA comparing all magnetic configurations.

5.15, and 5.16 show the electron temperature, number density, and anode fall voltage, respectively, for all magnetic configurations at 8 kA. At this 8 kA operating point, only two locations near the anode at axial positions $z = -179$ mm and $z = -29$ mm were measured, thus focusing on the regions observed to have the highest current densities. In general, we see a reduction in the electron temperature from the values measured previously at 10.7 kA. However, we still observe a similar increase in the electron temperature at 8 kA with both applied B fields relative to the self-field case. This is again likely due to increased azimuthal currents driven in the plasma with the applied magnetic field, which are discussed later in Chapter 6.

We do not observe a statistically significant difference in number densities from the values measured at the higher current. At higher current, increased flow acceleration should cause lower local number densities (from conservation of mass at increased velocity), and higher electromagnetic radial pumping forces should also decrease number densities near the anode. However, at higher

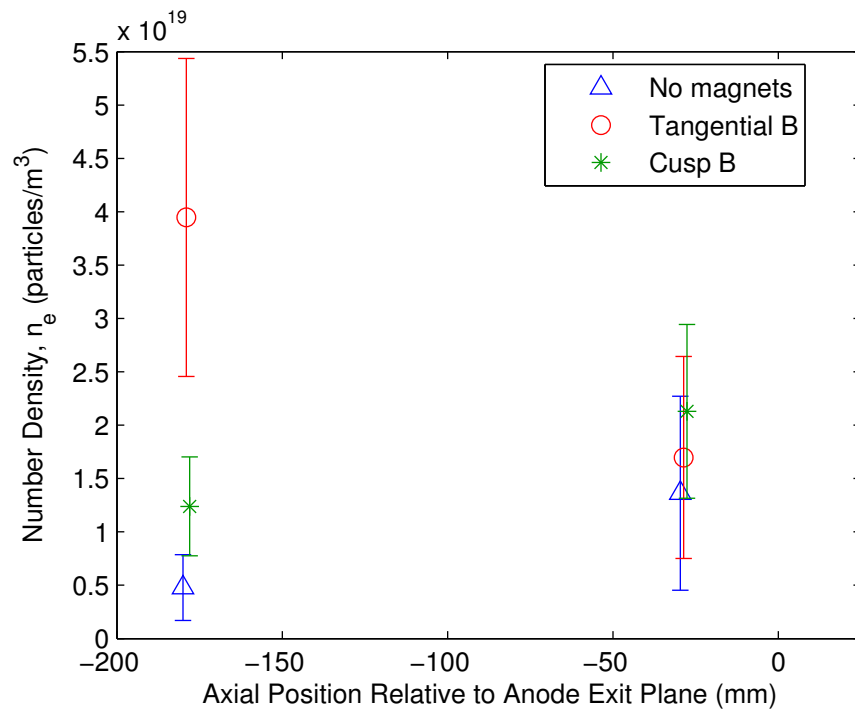


Figure 5.15: Plasma number density for two axial positions along the anode at 8 kA comparing all magnetic configurations.

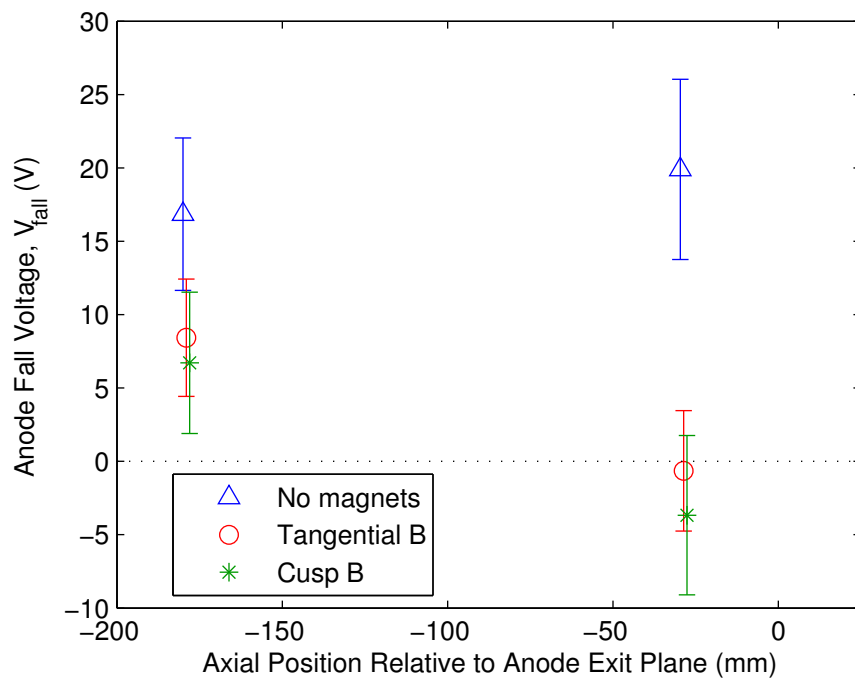


Figure 5.16: Anode fall voltage for two axial positions along the anode at 8 kA comparing all magnetic configurations.

current, there may be increased ionization, which would increase local plasma number densities. These two effects may mostly offset each other, resulting in similar magnitudes for the measured number densities at 8 kA and 10.7 kA. Nonetheless, relative to without the magnets, the data at 8 kA exhibit a similar pronounced increase in n_e upstream at $z = -179$ mm with the tangential applied B field relative to the self-field case. Modest increases in n_e are also measured with both applied magnetic fields relative to the self-field case downstream at $z = -29$ mm.

Overall, we observe lower fall voltages than were measured at higher current, which is consistent with the trends measured in other experiments by Gallimore [43] and Soulas et al. [53]. However, there is now a clear benefit of reduced anode fall voltage with both applied magnetic fields at this 8 kA current relative to the self-field case. This is also consistent with the earlier plot of terminal voltage versus current in Figure 3.4, which demonstrated that the tangential applied B field also had a pronounced reduction in terminal voltage at 8 kA but not significantly at 10.7 kA. At $z = -29$ mm, the calculated anode fall voltages are negative at this lower current, implying an electron-repelling anode fall. This can physically occur if the electron random thermal flux to the anode is more than sufficient to sustain the required current density [43], an effect which will be discussed in more detail in Chapter 6.

5.5 Analysis of Langmuir Probe Measurements in the Thruster Interior

Although the primary focus of the Langmuir probe measurements was on the near-anode region, additional data were obtained at locations in the interior of the thruster, albeit only in the self-field configuration. At 10.7 kA self-field operation, these data were obtained with the triple Langmuir probe along the anode (as shown previously), at the centerline near the cathode downstream face

and anode exit plane, near the cathode downstream radius, and at one location downstream about 20 mm radially inward from the anode. In addition, in earlier tests with a single Langmuir probe, we were able to reliably obtain data at currents up to 9 kA but not above, as discussed earlier in Section 2.6.4 on the Langmuir probe diagnostics. Nonetheless, the measurements at 9 kA provide insight regarding the general variations and trends within the thruster interior, as these measurements spanned a broad region in the interior of the thruster radially from the centerline to 24 mm away from the anode and axially from the anode exit plane to 15 mm downstream of the cathode exit plane.

Measurements at these locations were used to calculate the electron temperatures shown in Figure 5.17 and the number densities shown in Figure 5.18 for the self-field case. These figures are “bubble plots,” wherein the circular “bubbles” are centered at the location of each data point, and the radius of each bubble is allowed to scale with the relative magnitude of the values. The data is shown in red for 10.7 kA and in blue for 9 kA. While the data are too coarse spatially to plot a proper contour plot, this bubble plot approach affords another way to visualize the variations in magnitude between the measurement locations, particularly for the number densities.

In Figure 5.17, electron temperatures at 10.7 kA near the anode increase from as low as 2 eV upstream to 6.1 eV at the exit plane. Measurements at 10.7 kA also show a higher electron temperature of 5.1 eV near the cathode outer radius, as compared to 2.1 eV at the centerline in front of the cathode downstream face. The lower temperature at the centerline is likely moderated by the much higher density at the centerline than at the cathode outer radius, which results in the energy from heating being distributed into more particles. At 9 kA, the electron temperatures show moderate variations but without any obvious trends.

However, there are very large gradients in the number densities over the thruster volume, as seen in Figure 5.18. The number densities upstream along the anode are a factor of 42 to 92 times smaller

than the values near the cathode downstream face at the centerline. Near the anode exit plane, the number densities near the anode are a factor of 3.8 to 4.4 times lower than at the centerline of the anode exit plane. These results highlight the effect of the radial pumping forces in the thruster that lead to significant reduction of the plasma density near the anode. The radial pumping forces are a consequence of the magnetic force densities having a significant radial component, as shown in Appendix A. Interestingly, we can also infer some information about the flow structure from the number densities. Along the centerline, we observe a compression just a short distance in front of the cathode and a trend of decreasing number density with increasing axial position. We also observe a trend of decreasing number density at the mid-radius with increasing axial position. These decreasing trends are likely due to the acceleration and expansion of the plasma flow. This is supported even further by data near the anode, where we see the opposite trend now of increasing number density with increasing axial position. Tikhonov et al. [44] have observed an expanding cathode jet flow field in their MPD thrusters with plasma flowing from a multi-channel hollow cathode of geometry similar to our thruster (as opposed to inter-electrode or backplate gas injection typical of most past gas-fed MPDT studies). This suggests that the plasma in our thruster expands from the cathode front face radially outward (sometimes referred to as a “cathode jet”), following a flow field which is expanding downstream to the near-anode region as a consequence of balancing the magnetic pressure (which is higher upstream) with the kinetic pressure. This type of plasma flow boundary expansion is consistent with the number density radial variations and axial profiles along the anode and centerline observed in our thruster. Figure 5.19 plots the same data as Figure 5.18 but with an overlay of qualitative flow field lines to illustrate the cathode jet expansion. Figure 5.19 also includes an overlay on the right side of a high-speed video image ($5 \mu\text{s}$ exposure time) of the near-exit plume of the thruster. The radial variations in luminosity support the higher number densities measured closer to the centerline than near the anode radius.

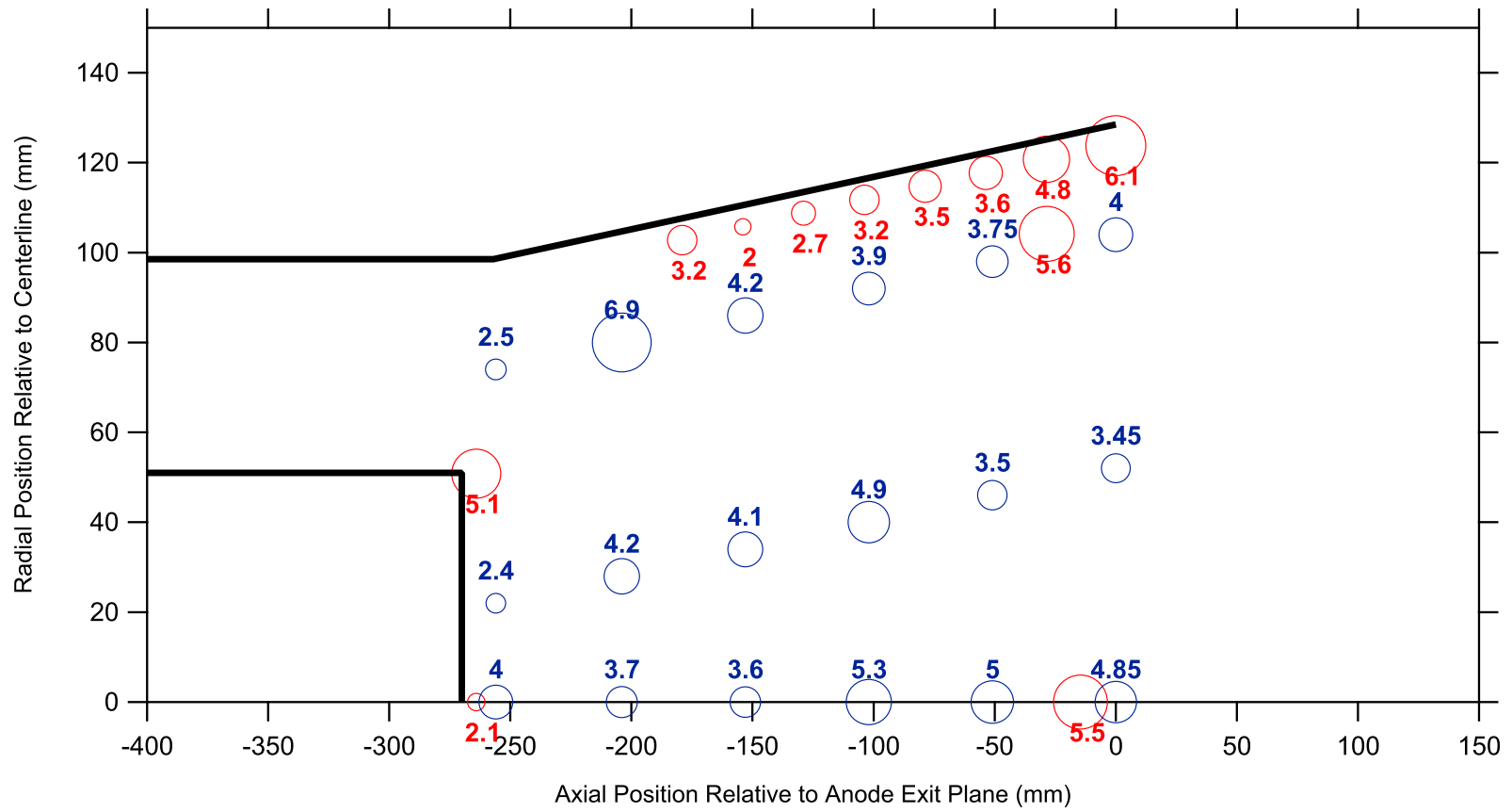


Figure 5.17: Bubble plot of electron temperature for the configuration without magnets at 10.7 kA (red) and 9 kA (blue). Radius of the circular bubbles scale with the relative magnitude of values. Absolute numerical values shown are in units of eV.

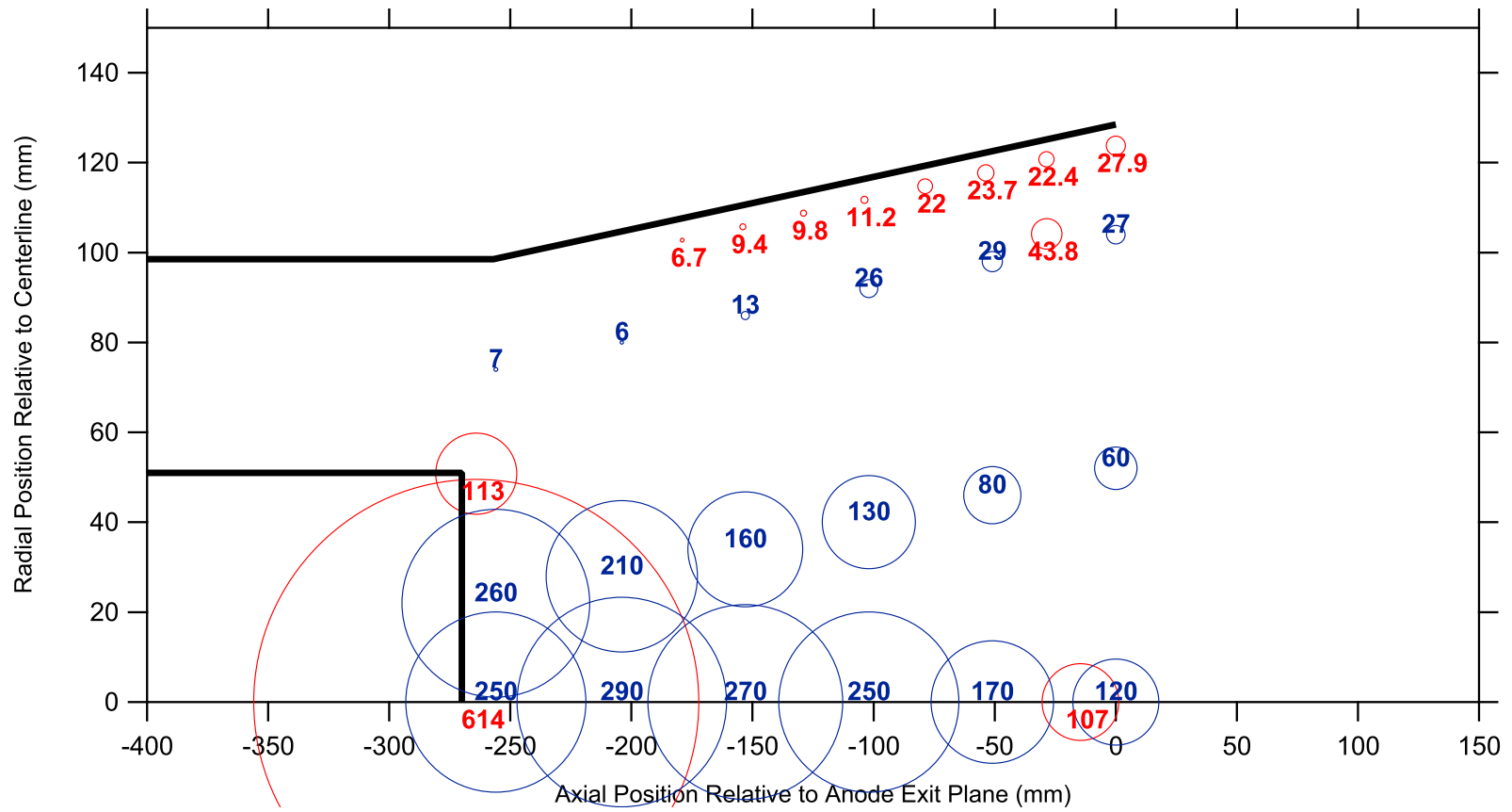


Figure 5.18: Bubble plot of number density for the configuration without magnets at 10.7 kA (red) and 9 kA (blue). Radius of the circular bubbles scale with the relative magnitude of values. Absolute numerical values shown are in units of 10^{18} m^{-3} .

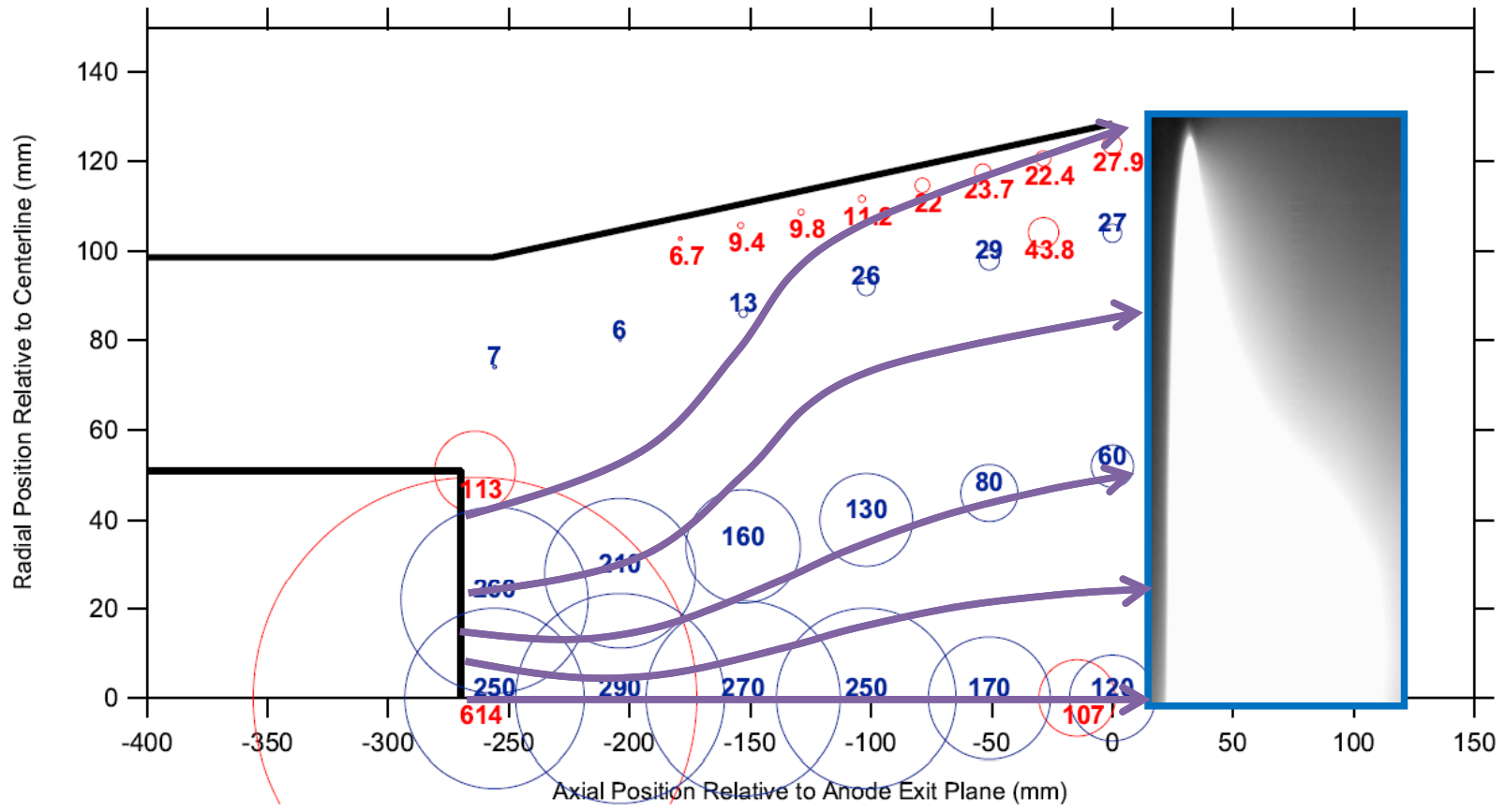


Figure 5.19: Bubble plot of number density with overlay of qualitative flow field lines for the configuration without magnets at 10.7 kA (red) and 9 kA (blue). Radius of the circular bubbles scale with the relative magnitude of values. Absolute numerical values shown are in units of 10^{18} m^{-3} . A high-speed video image of plume luminosity shown on the right side supports the measured radial variations in number densities.

5.6 Assessment of Ion Saturation Current Fluctuations

The data previously shown in this chapter represented the plasma properties averaged during the quasi-steady period. Given that we observed various temporal transients in the thruster terminal voltage signals studied in Chapter 3, it is of interest to at least briefly examine the effects of the applied magnetic fields on the ion saturation current fluctuations. The ion saturation current collected by the Langmuir probe is directly proportional to the plasma number density. Therefore, fluctuations and transients in the ion saturation current signal represent fluctuations in the local number density. As we will discuss later, the same anode spotting mechanisms that drive terminal voltage fluctuations could drive fluctuations in the near-anode number densities.

Figures 5.20 and 5.21 show typical examples of the ion saturation current time-series signals during the quasi-steady period at 10.7 kA and 8 kA discharge currents, respectively. These figures show data taken near the anode at axial position $z = -29$ mm upstream of the anode exit plane for all three magnetic configurations. These signals were low-pass filtered at 120 kHz and had the means subtracted to more clearly show the major temporal transients relative to the means.

Figures 5.22 and 5.23 show the ion saturation current power spectral density (PSD) plots in the frequency domain at 10.7 kA and 8 kA, respectively. These data represent the same signals as shown in Figures 5.20 and 5.21 at axial position $z = -29$ mm. The signals used in the PSD analyses were taken at the full bandwidth (2.5 MHz) of the data acquisition system from the current probe to ensure no lower-frequency attenuation. However, the power in the signals was identified to be clearly dominant in the lower-frequency range, so only values up to 200 kHz are plotted.

At 10.7 kA, there are clearly large excursions from the means that occur during the time signals. The magnitude and frequency of the large spikes (e.g., greater than 20 mA) in the ion saturation current signal are reduced in the configuration with the cusp applied B field relative to the self-

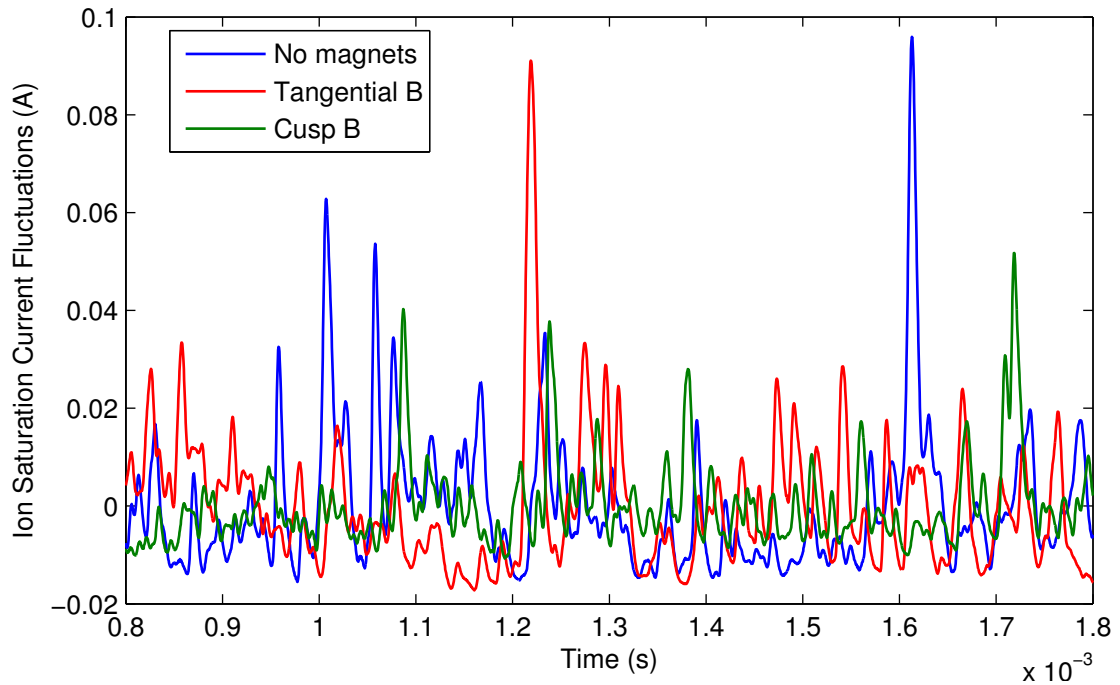


Figure 5.20: Ion saturation current signal fluctuations relative to the mean versus time during quasi-steady period at 10.7 kA and $z = -29$ mm. Typical examples from all three magnetic configurations are shown for comparison.

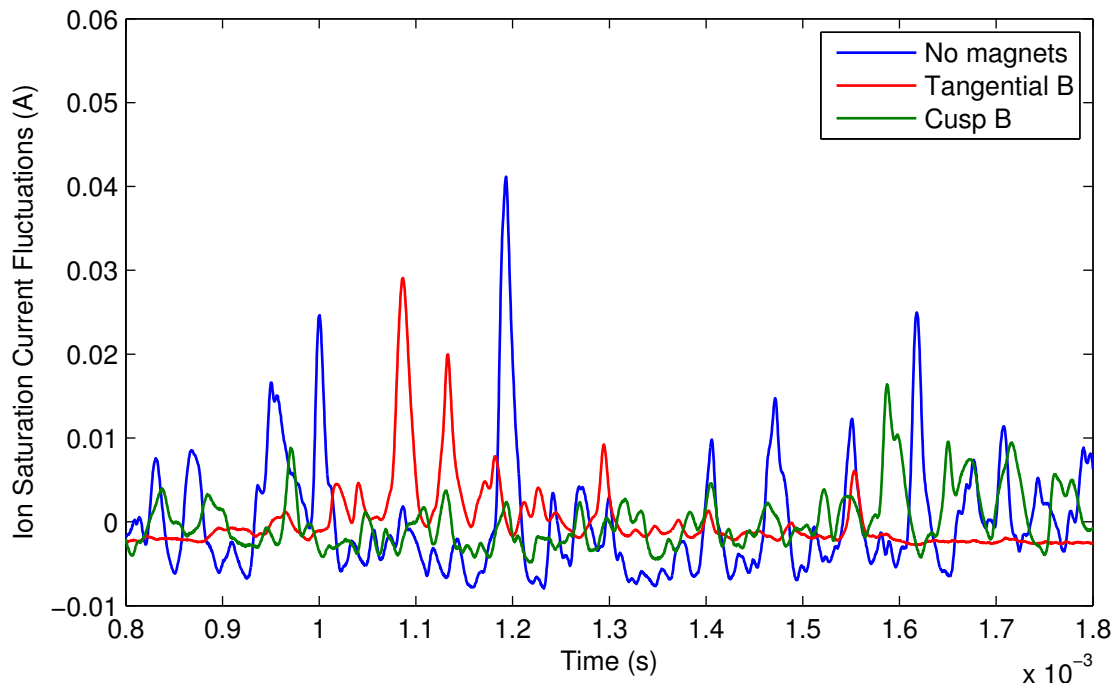


Figure 5.21: Ion saturation current signal fluctuations relative to the mean versus time during quasi-steady period at 8 kA and $z = -29$ mm. Typical examples from all three magnetic configurations are shown for comparison.

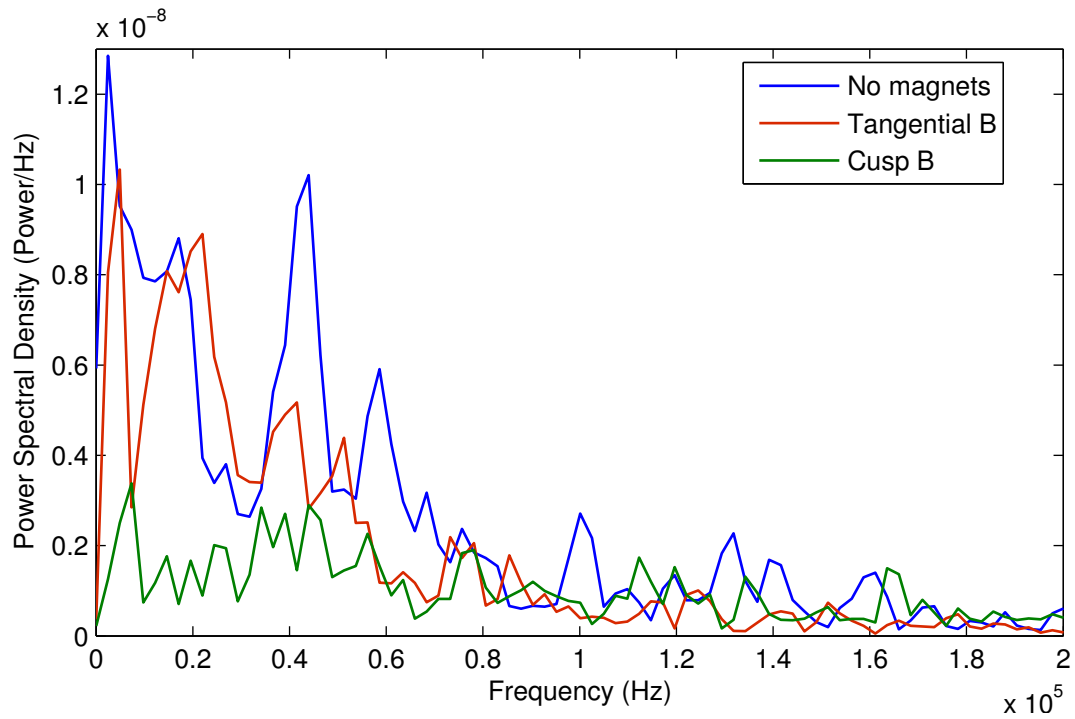


Figure 5.22: Ion saturation current power spectral density (PSD) at 10.7 kA and $z = -29$ mm. Typical examples from all three magnetic configurations are shown for comparison.

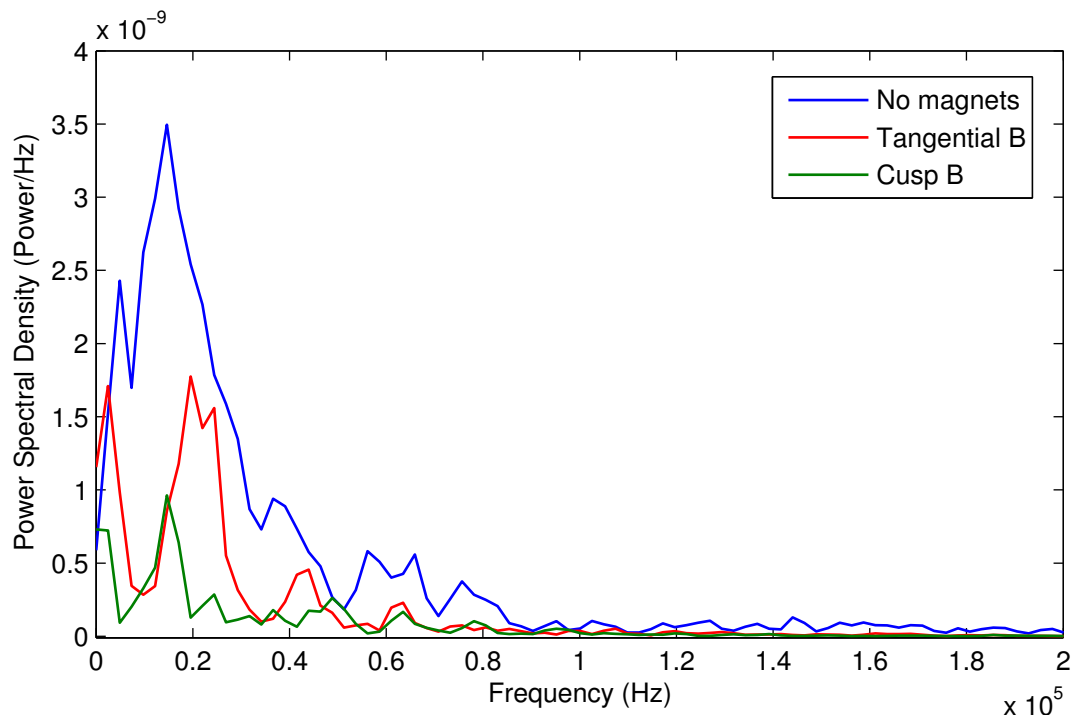


Figure 5.23: Ion saturation current power spectral density (PSD) at 8 kA and $z = -29$ mm. Typical examples from all three magnetic configurations are shown for comparison.

field case. This effect can be seen most clearly in the PSD in Figure 5.22, where the power over the frequency range is systematically lower for the cusp applied-field case than the self-field case. However, at this high discharge current, the tangential applied B field shows only limited benefit in reducing the power in the fluctuations. These results are consistent with the reduction in magnitude and frequency of thruster terminal voltage fluctuations with the cusp applied B field at this higher 10.7 kA current seen in Chapter 3 in Figure 3.5 of the standard deviations, Figure 3.12 of the number of large voltage spikes, and Figures 3.20 to 3.22 of the PSDs. The peaks that occur at approximately 20–60 kHz in the ion saturation current PSDs are relatively close to the peaks that occur at about 40–60 kHz in the PSDs for the terminal voltage signals.

At 8 kA, we again see large fluctuations from the mean ion saturation current during the time-series signals. However, the amplitudes of the deviations in ion saturation current are smaller in general than at 10.7 kA. Moreover, we now observe that there are fewer of these spikes in the ion saturation current at 8 kA than at higher current. Again, the cusp applied B field greatly reduces the magnitude and frequency of the large spikes (e.g., greater than 15 mA). In addition, we now see that the tangential applied B field has an effect also on reducing the number and frequency of the large-amplitude fluctuations relative to the self-field case, albeit not as much as the cusp applied B field. The PSD in Figure 5.23 also shows the effect of the applied B fields on reducing the magnitude of the PSDs relative to the self-field case. Once again, these findings are consistent with the observed reduction in magnitude and frequency of thruster terminal voltage fluctuations with both the tangential and the cusp applied B fields at the lower 8 kA current level seen in Chapter 3 in Figure 3.5 of the standard deviations, Figure 3.12 of the number of large voltage spikes, and Figures 3.23 to 3.25 of the PSDs. At 8 kA, the peaks at approximately 15–45 kHz in the ion saturation current PSDs are also relatively close to the peaks that occur at approximately 30–50 kHz in the PSDs for the terminal voltage signals.

These results suggest a relation between the terminal voltage signal fluctuations studied earlier and the ion saturation current fluctuations. The fluctuations or spikes in the ion saturation current represent fluctuations associated with the number density of the local plasma. Diamant [37, 38] and Uribarri [42, 18] discuss that such number density variations could be associated with erosion and vaporization of anode material that seeds the local plasma in response to anode spots. Thus, we may be observing a direct response to the same anode spotting mechanism in both the terminal voltage fluctuations and number density fluctuations associated with anode erosion.

The reduction in intensity and magnitude of the fluctuations due to the rotation of the plasma with the applied B field. The applied B field induces an azimuthal rotational motion to the plasma due to the $j_r \times B_z$ and $j_z \times B_r$ terms of the electromagnetic Lorentz force. It is possible that this swirling motion to the plasma could help mitigate some of the local number density fluctuations near the anode and anode spot mode erosion by forcing the plasma attachment to rotate azimuthally around the anode. Localized filamentary current attachment points should be forced to move around the anode surface, spreading out the heating over the anode surface and reducing erosion at local hot spots.

Local plasma number density fluctuations could also be caused by azimuthal asymmetries in the overall current discharge pattern, particularly in the self-field case. For example, Hoskins [73] observed azimuthal asymmetries in self-field MPDT operation and related these asymmetries to deviations in the radial centroid of the current discharge from the true geometric centerline of the thruster. Evidence of fluctuations in the current discharge of our thruster was obtained via high-speed video imaging. Figure 5.24 shows 8 frames taken with $5 \mu s$ exposure times and separated by $100 \mu s$ intervals during the quasi-steady period of the thruster firing at 9 kA in self-field mode (no magnets). These images show fluctuations in the luminosity associated with the denser plasma regions in the plume near the thruster exit. The anode is on the left in these images, and the flow

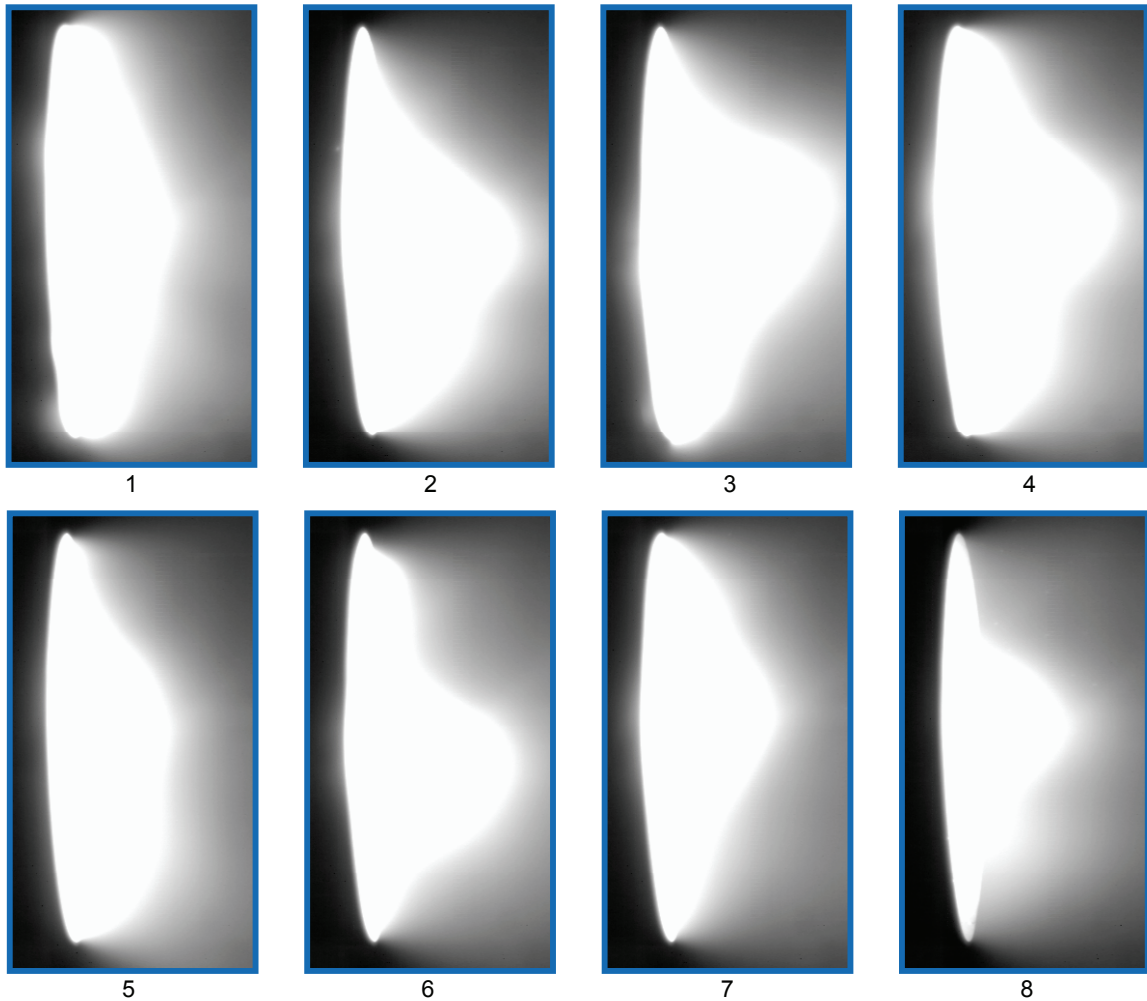


Figure 5.24: High-speed video imaging frames of thruster discharge fluctuations at 9 kA. Frames represent $5 \mu\text{s}$ exposure times separated by $100 \mu\text{s}$ intervals.

direction is to the right. Coupled with the observations by Hoskins, these oscillations in the luminous discharge regions suggest that asymmetries in the discharge pattern may indeed be another mechanism for increased number density fluctuations at higher currents. The induced azimuthal rotational motion with our applied magnetic fields could potentially have a gyroscopic stabilizing effect against such asymmetries, which would act to reduce fluctuations in the local number densities in the near-anode region.

5.7 Summary of Results

In this chapter, we examined the calculated electron temperatures, number densities, and anode fall voltages from Langmuir probe measurements. Data were obtained along the anode at a higher current condition at 10.7 kA and an intermediate current of 8 kA. In addition, a limited set of spatially coarse data taken in the interior of the thruster at both 10.7 kA and 9 kA were shown to illustrate general variations and trends, particularly for the number densities in the discharge. The following key findings were identified:

A reduction in the anode fall voltage is clearly observed for both applied B fields at 8 kA and for the cusp applied B field at 10.7 kA. At 10.7 kA, the cusp applied B field significantly reduces average anode fall voltages to only 3–14 V over most much of the near-anode profile. At 8 kA, both applied B field configurations show a substantial reduction in anode fall voltages down to a range from 8 to -4 V, with negative values implying an electron-repelling anode fall. In these cases, a likely cause could be the radial component of the applied magnetic fields leading to increased current conductivity in regions where the applied B field lines intersect the anode (e.g., in regions of high current density). In addition, modest increases in T_e and n_e lead to increased random thermal flux of electrons to the anode to support the current densities demanded. These effects combine to increase electron transport to the anode surface in regions of high current density (e.g., circa $z = -29$ mm), thus mitigating the need for large anode fall voltages. In general, the reductions in anode fall voltages suggest a link to the reduced average thruster terminal voltages previously observed with the magnetic fields. This relationship will be discussed further in Chapter 6.

The applied B fields result in increases in electron temperatures near the regions of high applied B field intensity and higher number densities in regions of high radial current density to the anode. Electron temperatures increase over much of the near-anode region with the applied

B fields. These increased temperatures may be associated with heating in regions of high azimuthal current densities induced by the applied B fields. In addition, we observe higher number densities with the applied B fields in the regions where the radial current densities to the anode are highest. The increased number density is particularly pronounced in the case of the tangential B field, where it increases by a factor of roughly 6 to 8 relative to self-field operation. In addition to the applied B field's effect on the flow field, the increase in n_e upstream for the tangential B field might be due to an increased ionization zone where the current density is higher. Again, these increased number densities support increased electron random thermal flux to the anode.

Variations of 1–2 orders of magnitude in the number densities between the near-cathode centerline and near-anode region clearly highlight the effects of the radial pumping forces on anode charge carrier depletion without the magnets. Number densities measured over a broad range of the interior discharge region without the magnets clearly showed significant reductions in the number density between the centerline and the near-anode region. These variations signify charge carrier depletion near the anode, which establishes one of the conditions that lead to onset. Moreover, the expansion of the plasma suggested by the number density variations results in a trend of decreasing number densities in the upstream direction along the anode, thus making it even more difficult to sustain significant current densities further upstream in the self-field configuration.

The applied B fields show a reduction in the magnitude and frequency of large fluctuations in the ion saturation current time-series signals, potentially implying a relation with the reduced terminal voltage fluctuations and anode spot damage. At 10.7 kA, we observed a reduction in the intensity and frequency of large spikes in the ion saturation current with the cusp applied B field relative to the self-field case. At 8 kA, we see that the same effect occurs with both the tangential B field and the cusp B field. These results suggest a relation to the earlier demonstrated reduction magnitude and frequency of the terminal voltage signal fluctuations with the applied B

fields, as is also supported by a relatively similar range of frequencies in the sets of PSDs. These fluctuations may be associated with anode spots seeding the near-anode plasma with vaporized anode material. It is also possible that the applied magnetic fields could help mitigate current filamentation and anode spot mode damage by forcing the plasma attachment to rotate azimuthally around the anode and thus smooth out heating at localized filamentary current attachment points. This may suggest a possible mechanism for mitigating anode spot damage, as such filamentation into anode spots would otherwise lead to anode erosion damage through vaporization of anode material in these local hot spots. High-speed video images were also shown highlighting fluctuations in the luminous discharge regions near the thruster exit plane, suggesting unsteady oscillations in the thruster discharge pattern at high currents as another possible mechanism for number density fluctuations.

These effects will be discussed in more detail later in Chapter 6 to examine the underlying physics.

Chapter 6

Interpretations and Conclusions

The data presented in Chapters 3, 4, and 5 followed a path of increasingly focused investigations. We started with the system-level behavior (e.g., terminal voltage characteristics), continued with investigations of the bulk plasma throughout the interior and near-anode regions, and ultimately focused on studying near-anode plasma properties. This chapter provides a synthesis of the experimental studies from these different scales, couples the various measurements to calculate important new plasma parameters, and relates the observed behaviors to the driving physics and processes. Section 6.6 closes with conclusions and recommendations based upon these findings.

6.1 Effects on the Current Pattern, Conductivity, and Current Densities

In Chapter 4, we observed the clear effects of the applied magnetic fields on the redistribution of the current pattern and regions of high current densities in the thruster. The current streamlines follow the applied B field lines in the near-anode attachment region, as seen in Figures 4.5, 4.7, and 4.9. These shifts in the current pattern are associated with similar shifts in the regions of high current densities along the anode, as shown in Figures 4.12, 4.22, 4.23, and 4.24. The tangential applied B field causes the current streamlines and regions of peak current densities to shift significantly

upstream, following along the applied magnetic field lines as they begin to turn radially outward toward the anode. In addition to higher current densities upstream mid-anode, current densities are significantly lowered in the downstream region where the applied B field lines are predominantly contoured parallel to the anode. The cusp applied B field results in a more subtle but still clear shift in the current streamlines to follow along the cusp applied B field lines as they intersect the anode surface in the downstream region. The high current density region downstream along the anode lip is slightly broadened and shifted upstream from the self-field case.

These shifts in the current patterns, anode attachment, and regions of highest current densities are evidently influenced by the shape of the poloidal applied B field lines. We can examine these behaviors on the basis of the physics governing the electron mobility. Consider the classical electrical conductivity for the plasma, σ_0 , given by

$$\sigma_0 = \frac{n_e q_e^2}{m_e \nu_e} \quad (6.1)$$

where n_e is the electron number density, q_e is the fundamental electron charge, and m_e is the electron mass. ν_e is the electron collision frequency, which can be approximated from the electron-ion collision frequency, ν_{ei} , given by the Spitzer model [43, 74]

$$\nu_e \approx \nu_{ei} = \frac{q_e^4 n_e \ln \Lambda}{3(2\pi)^{3/2} \sqrt{m_e} \epsilon_0^2 (k_B T_e)^{3/2}} \quad (6.2)$$

where T_e is the electron temperature, k_B is the Boltzmann constant, ϵ_0 is the permittivity of free space, the plasma parameter, Λ , is

$$\Lambda = 12\pi n_e \lambda_{De}^3 \quad (6.3)$$

and the electron Debye length, λ_{De} , is

$$\lambda_{De} = \sqrt{\frac{\epsilon_0 k_B T_e}{n_e q_e^2}} \quad (6.4)$$

Note that electrical conductivity is simply the reciprocal of the resistivity, η_0 , i.e.,

$$\eta_0 \equiv \frac{1}{\sigma_0} \quad (6.5)$$

Note that we assumed we can ignore collisions with neutrals to express $nu_e \sim nu_{ei}$ in equation 6.2. To establish why this assumption is valid, note that the collision frequency scales as

$$\nu = A_{cs} n v_{rel} \quad (6.6)$$

where A_{cs} is the collision cross section, n is the number density of target particles and v_{rel} is the (average) relative velocity between the interacting particles. In MPD thrusters, the plasma is highly ionized, and our thruster plasma should be fully ionized at higher current conditions such as 10.7 kA. However, there is still neutralization of ions hitting the anode wall in the near-anode region. The number density of these neutrals will be much lower than the background plasma. In addition, consider the collision cross section, A_{cs} . For neutrals, where the radius of the atom is of order 10^{-10} m, the collision cross section is of order $A_{cs} \sim 3 \times 10^{-20}$ m². For electron-ion Coulomb collisions, the collision cross section can be calculated from the Spitzer model equation 6.2 for nu_{ei} and dividing by the electron number density, n_e , and v_{rel} taken as the electron thermal velocity, $v_{th,e}$, given by

$$v_{th,e} = \sqrt{\frac{8k_B T_e}{\pi m_e}} \quad (6.7)$$

For parameters of interest in our experiments, where $n_e \sim 10^{19}$ m⁻³ and $T_e \sim 5$ eV, we estimate

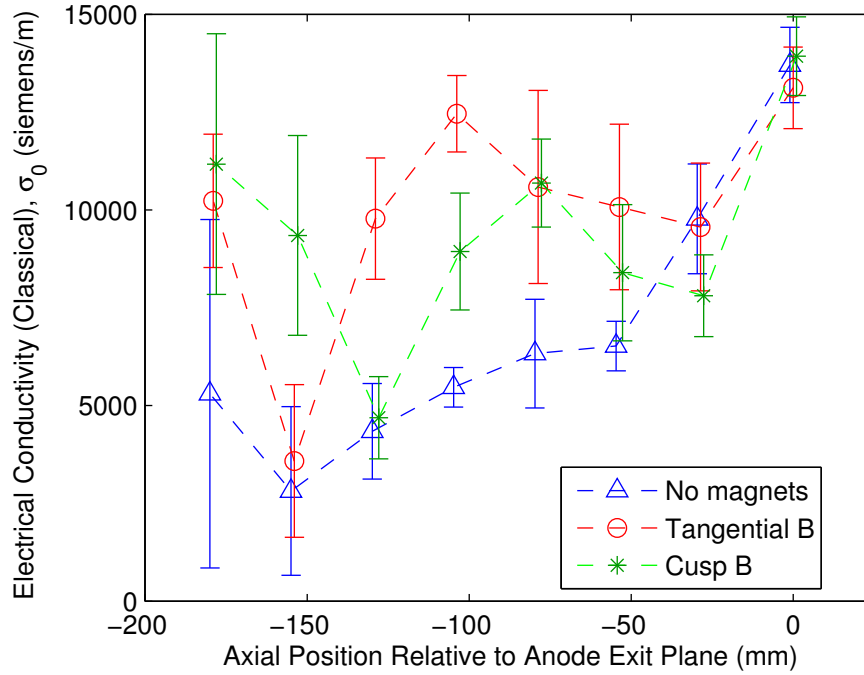


Figure 6.1: Electrical conductivity (classical, uncorrected) calculated along the near-anode region at 10.7 kA.

$A_{cs} \sim 2 \times 10^{-18} \text{ m}^2$. This is two orders of magnitude higher than the neutral cross section, so $nu_e \sim nu_{ei}$. More generally, the electron-ion Coulomb collisions should occur at much higher frequency than electron-neutral collisions for ionization fractions greater than order of 1% [20].

The classical electrical conductivity, σ_0 , is calculated along the near-anode region for the thruster operating at 10.7 kA without magnets, with tangential applied B field, and with cusp applied B field, as shown in Figure 6.1. These data were calculated using the Langmuir probe measurements in this region. Note that the dashed lines between data points are merely to guide the eye, not to suggest any specific functional dependence. Since σ_0 is a strong function of temperature, we see somewhat increased values for σ_0 with the applied B fields over much of the anode, following the results of the electron temperature data seen in the previous chapter in Figure 5.5.

The electrons also become tightly bound to their Larmor orbits (i.e., gyro-orbits) around the magnetic field lines as the B field magnitude increases [13]. The electron Larmor radius, r_{Le} , is

given by

$$r_{Le} = \frac{v_{th,e}}{\omega_{ce}} \quad (6.8)$$

where ω_{ce} is the electron cyclotron frequency (i.e., the gyrofrequency), given as a function of the magnetic field intensity B by

$$\omega_{ce} = \frac{|q_e|B}{m_e} \quad (6.9)$$

A measure of how magnetically bound the electrons are to motion along the B field lines is the electron Hall parameter, Ω_e . The electron Hall parameter is defined as the ratio of the electron cyclotron frequency to the collision frequency and can be expressed as

$$\Omega_e \equiv \frac{\omega_{ce}}{\nu_e} \approx \frac{\omega_{ce}}{\nu_{ei}} = \frac{qB}{m_e \nu_{ei}} = \frac{3(2\pi)^{3/2} \epsilon_0^2 (k_B T_e)^{3/2} B}{\sqrt{m_e} q_e^3 n_e \ln \Lambda} \quad (6.10)$$

This is a measure of how many gyro-orbits around the B field lines the electrons will undergo before they experience an elastic collision. Thus, the higher the Hall parameter, the stronger the electrons will be bound to the magnetic field lines and will be impeded for motion perpendicular to the B field. Figure 6.2 shows the electron Hall parameter calculated for the thruster at 10.7 kA along the same near-anode region as our conductivity calculations. The data show that the Hall parameter is indeed much greater than 1 over the entire region for all configurations, and the Hall parameter is generally higher with the applied B fields. The applied B field magnitudes are highest in this mid-range to downstream near-anode region, which is in closest proximity to the magnets' coils. Thus, the electrons are indeed strongly bound to the magnetic field lines, which is typically referred to as the electrons being “magnetized.” As will be discussed later, the high Hall parameter in the case of the self-field configuration impedes electron conduction radially to the anode, as the magnetic field is purely azimuthal. However, the applied magnetic fields introduce significant radial B components

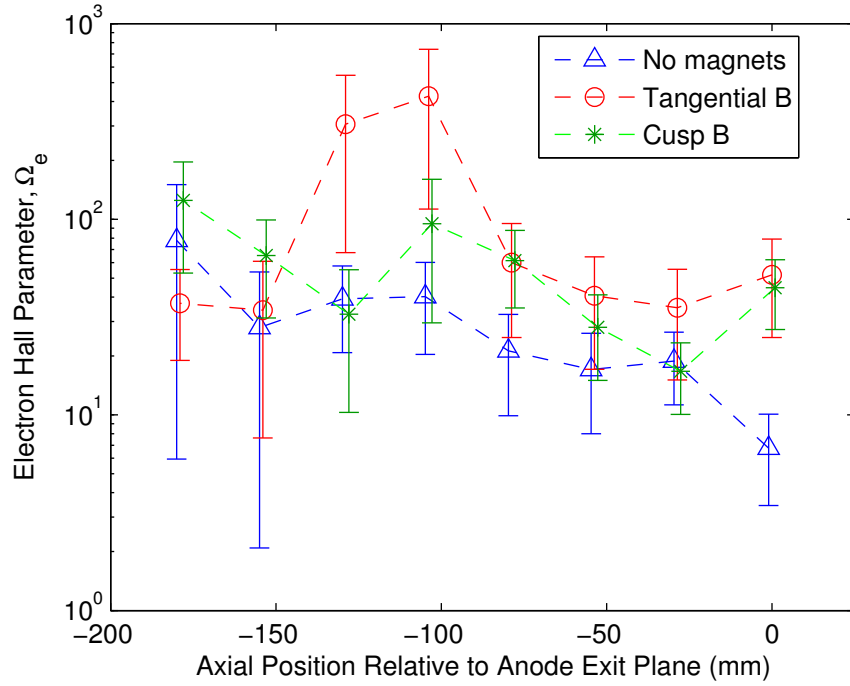


Figure 6.2: Electron Hall parameter calculated along the near-anode region at 10.7 kA.

that provide the magnetized electrons a path to the anode.

Let us consider multiple different models and viewpoints for expressing the current density to examine the effects of the Hall parameter and B field on current conduction in the plasma. First, examine the generalized Ohm's law from MHD given by [13]

$$\mathbf{j} = \sigma_0 \left(\mathbf{E} + \frac{\nabla P_e}{n|q_e|} + \mathbf{u} \times \mathbf{B} - \frac{1}{n|q_e|} \mathbf{j} \times \mathbf{B} \right) \quad (6.11)$$

where \mathbf{u} is the streaming velocity of the plasma (bulk velocity), and we assume $n = n_e = n_i$ in the quasineutral bulk plasma. If we ignore the pressure gradient contribution as small for now, we can

write this in tensor form as [43, 75]

$$\mathbf{j} = \sigma_0 \begin{bmatrix} \frac{1}{1+\Omega^2} & \frac{\Omega}{1+\Omega^2} & 0 \\ -\frac{\Omega}{1+\Omega^2} & \frac{1}{1+\Omega^2} & 0 \\ 0 & 0 & 1 \end{bmatrix} (\mathbf{E} + \mathbf{u} \times \mathbf{B}) \quad (6.12)$$

where the coordinate system is in orthogonal coordinates with unit vectors denoted as $\hat{\mathbf{a}}$, $\hat{\mathbf{b}}$, and $\hat{\mathbf{c}}$, and the component $\hat{\mathbf{c}}$ defined by the B field direction with $\mathbf{B} \equiv B_c \hat{\mathbf{c}}$. For Hall parameter much less than one, the tensor in this equation simply reduces to the unit tensor, resulting in the scalar conductivity solution. However, high Hall parameter clearly has anisotropic effects.

For the self-field case, the B field is purely azimuthal. In this B field geometry, the current density to the anode in the radial direction is given by the $\hat{\mathbf{b}}$ component as

$$j_b = \sigma_0 \left(\frac{-\Omega}{1+\Omega^2} E_a + \frac{1}{1+\Omega^2} E_b + \frac{-\Omega}{1+\Omega^2} v_b B_c + \frac{-1}{1+\Omega^2} v_a B_c \right) \quad (6.13)$$

This expression shows how the current density to the anode in the self-field case (in the presence of purely azimuthal B field) is greatly reduced by high Hall parameter due to conduction perpendicular to the B field.

In addition, the case of B field in the radial direction toward the anode can be examined. This is relevant for regions where there is a strong applied B field in the radial direction. For this B field geometry, the $\hat{\mathbf{c}}$ component of the current density co-aligned with the B field direction gives the current density to the anode (in the same direction) as simply

$$j_c = \sigma_0 E_c \quad (6.14)$$

where E_c in this geometry is now just the radial electric field. Therefore, this B field orientation

simply results in the classical scalar conductivity times the radial electric field, with no reduction by the Hall parameter. Relative to the self-field case, the current conduction is greatly increased. The current density can either be much larger for a given electric field, or can sustain the same current density with a much lower electric field. We will consider the latter case further in Section 6.3.

Another way to examine the effects of the Hall parameter and B field on current conduction is by analyzing the equation of motion for the electrons, since the electrons are the dominant source of current conduction due to their much smaller mass than the ions. Jahn [20] performed an analysis of AC conductivity for averaged electron motion. If we take the steady-field DC limit as frequency ω goes to zero and examine the case where $\Omega \gg 1$, we obtain an expression for the DC electron current density vector in terms of the Hall parameter as

$$\mathbf{j}_{DC} = \frac{\sigma_0}{\Omega^2} \mathbf{E} + \frac{\sigma_0}{\Omega} \frac{\mathbf{E} \times \mathbf{B}_0}{B_0} + \sigma_0 \frac{(\mathbf{E} \cdot \mathbf{B}_0) \mathbf{B}_0}{B_0^2} \quad (6.15)$$

where \mathbf{E} is the electric field vector, \mathbf{B}_0 is the magnetic field vector, and B_0 is the magnitude of the magnetic field vector. This expression provides a form for the current density dominated by the electrons, albeit neglecting the pressure gradient term for now (i.e., we assume the effects of the electric and magnetic field terms to dominate the ∇P term). This equation shows how high Hall parameter affects the current density and allows a simpler view of how the general form of the magnetic field affects the current density. Again, the conductivity is no longer scalar in nature, as it would be for Hall parameter much less than one. This equation reveals three major contributions. In the first term, the component directly associated with the electric field is reduced by the inverse square of the Hall parameter, making the contribution of that term very small. The second term is associated with the $\mathbf{E} \times \mathbf{B}_0$ drift motion, which is also reduced by the inverse of the Hall parameter. This Hall current term introduces motion perpendicular to the B field lines. For example, the

self-generated azimuthal component B_θ of the B field crossed with the radially inward component E_r of the electric field acts to direct the current downstream. In addition to the electric field, this Hall current term contributes to the current streamlines having such a strong axial component, particularly along the radial distance about half way to the anode, where the B field magnitudes are highest. The third term in the equation is perhaps the most compelling. It is not reduced at all by the Hall parameter, but it essentially scales with the angle between the electric field vector and the magnetic field vector. In the case of the self-field operation, this term is small, as the electric field is nominally oriented poloidally (radially and axially), and the self-generated magnetic field is purely azimuthal, i.e., perpendicular to the electric field. Thus, the third term goes to zero for self-field operation. However, with an applied magnetic field that has a significant component aligned with the electric field (which is primarily radial in the near-anode region), this third term dominates. Classical conductivity along the B field lines supports high current densities compared to cross-field conduction, which is reduced by the high Hall parameter.

This effect is undoubtedly responsible for the change in the current density profile under the influence of the applied B fields in the near-anode region. Current attachment is preferentially moved to regions where there is strong co-alignment of the electric and magnetic field vectors (predominantly, the radial components). Namely, the highest current densities can occur for the tangential B field upstream on the anode where the magnetic field begins to turn radially toward the anode. Highest current densities can occur for the cusp B field in the downstream region where the cusp B field lines intersect the anode. This conduction behavior also partly explains why the high current density anode attachment zone for the self-field configuration occurs far downstream on the anode lip, where the self-generated azimuthal magnetic fields are weakest, yielding lower Hall parameter and higher cross-field current density. This effect is in addition to the overall downstream convection of the current streamlines at high magnetic Reynolds number in the flowing plasma, as

discussed briefly in Section 4.6.

The general effect of the B field seen from equation 6.15 is to significantly decrease the conduction perpendicular to the B field lines but allow for much greater conduction along the directions parallel to the B field. In the self-field configuration, the B field is only azimuthal, as created by its own purely poloidal discharge current pattern. This magnetic field geometry thus requires the current pattern to cross transverse to the self-generated azimuthal B field to reach the anode. However, conduction across these B field lines is impeded by the high Hall parameter. With the applied B fields, conduction to the anode is higher where the applied B field lines turn radially outward toward the anode.

This effect can also be understood from the viewpoint of tracking individual charged particles. Electrons are strongly bound to the B field lines in the regions of high Hall parameter (both through the contributions of the azimuthal self-field and the poloidal applied field), as they are much lower mass than the ions and thus have much smaller Larmor orbits around the B field lines. The much heavier ions have significantly larger gyro-radii and are not “magnetized” in the modest B field magnitudes of our thruster operating conditions. The ions predominantly follow the electric field. The magnetized electrons, however, are driven to follow along the applied B field lines to the anode-intersecting regions of highest current attachment, where the magnitudes of the applied B field are also relatively larger (greater than the local self-field azimuthal B in this near-anode region). This results clearly in the experimentally observed effect of focusing the higher current conduction to the anode in the regions where there is a sufficiently large radial component to the applied B field (relative to the axial and azimuthal components) and significant co-alignment of the local B field vector and E field vector.

Therefore, the anode-intersecting applied B field mitigates the otherwise limiting effect of the Hall parameter on current density to the anode for self-field operation, where the plasma experiences

only the self-generated azimuthal B field and is forced into cross-field transport. This behavior can also be examined in terms of the diffusion process and the effect of the B field on the diffusion coefficient. This modeling viewpoint is relevant if the pressure gradient term is significant. Either assuming isothermal electrons or that the pressure gradient is simply dominated by the gradient in number density, ∇n_e (and the temperature gradient is much smaller), this yields a diffusion process for the electrons. The equation for classical diffusion of electrons across a magnetic field can then be written in terms of the electron flux given by Goebel and Katz [76] as

$$\Gamma_e = \mu_{\perp,e} n_e \mathbf{E} - D_{\perp} \nabla n \quad (6.16)$$

where $\mu_{\perp,e}$ is the perpendicular electron mobility given by

$$\mu_{\perp,e} = \frac{\mu_{0,e}}{1 + \Omega_e^2} = \frac{1}{1 + \Omega_e^2} \frac{q_e}{m_e \nu_e} \quad (6.17)$$

and where D_{\perp} is the perpendicular diffusion coefficient,

$$D_{\perp} = \frac{1}{1 + \Omega_e^2} D_0 = \frac{1}{1 + \Omega_e^2} \frac{v_{th,e}^2}{\nu_e} \quad (6.18)$$

This equation shows that the diffusion coefficient is strongly dependent on the Hall parameter for cross-field diffusion. Consider the basis of the classical diffusion coefficient, $D_0 = D_{\parallel}$ (the same as the diffusion coefficient parallel to the B field lines). As discussed by Bellan [13], D is a consequence of the random walk motion of particles and collisions, with $D \sim \frac{(\text{step size})^2}{(\text{time between collisions})}$. D_0 is thus a function of the mean free path, λ_{mfp} , and collision frequency given by

$$D_0 = D_{\parallel, \text{classical}} = \lambda_{mfp}^2 \nu_e = \left(\frac{v_{th,e}}{\nu_e} \right)^2 \nu_e = \frac{v_{th,e}^2}{\nu_e} \quad (6.19)$$

Further, we can examine the case of high magnetic fields and high Ω , where the diffusion coefficient perpendicular to the B field is reduced because the electrons are orbiting the magnetic field lines in a new length scale associated with the Larmor orbit gyro-radius. This new length scale results in

$$D_{\perp, classical} \sim r_{Le}^2 \nu_e = \left(\frac{v_{th,e}}{\omega_{ce}} \right)^2 \nu_e = \frac{1}{\Omega^2} \frac{v_{th,e}^2}{\nu_e} = \frac{1}{\Omega^2} D_0 \quad (6.20)$$

For Hall parameters much greater than one, this is the same as the expression for D_{\perp} from Goebel and Katz. Thus, the diffusion coefficient, D_{\perp} , for the diffusion perpendicular to the magnetic field is significantly reduced by the Hall parameter. In our MPD thruster, the electrons are greatly impeded from diffusing toward the anode in the presence of large azimuthal (and axial) B fields. However, the diffusion parallel to the magnetic field lines is unimpeded from the classical diffusion coefficient, D_0 . This effectively allows for much greater electron diffusion radially toward the anode in the regions where there is a substantial B_r radial component. Again, this is consistent with the measured current pattern and regions of high current densities in our thruster.

6.2 Regions of Increased Heating and Induced Azimuthal Current Densities

In Chapter 5, we observed increases in the local electron temperatures at 10.7 kA in the near-anode region as shown in Figure 5.5 operating at 10.7 kA. For convenient reference, the measured temperature profiles for the three magnetic field configurations are shown again here in Figure 6.3. These regions of increased temperatures can be shown to relate to the regions of highest current densities in the thruster.

The induced azimuthal current density, j_{θ} , caused by the externally applied magnetic fields may be estimated using the vector form of the generalized Ohm's law. This was given in equation 6.11,

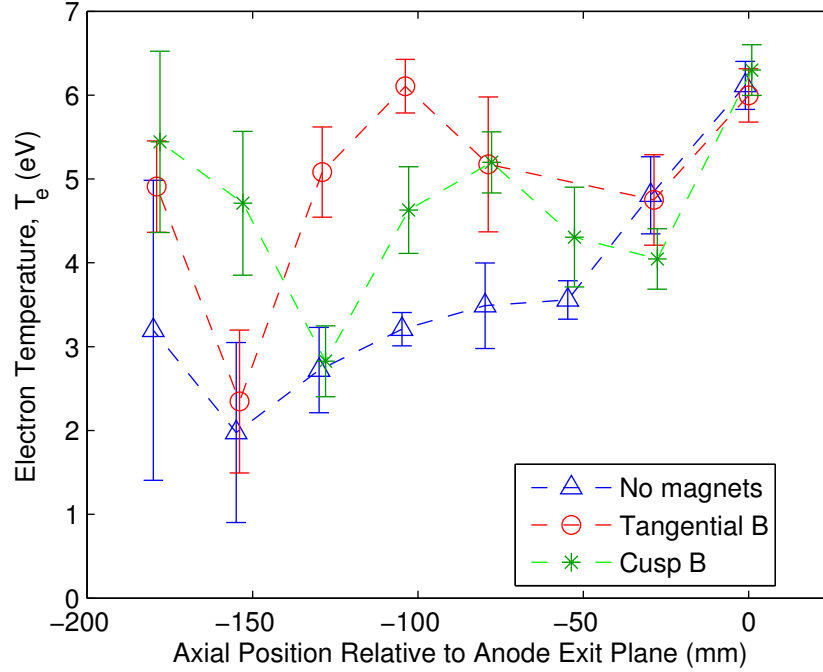


Figure 6.3: Electron temperature measurements along the near-anode region at 10.7 kA.

re-stated here for reference as

$$\mathbf{j} = \sigma_0 \left(\mathbf{E} + \frac{\nabla P_e}{n|q_e|} + \mathbf{u} \times \mathbf{B} - \frac{1}{n|q_e|} \mathbf{j} \times \mathbf{B} \right) \quad (6.21)$$

where \mathbf{u} is the streaming velocity of the plasma (bulk velocity), and we assume $n = n_e = n_i$ in the quasineutral bulk plasma. The azimuthal current density, j_θ , is obtained from the azimuthal component of this equation as

$$j_\theta = \sigma_0 \left(E_\theta + \frac{1}{n|q_e|} \nabla_\theta P_e + u_z B_r - u_r B_z - \frac{1}{n|q_e|} (j_z B_r - j_r B_z) \right) \quad (6.22)$$

where subscripts r , θ , and z represent the radial, azimuthal, and axial components, respectively.

However, we can make some simplifying assumptions that are generally true for MPD thruster acceleration processes [43], particularly near the anode, such as $u_z \gg u_r$, \mathbf{E} is mostly radial, and

E_θ and $\nabla_\theta P$ go to zero (or the gradient is vanishingly small) due to azimuthal symmetry in steady state. With these assumptions, we get the following expression for the azimuthal current density

$$j_\theta = \sigma_0 \left(u_z B_r - \frac{1}{n|q_e|} (j_z B_r - j_r B_z) \right) \quad (6.23)$$

We use this expression to then calculate an estimate of j_θ in the near-anode region given the applied poloidal B field and our measured n_e , j_r , and j_z . The calculated j_θ values for the tangential and cusp applied B field configurations are shown in Figure 6.4. For u_z , we assume an average from the estimated thruster exhaust velocity obtained from the bJ^2 thrust and I_{sp} model described separately in Section 6.5. A sensitivity analysis showed that the results were not significantly sensitive to the expected range of u_z for our parameters. The classical electrical conductivity, σ_0 , given by equation 6.1 was assumed for the calculation. We observe substantial azimuthal current densities in the regions where the thruster experiences high applied B field crossed with the current density vector. Therefore, the azimuthal current densities are moderated somewhat in the regions of highest current attachment, as these locations happen to also occur where the current streamlines are mostly parallel to the local applied B field lines. Also, note that the reversal in polarity of j_θ for the cusp applied B field case is associated with the reversal in the direction of the B field vector across the cusp region caused by the opposing currents in the two magnets.

The magnitude of the total current density, $|\mathbf{j}_{total}| = (j_r^2 + j_\theta^2 + j_z^2)^{1/2}$, is calculated using the estimated j_θ and shown in Figure 6.5. For the self-field configuration, j_{total} generally increases in the downstream direction, as do the electron temperatures. The contribution of the calculated j_θ component greatly increases the total current density for the tangential and cusp applied B field configurations. For the applied B field cases, the regions of increased and decreased electron temperatures also roughly follow the trends in the total current densities.

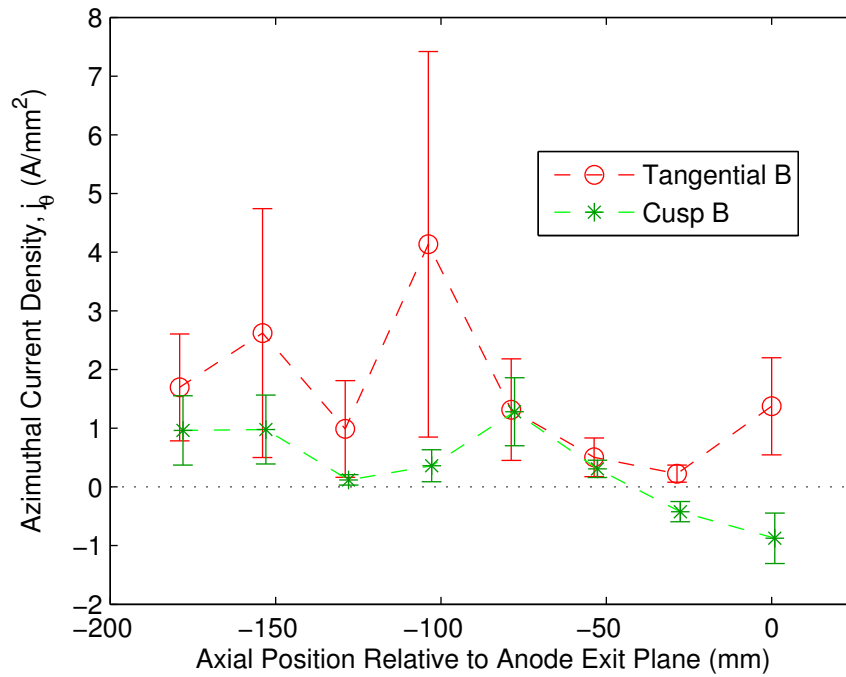


Figure 6.4: Azimuthal current density estimated along the near-anode region at 10.7 kA.

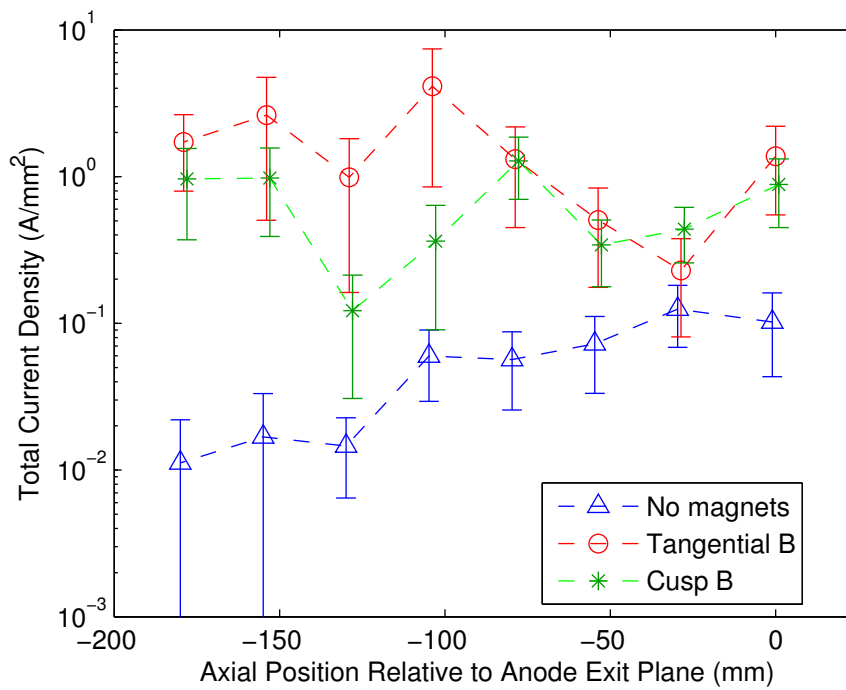


Figure 6.5: Total current density estimated along the near-anode region at 10.7 kA.

The increased temperatures are likely due to Ohmic heating of the plasma in the high current density regions. Ohmic heating scales with the resistivity (and thus with the inverse of the conductivity) as $\sim \eta j_{total}^2 = \frac{j_{total}^2}{\sigma}$ [20]. This is consistent with our observation that the regions of increased temperatures seem to follow the local trends in higher current density (and thus regions of greatest heating). The applied B fields lead to higher temperatures (relative to the self-field case) in regions of high azimuthal current densities.

In addition to the immediate vicinity of the anode, regions of high current densities can be clearly identified in the interior of the thruster discharge. All operating configurations exhibited high current densities around the downstream perimeter and in front of the cathode, as associated with regions of high current attachment to the cathode outer body and front face. High axial current densities were also observed along the thruster centerline, where electromagnetic $\mathbf{j} \times \mathbf{B}$ pinching forces compress the plasma and current streamlines. Additionally, the regions of high radial current density identified along the anode extend into the interior of the discharge, generally following along the enclosed current streamlines. This is as expected since we observe a compression of the current streamlines as they converge close the anode in the regions of highest anode current densities.

Heat generated in these interior regions can thermally conduct to the anode, which is another possible cause of increased electron temperatures. The plasma thermal conductivity is not scalar in the presence of the magnetic field. As shown by Woods [77], the electron contribution to the thermal conductivity in the direction parallel to the B field, $\kappa_{\parallel, the}$, scales as

$$\kappa_{\parallel, the} = \kappa_{0, the} = \frac{5}{2} \frac{k_B}{m_e} \frac{P_e}{\nu_e} = \frac{5}{2} \frac{k_B^2 n_e T_e}{m_e \nu_e} \quad (6.24)$$

which is the same as the classical thermal conductivity value, whereas the thermal conductivity in

the direction perpendicular to the B field, $\kappa_{\perp,the}$, scales as

$$\kappa_{\perp,the} = \frac{1}{1 + \Omega_e^2} \kappa_{\parallel,the} \quad (6.25)$$

The thermal conductivity is not scalar and scales as the inverse square of the Hall parameter perpendicular to the B field, much like the electrical conductivity, as discussed in Section 6.1. Therefore, thermal conduction from the interior plasma radially outward to the anode region is higher in regions of substantial radial applied B field, but the thermal conductivity is decreased in the direction perpendicular to the B field. In the regions where the applied magnetic field has a high axial component but little to no radial component, this results in a decrease of the thermal conduction from the plasma radially outward toward the anode. This occurs, for example, in the region close to the axial positions of the applied-field magnets, which helps explain the relatively lower electron temperatures with the applied-field magnets that occur upstream around axial positions $z = -129$ mm and $z = -154$ mm and at the downstream location $z = -29$ mm.

We have thus far considered only the classical electrical conductivity from equation 6.1. However, studies have shown (cf., Choueiri and Caldo [52, 78]) that microturbulence instabilities in MPD thrusters can trigger so-called “anomalous resistivity,” wherein the resistivity can be much higher (i.e., the electrical conductivity can be much lower) than the estimate of classical resistivity and electrical conductivity. Caldo [78] showed that the threshold at which this would begin to occur was of order $v_d \sim 1.5v_{th,ion}$, where v_d is the drift velocity given by

$$v_d = \frac{j}{n_e |q_e|} \quad (6.26)$$

and $v_{th,ion}$ is the ion thermal velocity,

$$v_{th,ion} = \sqrt{\frac{8k_B T_i}{\pi m_i}} \quad (6.27)$$

where T_i is the ion temperature (assumed to be of similar order to T_e for our plasma) and m_i is the ion mass (argon in our plasma). Gallimore [43] measured electrical conductivities in his Princeton Benchmark Thruster that were up to 30 times lower than his estimates for the classical conductivity. In Figure 6.6, we plot the calculated ratio of $v_d/v_{th,ion}$ for our thruster configurations. For the applied B field cases, this ratio is estimated to be of order 10 to 100 based upon our calculated values of j_θ . Therefore, anomalous resistivity is likely to be present, and our estimates of the electrical conductivity, j_θ , and j_{total} are likely to be overestimated. This makes it impossible to quantitatively estimate the absolute heating rates. Nonetheless, the trends in functional forms for the conductivity, j_θ and j_{total} , suggest a relationship between the induced azimuthal current densities and the measured increases in electron temperature.

6.3 Reduction of Anode Fall Voltages

In our experiments, the applied magnetic fields led to three major beneficial effects related to the voltages: (1) reduced anode fall voltages, (2) lower mean terminal voltages (thus, reduced input power for the same discharge current), and (3) reduced intensity and frequency of the large fluctuations and spikes in the thruster terminal voltage. Let us examine the anode fall voltage reduction in some detail first, then consider how it may relate to the reduction in mean terminal voltage and voltage fluctuations.

As seen in Figure 5.13 at 10.7 kA and Figure 5.16 at 8 kA, the cusp applied B field caused a very significant reduction in the anode fall voltage, V_{fall} , at 10.7 kA, and both applied B fields resulted

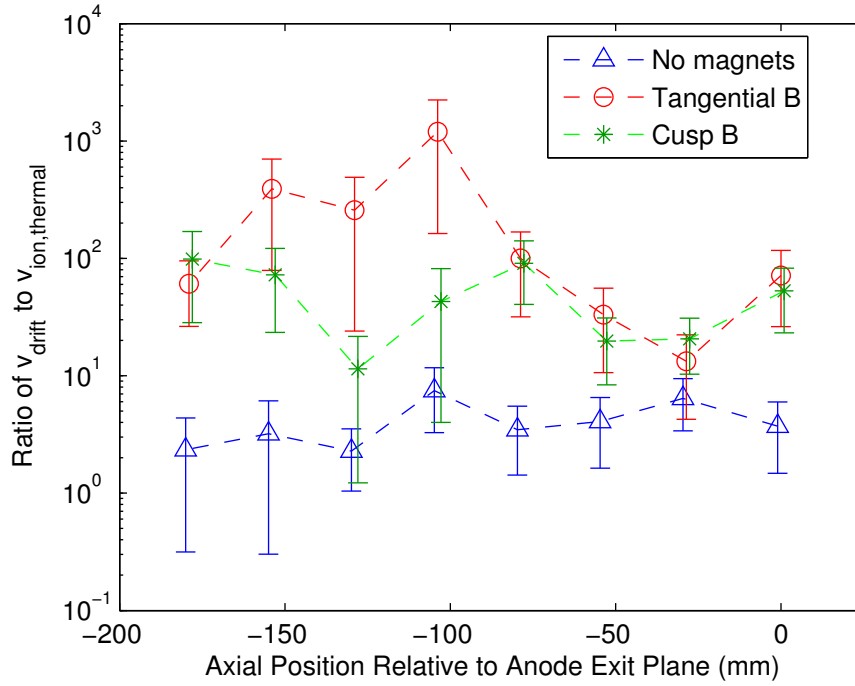


Figure 6.6: Ratio of drift velocity to ion thermal velocity along the near-anode region at 10.7 kA.

in significant reductions in V_{fall} at 8 kA relative to the self-field case. As discussed in Section 6.1, there is a significant decrease in the electrical conduction to the anode in the self-field case due to both high Hall parameter and conduction perpendicular to the purely azimuthal B field. In the applied B field cases, the introduction of radial B field components intercepting the anode surface greatly increase electron mobility to the anode.

The applied B fields can result in greatly reduced electric fields near the anode as a consequence of the increased conduction to the anode. Equation 6.15 relating the vectors for the steady-state (DC) current density, electric field, and magnetic field in the high Hall parameter limit is re-stated here for convenient reference,

$$\mathbf{j}_{DC} = \frac{\sigma_0}{\Omega^2} \mathbf{E} + \frac{\sigma_0}{\Omega} \frac{\mathbf{E} \times \mathbf{B}_0}{B_0} + \sigma_0 \frac{(\mathbf{E} \cdot \mathbf{B}_0) \mathbf{B}_0}{B_0^2} \quad (6.28)$$

The radial component of the current density near the anode surface is given by

$$j_r = \frac{\sigma_0}{\Omega^2} E_r + \frac{\sigma_0}{\Omega} \frac{(E_\theta B_z - E_z B_\theta)}{B_0} + \sigma_0 E_0 \cos(\psi) \hat{\mathbf{B}} \cdot \hat{\mathbf{r}} \quad (6.29)$$

where B_0 is the total magnitude of the B field, E_0 is the total magnitude of the E field, ψ is the angle between the B field and E field vectors, $\hat{\mathbf{B}}$ is the unit vector in the B field direction, and $\hat{\mathbf{r}}$ is the radial unit vector. In the case of self-field operation, the B field is purely azimuthal, and the E field components are purely poloidal. Thus, the third term vanishes. In MPD thrusters near the anode, we also expect the electric field to be predominantly radial, so E_r will be much larger than E_z and E_θ [43]. In the simplified case of only radial E field, the current density equation reduces to the first term for the self-field configuration, given by

$$j_{r, self\ field} \sim \frac{\sigma_0}{\Omega^2} E_r \quad (6.30)$$

$$E_{r, self\ field} \sim \frac{\Omega^2}{\sigma_0} j_{r, self\ field} \quad (6.31)$$

Thus, to sustain a given radial current density, the electric field E_r must grow, scaling with the square of the Hall parameter. However, with the anode-intersecting applied B fields, there are regions where the E field and B field are significantly co-aligned radially ($E_0 \sim E_r$ and $\cos(\psi) \sim 1$). This gives an expression for the radial current density and radial E field component in terms of the Hall parameter,

$$j_{r, applied\ field} \sim \frac{\sigma_0}{\Omega^2} E_r + \sigma_0 E_0 = \sigma_0 \left(\frac{1}{\Omega^2} + 1 \right) E_r \approx \sigma_0 E_r \quad (6.32)$$

$$E_{r, applied\ field} \sim \frac{1}{\sigma_0} j_{r, applied\ field} \quad (6.33)$$

For the applied B field configurations, in regions where there is significant radial B field, the electric field E_r can thus be much smaller to sustain a similar order of radial current density. As discussed in Section 6.1, it is no surprise that we found the highest current densities associated with regions of significant radial B field and much lower current densities where the B field was only tangential to the anode. Moreover, the result above suggests that the much smaller electric field required to sustain a high current density could be obtained with a much smaller anode fall voltage, as the steady-state electric field near the anode scales as

$$\mathbf{E} = -\nabla V \quad (6.34)$$

$$E_r \sim -\nabla_r V_{fall} \quad (6.35)$$

Therefore, we suggest the increased conduction along the applied B field lines radially intercepting the anode and the associated reduction in E field as a prevailing cause of the reduced anode fall voltage.

Another way to examine the cause of large anode fall voltages is to consider the random thermal flux of electrons to the anode. When the electron random thermal flux to the anode surface is insufficient to provide the current density required at the anode, the potential in the anode fall region must reverse from an electron-repelling potential to an electron-attracting anode fall voltage. This must form to accelerate the electrons beyond the random thermal flux alone and sustain the higher current densities with increasing total thruster discharge current. This condition where the requisite anode current density exceeds the “thermal” current density from random thermal flux to the anode surface has been presented as a condition for the inception of so-called “onset” and “critical current” regimes in MPD thrusters by many authors, beginning perhaps with Baksht et al. [21, 22, 34, 43, 42]. Thus, we can examine the conditions in our thruster to determine whether we

exceed this criteria and how this was affected by the applied magnetic fields.

First, we consider the case assumed by the previous authors, wherein the random thermal current density to the anode surface is simply given by the electron charge times the classical kinetic theory expression for electron random thermal flux to the anode surface (not accounting for B field effects),

$$j_e = q_e \Gamma_{0,e} = q_e \frac{1}{4} n_e v_{th,e} \exp\left(\frac{-q_e V_d}{k_B T_e}\right) \quad (6.36)$$

where $v_{th,e}$ is the electron average thermal velocity,

$$v_{th,e} = \sqrt{\frac{8k_B T_e}{\pi m_e}} \quad (6.37)$$

and V_d is the potential difference between the anode wall and the local ambient plasma. Taking the limit of V_d going to zero gives an expression for the maximum “saturation” current density before an electron-attracting sheath must form to draw any more current, given by

$$j_e = q_e \frac{1}{4} n_e v_{th,e} \quad (6.38)$$

Figure 6.7 shows the ratio of the measured radial current density to this electron thermal current (flux) along the near-anode region. These data are calculated from the measurements in this region with the thruster operating at 10.7 kA with the three different magnetic configurations. This figure shows that the measured current density never exceeds the values calculated for the random thermal current density in this region.

However, we suspect that this expression is likely to be overestimating the actual random thermal current density to the anode due to impeded electron motion in the presence of the magnetic fields. For the conditions in our thruster, the electron Larmor radius is large (order of mm) com-

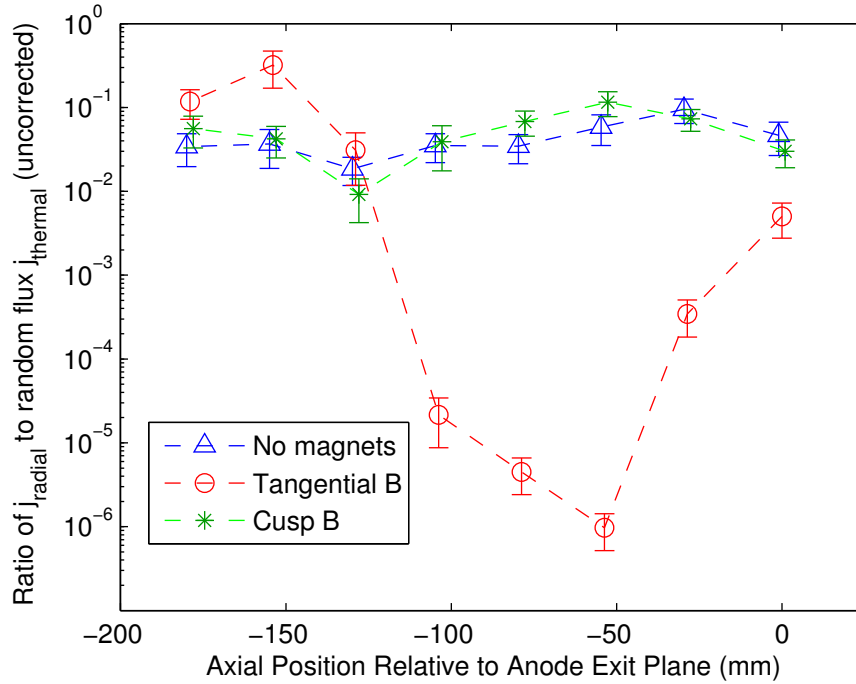


Figure 6.7: Ratio of measured radial current density to electron random thermal current (flux) along the near-anode region at 10.7 kA. Electron thermal current is calculated using classical flux uncorrected for B field effects.

pared to the electron Debye length (order of micrometers). Thus, we expect that the anode sheath does not extend far enough (order of several Debye lengths) to prevent the motion of the electrons just outside of the sheath from entering the sheath and impacting the anode within the scale of their Larmor radius orbits. However, the electrons that are effectively lost to the anode surface must be replenished by diffusion of electrons from the plasma further away, in which electrons must transport across the B field.

In an attempt to make a rough order-of-magnitude correction to the electron random thermal current in the presence of the B fields, we consider scaling arguments based on diffusion and the diffusion coefficient. As discussed in Section 6.1, the diffusion coefficient D is a consequence of the random walk motion of particles and collisions, with $D \sim \frac{(\text{step size})^2}{(\text{time between collisions})}$. We showed in equations 6.20 and 6.19 that the diffusion coefficient parallel to the B field is effectively unchanged, while the diffusion coefficient perpendicular to the B field is greatly reduced by the Hall parameter.

In the direction perpendicular to the B field, electron motion is associated with step sizes on the scale of the Larmor radius rather than the mean free path, resulting in this reduction in the diffusion coefficient. Therefore, we might argue that the electron flux perpendicular to the B field lines will be impeded in a similar way. This matters because our number density estimates with the triple Langmuir probe were obtained roughly 4 mm away from the anode surface. However, local Larmor orbit length scales for the electrons were smaller than this distance, typically in a range of 0.4–1.2 mm for our measurements at 10.7 kA.

For our rough order-of-magnitude estimate of the corrected electron flux, we first account for diffusion along the B field lines using D_{\parallel} and flux perpendicular to the B field lines using D_{\perp} and then assume that an effective diffusion coefficient can be written as

$$D_{effective} = \alpha D_{\parallel} + (1 - \alpha) D_{\perp} = \left(\alpha + \frac{1 - \alpha}{\Omega^2} \right) D_0 = \gamma D_0 \quad (6.39)$$

$$\gamma \equiv \left(\alpha + \frac{1 - \alpha}{\Omega^2} \right) \quad (6.40)$$

where α is a ratio to account for what fraction of the total B field is in the radial direction (equivalently, the sine of the angle at which the B field vector intercepts the anode surface). This ratio α is given by

$$\alpha = \frac{|B_r|}{\sqrt{B_r^2 + B_{\theta}^2 + B_z^2}} \quad (6.41)$$

where B_r , B_{θ} , and B_z are the radial, azimuthal, and axial components of the B field, respectively. Given that the flux of electrons is proportional to the diffusion coefficient, we first assume that the flux of electrons to the surface in the direction parallel to the B field is unaffected and is simply the

classical electron flux Γ_0 given by

$$\Gamma_0 = \Gamma_{\parallel} = \frac{1}{4}n_e v_{th,e} \quad (6.42)$$

Again, we assumed here that the potential difference V_d between the anode surface and the local plasma goes to zero to find the electron “saturation” limit (before the reversal of potential to electron-attracting voltage falls is required to draw more current). This Γ_0 is appropriate for motion parallel to the B field.

Perpendicular to the B field, we then make a rough order-of-magnitude estimate for the “corrected” electron random thermal flux to the anode surface in a similar manner to the diffusion coefficient by scaling with the same Hall parameter-dependent factor to obtain

$$\Gamma_{\perp} = \frac{1}{\Omega^2} \Gamma_0 \quad (6.43)$$

and thus estimate an effective overall flux for the components parallel and perpendicular to the B field as

$$\Gamma_{effective} = \gamma \Gamma_0 \quad (6.44)$$

Multiplying the flux by the electron charge gives a model for the corrected estimate for the radial current density from electron random thermal flux to the anode surface in the presence of the B field

$$j_r = q_e \Gamma_{effective} \quad (6.45)$$

Figure 6.8 shows the ratio of measured radial current density to the radial thermal current density values calculated assuming this corrected model for the influence of the B field in the manner described above by taking $\Gamma = \Gamma_{effective}$. This corrected thermal flux results in a ratio of measured

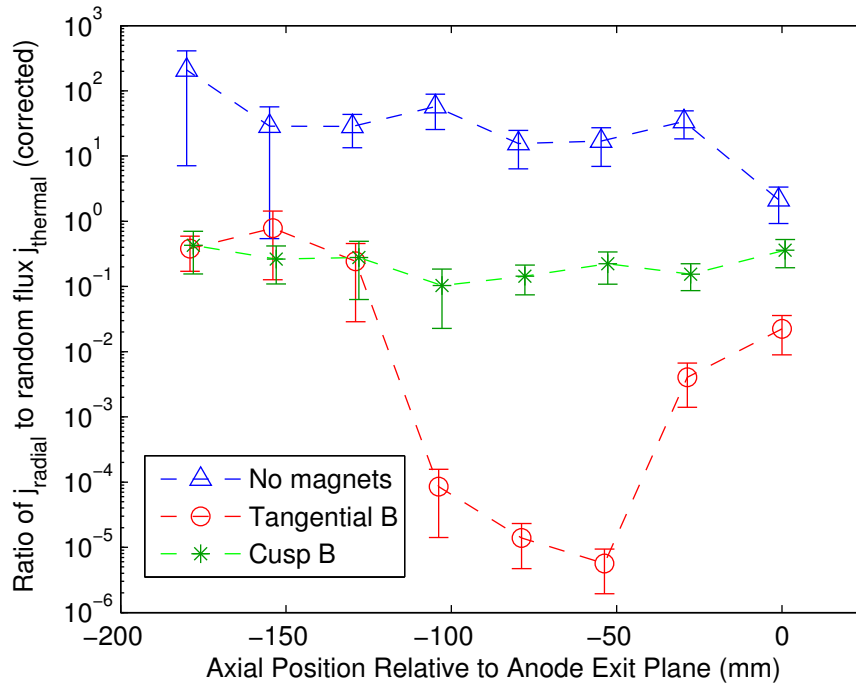


Figure 6.8: Ratio of measured radial current density to electron random thermal current (flux) along the near-anode region at 10.7 kA. Here, a correction to electron thermal current is calculated for B field effects using Hall parameter.

radial current density to calculated thermal current density that is always less than 1 with the applied B fields but always greater than 1 for the self-field case. In the self-field case, the purely azimuthal B field acts only to reduce the effective flux to the anode. The presence of radial B field components with the applied-field configurations greatly increases the effective flux to the anode surface. Given that these radial B fields also arise in the regions of highest current densities, the discharge is able to sustain the increase in current density (i.e., increased demand) via the increased flux along the B field lines (i.e., increased supply of electron flux). Further, in regions where there is little to no radial component of the applied B field, the measured current densities demanded by the discharge are also so much lower such that the limited supply of electron thermal flux across the transverse B field lines is sufficient.

This corrected model of electron flux to the anode in the presence of the B field is most likely an excessive, conservative reduction resulting in an underestimate of the actual electron flux. The true

electron flux is probably somewhere between this correction and the classical flux of $\frac{1}{4}n_e v_{th,e}$. The simple case of the 1-D diffusion problem purely perpendicular to the B field can be readily solved (cf., Krall and Trivelpiece [75]). However, this solution requires an assumed or specified length scale for the diffusion layer (i.e., treating the plasma effectively as a planar or line source some prescribed distance away from the wall). Sugawara [45] derived an expression for the electron flux purely perpendicular or purely parallel to the B field for the finite geometry of a disk probe, which does not require specifying a separate diffusion layer length scale. However, for our quasi-1-D anode geometry, a proper solution still requires some empirical knowledge about the length scale of the diffusion layer as a solution parameter and involves solving the diffusion problem with corrections to the diffusion coefficient for both perpendicular and parallel components of the B field with respect to the anode.

Nonetheless, if our corrected model is at least valid in a relative sense, it suggests that anode-intersecting applied B fields have a greatly beneficial effect on increasing the local current density that can be supplied by the electron random thermal motion relative to the self-field configuration. As the ratio of local current density demand to electron thermal flux supply is reduced by the applied B fields, lower anode fall voltages are required to augment electron random thermal current to the anode, which supports the observed reduction in the anode fall voltages with the applied B fields.

6.4 Reduced Terminal Voltages, Fluctuations, Anode Heating, and Anode Spotting

Given what we learned in Section 6.3, we can attempt to relate the anode fall reduction to the other observed effects. A significant reduction in mean terminal voltages was observed over a large range

of currents, as seen in Figure 3.4. The average input power is

$$P_{in} = VJ \quad (6.46)$$

where V is the average voltage and J is the average total discharge current. By achieving the same discharge current at lower operating voltages with the thruster, we are reducing the power for a given current. As will be discussed later in Section 6.5, this leads to an increase in thruster efficiency.

For now, let us focus on why the mean terminal voltage decreases. Consider the terms of the thruster voltage decomposed as [79]

$$V = V_{back\ EMF} + V_{ionization} + V_{thermal} + V_{fall} \quad (6.47)$$

where $V_{back\ EMF}$ is the electromagnetic induced electromotive force (“back-EMF”) term, $V_{ionization}$ is the power going into ionization divided by the current J , $V_{thermal}$ is the thermal contribution to the heating power dissipation divided by J , and V_{fall} is the anode fall voltage.

This study clearly showed a significant reduction in the anode fall voltage over much of the anode with the applied B fields. This effect was pronounced for the cusp B field at 10.7 kA and for both magnetic field configurations at 8 kA. If we compare this result to the measured reduction in mean terminal voltages in Figure 3.4, we can see that both applied B fields resulted in substantially lower terminal voltages at 8 kA and a significant reduction only in the case of the cusp applied B field at 10.7 kA. Therefore, we suggest that the reductions observed in the anode fall voltage directly lower the mean terminal voltages by reducing the V_{fall} contribution to the total discharge voltage.

Further, the power lost to the anode includes energy deposition from electron impacts, ion impacts, thermionic emission, radiation, and convection [53]. Gallimore showed that 65-95% of the total power deposition to the anode came from the current-carrying electrons. Power lost to the

anode from electron heating due to V_{fall} is reduced with the applied B fields, particularly with the cusp configuration in general and the tangential B field at lower current. The power lost to anode heating via electron bombardment is related to the radial current density as [53]

$$P = \int \Gamma_{r,e} q_e (V_{fall} + \frac{5k_B T_e}{2|q_e|}) dA = \int j_r (V_{fall} + \frac{5k_B T_e}{2|q_e|}) dA \quad (6.48)$$

where $\Gamma_{r,e}$ is the radial electron flux and the integral is taken over the entire anode surface. In general, the anode fall voltages in the regions of highest current density contribute the most to this integral. This assumes that all of the power deposited in the anode fall region is deposited to the anode. The cusp applied B field case results in a substantial reduction in V_{fall} at similar radial current densities as the self-field configuration. This would therefore result in an appreciable reduction in the overall power lost to the anode.

Next, we consider the measured reduction in intensity and frequency of the terminal voltage fluctuations. Where the applied B fields radially intercept the anode, we proposed expressions in Section 6.3 showing a markedly higher electron flux than the self-field case, as given in equation 6.44. We also observed how this could result in conditions for the measured radial current density to be sufficiently supplied by the random thermal current flux with the applied B field configurations, as shown in Figure 6.8. Several authors [21, 22, 43, 37] have attributed the transition to where the ratio of j_r to $j_{thermal,e}$ is greater than 1 as a condition for the inception of significant voltage fluctuations observed in the terminal voltage. Therefore, increasing the thermal electron flux to the anode with the applied B fields should act to mitigate transition to this condition.

Further, Uribarri [18] and Diamant [38] have directly attributed the terminal voltage fluctuations to anode spot formation on the surface of the anode. High-speed video imaging evidence that anode spots occur in our thruster was shown in Figure 3.13 for self-field operation at 9 kA, and Figure 3.14

shows evidence of anode erosion due to melting and spotting. The concentration and extinction of these anode spots were shown by Uribarri to result in the release of anode material vapor to the near-anode plasma. Measurements of local ion saturation currents and spectroscopy near the anode by these authors also showed a direct link between fluctuations in local measured plasma density and the release of anode material into the plasma flow. Such spotting behavior was strongly associated with anode erosion. Uribarri [42] proposed a capacitively-coupled model for the interactions in the anode sheath that showed how the formation and extinction of anode spots can be related to the creation of voltage fluctuations (“voltage hash”).

Additionally, both Uribarri [42] and Giannelli et al. [24, 49] described the formation of a current filamentation instability and link this to near-anode current concentration and formation of anode spots. Giannelli also described a similar capacitively-coupled voltage model wherein he linked the formation and extinction of current filaments to voltage fluctuations.

These models and experiments by Uribarri and Giannelli et al. established a relationship between current filamentation, anode spots, and the voltage fluctuations. Assuming these models are correct in their interpretation relating these phenomena, our observed reductions in the frequency and intensity of the terminal voltage fluctuations with the applied B fields strongly suggest reductions in the frequency of anode spotting events and the average current being driven to concentrated anode spots (intensity). The reductions in anode spots with the applied magnetic fields would likely be associated with notably less anode erosion over time in quasi-steady and steady-state MPD thrusters operating at ranges of high current conditions (i.e., high J^2/\dot{m}) similar to our thruster operating conditions.

In addition to measured reductions in the voltage fluctuations, we observed a reduction in the magnitude and frequency of spikes in ion saturation currents measured near the anode with the applied B fields. Examples of these ion saturation current measurements and associated PSDs were

shown in Section 5.6, and these were found to exhibit similar behavior to the terminal voltage fluctuations (relatively similar range of frequencies and attenuation of fluctuations with the applied B fields). Since ion saturation current is directly proportional to the local plasma number density, these spikes are associated with transient increases in the local number density, as was observed by Diamant [38, 37] and Uribarri [42] and linked to anode material vaporization due to anode spots and filamentary current concentrations.

The azimuthal rotational motion of the plasma induced by the applied magnetic fields could be the cause of the reduced magnitude of the ion saturation current fluctuations. The poloidal current densities interact with the applied poloidal B field to create electromagnetic Lorentz forces $j_r B_z$ and $j_z B_r$ in the azimuthal direction. Azimuthal rotational swirling motion should cause azimuthal migration of any current-concentrating filaments formed. Motion of these filaments should also lead to similar migration of local attachment points at anode spots, which would result in reduced residence time for a given anode spot at a fixed point on the anode. Reduced residence time at a particular location would decrease heating at that particular location from the shorter-lifetime spot. This would decrease the energy going into vaporizing anode surface material in a given, fixed local area. Even if the same amount of energy were going into the spots, it would effectively be spread out over a larger area. More of the anode would be heated, but less concentration of that heat at specific spot locations would yield less vaporization of anode material. Reduced vaporization of anode material seeding the near-anode plasma would be another possible explanation for the observed reduction of number density fluctuations. Given the link between terminal voltage fluctuations, anode spots, current filamentation, and anode erosion established by other studies [37, 42, 24], a reduction in residence times of local anode spot concentrations is expected to result in less erosion (shorter time for concentrated heating at a fixed point) and decreased voltage fluctuations. Coupled with the decreased anode heating from the reduced anode fall voltage, anode erosion could potentially be

reduced even further with the applied B fields.

Let us briefly summarize these inferred influences on the fluctuations of terminal voltages and ion saturation currents (i.e., number densities). In the spotting model proposed by Uribarri [42], (1) starvation caused the growth of a large anode fall; (2) current-concentrating spots formed as a response to the large anode fall, perhaps through an instability in the plasma; and (3) the formation of a spot allowed more current to flow to the anode, solving the starvation problem and causing the anode fall voltage to drop and releasing anode material. In our experiments with the applied B fields, if a given spot instead dissipates more slowly or not at all (as may be the case if it is kept continually moving over the surface by the applied B field), then the anode does not necessarily “starve” for sufficient current conduction again, and the voltage need not rise again (or at least not rise as much). Current concentrations could migrate around the anode with the applied B field without causing significant ablation of anode material. Whether this occurs with a particular spot or not is merely stochastic, so there would still be terminal voltage fluctuations (“voltage hash”). However, these voltage fluctuations would be lower in magnitude with the applied B field than the self-field case because of the probability of current-concentrating spot migration under the influence of the applied B field.

In addition, we speculate that the spikes in the number density could be associated with measurement of local transients due to other general deviations from azimuthal symmetry in the current attachment pattern, which would also be expected to cause concentrated spikes in the local number density. It is possible that the intensity and frequency of these number density fluctuations could also be reduced because of the induced swirling azimuthal motion of the plasma in response to the applied poloidal magnetic field. The induced azimuthal rotation of the plasma may act to smooth out unsteady asymmetries in the discharge pattern. For example, Hoskins [73] observed azimuthal asymmetries in self-field MPDT operation and related these asymmetries to deviations in the radial

centroid of the current discharge from the true geometric centerline of the thruster. Such asymmetries are supported by evidence from high-speed video images of our thruster in self-field operation in Figure 5.24. These images show fluctuations in the luminous discharge regions near the thruster exit plane, suggesting unsteady oscillations in the thruster discharge pattern at high currents as another possible mechanism for number density fluctuations. The induced rotational motion with our applied magnetic fields could potentially have a gyroscopic stabilizing effect against such asymmetries, which would act to reduce fluctuations in the local number densities in the near-anode region.

Lastly, distinct peaks were observed typically in the range of 30–60 kHz in the power spectral density (PSD) plots of the terminal voltage signals and approximately 15–60 kHz in the PSDs of the ion saturation current fluctuations at 10.7 kA and 8 kA. In addition to the relationship to the frequency of formation and extinction of anode spots, these frequency-domain peaks could be associated with excitation of wave oscillations in the plasma near the low-frequency ion acoustic or Alfvén modes. Tikhonov et al. [44] measured ion acoustic instability driven waves in conditions typically associated with onset. Tilley et al. [47] and Mikhailovskii et al. [80] also described a drift cyclotron instability (DCI) that occurs at frequencies near the harmonics of the ion cyclotron frequency. Since the ion cyclotron frequency is on the order of 10–100 kHz in our plasma conditions, such wave instabilities could be a possible source of the observed peaks in the PSDs. Alternatively, these peaks could simply be associated with resonance at the characteristic frequencies of the L-R-C (inductance-resistance-capacitance) circuit effectively formed by the plasma discharge and sheath themselves. Such a view is a simple extension of the R-C model of capacitively-coupled voltage fluctuations created in the near-anode region in response to spot formation and extinction proposed by Uribarri [42] and Giannelli [24]. Nonetheless, the identification of a similar range of frequencies of ion saturation current fluctuations and terminal voltage fluctuations suggests that the mechanism driving the terminal voltage fluctuations is also likely a process that can cause local plasma density

fluctuations (e.g., anode spotting, unsteady plasma current pattern fluctuations, and plasma waves).

6.5 Effect on Thrust and Efficiency

Finally, we consider the voltage-current response of the thruster in the three magnetic configurations and attempt a first-order comparison of performance parameters. Namely, we estimate the thrust, specific impulse, and thrust efficiency for our three configurations.

The thrust, T_{total} , will include multiple components and can be expressed as [16]

$$T_{total} = T_{self\ field} + T_{Hall} + T_{swirl} + T_{thermal} \quad (6.49)$$

$T_{self\ field}$ is the contribution from the poloidal current densities crossed with the self-generated azimuthal B field, which creates radially pinching ($j_z B_\theta$) and axially blowing ($j_r B_\theta$) force densities. This is the only component of thrust that is present in the self-field case. With the applied B fields, three additional terms arise. T_{Hall} is the thrust associated with the azimuthal current crossed with the applied poloidal B field, which creates pinching ($j_\theta B_z$) and blowing ($j_\theta B_r$) force density components. T_{swirl} is the thrust associated with the conversion of the azimuthal rotational momentum into axial kinetic energy through expansion in the magnetic field as the plasma exits the thruster. T_{swirl} also results in inertial centrifugal forces on the plasma radially outward, counteracting the direction of the electromagnetic pinching forces. $T_{thermal}$ is the thermal component of the thrust associated with resistive heating and expansion of the plasma through a nozzle (physical or magnetic), but is generally only significant for higher flow rates, where the MPD thruster acts more like an electrothermal arcjet.

The applied-field thrust terms are complicated to model for our thruster conditions. While others have done so for the case of applied-field MPD thrusters with significantly higher relative B

field magnitudes and with much lower curvature (mostly strong axial B fields) than we have used in our thruster, such models would not be appropriate for our thruster. For simplicity, we will only calculate the thrust from the self-field term for comparison. This will give us a lower bound estimate for the thrust of our applied-field cases, as the thrust will likely be even higher than the self-field term alone with the applied magnetic fields (as evidenced by measurements of applied-field MPD thruster performance by various authors [16, 81, 61, 60, 59]).

We calculate a rough estimate of the self-field thrust given by the modified form for the Maecker formula derived by Jahn [20], given by

$$T = bJ^2 \quad (6.50)$$

where T is the thrust, μ_0 is the permeability of free space, r_a is the anode radius, r_c is the cathode radius, J is the total thruster discharge current, and b is a constant defined as

$$b \equiv \frac{\mu_0}{4\pi} \left(\ln\left(\frac{r_a}{r_c}\right) + \frac{3}{4} \right) \quad (6.51)$$

This formula for the thrust accounts for the self-field electromagnetic forces and pressure over the thruster discharge volume and also accounts for current attachment over the front face of the cathode in the expression for b .

The specific impulse can be calculated directly from the average effective exhaust velocity, u_{ex} , given the definition

$$I_{sp} \equiv \frac{u_{ex}}{g_0} = \frac{1}{g_0} \frac{T}{\dot{m}} \quad (6.52)$$

where \dot{m} is the mass flow rate and g_0 is a constant given by the gravitational acceleration at Earth's surface, 9.807 m/s^2 .

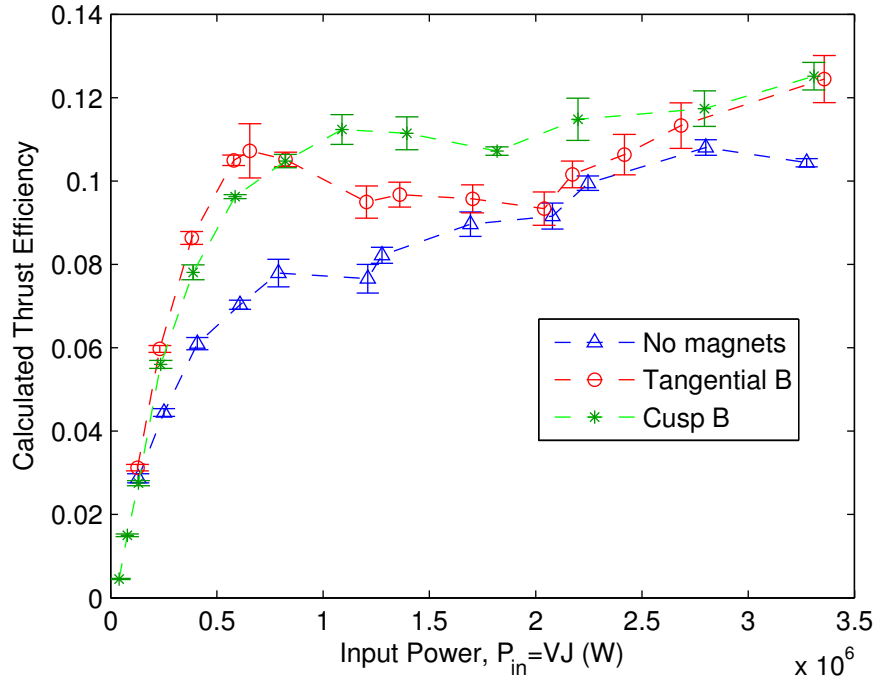


Figure 6.9: Calculated thrust efficiency for the three magnetic configurations.

The thrust efficiency can then be calculated as

$$\eta = \frac{P_{jet}}{P_{in}} = \frac{\frac{1}{2}T u_{ex}}{P_{in}} = \frac{T^2}{2\dot{m}VJ} = \frac{b^2 J^3}{2\dot{m}V} \quad (6.53)$$

where P_{jet} is the power in the thrust jet, $P_{in} = VJ$ is the electrical input power, and V is the terminal discharge voltage.

Figures 6.9, 6.10, and 6.11 show the calculated estimates of efficiency, thrust, and specific impulse, respectively, versus input power for our three magnetic configurations. The uncertainties shown only account for propagated errors from the measured data. The error bars do not include any uncertainty for the model itself. The dashed lines between data points are merely to guide the eye, not to suggest any specific functional dependence.

Note that the overall magnitude of the efficiency is rather low. This is because we were conducting our operating tests with argon, which is a particularly inefficient propellant (ionization losses,

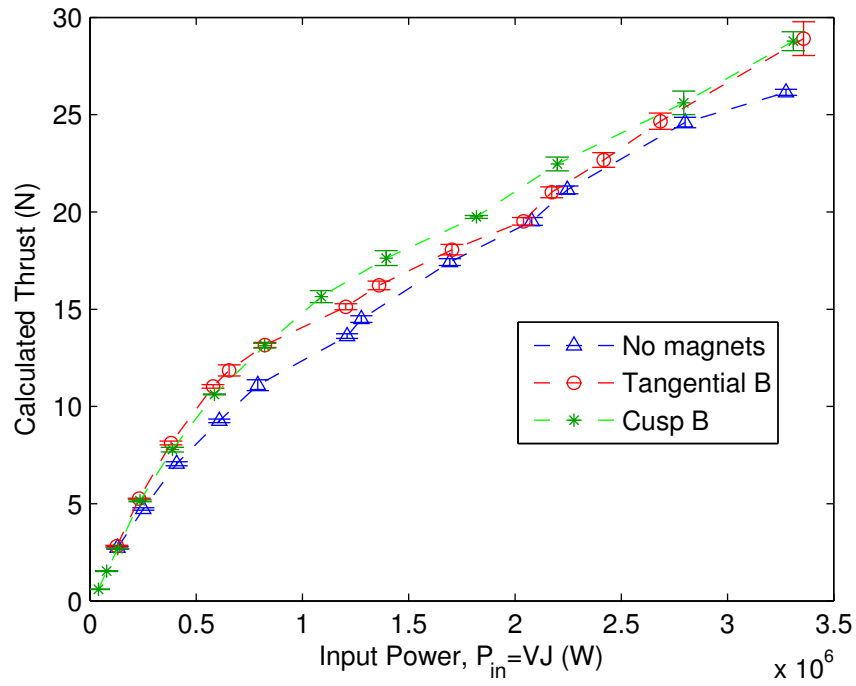


Figure 6.10: Calculated thrust (N) for the three magnetic configurations.

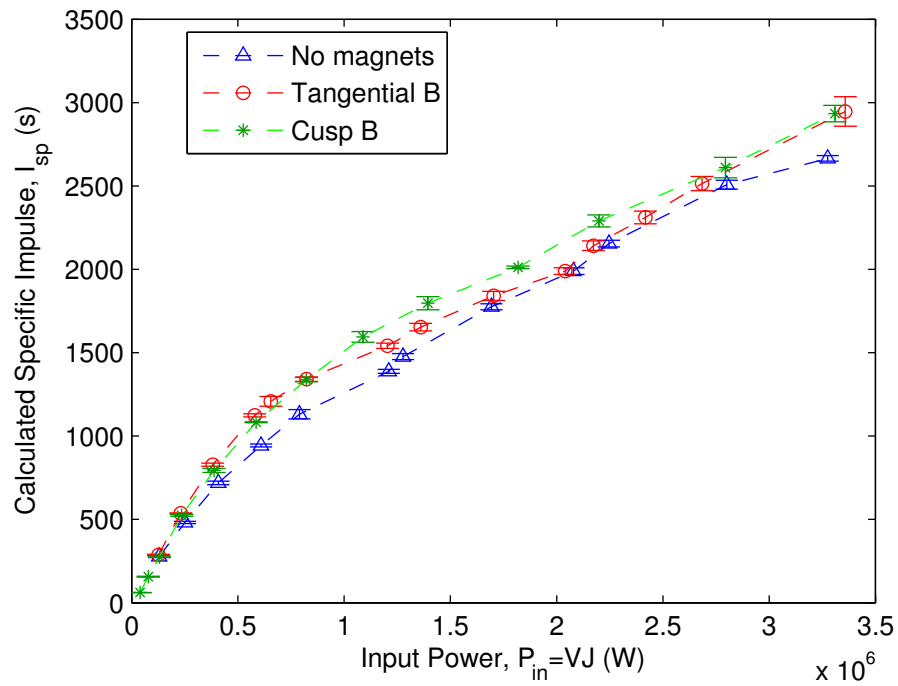


Figure 6.11: Calculated I_{sp} (s) for the three magnetic configurations.

high particle mass, energy lost to multiply-ionized species, etc.). For example, in the self-field Princeton Benchmark Thruster, Choueri and Ziemer [28] measured a range of approximately 7–14% efficiency with argon at 1 g/s over a range of I_{sp} from 800 s to just over 3000 s. Notably higher efficiencies were obtained with argon at higher flow rates.

For our thruster, consider the relative efficiencies, whose general form and trends should also be seen at much higher efficiencies with other propellants such as lithium. Overall, we see a substantial increase in the efficiency with the applied B field configurations than with the self-field configuration. Also, we see modest improvements in thrust and specific impulse with the applied B fields. These results are directly associated with the improvements from the applied B fields' effect on reducing the mean terminal discharge voltages over a wide range of currents, as previously seen in Figure 3.4. Again, these results should only improve if we were able to take into account the additional components of the thrust introduced by the applied B field.

For example, relative to the self-field case, we estimate a 41% increase in efficiency with the tangential applied B field and 28% increase with the cusp applied B field at 400 kW. We also calculate a 35% increase in efficiency with both applied B fields at 800 kW. The cusp applied B field has a particularly pronounced increase in efficiency over a large range of power levels. The cusp applied B field still improves efficiency by 17% even at 2.2 MW. The tangential B field case maintains its beneficial increase in efficiency at least to approximately 1.7 MW.

Overall, we observe an impressive relative improvement in the estimated efficiencies and modest increases in thrust and specific impulse at a given power for the thruster with the applied B field configurations, and this result is a direct consequence of the beneficial terminal voltage reduction effect of the applied B fields. The calculated thrust, specific impulse, and efficiency that we present here for the applied magnetic field cases should only increase further if the applied-field thrust components were included.

6.6 Summary and Conclusions

The goal of this work was to investigate the effects of externally-applied magnetic fields at modest field strengths on the plasma discharge and examine the prospect of their use for mitigating the behaviors associated with onset. In particular, we posed the following questions:

1. Can we mitigate behaviors such as the large-amplitude terminal voltage fluctuations and large anode fall voltages with applied magnetic fields primarily focused on the near-anode region?
2. What are the effects of the applied magnetic fields on the plasma properties and current transport in the thruster plasma discharge, particularly in the near-anode region?

The issues of onset voltage fluctuations and large anode fall voltages are linked to anode spotting and anode erosion (a lifetime issue), as well as power lost to the anode (an issue for efficiency). Therefore, the attempt to mitigate these onset behaviors is ultimately related to the desire to improve efficiencies and lifetimes in future MPD thrusters. We developed a new MPD thruster, applied-field magnets, associated driving circuitry, and a new set of plasma diagnostic probes to address these questions. The thruster was operated in 1 ms quasi-steady pulses at 1 g/s mass flow rate with argon over a range of power levels and currents from 36 kW (20 V, 1800 A) to 3.3 MW (255 V, 13.1 kA) in configurations without magnets (self-field), with applied tangential B field, and with applied cusp B field.

This investigation identified significant beneficial reductions in onset-related behaviors with the applied magnetic fields relative to self-field operation. Indeed, over a broad range of currents, the amplitude and frequency of the voltage fluctuations were reduced, the anode fall voltages were greatly lowered, and the mean terminal voltages were decreased. These results imply substantial improvements in efficiency and lifetime are likely to be obtained through the use of appropriately designed applied magnetic fields to locally influence near-anode phenomena

that drive onset.

Consider each of these interrelated findings. A primary finding was that the current pattern and current densities redistributed to follow the applied poloidal magnetic field lines, which created increased conduction paths to the anode. This led to shifts in the current pattern inside the plasma discharge region and the current densities along the anode. This shift was most pronounced for the tangential applied B field configuration, for which the current pattern moved notably upstream along the anode to attach where the applied B field lines curved to intersect the anode. This shift was shown to be driven by conduction that was increased along the directions parallel to the B field and reduced in directions perpendicular to the B field. Also, increased electron temperatures were measured in regions identified as having high azimuthal current densities induced by the applied B fields.

A second major finding was that the anode fall voltage is substantially reduced with both applied magnetic field topologies over a large range of currents. At 8 kA, the 20 V anode fall measured in the self-field configuration was completely eliminated in both applied-field configurations. At 10.7 kA, the tangential B field had little benefit, but the cusp applied B field decreased anode fall from 45-83 V down to 15 V or lower along much of the anode. We interpreted this result as also caused by the increased conduction to the anode along the anode-intersecting applied B field lines, which results in a substantial reduction in the local electric field required to sustain the radial current densities at the anode.

The amplitude and frequency of the voltage fluctuations were also reduced over a broad range of currents with the applied fields. The standard deviations of the fluctuations were lowered by 37–49% at 8–9 kA with both applied B fields, and the cusp applied field still exhibited a 15% decrease at 10.7 kA. The self-field case transitioned to voltage spikes greater than 10% of the mean voltage circa 6 kA. The current threshold at which the rapid increase in the magnitude and frequency of the

voltage spikes occurred was typically increased by 1–2 kA with the applied fields. Nonetheless, for a given operating current up to approximately 10.7 kA, the applied fields consistently reduced the magnitude of the voltage fluctuations. Above 10.7 kA, the voltage fluctuations for the applied-field cases generally approached similar values as without the magnets.

Enhanced electron mobility to the anode along the anode-intercepting applied B field lines results in an increase in the electron random thermal flux to the anode. The associated reduction in anode fall voltage means there is a decreased electron-attracting potential for accelerating electrons to the anode. This results in reduced electron kinetic energy deposited to the anode, which decreases power lost to the anode in general (a benefit for overall efficiency) but also reduces the local power deposition at anode spot concentrations. This should directly result in less energy going into vaporization of anode material, and thus less anode vapor to seed the near-anode plasma. This is consistent with measured decreases in the ion saturation current spikes (i.e., number density spikes) with the applied magnetic fields, and the similar range of frequencies observed in the PSDs for both the terminal voltage fluctuations and ion saturation current spikes. The applied fields also induce azimuthal rotation of the plasma, which may reduce fluctuations in local number densities in multiple ways (cf., discussion in Section 6.4). In particular, the applied B fields should cause azimuthal rotational migration of any current-concentrating filaments formed. Motion of these filaments should also lead to similar migration of local attachment points at anode spots, which would result in reduced residence time for a given anode spot at a fixed point on the anode. High-speed video imaging evidence of anode spots occurring in our thruster in self-field operation at 9 kA was shown in Figure 3.13. Given the link between anode spots, current filamentation, and anode erosion established by other studies [37, 42, 24], then a reduction in residence times of local anode spot concentrations is expected to result in less erosion (shorter time for concentrated heating at a fixed point) and decreased voltage fluctuations.

A final relation back to the mean terminal voltages and efficiency can be made. The applied B fields resulted in a significant reduction in the mean terminal voltages, with decreases as large as 31% at 9 kA. For the cusp applied B field, terminal voltages were moderately reduced over the entire range of discharge currents. The tangential B field lowered terminal voltages below 10.7 kA. Because the anode fall voltage is a direct contributor to the terms that comprise the total thruster discharge voltage, the anode fall reduction is proposed as the primary cause of the measured decrease in terminal voltage. Given that the electromagnetic thrust scales with the square of the current, J^2 , these voltage decreases were shown to generate notable increases in the estimated thruster efficiency by up to 41% relative to self-field operation, as discussed in Section 6.5. Moreover, these results should only improve further if we were able to take into account the additional components of the thrust introduced by our particular applied B field configurations, for which existing applied magnetic field thrust models are not directly applicable.

Overall, these onset-mitigating improvements with the applied magnetic fields should lead to reduced anode erosion, i.e., improved thruster lifetime, and increased thruster efficiency relative to self-field operation. The measured benefits of the applied B fields were shown to be effective over a broad range of current levels at least to 10.7 kA ($J^2/\dot{m} = 115 \text{ kA}^2\text{s/g}$). Additionally, the cusp applied B field lowered terminal voltages over the entire range of currents (up to the maximum value of 13.1 kA and $J^2/\dot{m} = 172 \text{ kA}^2\text{s/g}$ studied and potentially higher). Given that J^2/\dot{m} has been shown to be one of the characteristic scaling parameters for MPD thrusters [14, 79, 62], we would expect that these relative advantages should translate to other MPD thrusters operating at a similar range of values. This also implies that if stable thruster operation can be achieved at lower mass flow rates in this thruster or other similar MPD thrusters (e.g., perhaps physically smaller geometry to increase local number densities for stable arc initiation), these beneficial effects could be observed at even higher discharge currents. Such higher-current operation should

directly result in higher thrust and efficiencies, as shown in Section 6.5. In addition, because others have identified that the critical value of J^2/\dot{m} where transition to onset begins scales as $\sim M_{ion}^{-1/2}$ [33], lower atomic mass propellants (e.g., lithium and hydrogen) should allow the extension of our work's findings to operation at even higher currents.

Applied magnetic fields analogous to those examined in this study should strongly be considered for application to future MPD thruster designs, experiments, and simulation efforts. The applied B fields used in this study differ from both the topologies and relative B field strengths typically used in the vast majority of conventional, so-called “applied-field MPD thrusters” (AF-MPDTs) [16]. Such AF-MPDTs generally use much higher applied B field magnitudes relative to the thruster self-field. Also, the applied B field geometries of AF-MPDTs are generally extremely axial in form, with very limited variation in curvature in the inter-electrode region. The applied B fields examined in our study were much lower in relative magnitude in the interest of localizing the applied magnetic fields to address near-anode phenomena. At the higher currents of interest for onset, our applied B fields yielded $B_{applied}/B_{selffield}$ much less than one near the outer radius at the cathode downstream face, and this ratio was only greater than one over the downstream section of the anode. Further, our applied magnetic field configurations introduced significant anode-intersecting radial components to the topologies, which was ultimately key in providing the improved electron conduction to the anode that led to many of the observed advantages. Our results suggest a distinctive and more effective approach to influencing the near-anode phenomena and mitigating the deleterious effects of onset with appropriately designed applied magnetic fields.

The results of this study suggest that the cusp applied B field is the preferred configuration over the tangential applied B field, given the broader range of currents at which the cusp case improved the onset-related phenomena. The cusp configuration gives a convenient path for the electrons to the downstream section of the anode. At increasingly higher discharge currents, the tangential applied

B field likely suffers more than the cusp case from the downstream shift in the accelerating flow field. As discharge current increases, the higher acceleration will cause number densities in general to decrease by conservation of mass in the flow. Electromagnetic radial pinching forces will also be increased with higher current and will be greater in the upstream region (higher B_θ upstream, yielding higher $j_z B_\theta$ in the radial direction) than in the downstream region, further reducing local number densities upstream. However, the tangential applied B field topology directs the higher current conduction path along applied B field lines that only turn radially outward toward the anode in this upstream region, where the number densities are more significantly reduced. Conversely, the cusp applied B field configuration directs the high current conduction path to the downstream region, where local number densities will be reduced less. A simple solution to operating more efficiently at higher currents with the tangential applied B field could be to create a similar applied B field topology but shift it downstream (e.g., by shifting the magnets farther downstream).

The results of this investigation should be extensible to both quasi-steady and steady-state MPD thrusters, as well as different propellants. The overall efficiency, in particular, should greatly improve for lower-atomic mass propellants such as lithium and hydrogen. Lithium, for example, would be a desirable propellant choice due to its low energy for the first ionization potential but high energy for the excited state and second ionization state, resulting in much less energy lost to energy sinks that would not contribute to useful thrust.

6.7 Recommendations for Future Work

The results of this study provide a number of interesting directions for potential future work. Further exploration of the trade space for applied-field topologies and relative B field strengths could be examined in future studies to identify optimal (or at least improved) operating configurations. One question to investigate is can one further extend the effective operating range of J^2/\dot{m} values

over which the identified onset-mitigating improvements occur? One approach to investigating this question could be to increase the magnitude of the applied B field with increasing thruster input power, e.g., scaling such that the ratio of the magnitude of the applied B field to the self-generated B field is held roughly constant. Another study could hold a fixed power level (constant discharge current) and examine the effect of varying the applied B field magnitude, i.e., essentially modifying the radial intercept angle of the total B field vector with respect to the anode surface.

Additionally, could a topology be identified that helps to distribute the current pattern over a wider area and thus reduce peak anode current densities, while still maintaining similarly increased performance? Lower current densities would contribute to further improvements in lifetime-limiting anode erosion due to heating. Such spreading of the anode current attachment could potentially be enabled by anode-intersecting B field lines spread over a broader region of the anode. Broadening of this attachment region could be explored both with a cusp-like applied B field with wider separation between the magnets and a tangential-like applied B field shifted further downstream.

Such questions and effects could initially be explored through modeling and simulation, followed by experiments to validate the simulated response. A detailed numerical MHD model for the bulk plasma dynamics should be coupled with an appropriate near-anode physics model of the electron transport and sheath effects. Further, to better understand the nature of the spotting events and instabilities that led to the voltage fluctuations and ultimately anode damage, a near-anode plasma-surface interactions model could be studied. The dynamics and conditions for inception of current filamentation and breakdown of azimuthal symmetry in the diffuse current pattern could be studied with a full 3-D model, as opposed to quasi-2-D models (assuming azimuthal symmetry). Including applied B fields in the model would provide insight into the azimuthal rotation or other mechanisms associated with reducing the fluctuations in the terminal voltages and near-anode number densities. In particular, the nature and source of the low-frequency (10s of kHz) peaks in the PSDs for the

terminal voltage signals and ion saturation currents could be studied from the perspectives of both induced instabilities in the plasma and a possible inductive component to the anode spotting and filamentation models proposed by Uribarri [42] and Giannelli et al. [24].

Also, direct measurements of performance (thrust, efficiency, and specific impulse) should be made to identify the absolute magnitude of the performance benefits of the applied B fields. We invoked very simplified thrust and efficiency models, which are likely conservative and underestimating performance with the applied B fields. Future studies should consider directly measuring the thrust with a thrust stand appropriate for pulsed, quasi-steady operation (e.g., a swinging gate thrust stand [28] or other method). Detailed modeling could further inform thrust and efficiency improvements. For example, identifying topologies that result in larger radial components (relative to the axial components) for the current streamlines would produce higher electromagnetic thrust. However, modeling would be needed to identify whether such configurations indeed increase overall thrust or simply increase electromagnetic thrust at larger radii at the expense of significant thrust contributions closer to the centerline.

Lastly, if facilities and resources would permit, future experiments with applied magnetic fields at these high power levels (100s of kW to several MW) should examine operation at flight-like conditions. For example, steady-state operation would validate that the observed improvements in quasi-steady operation also manifest in steady-state conditions relevant to high-power, long-duration missions. However, this would introduce challenges with steady-state, high-power supplies, increased vacuum chamber pumping requirements, and thermal challenges for cooling the electrodes and magnets. In addition, operation with propellants such as lithium would address performance questions with a propellant that is most favorable to high-efficiency operation. Lithium has some challenges and complexities for safe handling and operation. However, facilities for operating at high power with lithium as a condensable metal propellant do exist, for example, at JPL.

Appendix A

Magnetic Force Densities

The magnetic force densities can be calculated in the plasma discharge of the thruster from the Lorentz force term, $\mathbf{j} \times \mathbf{B}$, in the magnetohydrodynamic (MHD) momentum equation introduced in equation 1.2. This equation is restated here as

$$\rho \frac{D\mathbf{u}}{Dt} = \mathbf{j} \times \mathbf{B} - \nabla P + \nu \rho \nabla^2 \mathbf{u} \approx \mathbf{j} \times \mathbf{B} - \nabla P \quad (\text{A.1})$$

where ρ is the mass density, $\frac{D\mathbf{u}}{Dt}$ is the convective derivative of the center-of-mass velocity vector, \mathbf{j} is the current density vector, \mathbf{B} is the magnetic field vector, P is the pressure, and ν is the kinematic viscosity. The viscous damping term as a function of the kinematic viscosity is often small and ignored for plasma conditions of interest. The Lorentz force term, $\mathbf{j} \times \mathbf{B}$, is the electromagnetic contribution to the force densities and becomes significant at high currents. Near the centerline, the pressure gradient term dominates. The contribution to the force densities exclusively due to the poloidal current distribution can be calculated from the poloidal current densities ($\mathbf{j}_{\text{poloidal}} = \mathbf{j}_r + \mathbf{j}_z$) and the associated induced azimuthal magnetic field (\mathbf{B}_θ) as $\mathbf{j}_{\text{poloidal}} \times \mathbf{B}_\theta$. These vectors are illustrated in Figure 1.1.

The axial “blowing” component of the Lorentz force density, f_z , is given by

$$f_z = j_r B_\theta \quad (\text{A.2})$$

and the radial “pumping” component of the Lorentz force density, f_r , is given by

$$f_r = j_z B_\theta \quad (\text{A.3})$$

and acts to radially constrain the plasma. In the radial direction, electromagnetic pumping forces are balanced by the radial kinetic pressure gradient. In the axial direction, electromagnetic blowing forces and the axial kinetic pressure gradient result in acceleration of the plasma.

The azimuthal B_θ is a direct consequence of the poloidal current densities in the thruster and can therefore be related to the enclosed current, J_{enc} , as obtained via Ampere’s law in equations 4.1 and 4.2. Bellan [13] derived an expression for calculating the magnetic force densities from J_{enc} given by

$$\mathbf{j}_{\text{poloidal}} \times \mathbf{B}_\theta = \frac{1}{2\pi} (\nabla J_{enc} \times \nabla \theta) \times \frac{\mu_0}{2\pi} J_{enc} \nabla \theta = \frac{-\mu_0}{(2\pi r)^2} \nabla \left(\frac{J_{enc}^2}{2} \right) \quad (\text{A.4})$$

where μ_0 is the permeability of free space, r is the radial position, $\nabla \theta = \hat{\theta}/r$, and $\hat{\theta}$ is the unit vector in the azimuthal direction.

The expression above was used to calculate the poloidal current distribution’s contribution to the poloidal force densities (radial and axial components) using our magnetic probe array measurements and calculated J_{enc} values in the thruster discharge from Chapter 4. Figures A.1, A.2, and A.3 show vector plots of the magnetic force densities at 10.7 kA for the configurations without magnets, with tangential applied B field, and with cusp applied B field, respectively. The arrows in these plots indicate the direction and relative magnitude of the $\mathbf{j}_{\text{poloidal}} \times \mathbf{B}_\theta$ vector component of the

force densities. The positions of the anode and cathode are also shown. Current streamlines for each configuration are overlaid on the figures to show that the force density vectors are always perpendicular to the current streamlines.

Each configuration clearly identifies significant forces directed radially inward, particularly closer to the cathode and at smaller radii. The magnetic force densities predominantly pinch the discharge toward the centerline and lead to reduced plasma number densities near the anode relative to near the centerline, as was shown in Figure 5.18. At higher currents, these increased magnetic forces will contribute to the “anode starvation” associated with onset due to depletion of charge carriers in the near-anode region.

It is important to note that these calculated forces only account for the contribution of the poloidal current distribution to the force densities in the MHD equation. These calculations do not include the pressure gradient component (particularly significant near the centerline) nor the magnetic components introduced by the applied magnetic fields. An applied magnetic field would introduce additional magnetic force density components due to $\mathbf{j}_\theta \times \mathbf{B}_{\text{poloidal}}$. However, sufficient data are not available in the interior discharge to support calculation of the full components of the force densities. The data in Figures A.1 to A.3 are merely shown to illustrate the general radial pumping effect in the discharge.

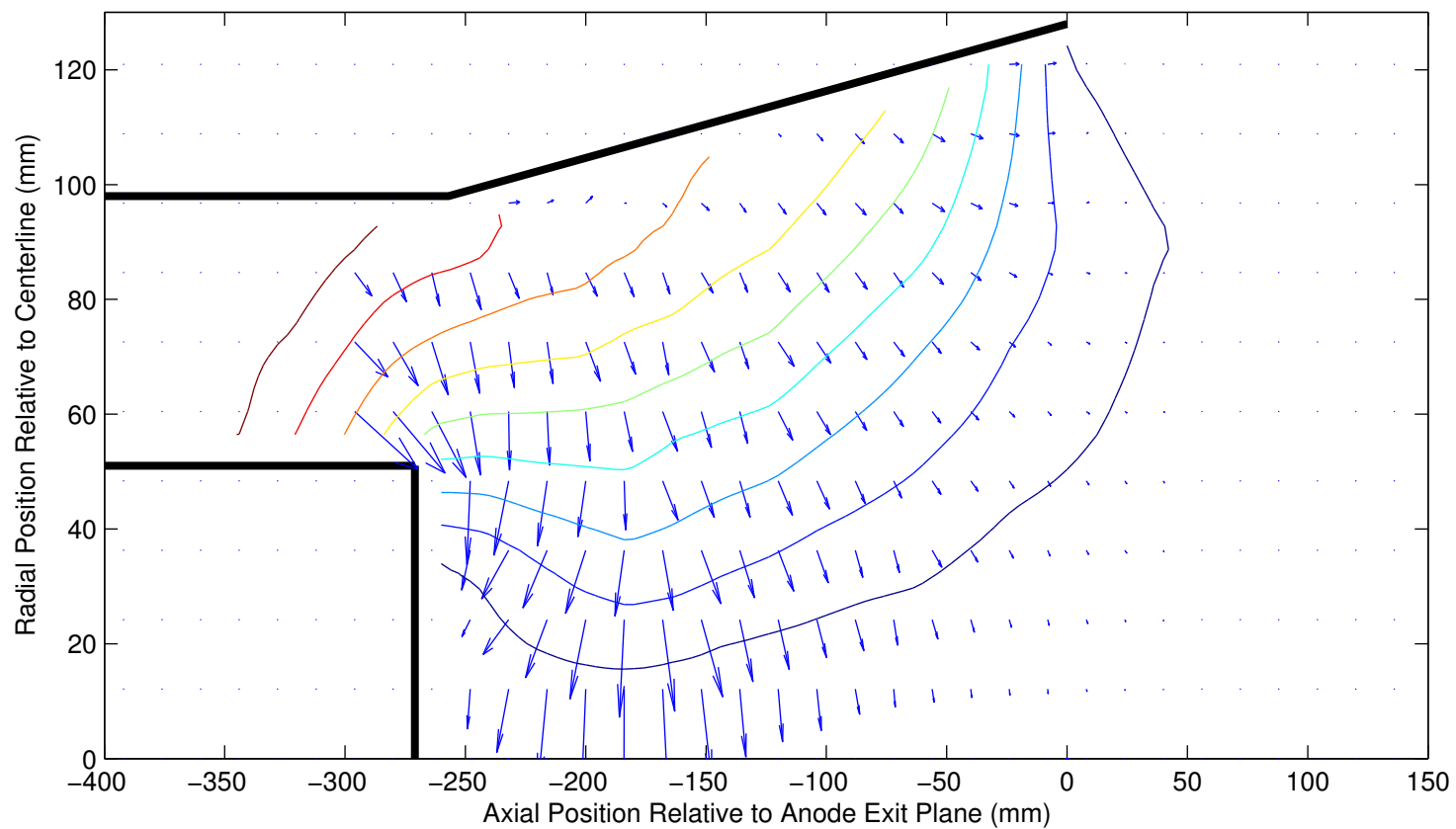


Figure A.1: Magnetic force density vector plot for the configuration without magnets at 10.7 kA. Arrows show the direction and relative magnitude of the $\mathbf{j}_{\text{poloidal}} \times \mathbf{B}_{\theta}$ vector component of the force density. Current streamlines are also shown for reference.

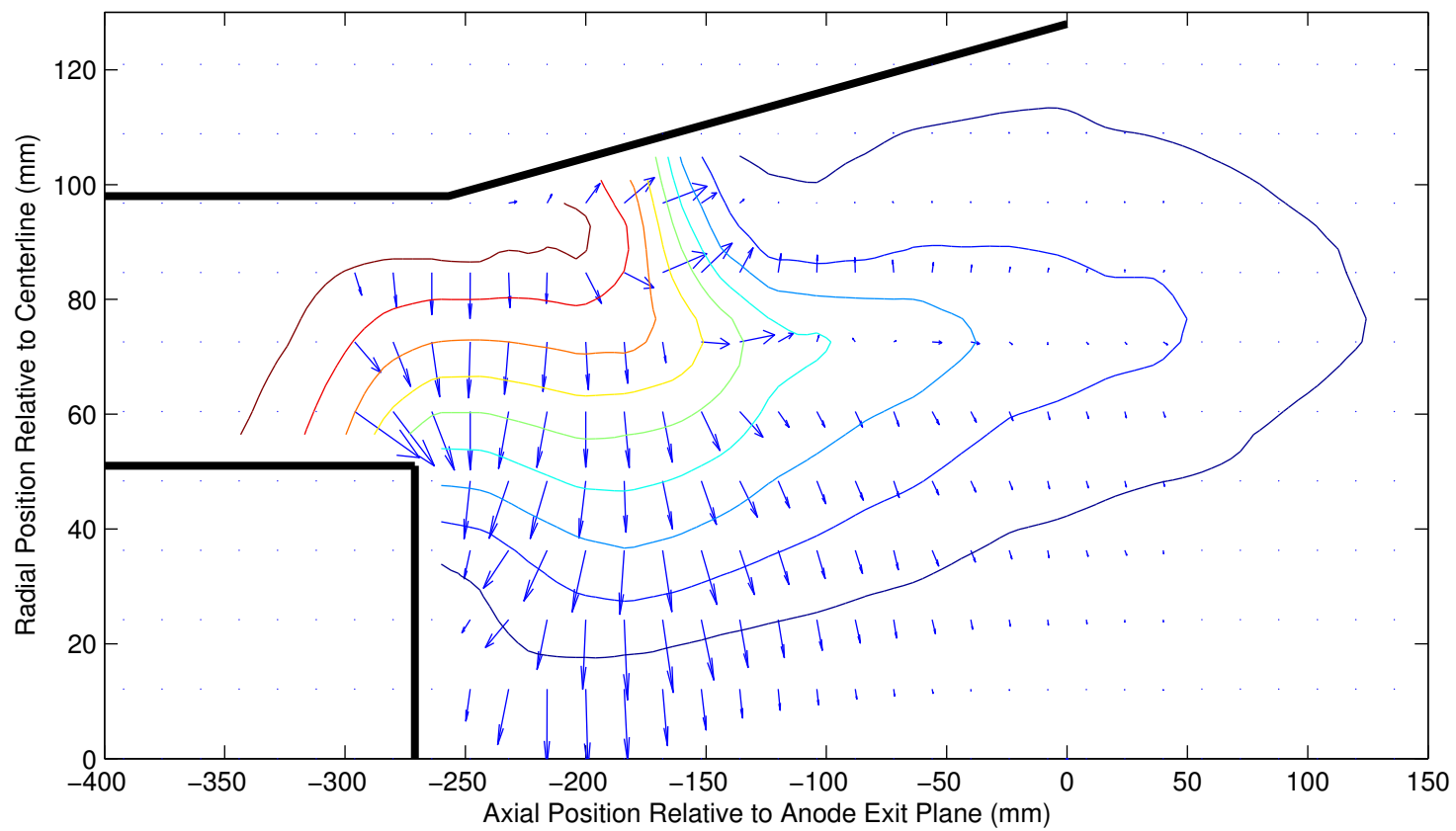


Figure A.2: Magnetic force density vector plot for the configuration with tangential applied B field at 10.7 kA. Arrows show the direction and relative magnitude of the $\mathbf{j}_{\text{poloidal}} \times \mathbf{B}_\theta$ vector component of the force density. Current streamlines are also shown for reference.

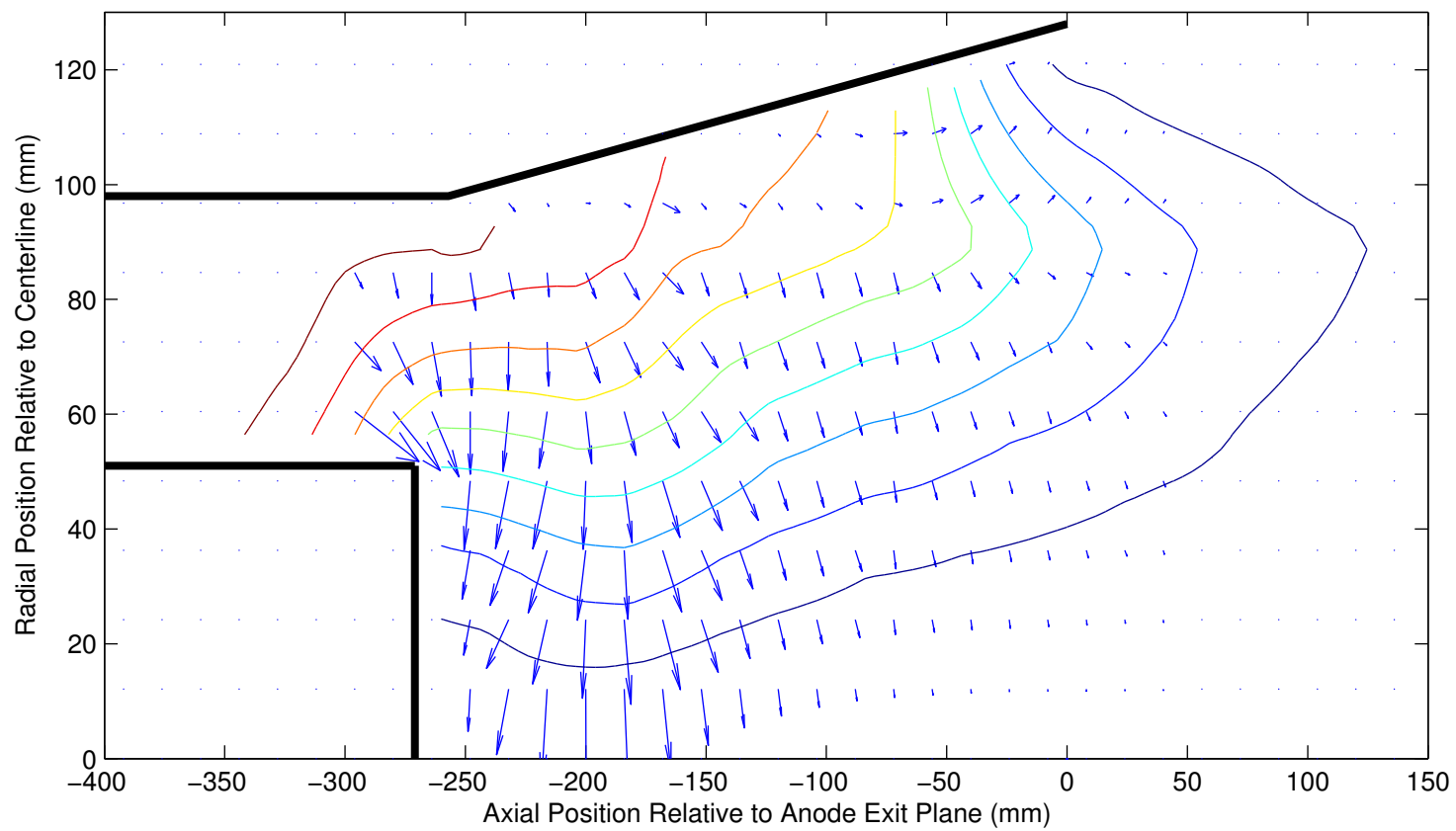


Figure A.3: Magnetic force density vector plot for the configuration with cusp applied B field at 10.7 kA. Arrows show the direction and relative magnitude of the $\mathbf{j}_{\text{poloidal}} \times \mathbf{B}_\theta$ vector component of the force density. Current streamlines are also shown for reference.

Bibliography

- [1] K. Sankaran, L. Cassady, A. D. Kodys, and E. Y. Choueiri. A survey of propulsion options for cargo and piloted missions to mars. *1st International Conference on New Trends in Astrodynamics*, Jan. 2003. College Park, MD.
- [2] R. H. Frisbee and R. C. Moeller. Identification of mission sensitivities for high-power electric propulsion systems. *41st Joint Propulsion Conference (JPC)*, (AIAA-2005-3894), July 2005. Tucson, AZ.
- [3] N. Strange, R. G. Merrill, D. Landau, B. Drake, J. Brophy, and R. Hofer. Human missions to phobos and deimos using combined chemical and solar electric propulsion. *47th AIAA Joint Propulsion Conference*, July 2011.
- [4] M. Okutsu, D. Landau, and J. Longuski. Low-thrust roundtrip trajectories to Mars with one-synodic-period repeat time. *AAS/AIAA Astrodynamics Specialist Conference and Exhibit*, (AAS Paper 05-395), Aug. 2005. Lake Tahoe, CA.
- [5] R. H. Frisbee and N. J. Hoffman. SP-100 nuclear electric propulsion for Mars cargo missions. *32nd Joint Propulsion Conference (JPC)*, (AIAA-96-3173), 1996. Lake Buena Vista, FL.
- [6] J. Gilland and S. Oleson. Combined high and low thrust for fast piloted Mars missions. NASA Contractor Report No. 190788, Sverdrup Technology, Inc., NASA Lewis Research Center, Nov. 1992.

- [7] J. A. George, K. J. Hack, and L. A. Dudzinski. Fast piloted missions to Mars using nuclear electric propulsion. *9th Symposium on Space Nuclear Power Systems*, Jan. 1992. Albuquerque, New Mexico, AIP Conf. Proc. 246, pp. 389-400.
- [8] M. Noca, J. Polk, and R. Lennard. Evolutionary strategy for use of nuclear electric propulsion in planetary exploration. *Annual Symposium on Space Nuclear Power*, 2000.
- [9] B. Palaszewski. Electric propulsion parameters for manned Mars exploration. *JANNAF Propulsion Meeting, Chemical Propulsion Information Agency*, May 1989. Laurel, Maryland.
- [10] G. P. Sutton and O. Biblarz. *Rocket Propulsion Elements*. Wiley, 2010.
- [11] L. K. Rudolph and K. M. Hamlyn. A comparison between advanced chemical and MPD propulsion for geocentric missions. *19th Joint Propulsion Conference (JPC)*, (AIAA-83-1391), 1983. Seattle, WA.
- [12] S. Samukawa et al. The 2012 plasma roadmap. *J. Phys. D: Appl. Phys.*, 45(25), 2012.
- [13] P. M. Bellan. *Fundamentals of Plasma Physics*. Cambridge University Press, 2006.
- [14] E. Choueiri. Scaling of thrust in self-field magnetoplasmadynamic thrusters. *Journal of Propulsion and Power*, 14(5):744–753, 1998.
- [15] V. P. Ageyev, V. G. Ostrovsky, and V. A. Petrosov. High-current stationary plasma accelerator of high power. *23rd International Electric Propulsion Conference*, (IEPC-93-117), 1993. Seattle, WA.
- [16] A. D. Kodys and E. Y. Choueiri. A critical review of the state-of-the-art in the performance of applied-field magnetoplasmadynamic thrusters. *41st AIAA Joint Propulsion Conference*, (AIAA-2005-4247), July 2005. Tucson, AZ.

- [17] J. E. Polk, D. M. Goebel, J. S. Snyder, A. C. Schneider, L. K. Johnson, and A. Sengupta. A high power ion thruster for deep space missions. *Rev. Sci. Instrum.*, 83(7), 2012.
- [18] L. Uribarri and E. Y. Choueiri. Relationship between anode spots and onset voltage hash in magnetoplasma dynamic thrusters. *Journal of Propulsion and Power*, 24(3):571–577, 2008.
- [19] A. C. Ducati, G. M. Giannini, and E. Muehlberger. Recent progress in high specific impulse thermo-ionic acceleration. *AIAA 2nd Aerospace Sciences Meeting*, Jan. 1965.
- [20] R. G. Jahn. *Physics of Electric Propulsion*. McGraw-Hill, Inc., 1968.
- [21] F. G. Baksht, B. Ya. Moizhes, and A. B. Rybakov. Critical regime of a plasma accelerator. *Sov. Phys. Tech. Phys.*, 18(12):1613–1616, June 1974.
- [22] A. P. Shubin. Dynamic nature of critical regimes in steady-state high current plasma accelerators. *Sov. J. Plasma. Phys.*, 2(1):18–21, Jan-Feb 1976.
- [23] H. L. Kurtz, M. Auweter-Kurtz, W. D. Merke, and H. O. Schrade. Experimental MPD thruster investigations. *19th International Electric Propulsion Conference (IEPC)*, (AIAA-87-1019), 1987.
- [24] S. Giannelli, T. Misuri, and M. Andrenucci. Current filamentation and onset in magnetoplasma dynamic thrusters. *Plasma Sources Science and Technology*, 20(3), April 2011.
- [25] H. Tahara, Y. Kagaya, and T. Yoshikawa. Quasisteady magnetoplasma dynamic thruster with applied magnetic fields for near-earth missions. *J. Propulsion*, 5(6), 1989. 713-717.
- [26] J. Polk, V. Tikhonov, S. Semenikhin, and V. Kim. Cathode temperature reduction by addition of barium in high power lithium plasma thrusters. *Space Technology and Applications International Forum (STAIF-2000)*, In *AIP Conference Proceedings*, 504:1556–1563, 2000.

- [27] D. B. Fradkin. *Analysis of Acceleration Mechanisms and Performance of an Applied Field MPD Arcjet*. PhD thesis, Princeton University, Princeton, NJ, 1973.
- [28] E. Y. Choueiri and J. K. Ziemer. Quasi-steady magnetoplasmadynamic thruster performance database. *J. Propulsion and Power*, 17(5), September–October 2001.
- [29] V. A. Petrosov et al. MPD thrusters, report no. 4, contract NIITP. Contract technical report, Russian Space Agency, Moscow, Russia, 1993.
- [30] G. A. Popov, V. Kim, V. Tikhonov, and S. Semenikhin. The final report on the contract on the research studies no. NASW-4851 between RIAME MAI and NASA. Contract technical report, Moscow Aviation Institute, Moscow, Russia, Dec. 1995.
- [31] G. A. Popov, V. Kim, V. Tikhonov, and S. Semenikhin. The fourth (final) quarterly report of contract no. 960938 between RIAME MAI and JPL. Contract technical report, Moscow Aviation Institute, Moscow, Russia, 1998.
- [32] V. Tikhonov, S. Semenikhin, J. Brophy, and J. Polk. The experimental performance of the 100 kW Li thruster with external magnetic field. *24th International Electric Propulsion Conference (IEPC)*, (IEPC-95-105), Sep. 1995. Moscow, Russia.
- [33] A. C. Malliaris, R. R. John, R. L. Garrison, and D. R. Libby. Performance of quasi-steady MPD thrusters at high powers. *AIAA Journal*, 10(2):121–122, Feb. 1972.
- [34] F. G. Baksht, B. Ya. Moizhes, and A. B. Rybakov. Critical mode in a coaxial plasma accelerator with external magnetic field. *Sov. Phys. Tech. Phys.*, 21(2):150–152, Feb. 1976.
- [35] L. Rudolph. *The MPD Thruster Onset Current Performance Limitation*. PhD thesis, Princeton University, Princeton, NJ, 1980.

- [36] H. Hugel. Flow rate limitations in the self-field accelerator. *10th AIAA Electric Propulsion Conference*, (AIAA-73-1094), 1973. Lake Tahoe, NV.
- [37] K. Diamant. *The Anode Fall in a High Power Pulsed MPD Thruster*. PhD thesis, Princeton University, Princeton, NJ, 1996.
- [38] K. Diamant, E. Choueiri, and R. Jahn. Spot mode transition and the anode fall of pulsed magnetoplasmadynamic thrusters. *Journal of Propulsion and Power*, 14(6):1036–1042, 1998.
- [39] D. Ho. Erosion studies in an MPD thruster. Master’s thesis, Princeton University, Princeton, NJ, 1981.
- [40] M. J. Boyle, K. E. Clark, and R. G. Jahn. Flowfield characteristics and performance limitations of quasi-steady magnetoplasmadynamic accelerators. *AIAA Journal*, 14(7):955–962, July 1976.
- [41] D. J. Merfeld, A. J. Kelly, and R. G. Jahn. MPD thruster performance: propellant distribution and species effects. *18th International Electric Propulsion Conference (IEPC)*, (AIAA-85-2022), Sep.-Oct. 1985. Alexandria, VA.
- [42] L. Uribarri. *Onset Voltage Hash and Anode Spots in Quasi-Steady Magnetoplasmadynamic Thrusters*. PhD thesis, Princeton University, Princeton, NJ, 2008.
- [43] A. D. Gallimore. *Anode Power Deposition in Coaxial MPD Thrusters*. PhD thesis, Princeton University, Princeton, NJ, 1992.
- [44] V. B. Tikhonov and S. A. Semenikhin. Research of plasma acceleration processes in self-field and applied magnetic field thrusters. *23rd International Electric Propulsion Conference (IEPC)*, (IEPC-93-076), 1993. Seattle, WA.

- [45] M. Sugawara. Electron probe current in a magnetized plasma. *Physics of Fluids*, 9(4):797–800, April 1966.
- [46] A. D. Gallimore, A. J. Kelly, and R. G. Jahn. Anode power deposition in magnetoplasma-dynamic thrusters. *AIAA Journal of Propulsion and Power*, 9(3):361–368, 1993.
- [47] D. L. Tilley, E. Y. Choueiri, A. J. Kelley, and R. G. Jahn. Microinstabilities in a 10-kilowatt self-field magnetoplasma-dynamic thruster. *J. Propulsion and Power*, 12(2), March–April 1996.
- [48] H. P. Wagner, H. J. Kaeppler, and M. Auweter-Kurtz. Instabilities in MPD thruster flows: 1. space charge instabilities in unbounded and inhomogeneous plasmas. *J. Phys. D: Appl. Phys.*, 31(5):519, 1998.
- [49] S. Giannelli and M. Andrenucci. Azimuthal instability of mpd thruster plasmas and inception of critical regimes. *47th AIAA Joint Propulsion Conference*, (AIAA-2011-5887), 2011. San Diego, CA.
- [50] K. Kuriki and H. Suzuki. Quasisteady MPD arcjet with anode gas injection. *14th International Electric Propulsion Conference (IEPC)*, (AIAA-79-2058), Oct.-Nov. 1979. Princeton, NJ.
- [51] A. D. Gallimore, R. M. Myers, A. J. Kelly, and R. G. Jahn. Anode power deposition in an applied-field segmented anode MPD thruster. *AIAA Journal of Propulsion and Power*, 10(2):262–268, 1994.
- [52] E. Y. Choueiri. *Electron-Ion Streaming Instabilities of an Electromagnetically Accelerated Plasma*. PhD thesis, Princeton University, Princeton, NJ, 1991.

- [53] G. C. Soulas and R. M. Myers. Mechanisms of anode power deposition in a low pressure free burning arc. *23rd International Electric Propulsion Conference (IEPC)*, (IEPC-93-194), 1993. Seattle, WA.
- [54] J. E. Foster. *An Investigation of the Influence of a Transverse Magnetic Field on the Formation of Large Anode Fall Voltages in Low-Pressure Arcs*. PhD thesis, University of Michigan, Ann Arbor, MI, 1996.
- [55] J. E. Foster and A. D. Gallimore. An investigation into the role that a transverse magnetic field plays in the formation of large anode sheath potentials. *Phys. Plasmas*, 3(11):4239–4249, Nov. 1996.
- [56] J. E. Foster and A. D. Gallimore. The effect of an auxiliary discharge on anode sheath potentials in a transverse discharge. *J. Appl. Phys.*, 81(8):3422–3432, April 1997.
- [57] R. P. Hoyt. *Optimization of Applied Magnetic Nozzles for Coaxial Plasma Accelerators*. PhD thesis, University of Washington, 1994.
- [58] J. Scheuer, R. Hoyt, K. Schoenberg, R. Gerwin, R. Moses, I. Henins, R. Mayo, and D. Black. Reduction of the anode fall in a coaxial plasma thruster with an applied magnetic nozzle. *Space Nuclear Power and Propulsion: Eleventh Symposium*, Jan. 1994. Albuquerque, New Mexico.
- [59] H. Tahara, M. Sasaki, Y. Kagaya, and T. Yoshikawa. Thruster performance and acceleration mechanisms of a quasi-steady applied-field MPD arcjet. *21st International Electric Propulsion Conference (IEPC)*, (AIAA 90-2554), 1990. Orlando, FL.

- [60] H. Tahara, Y. Kagaya, and T. Yoshikawa. Performance and acceleration process of quasisteady magnetoplasmadynamic arcjets with applied magnetic fields. *J. Propulsion and Power*, 13(5), SeptemberOctober 1997.
- [61] Y. Kagaya, H. Tahara, and T. Yoshikawa. Effect of applied magnetic nozzle in a quasi-steady MPD thruster. *28th International Electric Propulsion Conference (IEPC)*, (IEPC-03-031), 2003. Toulouse, France.
- [62] E. Y. Choueiri, A. J. Kelly, and R. G. Jahn. The manifestation of Alfvén's hypothesis of critical ionization velocity in the performance of MPD thrusters. *18th International Electric Propulsion Conference (IEPC)*, (AIAA-85-2037), Sept. 1985. Alexandria, VA.
- [63] J. H. Gilland. The effect of geometrical scale upon mpd thruster behavior. Master's thesis, Princeton University, Princeton, NJ, 1988.
- [64] C. A. Romero-Talamas, P. M. Bellan, and S. C. Hsu. Multielement magnetic probe using commercial chip inductors. *Review of Scientific Instruments*, 75(8):2664–2667, Aug. 2004.
- [65] S. L. Chen and T. Sekiguchi. Instantaneous direct-display system of plasma parameters by means of triple probe. *Journal of Applied Physics*, 36(8):2363–2375, Aug. 1965.
- [66] I. H. Hutchinson. *Principles of Plasma Diagnostics*. Cambridge University Press, 2002.
- [67] D. L. Tilley, A. J. Kelly, and R. G. Jahn. The application of the triple probe method to MPD thruster plumes. *21st International Electric Propulsion Conference (IEPC)*, (AIAA-90-2667), 1990. Orlando, FL.
- [68] J. G. Laframboise. Theory of spherical and cylindrical Langmuir probes in a collisionless Maxwellian plasma at rest. Technical report Rept. 100, University of Toronto Institute for Aerospace Studies, 1966.

- [69] A. P. Bruckner and R. G. Jahn. Exhaust plume structure in a quasi-steady MPD accelerator. *AIAA Journal*, 12(9):1198–1203, 1974.
- [70] D. B. Kilfoyle et al. Spectroscopic investigation of the exit plane of an MPD thruster. *20th International Electric Propulsion Conference (IEPC)*, (IEPC-88-027), 1988. Garmisch-Partenkirchen, W. Germany.
- [71] W. B. Thompson. *An Introduction to Plasma Physics*. Addison-Wesley Publishing Co., 1962.
- [72] R. L. Burton, S. G. DelMedico, and J. C. Andrews. Application of a quadruple probe technique to MPD thruster plume measurements. *J. Propulsion and Power*, 9(5):771–777, Sep.-Oct. 1993.
- [73] W. A. Hoskins. Asymmetric discharge patterns in the MPD thruster. Master's thesis, Princeton University, Princeton, NJ, 1990.
- [74] F. F. Chen. *Introduction to Plasma Physics and Controlled Fusion, Volume 1: Plasma Physics*. Plenum Press, New York, 1984.
- [75] N. A. Krall and A. W. Trivelpiece. *Principles of Plasma Physics*. McGraw-Hill, 1973.
- [76] D. M. Goebel and I. Katz. *Fundamentals of Electric Propulsion: Ion and Hall Thrusters*. Wiley, 2008.
- [77] L. C. Woods. *Principles of Magnetoplasma Dynamics*. Oxford University Press, 1987.
- [78] G. Caldo, E. Y. Choueiri, A. J. Kelly, and R. G. Jahn. An MPD code with anomalous transport. *22nd International Electric Propulsion Conference (IEPC)*, (IEPC-91-101), 1991. Viareggio, Italy.

- [79] E. Y. Choueiri, A. J. Kelly, and R. G. Jahn. MPD thruster plasma instability studies. *19th International Electric Propulsion Conference (IEPC)*, (AIAA-87-1067), 1987. Colorado Springs, CO.
- [80] A. B. Mikhailovskii and A. V. Timofeev. Theory of cyclotron instability in a non-uniform plasma. *Soviet Physics-JETP*, 17(3):626–627, 1963.
- [81] R. M. Myers. Applied-field MPD thruster performance with hydrogen and argon propellants. *J. Propulsion and Power*, 9(5):781–784, 1993.